

DISS. ETH NO. 29071

**NOVEL SENSING AND CONTROL STRATEGIES  
TOWARDS INTELLIGENT VENTRICULAR ASSIST  
DEVICES**

A thesis submitted to attain the degree of  
DOCTOR OF SCIENCES of ETH Zurich  
(Dr. sc. ETH Zurich)

presented by

**Konstantinos Magkoutas**

MSc in Thermal Power, Cranfield University, UK  
born on 16.03.1992  
citizen of Greece

accepted on the recommendation of

Prof. Dr. Mirko Meboldt, examiner

Prof. Dr. Med. Volkmar Falk, co-examiner

Dr. Marianne Schmid Daners, co-examiner

Dr. Med.Vet Nikola Cesarovic, co-examiner

2023



Konstantinos Magkoutas  
magkoutk@ethz.ch

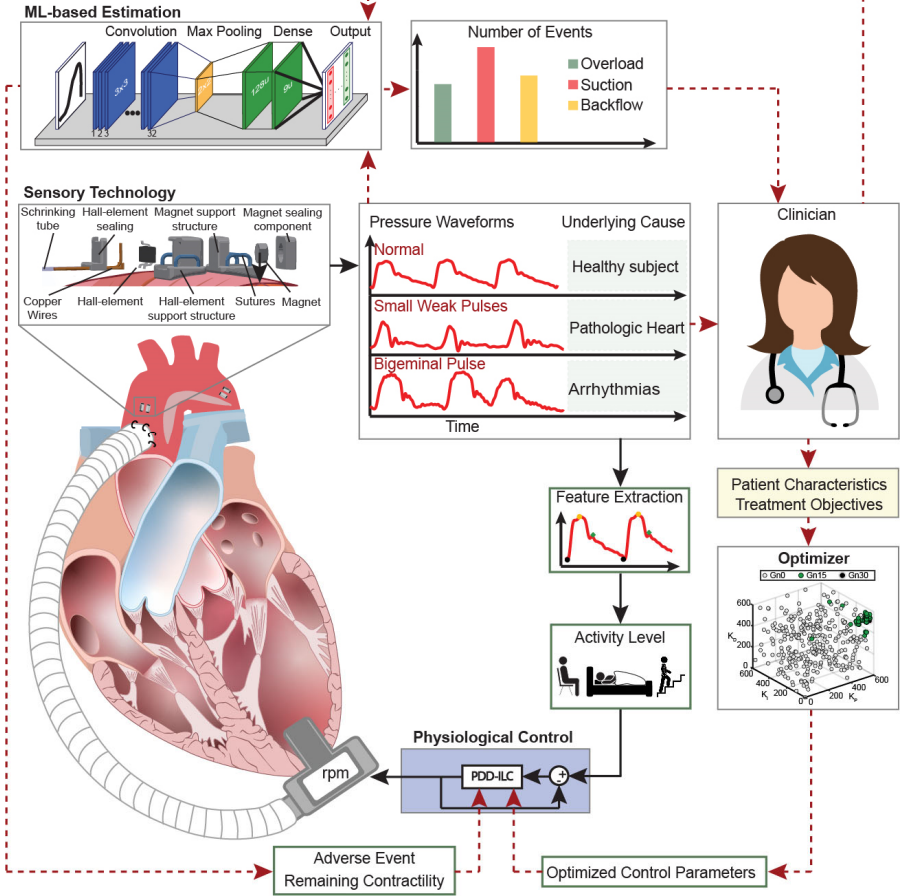
© 2023  
ETH Zurich  
Product Development Group Zurich  
Leonhardstrasse 21  
8092 Zurich  
Switzerland

**pd** | **z** Product Development Group Zurich  
Produktentwicklungsgruppe Zürich





— Closed Loop Control    - - - Monitoring & Controller Adaptation





## *Acknowledgements*

The current dissertation is the culmination of my research work carried out under the umbrella of the Zurich Heart Project, an interdisciplinary collaboration involving ETH Zurich, University Hospital Zurich and German Heart Institute Berlin. Hence, in the first place, I would like to express my gratitude to the organizers of this project and to the Stavros Niarchos Foundation for providing the funding necessary for me to conduct my research on a fascinating topic and under extraordinary conditions.

I would like also to express my sincere appreciation to the members of my doctoral committee and the people who have played a vital role in the successful completion of my Ph.D. thesis. Their support and invaluable contributions have been crucial in achieving this milestone. Below, I take this opportunity to express my personal gratitude to each of them.

Primarily, I would like to thank Prof. Mirko Meboldt for granting me this opportunity and providing guidance and support throughout the research journey. Specifically, I am grateful for his trust in my abilities, which enabled me to pursue my research endeavors and shape my projects according to my strengths and interests. I would also like to express my gratitude to my co-examiner and leader of the Zurich Heart Project, Prof. Volkmar Falk for his unconditional support and constructive feedback over the course of the past years, as well as, for the chance to visit and participate in the clinical practice at the German Heart Institute Berlin. Further, I wish to extend my appreciation to Dr. Marianne Schmid Daners, whose contribution in shaping the research environment, providing critical feedback and ensuring stability was crucial in the successful completion and subsequent publication of my research. Additionally, I would like to express my deepest gratitude to one of the most dedicated and inspiring individuals, Dr. Nikola Cesarovic, whose commitment and countless hours spent in the operating room for the execution of my experiments as well as his continuous and critical input were invaluable for the successful completion of my Ph.D. thesis.

I consider myself exceptionally fortunate to have had the opportunity to work in an environment that was highly supportive, both at the Product Development Group Zurich (Pd|z) and within the Zurich Heart consortium. In particular, I would like to thank my colleagues in Pd|z as well as Dario Fenner, Stefanie Dennis, Carole Haerry and especially, Miriam Weiskopf, Sara Mettler, Nafsika Chala, Xi Wu, Constanza Giampietro, Marcel Gort, Kai von Petersdorff Campen, Mathhias Dupuch, Vasileios Exarchos, Thomas Gwosch, Jonas Abeken and Aldo Ferrari. Their contributions were paramount to pursue my research projects.

I would also like to express my gratitude to all the students I supervised and worked with and, especially Mattia Arduini, Nicola Steffen, Raffael Zuber, Oliver Forster, Marco Heim, Linus Gloor, Leonardo Nunes, and Philip Arm, who contributed to my knowledge during our interactions and supported the findings and the publication of this research.

Furthermore, my sincere thank you goes to the “Pd|z gang”, Jan Zimmerman, Felix Wang, Nikolaos Tachatos, Mark Zander, Urs Hofmann, Seline Steffanoni, and Patrick Beutler. They created for me a positive, supportive and fulfilling atmosphere to work at and we shared great and memorable moments that led to our friendship.

Last but not least, I would like to express my deepest thank you to my family, Xanthi Gkounela and Areti Magkouta, my close friends Alex Chasoglou, Ilias Papagiannis, and Mary Kazakou, and my partner, Tatiana Tziola, for their unwavering support, patience, and encouragement throughout the course of my studies; I could not have completed this work without them.



# *Contents*

<b>Acknowledgements</b> .....	<b>i</b>
<b>Contents</b> .....	<b>iii</b>
<b>Abstract</b> .....	<b>ix</b>
<b>Zusammenfassung</b> .....	<b>xi</b>
<b>Nomenclature</b> .....	<b>xv</b>
<b>1 Introduction</b> .....	<b>1</b>
1.1 Cardiovascular Diseases and Heart Failure .....	1
1.2 Management and Treatment of Heart Failure.....	3
1.3 Ventricular Assist Devices: Evolution and Outcomes.....	6
1.4 Physiologic Control Schemes for Ventricular Assist Devices.....	9
1.5 Monitoring of Heart Failure Patients: Sensory and estimation approaches .....	13
1.6 Research Aim and Objectives .....	15
1.7 Scientific Contribution .....	17
<b>2 Continuous Monitoring of Blood Pressure and Vascular Hemodynamic Properties with Miniature Extravascular Hall-Based Magnetic Sensor</b> .....	<b>23</b>
2.1 Introduction.....	23
2.2 Methods.....	25
2.2.1 Design and fabrication.....	25
2.2.2 Working principle.....	25
2.2.3 Characterization of hall-based sensing device.....	29
2.2.4 In-vitro setup and experiments .....	29
2.2.5 In-vivo setup and experiments.....	30
2.2.6 Data post-processing .....	31
2.2.7 Statistical analysis. ....	31
2.3 Results.....	32
2.3.1 Characterization of HBSD.....	32
2.3.2 In-vitro performance validation.....	32
2.3.3 In-vivo performance validation .....	34
2.4 Discussion .....	38
2.5 Conclusions/Outlook.....	40

2.6	Competency in Patient Care and Procedural Skills .....	41
2.7	Translational Outlook.....	41
<b>3</b>	<b>Cardiac Contractility Estimation Based on Left Ventricular Pressure: Comparison of Time Series Classifiers and Graph-based Neural Networks.....</b>	<b>43</b>
3.1	Introduction.....	43
3.2	Methods and Materials .....	43
3.3	Results.....	43
3.4	Conclusions.....	45
<b>4</b>	<b>Physiologic Data-Driven Iterative Learning Control for Left Ventricular Assist Devices.....</b>	<b>47</b>
4.1	Introduction.....	47
4.2	Methods and materials .....	48
4.2.1	Cardiovascular system model.....	48
4.2.2	Numerical models of blood pumps.....	48
4.2.3	Overview of PDD-ILC .....	49
4.2.4	Physiological flow PID controller.....	55
4.2.5	Experiments for performance evaluation.....	56
4.2.6	Optimization of controller parameters.....	56
4.3	Results.....	59
4.3.1	Trajectory tracking and convergence.....	59
4.3.2	Ventricular unloading, pulsatility and hemodynamic response .....	63
4.3.3	Preload and afterload sensitivity.....	65
4.4	Discussion .....	65
<b>5</b>	<b>Genetic Algorithm-Based Optimization Framework for Control Parameters of Ventricular Assist Devices .....</b>	<b>69</b>
5.1	Introduction.....	69
5.2	Materials and Methods .....	71
5.2.1	Framework overview.....	71
5.2.2	Numerical model of the human cardiovascular system .....	71
5.2.3	Numerical model of ventricular assist devices .....	71
5.2.4	Control strategies for ventricular assist devices.....	72
5.2.5	Dynamic experiments.....	74
5.2.6	Controller optimization .....	74

5.2.7	Interpatient variability .....	78
5.2.8	Characterization of optimum controllers .....	79
5.3	Results .....	79
5.3.1	1DOF-PID and 2DOF-PID controllers .....	79
5.3.2	Optimization of PDD-ILC .....	84
5.3.3	Interpatient variability .....	86
5.3.4	Interpatient variability .....	86
5.3.5	Controller optimization for specific VAD characteristics .....	87
5.4	Discussion .....	88
5.5	Conclusions .....	89
<b>6</b>	<b>Conclusion and Outlook .....</b>	<b>91</b>
6.1	Conclusion .....	91
6.2	Outlook .....	92
	<b>Appendix .....</b>	<b>95</b>
<b>A.</b>	<b>Continuous Monitoring of Blood Pressure and Vascular Hemodynamic Properties with Miniature Extravascular Hall-Based Magnetic Sensor.....</b>	<b>95</b>
	<b>Supplemental methods .....</b>	<b>95</b>
	Appendix A1. Magnetic field expressions .....	95
	Appendix A2. Fabrication procedure of the HBSD .....	98
	Appendix A3. Extraction of cardiac cycle onset/EDP and systolic pressure .....	99
	Appendix A4. Extraction of dicrotic notch and systolic phase .....	99
	Appendix A5. Calculation of respiration frequency .....	100
	Appendix A6. Calibration procedure of the HBSD .....	100
	Appendix A7. Acceptance criteria .....	101
	Appendix A8. HBSD material selection .....	102
	<b>Supplemental tables.....</b>	<b>103</b>
	Supplemental Table A1. HBSD acceptance criteria. ....	103
	<b>Supplemental figures.....</b>	<b>104</b>
	Supplemental Figure A1. Magnetic field calculation.....	104
	Supplemental Figure A2. Fabrication procedure of the HBSD.....	105
	Supplemental Figure A3. Extraction of cardiac cycle onset/EDP and systolic pressure. ....	107
	Supplemental Figure A4. Extraction of dicrotic notch and systolic phase. ....	108
	Supplemental Figure A5. Extraction of respiration frequency.....	109

Supplemental Figure A6. Response of HBSD under cycling loading conditions. ....	110
Supplemental Figure A7. Distance and misalignment quantification after implantation. ....	111
Supplemental Figure A8. Roadmap of HBSD acceptance. ....	112
Supplemental Figure A9. Qualitative distribution of HBSD weight along the vascular wall surface.....	113
<b>B. Physiologic Data-Driven Iterative Learning Control for Left Ventricular Assist Devices.....</b>	<b>115</b>
<b>Supplemental tables.....</b>	<b>115</b>
Supplemental Table B1.....	115
Supplemental Table B2.....	116
Supplemental Table B3.....	117
Supplemental Table B4.....	119
<b>Supplemental figures.....</b>	<b>120</b>
Supplemental Figure B1. ....	120
Supplemental Figure B2. ....	121
Supplemental Figure B3. ....	122
Supplemental Figure B4. ....	123
<b>C. Genetic Algorithm-Based Optimization Framework for Control Parameters of Ventricular Assist Devices .....</b>	<b>124</b>
Appendix C1. Numerical model of Deltastream.....	124
Appendix C2. Numerical model of HeartMate 3 .....	124
Appendix C3. Numerical model of the cardiovascular system .....	125
<b>Supplemental Tables .....</b>	<b>127</b>
Supplemental Table C1.....	127
Supplemental Table C2.....	129
Supplemental Table C3.....	129
Supplemental Table C4.....	130
Supplemental Table C5.....	131
Supplemental Table C6.....	131
Supplemental Table C7.....	132
<b>Supplemental Figures.....</b>	<b>133</b>
Supplemental Figure C1. ....	133
Supplemental Figure C2. ....	134



Supplemental Figure C3. ....	135
Supplemental Figure C4. ....	136
Supplemental Figure C5. ....	137
Supplemental Figure C6. ....	138
Supplemental Figure C6. ....	139
<b>Bibliography.....</b>	<b>141</b>
<b>Curriculum vitae .....</b>	<b>157</b>
<b>List of Publications .....</b>	<b>158</b>



## ***Abstract***

Heart failure (HF) is the final common pathway of many, usually coexisting, cardiovascular diseases (CVDs) that on a global scale affects more than 64 million people. HF results in structural and functional impairment of the ventricles, rendering the heart unable to provide sufficient cardiac output for organ perfusion. Although advanced therapeutical protocols have been developed over the last decades, the absence of adequate monitoring technologies in the outpatient setting limits the surveillance of the therapy. This often results in suboptimal patient management and severe progression of HF. For these patients, the treatment is limited to only two options, namely heart transplantation (HTx) and mechanical circulatory support with ventricular assist devices (VADs). Following their technological advancements, approximately 6.000 VADs are implanted yearly, with the vast majority of the devices being continuous-flow turbodynamic pumps. VAD patients nowadays can reach similar survival rates to HTx-recipients, however, their quality of life (QoL) is diminished. This shortcoming stems from the remaining VAD-related adverse events (AE) that result in high rates of rehospitalizations. These AEs are commonly related to the inability of current VADs to imitate the physiological response with respect to cardiac output adjustment to changing perfusion demands of the patients. By lacking physiological response, VADs are prone to over- or under-pumping conditions that provoke life-threatening events of suction or overload. To pave the burden of such events, many physiological controllers have been proposed for VADs. Although some of these controllers improve the responsiveness of the VADs, none has been implemented in the clinical setting. Shortcomings that restrict the clinical implementation of physiological controllers are the lack of reliable monitoring approaches to provide the feedback parameters, the lack of adaptiveness to changes in the time-varying parameters of the cardiovascular system (CVS), and the enormous variability in patient characteristics that constitute the identification of universal control parameters challenging.

In this context, the aim of this thesis was the realization of sensory technology that enable continuous and accurate monitoring of vascular and hemodynamic properties of HF patients, as well as the development of control approaches that restore the physiological response of VADs and, at the same time, account for long-term biological changes of the patient.

To achieve the overall aim, four studies were conducted over the course of this thesis. The first study focused on sensing approaches that enable the outpatient surveillance of HF patients and provide the necessary parameters for control purposes. Hence, after exploring various sensing approaches, an extravascular, magnetic-flux sensing device was developed and validated. The sensing device was capable of capturing the waveforms of the arterial wall diameter, arterial circumferential strain and arterial blood pressure (ABP) without restricting the arterial wall. Based on the continuous ABP waveform, the sensor allowed the deduction of pulse wave velocity, respiration frequency, and duration of the systolic phase of the cardiac cycle. The implantable sensing device demonstrated unaffected performance after sterilization, immersion in liquid, and temperature changes, while it was able to accurately capture the monitored parameters in-vitro and in-vivo, under various and extreme physiologic and pathologic conditions induced by cardiopulmonary bypass support. The information hidden in the arterial blood pressure waveform, as well as other vascular properties captured with the implantable sensing device, could offer new capabilities in HF patient management, allowing patient-specific treatment and new prospects in the physiological control of VADs.

The objective of the second study was to develop a novel algorithmic approach that can exploit the hemodynamic data provided by the sensing device of the first study, to resolve the unmet need for continuous monitoring of the remaining contractility of HF patients and enable adaptive physiological controllers. To meet this objective, the estimation of the remaining contractility by applying state-of-the-art machine learning models and using left ventricular pressure (LVP) signals was assessed. Specifically, LVP data were generated on an in-vitro, hybrid

mock circulation for nine contractility levels by varying preload, afterload, pump speed, and heart rate parameters. Based on these data, the estimation accuracy of two time series classifiers and two graph-based neural networks were evaluated and compared. From the time series classifiers, the dynamic time warping nearest neighbor (DTW-NN) classifier and the support vector (SVM) classifier were selected, while from the plethora of graph-based neural networks, a pre-trained architecture and a custom architecture were implemented. The results showed that all classifiers were able to correctly estimate the contractility level, with accuracy higher than 98%; however, the SVM showed superior performance. The continuous and accurate estimation of the remaining contractility with the developed approach could substantially support patient surveillance, treatment adjustments, and real-time adaptation of the control parameters of physiological controllers.

Once the necessary technology and algorithms to allow continuous monitoring of CVS hemodynamics and time-varying properties were realized with the first two studies, the third study aimed to the development of a physiologic data-driven iterative learning controller (PDD-ILC) that achieves physiologic, pulsatile, and treatment-driven VAD response. In detail, the PDD-ILC enabled the generation of preload-adaptive reference pump-flow trajectories based on the Frank-Starling mechanism and treatment objectives, such as pulsatility maximization or left ventricular stroke work (LVSW) minimization. To eliminate the need for a model of the CVS and the pump, the tracking of the reference flow trajectories was achieved by implementing a data-driven iterative learning controller based on signals of LVP and pump flow. The physiologic responsiveness and trajectory tracking of the PDD-ILC was assessed with in-silico experiments that emulated various physiologic conditions, and compared with physiological pump flow proportional-integrative-derivative controller (PF-PIDC) (developed in this study too) as well as the constant speed (CS) control that is the current state-of-the-art in clinical practice. Under all experimental conditions, the PDD-ILC as well as the PF-PIDC showed high accuracy in tracking the reference pump flow trajectories, outperforming existing model-based iterative learning control approaches. Additionally, the developed controllers were able to meet the predefined treatment objectives resulting in improved hemodynamics and preload sensitivities compared to the CS support. The implementation of the PDD-ILC in current VADs would allow artificial pulsatility and patient-specific preload sensitivity, offering new opportunities in VAD patient management.

The realization of the PDD-ILC, which features six control parameters, showed that the identification of the control parameters with the non-intuitive, trial-and-error methods that are used nowadays results in suboptimal controllers and restricts the development of patient-specific controllers. As a result, the fourth study of this thesis was dedicated to the development of an optimization framework (GAOF) for VAD control parameters. The GAOF offered the opportunity to develop an objective function based on patient characteristics and treatment objectives and by using genetic algorithm-based optimization algorithms enabled the identification of optimum control parameters. The efficacy of the GAOF was assessed with three control structures of different complexity, two different VAD designs, and various patient disease scenarios. The results showed that the optimized controllers outperformed the hand-tuned controllers. This highlighted the potential improvement in the performance of any VAD controller by deploying the GAOF and, consequently, the possibility to increase the survival rates and enhance the quality of life of VAD patients.

In conclusion, the studies conducted in this thesis contribute to the realization of continuous monitoring of the hemodynamic status of HF patients and control algorithms that, through patient- and treatment-specific optimization, enhance the pulsatility and the physiological response of VADs. The combination and implementation of the developed algorithms and sensory technology in the clinical setting may lay the foundation for clinicians to apply and adapt their therapeutic protocols and, hence, improve the survival rates and the QoL of HF patients.

## **Zusammenfassung**

Herzsuffizienz (HI) ist eine häufige Erkrankung, die weltweit mehr als 64 Millionen Menschen betrifft. Diese Erkrankung tritt in der Regel gleichzeitig zu einer kardiovaskulären Erkrankung auf und führt zur strukturellen und funktionellen Beeinträchtigung des Herzens, die zu einer unzureichenden Versorgung der Organe mit Blut führt. Trotz fortgeschrittener Therapie gibt es immer noch Herausforderungen bei der Überwachung und Behandlung von HI-Patienten im ambulanten Bereich aufgrund des Fehlens geeigneter Überwachungstechnologien. Dies kann zu suboptimalem Patientenmanagement und schwerwiegendem Fortschreiten der Erkrankung führen. Die verfügbaren Behandlungsmöglichkeiten für Patienten mit HI beschränken sich auf Herztransplantation und mechanischer Kreislaufunterstützung mit ventrikulären Unterstützungssystemen (VADs), von denen jedes Jahr etwa 6.000 implantiert werden. Obwohl die Überlebensrate von VAD-Patienten ähnlich wie die von Herztransplantations-Patienten ist, kann die Lebensqualität durch VAD-bedingte Komplikationen (AE) beeinträchtigt sein, die zu hohen Rehospitalisierungsraten führen. Die Entwicklung physiologischer Regelung für VADs soll dazu beitragen, die Belastung von Patienten durch solche Ereignisse zu reduzieren. Allerdings gibt es nach wie vor Defizite bei der klinischen Implementierung solcher Regelung, einschließlich fehlender zuverlässiger Überwachungsmethoden, mangelnder Anpassungsfähigkeit an Veränderungen im Herz-Kreislauf-System und der großen Variabilität in den Patientencharakteristika, die die Identifizierung universeller Regelparameter erschweren. In diesem Zusammenhang war das Ziel dieser Arbeit die Umsetzung einer Sensorik, die die vaskulären und hämodynamischen Eigenschaften von HI-Patienten kontinuierlich und genau überwachen, sowie die Entwicklung von Regelungsansätzen, die die physiologische Reaktion von VADs wiederherstellen und gleichzeitig die langfristigen biologischen Veränderungen des Patienten berücksichtigen kann.

Um das Gesamtziel zu erreichen, wurden in dieser Arbeit vier Studien durchgeführt. Zunächst wurde ein extravaskulärer, magnetischer Durchflussmesser entwickelt und validiert, welcher in der Lage ist, die Signaländerung bei sich änderndem des arteriellen Wanddurchmessers, arteriellen Umfangsdehnung und arteriellen Blutdrucks (AB) zu erfassen, ohne die Arterienwand einzuschränken. Der Sensor ermöglicht auf Basis der kontinuierlichen AB-Wellenform die Ableitung der Pulswellengeschwindigkeit, der Atemfrequenz und der Dauer der Systole. Der implantierbare Sensor zeigte nach Sterilisation, Eintauchen in Flüssigkeit und Temperaturschwankungen keine Leistungseinbußen und war in der Lage, die überwachten Parameter *in vitro* und *in vivo* unter verschiedenen und extremen physiologischen und pathologischen Bedingungen, die durch kardiopulmonale Bypassunterstützung hervorgerufen werden, genau zu erfassen. Die Erfassung von Informationen, die in der Wellenform des AB verborgen sind sowie andere vaskulären Eigenschaften durch das implantierbare Messgerät könnten neue Möglichkeiten für das Management von HI-Patienten bieten. Diese ermöglichen eine patientenspezifische Behandlung und bieten neue Perspektiven für die physiologische Regelung von VADs.

Um das Ziel der zweiten Studie zu erreichen, wurde ein neuartiger Ansatz entwickelt, der auf den hämodynamischen Daten des Sensors aus der ersten Studie basiert und den Bedarf an einer kontinuierlichen Überwachung der Restkontraktilität von HI-Patienten decken und eine adaptive physiologische Regeln ermöglichen soll. Die Hypothese, dass die verbleibende Kontraktilität aus den Signalen des linksventrikulären Drucks (LVD) durch Machine Learning Modelle geschätzt werden kann, wurde geprüft. Dazu wurden LVD-Daten in einem hybriden *In-vitro*-Scheinkreislauf für neun Kontraktilitätsniveaus durch Variation der Parameter Vorlast, Nachlast, Pumpendrehzahl und Herzfrequenz erzeugt. Die Schätzgenauigkeit von zwei Zeitreihenklassifikatoren und zwei graphbasierten neuronalen Netzen wurde anhand dieser Daten bewertet und verglichen. Unter den Zeitreihenklassifikatoren wurden der DTW-NN-Klassifikator (Dynamic Time Warping Nearest Neighbour) und der SVM-Klassifikator (Support Vector

Machine) ausgewählt, während aus der Vielzahl der graphbasierten neuronalen Netze eine vortrainierte Architektur und eine benutzerdefinierte Architektur ausgewählt wurden. Die Ergebnisse zeigen, dass alle Klassifikatoren das Kontraktilitätsniveau mit einer Genauigkeit von über 98 % korrekt schätzen konnten, wobei die SVM die beste Performance zeigte. Durch diesen entwickelten Ansatz könnte die kontinuierliche und genaue Schätzung der verbleibenden Kontraktilität die Patientenüberwachung, Behandlungsanpassungen und die Anpassung der Parameter physiologischer Regler in Echtzeit wesentlich unterstützen.

In den ersten beiden Studien wurden die Technologie und die Algorithmen für die kontinuierliche Überwachung der Hämodynamik und der zeitlich veränderlichen Eigenschaften des CVS entwickelt. Ziel der dritten Studie war es, einen physiologischen, datengesteuerten, iterativ lernenden Regler (PDD-ILC) zu entwickeln, der ein physiologisches, pulsatile und behandlungsgeregeltes Ansprechen des VAD ermöglicht. Der PDD-ILC ermöglicht die Generierung von vorlastadaptiven Referenz-Pumpenfluss-Trajektorien basierend auf dem Frank-Starling-Mechanismus und Behandlungszielen wie der Maximierung der Pulsatilität oder der Minimierung des LVSW. Die Verfolgung der Referenzfluss-Trajektorien wurde durch die Implementierung einer datengesteuerten, iterativ lernenden Regelung auf der Grundlage von Signalen der LVD und des Pumpenflusses erreicht, um ein Modell des CVS und der Pumpe zu vermeiden. Der PDD-ILC wurde mit dem physiologischen proportional-integrativen-derivativen Pumpenflussregler (PF-PIDC) sowie mit der Konstantdrehzahlregelung (CS) verglichen. Der PDD-ILC und der PF-PIDC zeigen eine hohe Genauigkeit bei der Verfolgung der Referenz-Pumpenstromkurven und übertrafen damit die bestehenden modellbasierten iterativ lernenden Regelungsansätze. Die Implementierung der PDD-ILC in aktuelle VADs würde eine künstliche Pulsatilität und eine patientenspezifische Vorlastsensitivität ermöglichen und damit neue Möglichkeiten im VAD-Patientenmanagement eröffnen. Der physiologische Ansprechverhalten und die Verfolgung der Trajektorien des PDD-ILC wurden mit In-silico-Experimenten bewertet, bei denen verschiedene physiologische Bedingungen nachgebildet wurden. Unter allen experimentellen Bedingungen erreichten der PDD-ILC und der PF-PIDC die vordefinierten Behandlungsziele und führten im Vergleich zur CS-Unterstützung zu einer verbesserten Hämodynamik und Vorlastsensitivität.

Die Umsetzung des PDD-ILC mit sechs Regelungsparametern hat gezeigt, dass die Identifikation der Regelungsparameter durch die heute üblichen, nicht intuitiven Trial-and-Error-Methoden zu suboptimalen Reglern führt und die Entwicklung von patientenspezifischen Reglern einschränkt. Aus diesem Grund war die vierte Studie dieser Arbeit der Entwicklung eines Optimierungsrahmens (GAOF) für VAD-Regelungsparameter gewidmet. Die GAOF ermöglichte die Entwicklung einer Zielfunktion auf Basis von Patientenmerkmalen und Behandlungszielen sowie die Verwendung von auf genetischen Algorithmen basierenden Optimierungsalgorithmen zur Ermittlung der optimalen Regelungsparameter. Die Wirksamkeit der GAOF wurde anhand von drei unterschiedlich komplexen Regelungsstrukturen, zwei verschiedenen VAD-Designs und verschiedenen Krankheitsszenarien der Patienten bewertet. Die Ergebnisse zeigten, dass die optimierten Regler eine bessere Leistung erzielten als die manuell abgestimmten Regler. Dies zeigt das Potenzial zur Verbesserung der Leistung jedes VAD-Reglers durch den Einsatz der GAOF und somit die Möglichkeit, die Überlebensraten zu erhöhen und die Lebensqualität von VAD-Patienten zu verbessern.

Zusammenfassend lässt sich sagen, dass die in dieser Arbeit durchgeführten Studien zur Realisierung einer kontinuierlichen Überwachung des hämodynamischen Status von HI-Patienten und zur Entwicklung von Regelungsalgorithmen beitragen. Durch patienten- und behandlungsspezifische Optimierung wird die Pulsatilität und physiologische Reaktion von VADs verbessert. Die Kombination und Implementierung der entwickelten Algorithmen und Sensoren im klinischen Umfeld kann die Grundlage für die Anwendung und Anpassung der

Therapieprotokolle durch die Kliniker bilden und somit die Überlebensraten und die Lebensqualität der HI-Patienten verbessern.





# *Nomenclature*

## **Acronyms and Abbreviations**

ABP	Arterial Blood Pressure
ACE	Angiotensin-converting Enzyme
ACS	Arterial Circumferential Strain
AD	Arterial Wall Diameter
AE	Adverse Events
BLE	Bluetooth Low Energy
BNP	Brain Natriuretic Peptides
bpm	Beats per minute
BTC	Bridge to Candidacy
BTD	Bridge to Decision
BTR	Bridge to Recovery
BTT	Bridge to Transplantation
BW	Body Weight
CAD	Coronary Artery Disease
cfVADs	Continuous flow turbodynamic VADs
C-GNN	Custom Graph-based Neural Network
CO	Cardiac Output
Co-PF	Copulsation Pump Flow
Counter-PF	Counter Pump Flow
CPB	Cardiopulmonary Bypass
CS	Constant Speed
CSC	Constant Speed Control
CVD	Chemical Vapor Deposition
CVDs	Cardiovascular Diseases
CVS	Cardiovascular System
DAQ	Data Acquisition
DD-ILC	Data-driven Iterative Learning Controller
DH	Diseased Heart
DH-CSC	Diseased Heart Constant Speed Control
DHQB	German Heart Institute Berlin
DOF	Degree of Freedom
DT	Destination Therapy
DTW-NN	Dynamic Time Warping Nearest Neighbor
E	Extracted
EM	Extracted Mean value
ECMO	Extracorporeal Membrane Oxygenation
ED	End-diastole
EDP	End-diastolic Pressure
EDPVR	End-diastolic Pressure-volume Relationship
EF	Ejection Fraction
ES	End-systole
ESPVR	End-systolic Pressure-volume Relationship
FDA	Food and Drug Administration
FDM	Fused Deposition Modelling
FIR	Finite Impulse Response

GA	Genetic Algorithm
GAOF	Genetic Algorithm Optimization Framework
GNN	Graph-based Neural Network
HBP	High Blood Pressure
HBSD	Hall-based Sensing Device
HD	Hall Diameter
HES	Hall-effect Sensor
HF	Heart Failure
HFmrEF	Heart Failure with mildly reduced Ejection Fraction
HFpEF	Heart Failure with preserved Ejection Fraction
HFrEF	Heart Failure with reduced Ejection Fraction
HH	Healthy Heart
HM3	HeartMate 3
HMC	Hybrid Mock Circulation
HMCS	Human Cardiovascular System
HR	Heartrate
HSR	High Support Ratio
HTx	Heart Transplantation
HVI	Heart Valve Insufficiency
ICD	Implantable Cardioverter Defibrillator
ILC	Iterative Learning Control
LB	Lower Boundary
LR	Linear Regression
LSR	Low Support Ratio
LV	Left Ventricle
LVAD	Left Ventricular Assist Device
LVP	Left Ventricular Pressure
LVEF	Left Ventricular Ejection Fraction
LVSW	Left Ventricular Stroke Work
MAE	Mean Absolute Error
MAP	Mean Arterial Pressure
maxE	Maximum Error
MCS	Mechanical Circulatory Support
MSR	Medium Support Ratio
MVO	Mean Voltage Output
N48	Neodymium
NI	National Instruments
VADs	Ventricular Assist Devices
Obj	Objective
OF	Objective Function
OMM	Optimal Medical Management
OOP	Optimum Operating Point
P	Proportional
PDD-ILC	Physiologic Data-driven Iterative Learning Controller
PF-PIDC	Pump Flow Proportional-Integrative-Derivative Controller
P-GNN	Pretrained Graphic-based Neural Network
PI	Proportional-Integral
PID	Proportional-Integral-Derivative
PLA	Polylactic acid
PM	Pressure Manipulation

PPD	Pseudo Partial Derivative
PS	Pump Speed
PWV	Pulse Wave Velocity
RAAS	Renin-Angiotensin-Aldosterone System
RCC	Remaining Cardiac Contractility
RD	Reference Diameter
RMSE	Root-Mean-Square-Error
rpm	Rotations per minute
RT	Respiration Time
RQ	Research Question
SCOFD	Summation of the Cardiac Output Finite Difference
SLA	Selective Laser Stereolithography
SLM	Selective Laser Melting
SNS	Sympathetic Nervous System
SOT	Small Outline Transistor
SP	Systolic Pressure
ST	Systolic Phase Duration
STD	Standard Deviation
SVM	Support Vector
SW	Stroke Work
TAH	Total Artificial Hearts
TSC	Time Series Classifiers
TSD	Time Series Data
QoL	Quality of Life
UpB	Upper boundary
USA	United States of America
USB	Universal Serial Bus
USZ	University Hospital Zurich
UZH	University of Zurich

### Latin Symbols

$a, b, c, d$	Exponential fitting coefficients
$B_z$	Magnetic-flux perpendicular to measuring surface
$D$	Diameter
$D_0$	Initial aortic diameter
$e_j$	Predicted PF tracking error used for minimization
$H$	Matrix containing operating pressure map of pump
$I$	Pump current
$J_q$	Tracking error
$J_u$	Input vector
$k_{FS}$	Preload sensitivity
$L$	Fluid inertance
$M_s$	Uniform magnetization
$n$	number
$n_{hp}^*$	Desired pump speed output
$n_{hp,FB}^*$	Feedback desired pump speed
$n_{hp,FF}^*$	Feed forward desired pump speed
$P$	Arterial pressure
$p_{ds}$	Pressure downstream of pump

$p_{us}$	Pressure upstream of pump
$R$	Arterial wall radius
$R_m$	Subject-specific elastic moduli
$Q$	Flow-rate
$q_{bp}$	Measured pump flow
$\bar{q}_{bp}^*$	Heart cycle average pump flow
$\mathbf{q}_{bp}^*$	Time vector of the desired pump flow trajectory
$r$	Misalignment in radial direction
$r$	Pearson correlation coefficient
$S$	Sensitivity
$t$	Time
$T$	Matrix containing operating torque map of pump
$V$	Voltage
$V_m$	Measured voltage
$z$	Translation distance
$z_0$	Initial translation distance

### Greek Symbols

$\gamma$	Pitch misalignment angle
$\delta$	Arterial wall thickness
$\Delta$	Denoted change in quantity
$\varepsilon_c$	Circumferential arterial strain
$E_Y$	Elastic Young modulus
$\eta$	Learning gain
$\theta$	Rotor inertia
$K$	Ziegler-Nichols approach coefficients
$\mu$	Normalization value
$\sigma_c$	Circumferential strain
$\varphi$	Yaw misalignment angle
$\hat{\Phi}_j$	Estimate of pseudo partial derivative
$\omega$	Rotational speed

### Sub/superscript

a	Afterload
Ben.	Benchmark controller
cc	counterpulsation
co	copulsation
ds	Downstream
FB	Feedback
FF	Feed Forward
Gn	Generation
us	Upstream
m	Measured
max	Maximum
min	Minimum
mo	Multi-objective
p	Preload
ref	Reference
so	Singe objective





# 1 Introduction

Nearly half of all deaths across Europe are attributed to cardiovascular diseases (CVDs), a proportion that is 46 times the cumulative number of deaths from acquired immune deficiency syndrome, tuberculosis and malaria. To battle this silent pandemic, important prevention strategies and technological improvements in the diagnosis and treatment of CVD have been developed during the last decades. However, considering that CVDs are the outcome of an interaction between genetic susceptibility, environmental conditions, socioeconomic conditions, and lifestyle choices, factors that dictate the modern societies such as poor diet, physical inactivity, and the aging population constitute the reduction of CVD prevalence a great challenge. To forge extraordinary advances that can decline the burden of CVDs, cross-disciplinary collaborations among engineers, cardiologists, radiologists, and pathologists are required.<sup>1,2</sup>

Following this line of thought, a multidisciplinary and inter-institutional project has been developed among the University of Zurich (UZH), the University Hospital Zurich (USZ), the German Heart Institute Berlin (DHZB) and ETH Zurich. This collaborative project, named Zurich Heart, aims to develop novel technologies that improve the treatment of heart failure (HF) and enhance the physiological and biological response of ventricular assist devices (VADs) used nowadays in the clinical setting. This thesis is part of the Zurich Heart project, focusing on the development of sensing approaches that enable the implementation of physiological control strategies on the next generation of VADs, as well as on the development of control approaches that adapt the VAD output to the perfusion needs of the patients and, at the same time, they account for long-term biological changes of the patient.

In this chapter, the necessary background to identify the technological and research shortcomings in the treatment of HF patients, along with the aim and the contributions of this work are described. In detail, the global burden of CVDs, the etiology of HF, the different HF phenotypes and their effect on the hemodynamic physiology of the heart are elaborated in Section 1.1. In Section 1.2 follows the analysis of the HF treatment options, including pharmacotherapy, device therapy, and heart transplantation (HTx). Section 1.3 focuses on the advancements of the VAD technology and the outcomes of the VAD therapy regarding survival rates, hospital readmission rates, and quality of life (QoL) of the patient. The mechanisms developed and deployed by the healthy heart to regulate the cardiac output are provided in Section 1.4, along with a thorough review of different control strategies that aim to reproduce some of these native regulation mechanisms. The main problems hindering the implementation of these controllers in the clinical setting are also explained in this section. Section 1.5 elucidates the state-of-the-art in sensory and estimation approaches that are deployed for the measurement of patient's hemodynamic properties to allow the surveillance of the therapy. Finally, the aim and the objectives of this work are described in Section 1.6, while the scientific contributions are listed in Section 1.7.

## 1.1 Cardiovascular Diseases and Heart Failure

CVDs have been characterized as an emerging epidemic for more than 25 years, with their prevalence in a global scale being continuously increasing from approximately 271 million in 1990 to a staggering 550 million in 2020.<sup>2,3</sup> The high prevalence of CVDs is also accompanied by the highest mortality rates among all diseases, accounting for about 19.1 million deaths worldwide in 2020 alone.<sup>2,4</sup> Considering the trends in population growth and aging, which are

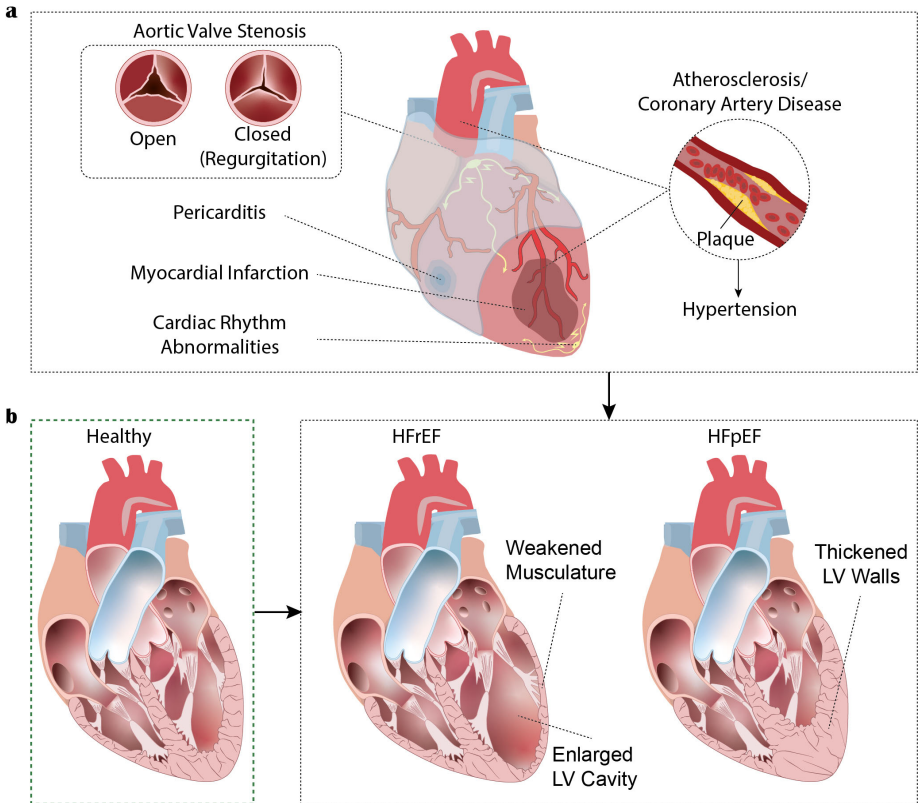


**Figure 1.1. a)** Cardiovascular diseases that result in cardiac remodeling and set a risk factor for heart failure, **b)** Remodeling of left ventricular (LV) walls under heart failure with reduced ejection fraction (HFrEF) and heart failure with preserved ejection fraction (HFpEF) phenotypes.

among the major contributing factors for CVDs development, the already crucial consequences of CVDs on health systems and socioeconomic status are expected to aggravate across the globe.<sup>1</sup>

Among all CVDs, HF is the most severe and life-threatening disease with more than 64 million people suffering from it in 2020.<sup>5</sup> In general, HF is a complex, chronic syndrome that primarily affects the elderly; however, recent statistical data show that HF incidences are also increasing among the younger population.<sup>6</sup> Pathophysiologically, HF can be defined as a progressive procedure encompassing structural and/or functional impairment of the ventricles, that constitutes the heart unable to adequately support the end-organs with oxygenated blood to meet their metabolic demands.<sup>7</sup> The etiology of HF is difficult to be uniquely defined since HF is considered the final common pathway of various, usually coexisting, CVDs. Underlying CVDs that can result in cardiac remodeling and set a risk factor for HF include cardiac rhythm abnormalities (brady- or tachycardia), coronary artery disease, myocarditis, hypertension, pericardial disease, valvular disease and hypertrophic obstructive cardiomyopathy (Fig. 1.1a).<sup>6-9</sup> This diversity in the morbidities precipitating HF significantly complicates the diagnosis and prognosis of the disease. Nowadays, the diagnosis of HF requires, but is not limited to, patient's



history data, echocardiography, cardiac magnetic resonance imaging, and blood testing to observe the level of natriuretic peptides (BNP).<sup>8</sup> The prognosis of the disease is highly dependent on the phenotype of HF, a classification that is based on the measurement of the left ventricular ejection fraction (LVEF). In detail, the first and most severe phenotype corresponds to HF with reduced EF (HFrEF), characterized by an LVEF  $\leq 40\%$  and systolic myocardial dysfunction. A failing heart classified in the HFrEF phenotype demonstrates an enlarged left ventricular (LV) cavity and weakened cardiac musculature (Fig. 1.1b) that together reduce the myocardial contraction forces. As it can be seen in the LV pressure – volume loops provided in Fig. 1.2, the reduced cardiac contractility of the HFrEF phenotype alters the end-systolic pressure-volume relationship (ESPVR), resulting in a shallower ESPVR and higher end-diastolic and end-systolic volumes. The second phenotype is predominantly characterized by diastolic myocardial dysfunction and an LVEF  $\geq 50\%$ , named as HF with preserved EF (HFpEF). This phenotype is distinguished by the thickened ventricular walls (Fig. 1.1b) that notably reduce the compliance of the heart wall. The LV pressure – volume loops for HFpEF (Fig. 1.2) show that the end-diastolic pressure-volume relationship (EDPVR) alters, resulting in higher end-diastolic pressure and LV overload. The last HF phenotype is characterized by an LVEF between the other two classes ( $40\% < \text{LVEF} < 50\%$ ), termed HF with mildly reduced EF (HFmrEF).<sup>9,10</sup>

## 1.2 Management and Treatment of Heart Failure

The management of HF patients focuses on alleviating their symptoms, improving their QoL, reducing hospitalization rates and, consequently, elongating their survival. However, considering the multifactorial etiology of HF and the structural differences among the HF phenotypes, the development, selection, and optimization of HF therapeutic protocols remains a complex procedure.<sup>7,11</sup>

In general, the management and treatment of HF patients are stage- and phenotype-dependent, incorporating pharmacotherapy, device therapy, and HTx.<sup>8,12</sup> At an early stage of HF, where diminished cardiac output (CO) due to ventricular impairment occurs, several compensatory mechanisms of the human body are activated, including the sympathetic nervous system (SNS), the renin-angiotensin-aldosterone system (RAAS), and the brain natriuretic peptides (BNP) system. More precisely, the neurohormonal activation of SNS and RAAS aims at increasing myocardial contractility, ventricular filling, and the peripheral vasoconstriction, to counteract the CO deficit and maintain the end-organ perfusion.<sup>11,12</sup> Although activation of the latter systems is initially beneficial in maintaining CO, prolonged activation can result in an increased LV afterload and preload, aggravating the pathological ventricular remodeling. To counterbalance the consequences of chronic overactivation of SNS and RAAS, BNP release is upregulated. However, in the long-term, a reduction of available active BNP forms occurs thus attenuating the effects of BNP upregulation. The resulting imbalance between the neurohormonal activation and the BNP effectiveness promotes further deterioration of the cardiac contractility and leads to symptom development and an increased risk of arrhythmias, myocardial hypertrophy, fibrosis, and apoptosis.<sup>12–14</sup> At this stage, to reduce morbidity and mortality rates, pharmacotherapy is considered essential, with the current guidelines suggesting a sequence of pharmacological therapies that include diuretics, angiotensin-converting enzyme (ACE) inhibitors, beta-blockers, neprilysin inhibitors, and sodium-glucose 2 co-transport inhibitors.<sup>7,9,13,14</sup>

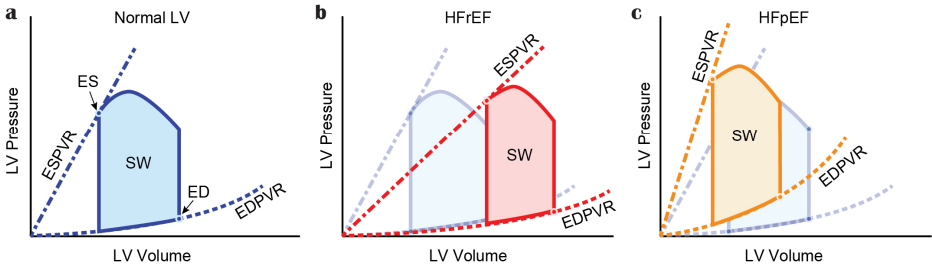


**Figure 1.2.** Hemodynamic physiology in terms of left ventricular pressure-volume loops for **a)** healthy heart, **b)** heart failure with reduced ejection fraction, and **c)** heart failure with preserved ejection fraction. *LV*, left ventricle; *ES*, end-systole; *ED*, end-diastole; *SW*, stroke work; *ESPVR*, end-systolic pressure-volume relationship; *EDPVR*, end-diastolic pressure-volume relationship; *HFrEF*, heart failure with reduced ejection fraction; *HFpEF*, heart failure with preserved ejection fraction.

Evidence from randomized trials over the last decades has demonstrated the efficacy of pharmacotherapy in patients with mild symptoms; however, it has been also observed that most of the HF patients receive suboptimal doses.<sup>7</sup> As a result, HF continues to progress and due to the high probability of a sudden death due to arrhythmic events, HF patients often receive supplemental treatment with an implantable cardioverter defibrillator (ICD) or cardiac resynchronization therapy. The latter device therapies improve substantially the morbidity and mortality rates, as well as the QoL of HF patients.<sup>13</sup>

When HF patients become refractory to guideline-directed pharmacotherapy and device-based resynchronization therapies, the progression of HF continues and they suffer from persistent, severe symptoms (hemodynamic compromise, cardiogenic shock, life-threatening ventricular arrhythmias), need recurrent hospitalizations, and encounter a high risk of 1-year mortality.<sup>11</sup> For this stage of advanced HF, heart transplantation (HTx) constitutes the gold-standard treatment, offering 1-year post-implant survival rates of 80-90%, a median survival of

**Table 1.1.** Indications suggesting the use of mechanical circulatory support (MCS) systems<sup>9,15</sup>

Usage term	Indications for mechanical circulatory support
Bridge to decision (BTD)	Use of short-term MCS in patients with cardiogenic shock until hemodynamics and end-organ perfusion are stabilized.
Bridge to candidacy (BTC)	Use of MCS to improve end-organ function and/or to make an ineligible patient eligible for heart transplantation.
Bridge to transplantation (BTT)	Use of MCS to support patients who are otherwise at high risk of death until they are able to proceed to a heart transplantation.
Bridge to recovery (BTR)	Use of MCS only for a short period to support patients with minimal myocardial damage until cardiac function recovers sufficiently to remove MCS.
Destination therapy (DT)	Long-term use of MCS to support the failing heart of patients that are not eligible for heart transplantation due to age, frailty level or other multi-organ dysfunctions.

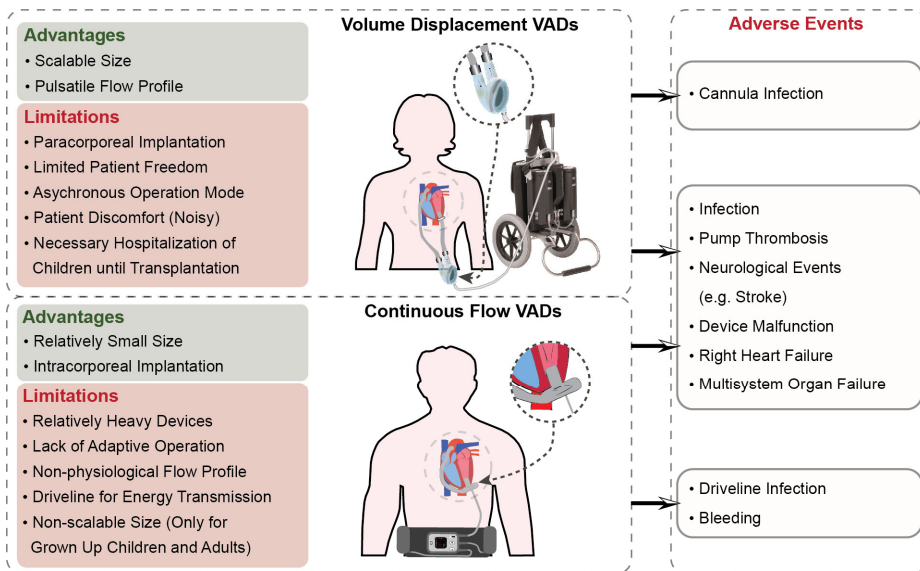


**Figure 1.3.** Limitations of current volume displacement (left top) and continuous flow (left bottom) ventricular assist devices (VADs) causing life-threatening adverse events (middle).

12.5 years, and substantially improved QoL.<sup>9,11,16</sup> Currently, approximately 50,000 patients diagnosed with advanced HF can be regarded as candidates for a heart transplantation worldwide each year; however, only a fraction of about 6,000 can finally get a HTx.<sup>17,18</sup> The notable discrepancy between the number of possible recipients and the performed HTx is twofold. In detail, a fraction of the advanced HF patients is precluded from HTx due to contradictions, including frailty, age (usually above 70 years), morbid obesity, irreversible pulmonary hypertension or renal dysfunction, severe cerebrovascular disease, drug or alcohol abuse, and malignancy. However, the cornerstone for the limited number of HTx is the shortage of organ donors. Although the recently extended criteria for heart organ donors resulted in 3,817 HTx in the US in 2021, the highest number ever achieved, the number of candidates continues to significantly outpace the supply of donors.<sup>9,13,17,18</sup>

To bridge the gap between the available donor organs and the people being in need of a HTx, mechanical circulatory support (MCS) systems have been developed as an alternative approach to support the failing human heart.<sup>19</sup> Those MCS systems comprise total artificial hearts (TAH), extracorporeal membrane oxygenation systems (ECMO), and predominantly ventricular assist devices (VAD). Depending on the treatment goal (Table 1.1), different MCS systems are used as bridge to decision (BTD), bridge to candidacy (BTC), bridge to transplantation (BTT), bridge to recovery (BTR), or destination therapy (DT). Over the last decades, MCS systems and especially VADs, have been tremendously evolved and nowadays, approximately 6,000 VADs are implanted worldwide every year.<sup>20</sup> The recipients of VADs reach survival rates of approximately 81% and 70% at one year and two years, respectively.<sup>21</sup> Although these rates are similar to the survival rates of patients that underwent heart transplantation, the HF therapy based on VADs is still associated with various adverse events, summarized in Fig. 1.3, that either reduce the survival rates, or affect the QoL of the patients.<sup>22</sup>

### 1.3 Ventricular Assist Devices: Evolution and Outcomes

Ventricular assist devices (VADs) are mechanical pumps that supplement the function of the failing ventricles of a HF patient to restore normal blood circulation and maintain the end-organ perfusion.<sup>7</sup> The evolution of the VAD field originates in the early 1960s, with the pioneering work of Spyridon Mouloupoulos, Willem Kolff, Adrian Kantrowitz, and Michael DeBakey.<sup>23,24</sup> From this point in time, a number of devices with different designs and operating principles have been investigated with a short overview given in Table 1.2.

The first generation of VADs comprised mainly pneumatically driven, volume displacement pumps (Fig. 1.3) that produce a pulsatile flow akin to the flow provided by the human heart. As it is shown in Fig. 1.4, these devices significantly improved the one- and two-year survival rates, compared to HF patients treated only with pharmacotherapy, and established the VADs as a viable therapy for end-stage HF patients. However, the noisy operation of these VADs due to the tilting discs and the pneumatic actuator, along with their large size and the high incidence of pump dysfunction, pump thrombosis and stroke events, diminished their usage over the years (Fig.1.5).<sup>25</sup>

The second generation of VADs was characterized by a revolutionary change in their design and operation. More precisely, by exploiting the principles of turbodynamic pumps, this generation was based on the deployment of an axial impeller in the blood stream to provide a continuous, unidirectional blood flow. The fact that the impeller of these VADs constituted the only moving part along with the elimination of valves, substantially decreased the size and increased the reliability of the devices. As a consequence, the incorporeal implantation was feasible, resulting in less invasive surgical procedures, less power and maintenance needs, and a tremendous improvement in the mobility and the QoL of the recipients. These improvements constituted the cornerstone to pave the burdens for the FDA to approve the application of the second generation of VADs as DT.<sup>19,25-27</sup> Although the approval for DT resulted in a dramatic increase in the usage of the VADs (Fig. 1.5) and the survival rates of HF patients (Fig. 1.4), device-related complications continued to affect the efficacy of the VAD therapy. These complications, including strokes, pump thrombosis, and bleeding, are often attributed to the blood damage due to the supraphysiologic shear stresses induced from the high rotational speed (6.000 -15.000 rotations per minute) of the VAD, as well as to clot formations at the bearing site due to the stagnant flow regimes developed around the contact point of the impeller.<sup>28</sup>

In an attempt to attenuate the adverse events that the second generation could not address, a third generation of VADs was developed (Fig. 1.3). This generation, the one predominantly used today, was based on sophisticated designs that enabled the contact-free rotation of the impeller by exploiting either hydrodynamic or magnetic levitation. By eliminating the mechanical contact of the impeller with the casing and allowing for larger clearances, these devices promised reduced critical flow regimes and, hence, a lower risk of clot formation.<sup>29</sup> Additionally, the third generation VADs exchanged the axial impellers with centrifugal impellers. This design-alteration resulted in a significant reduction of the rotational speed of the VADs (1.800 – 6.500 rotations per minute) with the aim to reduce the shear stresses exerted on the blood cells, and consequently reduce the blood damage. To further enhance their hemocompatibility, VADs of the third generation used coating materials for the impeller that prevent platelet adherence and thus diminish the risk of thrombus formation and hemolysis.<sup>23,25,28,30</sup> These technological advancements resulted in high implantation rates (Fig. 1.5) and shifted the main application of VADs from BTT to DT.<sup>31</sup> The high usage slightly increased the survival rates (Fig. 1.4) and

improved the QoL of the patients, however, the risk of bleeding remains high,<sup>32</sup> highlighting that achieving hemocompatibility is not trivial. Nonetheless, a significant reduction of stroke incidences has been achieved with the HeartMate 3 (HM3) VAD (Abbott Laboratories, Chicago, IL, USA).<sup>33</sup> This reduction is attributed not only to the wider gaps that the device offers, but also to the artificial pulse that the HM3 applies every 2 seconds to enhance the washout of the flow at the separation regions.<sup>34</sup>

**Table 1.2.** Overview of ventricular assist devices (VADs), their location and application characteristics<sup>7,25</sup>

Device	Pump Location	Application
<b>Pulsatile</b>		
EXCOR Pediatric VAD (Berlin Heart, GmbH, The Woodlands, TX)	Paracorporeal	<sup>a</sup>
Heartmate I or XVE (Thoratec Corp, Pleasanton, CA)	Intracorporeal	BTT, DT
Abiomed AB5000 (Abiomed Inc, Danvers, MA)	Paracorporeal	BTT, BTR
Abiomed BVS 5000 (Abiomed Inc., Danvers, MA)	Extracorporeal	BTT, BTR
Novacor LVAS (Baxter Healthcare Corporation, Novacor Division, Oakland, CA)	Intracorporeal	BTT
IVAD (Thoratec Corp, Pleasanton, CA)	Intracorporeal	BTT, BTR
PVAD (Thoratec Corp, Pleasanton, CA)	Paracorporeal	BTT, BTR
<b>Turbodynamic Axial</b>		
Incor VAD (Berlin Heart, GmbH, The Woodlands, TX)	Intracorporeal	<sup>a</sup>
MicroMed DeBakey VAD (Micromed Cardiovascular)	Intracorporeal	BTT
Heartmate II (Abbott Laboratories, Chicago, IL, USA)	Intracorporeal	BTT, DT
Impella 2.5, CP, or 5.0 (Abiomed Inc, Danvers, MA)	Intracorporeal	BTR
HeartAssist 5 (MicroMed Cardiovascular)	Intracorporeal	<sup>a</sup>
Jarvik 2000 (Jarvik Heart Inc., New York, NY)	Intracorporeal	BTT
<b>Turbodynamic Centrifugal</b>		
Duraheart (Terumo Heart Inc., Ann Arbor, MI)	Intracorporeal	<sup>a</sup>
EvaHeart (Sun Medical Technology Research Corp., Nagano, Japan)	Intracorporeal	BTT
Heartmate III (Abbott Laboratories, Chicago, IL, USA)	Intracorporeal	BTT, DT
HeartWare MVAD (HeartWare, Inc., Miami Lakes, FL)	Intracorporeal	<sup>a</sup>
VentrAssist (Ventracor Ltd)	Intracorporeal	BTT (CE Marked)
HeartWare HVAD (HeartWare, Inc., Miami Lakes, FL)	Intracorporeal	BTT, DT

<sup>a</sup>Investigational device as per FDA

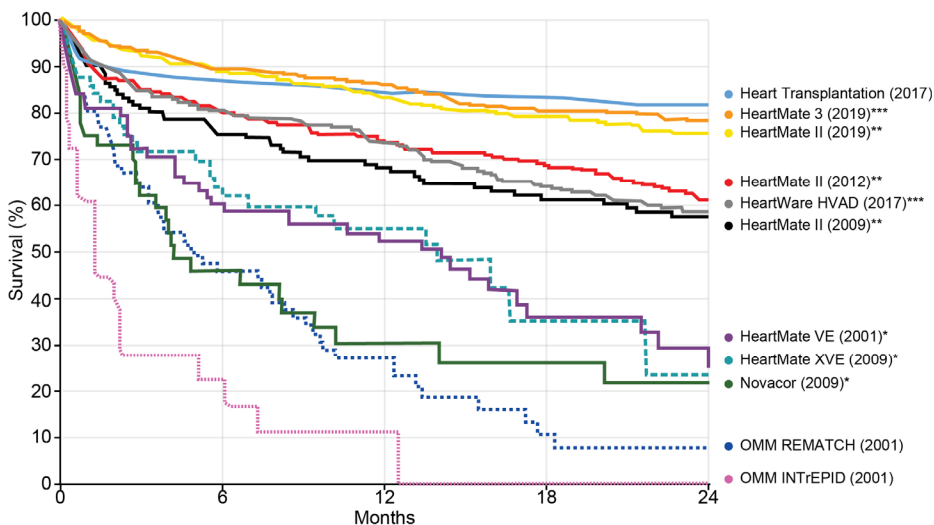


**Figure 1.4.** Historical and current status of survival rates of end-stage heart failure patients based on randomized trials of different treatment options. The figure is created based on data retrieved from<sup>24,35,36</sup>. OMM, optimal medical management; \*, first generation; \*\*, second generation; \*\*\*, third generation.

The described evolution in VAD technology, along with the improvements made in patient selection and management, allowed for the VAD therapy to be more readily adopted in the current clinical setting, achieving 27,298 implantations from January 2010 to December 2019 (Fig. 1.5) in the USA.<sup>31</sup> However, during the same period, the adverse events and hospitalization rates continued to remain high, contributing the greatest risk to mortality and questioning the economic benefit of VADs.<sup>37</sup> The majority of the complications attributed to the VAD therapy, summarized in Fig. 1.3, are related to the continuous flow and the constant speed of the VADs that are currently used. More precisely, the constant speed operation of VADs do not allow adaptation of the pump flow to the perfusion needs of the patient, resulting often to critical condition such as ventricular suction or under- and overpumping.<sup>25,26,29</sup> It is believed that those unfavorable conditions are related to right heart failure and arrhythmia events, which negatively influence the results of the therapy.<sup>29</sup> On the other hand, the continuous flow provided by the third generation VADs, which are primarily used nowadays, significantly attenuates the flow pulsatility and increases the pressure downstream the aortic valve. These phenomena can negatively affect the endothelial and peripheral vascular function<sup>38–40</sup> and, hence, increase the risk of nonsurgical bleeding and aortic valve insufficiency, which both affect the therapy outcomes and the QoL of the patients.<sup>41</sup>

The remaining complications mentioned above, have been thoroughly investigated over the last decades and, based on the better understanding of their causes, novel VAD concepts have been conceived and are currently under development. Among the most promising of these concepts are the CorWave LVAD (CorWave SA, Clichy, France) and the TORVAD (Windmill Cardiovascular Systems Inc., Austin, TX, USA). Both devices offer the benefits of the third generation VADs and provide a pulsatile flow that better imitates the function of the native heart. However, since the necessary data from clinical trials are missing, it remains questionable whether these devices can achieve the long-awaited improvements in the clinical setting or they will carry the reliability problems from the pulsatile VADs of the first generation.

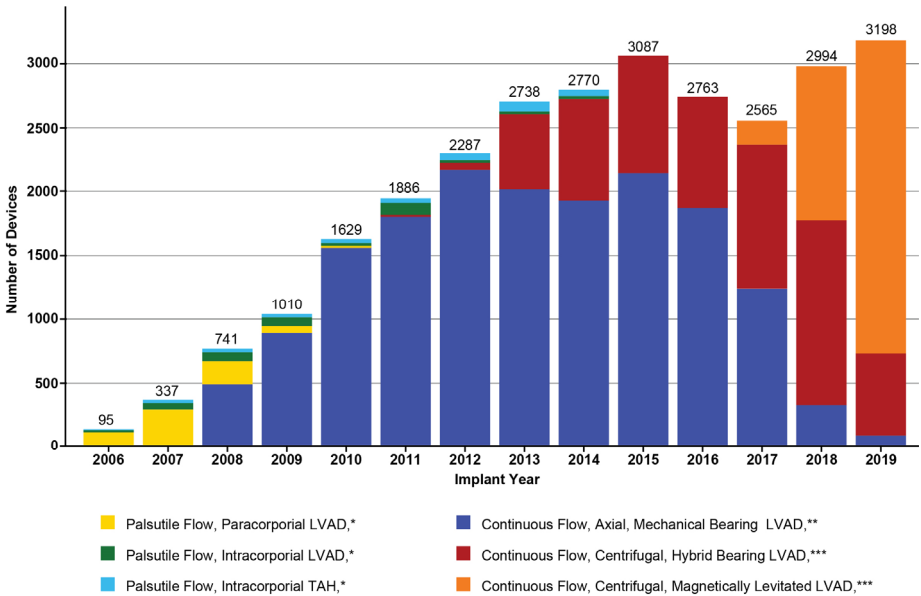


**Figure 1.5.** Overview of left ventricular assist device implants by pump type and by implant year based on data collected by INTERMACS.<sup>31,42</sup> *LVAD, left ventricular assist device; \*, first generation; \*\*, second generation; \*\*\*, third generation.*

Along with the novel VAD concepts, notable efforts have been made in order to develop control schemes that allow the adjustment of the pump speed and restore the physiological response and the pulsatility of the currently used VADs.<sup>15,43</sup> Some of these approaches and their prospects to reduce the life-threatening adverse events related to the VAD therapy are elaborated in the next section.

## 1.4 Physiologic Control Schemes for Ventricular Assist Devices

The cardiovascular system and, especially the heart, are complex entities that have developed sophisticated mechanisms to regulate the amount of cardiac output (CO) based on the end-organ metabolic demands. These regulation mechanisms include the sympathetic and parasympathetic systems, which control the cardiac rhythm (heart rate) and the peripheral vasoconstriction, but most importantly the Frank-Starling mechanism. Named after Otto Frank and Ernest Starling, who were the first physiologists to study it, the Frank-Starling mechanism describes the ability of the heart to adjust the contraction force of the ventricular muscles depending on the amount of blood volume that returns to the heart at the end of each cardiac cycle (venous return).<sup>44</sup>

The cumulative effect of the regulation mechanisms on the CO produced by a healthy heart (HH) is explained in Fig. 1.6 where the preload and afterload sensitivities (light-blue surface) are depicted. More precisely, the CO delivered by the HH is continuously adjusted based on the left ventricular end-diastolic pressure (EDP) and the mean arterial pressure (MAP) that express the varying preload and afterload conditions against which the heart has to operate. In the same figure

it can be observed that the CO of the HH is highly responsive to preload changes but less responsive to afterload changes. Based on Fig 1.6a (light-red surface), in patients with severe HF, the deteriorated function of the diseased heart (DH) results in a substantial reduction of the overall CO, and, at the same time, an alteration of the responsiveness of the heart to preload and afterload changes. In these patients, as described in the previous sections, the CO can be restored by supporting the DH with a VAD. The majority of the VADs used today in the clinical setting are continuous flow turbodynamic VADs of the third generation that are mainly operating with a constant rotational speed. The selection of their constant speed is made along with the consultation of echocardiography that provides the total CO achieved by the accumulation of the pump flow and the blood flow produced by the remaining function of the DH.<sup>45</sup> Based on the interpatient variabilities, the selected speed and the corresponding interaction with the native DH can vary among patients. As it is illustrated in Fig. 1.6b (light-green surface), the DH supported with a constant-speed operated VAD presents a preload sensitivity almost three times lower than the one of the HH<sup>46,47</sup> and an afterload sensitivity that is almost four times higher than the HH. When considering the inpatient variability in the perfusion needs, the altered CO responsiveness can result in a mismatch between the venous return and the total CO produced by the VAD supported DH. In the event of such mismatches, critical flow conditions can be developed in the LV that result in over- or underpumping occurrences (Fig. 1.7).<sup>48,49</sup> In detail, overpumping occurs when the metabolic demands are diminished and the selected constant speed of the VAD is high enough to produce a blood flow that exceeds the venous return (Fig. 1.7b). In this case, the ventricle is completely emptied, creating negative pressure gradients that shift the septum and the LV wall towards the inflow canula of the VAD.<sup>50</sup> This condition is often referred as suction and is related to higher risk of tissue and blood damage, due to contact with the surface of the inflow canula and the high shear stress developed at the restricted area, respectively.<sup>48,51</sup> In contrary, as it is illustrated in Fig. 1.7c, underpumping events occur when the metabolic demands increase and the selected constant speed of the VAD is not adequate to propel the amount of blood necessary to match the venous return. These events result in LV overload, wherein the higher LV pressures increase the risk of blood congestion in the lungs and constitute the patient susceptible to pulmonary edema.

To avoid the life-threatening consequences of over- and underpumping events in the clinical setting, the VAD-supported HF patients are subjected to regular CO assessments through echocardiography ramp tests and the optimal constant speed of the VAD is adjusted accordingly.<sup>45</sup> However, between the in-hospital examinations, and most importantly, the long intervals once the patient is discharged from the hospital, the rotational speed of the VAD remains fixed. During these intervals, the CO demands can vary notably due to changes in the pathological state, postural changes, or activity level as the condition of the patient improves. As a consequence, when these changes in the perfusion need occur, the fixed rotational speed contributes the highest risk to over- and underpumping events.<sup>48</sup>

In an attempt to minimize this risk in the out-patient setting or between the examination visits, various research groups have been investigating control strategies that restore the physiological response of VADs to changes in the perfusion needs. To achieve this, the majority of these strategies aims to monitor hemodynamic or pump intrinsic parameters that reveal the state of the cardiovascular system. By comparing these parameters with the desired setpoint values, the physiological controllers automatically adjust the output flow of the VAD by adapting its rotational speed.<sup>15,43,48,49</sup> The selection of the monitored parameters along with the control



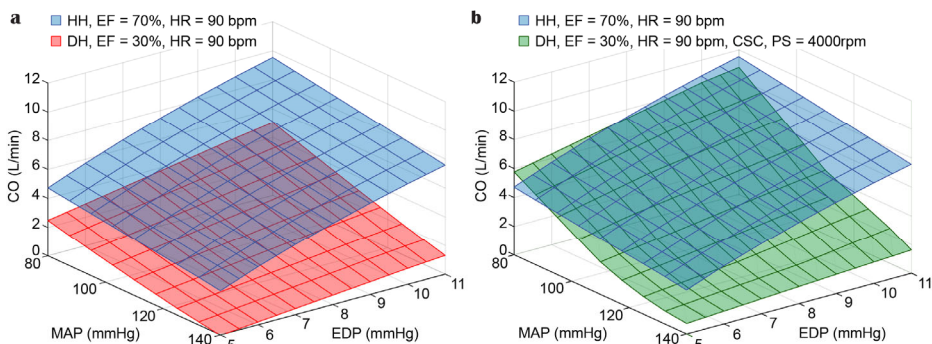


**Figure 1.6.** Comparison of preload and afterload sensitivity ( $Lmin^{-1}/mmHg$ ) of a healthy heart with **a)** a diseased heart with ejection fraction of 30%, and **b)** a diseased heart with ejection fraction of 30% supported with a continuous flow ventricular assist device (VAD) operating at a constant speed of 4000 revolutions per minute. The left ventricular end-diastolic pressure and the mean arterial pressure are used as surrogates of the preload and afterload, respectively. The diseased heart presents significant reduction in preload sensitivity and a mild increase in afterload sensitivity. The diseased heart supported with the VAD shows significant reduction in preload sensitivity and notable increase in afterload sensitivity. The data have been produced by the author in an in-silico environment using the cardiovascular system described by Colacino et al.<sup>52</sup> and implemented by Ochsner et al.<sup>53</sup> The ventricular assist device was simulated with the numerical model of a non-implantable mixed-flow turbodynamic blood pump (Deltastream DP2, Medos Medizintechnik AG, Stolberg, Germany).<sup>53</sup> *HH*, healthy heart; *DH*, diseased heart; *EF*, ejection fraction; *HR*, heartrate; *CSC*, constant speed control; *PS*, pump speed; *EDP*, end-diastolic pressure; *MAP*, mean arterial pressure; *CO*, cardiac output; *rpm*, rotations per minute.

objectives dictate the complexity, the performance, and the robustness of the different control approaches proposed in the literature.

At the early stages of the VAD controllers, the necessary feedback for the perfusion need of the patient was provided by non-invasive monitoring of hemodynamic and pump parameters based on pump intrinsic signals and estimation approaches.<sup>15</sup> Although these approaches eliminated the need for additional sensory technology, their performance was found to be highly affected by changes in the blood hematocrit<sup>54</sup> and thrombus formation.<sup>55</sup> This lack of robustness could provoke unwanted instabilities in the performance of the controller and, hence, set the life of the patient at risk. As a result, physiological control algorithms based on feedback provided by invasive sensors started to gain interest. These controllers can be grouped into two main categories, termed preload- and afterload-based controllers, depending on the hemodynamic parameter they use as control variable. For the preload controllers, the major objective is the restoration of the Frank-Starling response.<sup>15,56-61</sup> To achieve this, they use hemodynamic parameters that act as preload surrogates, such as LV systolic pressure,<sup>59</sup> LV end-diastolic pressure,<sup>57,62-64</sup> and LV end-diastolic volume.<sup>60</sup> For the afterload controllers, the mean arterial pressure and the pressure difference across the pump are the most common control parameters.<sup>65-67</sup> The aim of the afterload controllers is to sustain the controlled parameter constant, such that the CO is regulated via the vascular resistance.

Considering both preload- and afterload-based controllers, various structures have been investigated over the years, including proportional (P), proportional-integral (PI), and proportional-integral-derivative (PID) controllers.<sup>15,56-61,66</sup> These controllers offer an easier

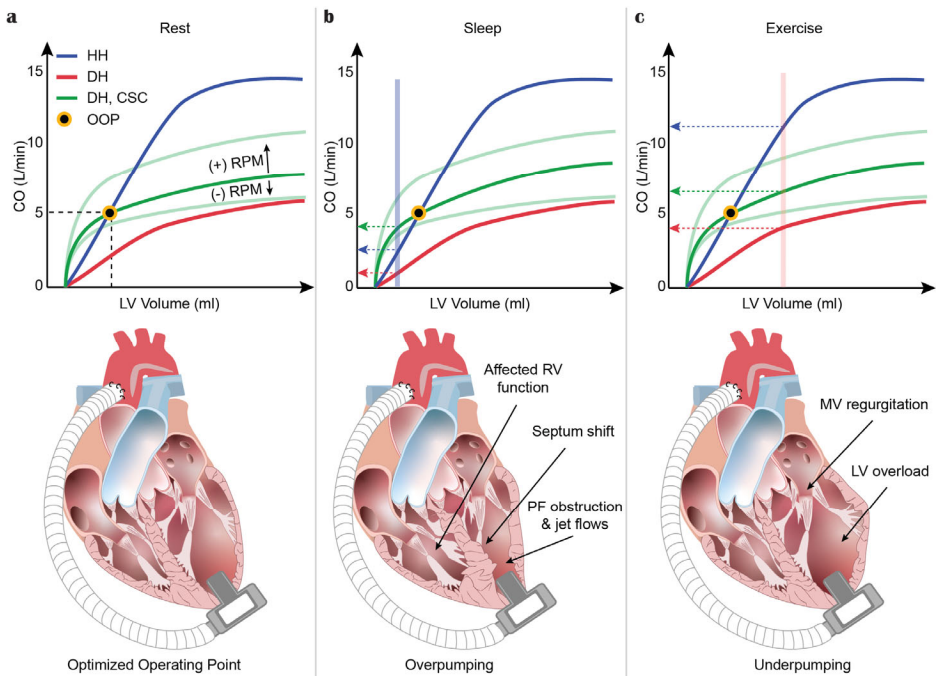


**Figure 1.7.** Schematic representation of critical flow conditions developed in the left ventricle (LV) of a diseased heart (DH) supported with continuous flow ventricular assist device (VAD) due to diminished responsiveness to preload changes. **a)** Preload response (Frank-Starling response) of a healthy heart (HH), a DH, and a DH supported with a continuous flow VAD operated with constant speed (DH-CSC) during rest conditions. The preload response of both the DH, and the DH-CSC are significantly diminished compared to the HH. The constant speed is selected to provide a total cardiac output (CO) of 5 L/min at rest, which is considered the optimum operating point (OOP). On the bottom layer, a DH with a VAD implanted at the apex of the LV is depicted at the optimum operating point of the VAD during rest conditions. **b)** Response of a HH, a DH, and a DH-CSC on a preload reduction during sleeping conditions. The selected constant speed is higher than the optimum for these conditions, resulting in overpumping. The effects of overpumping on the ventricular walls and the function of the heart are presented on the bottom layer. **c)** Response of a HH, a DH, and a DH-CSC on a preload increase during exercise conditions. The selected constant speed is lower than the optimum for these conditions, resulting in underpumping. The effects of underpumping on the ventricular walls and the function of the heart are presented on the bottom layer. *PF*, pump flow.

clinical implementation. Their operation is based only on a feedback parameter without awaiting information about the underlying interactions between the VAD, the DH, and the entire cardiovascular system (CVS). Although these controllers can improve the physiological response of the VAD to preload and afterload variations, their performance can be substantially affected by sudden alterations in the CVS and, consequently, they can be unreliable and prone to suction and backflow events.<sup>48</sup> To account for these critical problems, various groups have developed safety controllers that detect and release suction and backflow events,<sup>68,69</sup> as well as more complex physiological controllers that pursue multiple objectives concurrently.<sup>64,70–73</sup> For instance, the multi-objective controller proposed by Petrou et al.<sup>64</sup> is based on the LV EDP to

imitate the Frank-Starling mechanism, while it also incorporates various estimators and safety controllers to achieve aortic valve opening for a predefined time, and prevent LV suction and pump backflow. Such controllers not only enable a more physiological response of the VAD, but also offer unprecedented opportunities to the clinicians for treatment adaptation. The bottleneck, however, for these controllers is the lack of adaptiveness to changes of the time-varying parameters of the CVS, such as the heart rate, the remaining contractility of the DH, and the vasculature properties (compliance, resistance, and inertia). To counteract this, recent approaches investigate the applicability of iterative learning control (ILC) theory in the VAD field.<sup>74,75</sup> These approaches exploit the repetitive nature of the heart cycles to identify changes of the time-varying parameters of the CVS and adapt accordingly the control input for the following cycles. Ketelhut et al.<sup>75</sup> and Rüschen et al.<sup>74</sup> showed that these approaches are promising; however, their performance can be restricted by the accuracy of the CVS and VAD models that are integrated in the control structure to allow the prediction of the control function.

The improved responsiveness of the VADs and the potential benefit for the VAD-supported HF patients with the deployment of the above-mentioned control strategies has been validated through extensive in-silico or in-vitro experiments. In some cases, the performance of the controllers has been further proven with in-vivo experiment<sup>56,58</sup> or even pilot clinical studies.<sup>72,76</sup> However, all the VADs being currently in clinical usage continue to operate with constant speed. Major burdens that restrict the implementation of any of the proposed controllers in the clinical setting are the lack of reliable monitoring approaches to provide the feedback parameters, the lack of adaptiveness to changes of the time-varying parameters of the CVS, and the enormous variability in patients' characteristics that constitute the identification of universal control parameters difficult.

## 1.5 Monitoring of Heart Failure Patients: Sensory and estimation approaches

The management of CVDs and, especially HF, constitutes the cornerstone for the survival and the QoL of the patients. To allow the development of an optimum management and timely clinical decision-making, a structured and accurate assessment of the progression of the disease and the status of the patient constitute prerequisites.<sup>77</sup> For this assessment, various vascular and hemodynamic properties can provide the necessary information; however, these properties have to be continuously monitored. When the VAD-supported patients are considered, except for their hemodynamic properties, parameters that reveal the VAD performance are also crucial not only to allow adequate treatment, but also to enable the implementation of the control approaches described in the previous section.

In the clinical setting, echocardiography, computer tomography, magnetic resonance imaging, electrocardiogram, and fluid-filled catheters are readily available to provide accurate monitoring of the remaining contractility of the heart, the ventricular volumes, the blood flow, and the blood pressure.<sup>48,78</sup> These hemodynamic data are valuable to the clinicians for the assessment of the status of the patient. However, due to the large scale and the high cost of the measuring devices, these data can be acquired only during in-hospital treatment or, once the patient is discharged, during the predefined clinical examinations. This non-continuous monitoring of the hemodynamics limits the surveillance of the therapy, while in the VAD therapy, it precludes the implementation of physiological control. Hence, the development of implantable transducers that provide continuous monitoring capabilities is paramount to ensure optimum medical management and allow real time deployment of physiological control.

Over the last decades, various concepts of continuous direct measurement of blood pressure, ventricular volume or pump flow have been researched.<sup>79–84</sup> In detail, Ruhhammer et al.<sup>81</sup> investigated a magnetic sensor to measure the distension of the aorta and then, estimate ABP. Their study showed that the silicone strip used to interlock the sensor on the aorta resulted in decreased measurement precision over time, due to silicone fatigue, while it was influenced significantly by the sensor implantation procedure and the position of the sensor on the aorta. Focusing also on the measurement of the blood pressure, Cleven et al.<sup>85</sup> developed a fully-implantable catheter-based sensor that is permanently implanted at the femoral artery. The initial in-vivo validation showed promising results, however, it remains to be seen during chronic experiments whether the sensor will be exempted from increased risk of vascular thrombosis, infections, and bleeding complications at the access site. Exploiting the advent and rapid evolution of stretchable electronics, Dual et al.<sup>86</sup> developed a flexible, piezo-resistive strain sensor that is placed directly on the outer surface of the heart to provide continuous information of the heart volume. The sensor showed high accuracy compared to reference measurement during in-vivo experiments; however, its performance quickly decayed after several hours, limiting the applicability of the sensor for short-term use. Vennemann et al.<sup>87</sup> have presented a wireless and batteryless implantable flow sensor, however the sensor has been validated only in an in-silico environment. Considering the VAD-supported patients, a new approach for integrating a pressure sensor at the inflow cannula to measure the LV pressure has been developed by v. Petersdorff-Campen et al.<sup>88</sup> By exploiting the design freedom of additive manufacturing, the latter approach offers also pump flow estimation capabilities, showing high potential for translation to the clinical setting after its validation in chronic in-vivo experiments. Despite the prospects of the aforementioned implantable sensing approaches, none has been reported in the clinical setting. This stems from the several obstacles that the implantable transducers have to overcome in order to succeed their approval for use in humans. More precisely, any implantable device has to be biocompatible, accurate, reliable, free from hardware failure, and resistant to drift.<sup>48</sup>

The only implantable technologies that have achieved the readiness level to enter the clinical setting are the pressure sensors Titan (ISS Inc., Ypsilanti, MI) and CardioMEMS™ (Abbott AG, IL, USA). The Titan sensor is fully implanted in any of the four chambers of the heart to provide pressure measurements in a daily basis. This sensor is validated in in-vivo and in pilot clinical studies, however, it is not yet FDA approved.<sup>89</sup> CardioMEMS™ is the only FDA approved implantable system that can be deployed for monitoring the pulmonary arterial pressure. CardioMEMS is currently in clinical use, highlighting the potential benefit of outpatient monitoring in optimizing the treatment of HF patients;<sup>90</sup> however, the sensor can provide only daily measurements and a significant reduction in measurement's precision after only 60 days of use has been reported.<sup>91</sup> As a result, the sensor requires recalibration. Hence, it can be used for monitoring purposes and in-hospital pump speed adaptation, however, it cannot facilitate a reliable feedback for the implementation of physiological controllers. Regarding the measurement of blood flow, there is no implantable sensor available for the HF patients. However, for the VAD-supported patients, the newly developed device aVAD (ReliantHeart Inc., Houston, TX, USA) features an ultrasonic flow probe embedded into the VAD outflow graft. It remains to be seen whether this sensor can be used for the deployment of physiological control, or the common problems of flow sensors regarding their sensitivity to fluid viscosity and temperature reduce its reliability and applicability.

To counteract the lack of reliable implantable sensors in the VAD therapy, many researchers have investigated indirect approaches to measure hemodynamic properties and pump variables.

To achieve this, they exploit the intrinsic signals of the pump (current, rotational speed) and estimation approaches.<sup>54,92-97</sup> More precisely, Granneger et al.<sup>92</sup> used the intrinsic signals of the VAD along with the pump hydraulic and electric characteristics to estimate the pump outlet flow. This flow estimator achieved the smallest estimation error compared to other, simpler approaches, and outperformed the one used clinically on the HVAD system. In an attempt to enable a better understanding of the interactions between the DH and the VAD, Petrou et al.<sup>98</sup> developed an algorithm for the estimation of the total cardiac output (accumulated flow through the pump and the aortic valve). The estimation approach showed minimal estimation error, however, it necessitates the measurement of the pressure at the inflow cannula of the VAD, limiting the application of the algorithm.

The proposed estimation approaches can support the monitoring of the patients in an out-patient setting. However, considering the effect of the blood viscosity and thrombus formation on the intrinsic signals of the pump, the usage of the estimated variables as feedback parameters for physiological controller can result in unpredictable instabilities of the controllers that can be life-threatening for the patient.<sup>49</sup>

## 1.6 Research Aim and Objectives

The tremendous impact of CVDs and especially the end-stage HF on the global society and economy, along with the shortcomings of the therapeutical protocols and the technology used for their treatment have been highlighted in the previous sections. Based on this information, as it is depicted in Fig. 1.8, the overall aim of this work is to reduce the hospitalization rates and improve the survival, QoL, and recovery rates of VAD-supported HF patients, based on the development of novel sensory technology that allows continuous surveillance of the patient status and control algorithms that enhance the physiological response of VADs. To make the necessary steps towards the achievement of this aim, the following objectives (Obj) are formulated:

- **Obj 1.** Develop sensory technology that allows the continuous and robust, over time, monitoring of principal vasculature and hemodynamic parameters, such as vascular distensibility, vascular strain, blood pressure, cardiac output, and heart rate.
- **Obj 2.** Assess the performance and the readiness level of the developed sensory technology based on in-vitro, ex-vivo, and in-vivo experiments.
- **Obj 3.** Develop algorithmic approaches that exploit the continuously monitored hemodynamic parameters and machine learning models to assess the remaining cardiac contractility and the overall status of the cardiovascular system.
- **Obj 4.** Develop control strategies that improve the physiological response of VADs to changes in perfusion needs of the patient, incorporate treatment objectives, and adapt to the time-varying properties of the CVS (remaining contractility and vasculature properties).
- **Obj 5.** Develop algorithmic approaches that allow the optimization of control parameters based on treatment- and patient-specific parameters to enable personalized control structures.

— Closed Loop Control    - - - Monitoring & Controller Adaptation

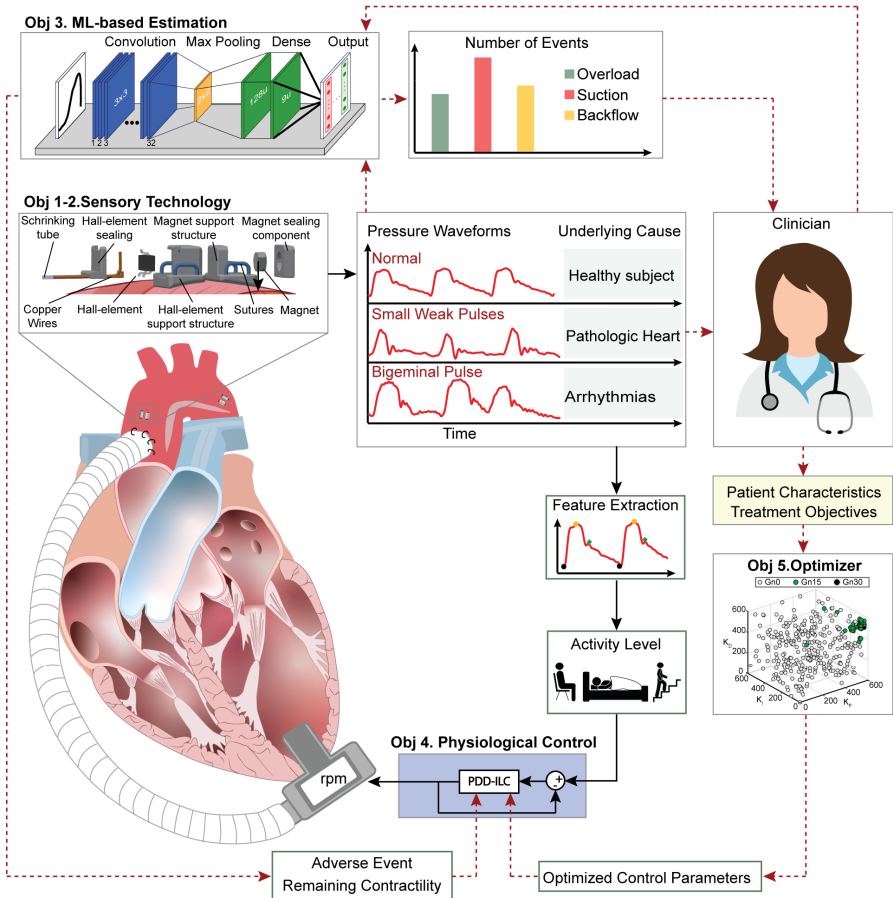


**Figure 1.8.** Conceptualization of the overall aim and the respective objectives (Obj) of the thesis. Sensory technology (Obj 1-2) allow direct continuous measurement of principal vasculature and hemodynamic parameters. These data are used to assess the activity level of the patient by extracting the systolic and end-diastolic pressure components. The data are also used from the machine learning-based estimator (Obj 3) to identify critical flow phenomena, adverse events and the remaining contractility of the diseased heart. This information is used directly from the controller, by adjusting the control parameters, but most importantly from the clinician to support the decision-making and the adaptation of the treatment protocol. The data from the sensor and the estimator are exploited from the data-driven iterative learning controller (PDD-ILC) (Obj 4) to regulate the pump speed (rpm) and achieve physiological response and adaptive behavior to changes in contractility, respectively. Finally, based on the patient characteristics and the treatment objective selected by the clinician, an optimization framework (Obj 5) is used to provide optimum, patient- and treatment-specific control parameters.

## 1.7 Scientific Contribution

In an attempt to address some of the shortcomings of the current treatment procedures for the VAD-supported HF patients, and following the objectives described in Section 1.6, four studies were conducted in the course of this work.

The first study aimed to fulfill the first two objectives and, hence, it was focused on the lack of implantable sensor technology for continuous measurement of vascular and hemodynamic parameters. Based on Section 1.5, various direct and indirect sensing approaches have been investigated over the last decades with limited success in the clinical setting. The main obstacles are issues related to biocompatibility, accuracy, reliability, and, most importantly, resistant to drift. In this context, the following research questions (RQ) were formulated:

### **RQ I:**

What are the most valuable and most easily derived hemodynamic variables that reflect the changes in the overall cardiovascular system?

### **RQ II:**

How can these variables be accurately and reliably monitored while the use of flexible materials that are prone to fatigue and increase the risk for long-term drift are avoided?

### **RQ III:**

What experimental procedures have to be followed to allow a thorough assessment of performance and reliability of the sensing device under conditions that adequately emulate the human body?

To adequately address these questions, Study I reported the design, the characterization and the validation of an extravascular, magnetic-flux sensing device, capable of capturing the waveforms of the arterial wall diameter, arterial circumferential strain and arterial pressure without restricting the arterial wall. The waveforms of the latter variables constituted the basis to further deduce pulse wave velocity, respiration frequency, and duration of the systolic phase of the cardiac cycle, which could offer new capabilities in CVD treatment management. The implantable sensing device, comprising a magnet and a magnetic-flux sensing assembly, showed to be reliable, with temperature and cyclic-loading stability. Continuous and accurate monitoring of arterial blood pressure and vascular properties was demonstrated with the proposed sensor in-vitro with a silicone artery model, and validated in-vivo in a porcine model mimicking physiologic and pathologic hemodynamic conditions. Revealing the information hidden in the arterial blood pressure waveform, as well as other vascular properties, could constitute the cornerstone to allow patient-specific treatment in patients suffering from CVDs, and new prospects in physiological control of VADs.

### **Study I:**

<sup>99</sup> **Magkoutas, K.** *et al.* Continuous Monitoring of Blood Pressure and Vascular Hemodynamic Properties with Miniature Extravascular Hall-Based Magnetic Sensor. *JACC Basic to Transl. Sci.* 1–28 (2023) (accepted for publication)

For the second study, the aim was the fulfillment of the third objective described in Section 1.6. As it was highlighted in the previous sections, time-varying parameters of the CVS, such as the remaining contractility of the DH, can have a significant influence on patient management and the performance of physiological controllers. Currently, there is no reliable approach to continuously monitor such parameters. Hence, considering that a significant amount of hemodynamic data can be enabled with Study I, along with the capabilities of machine learning algorithms the following research questions were raised:

**RQ IV:**

How does the performance of traditional time series classifiers compare to graph-based neural networks when the left ventricular pressure is used to estimate the remaining cardiac contractility of a diseased heart?

**RQ V:**

Are the classification accuracy and prediction time adequate to be used for real-time adaptation of the control parameters of physiological controllers?

In Study II, the first, preliminary results to address these questions were presented. In detail, artificial data of the left ventricular pressure were generated by executing 63 experiments on an in-vitro, hybrid mock circulation. To allow the estimation of the remaining contractility, these experiments included preload, afterload, pump speed, and heart rate variations and they were performed for nine contractility levels. From the plethora of machine learning models, the dynamic time warping nearest neighbor (DTW-NN) classifier and the support vector (SVM) classifier were selected from the family of time series classifiers, while from the family of graph-based neural networks a pretrained architecture and a custom architecture were selected. By using the generated data of left ventricular pressure, the different machine learning algorithms were compared with respect to their accuracy in estimating the remaining contractility. All classification methods were able to estimate the remaining contractility with more than 98% accuracy; however, the SVM showed superior performance. The continuous and accurate estimation of the remaining contractility of the DH could substantially support patient surveillance, treatment adjustments, and real-time adaptation of the control parameters of physiological controllers.

**Study II:**

<sup>100</sup> **Magkoutas, K.**, Wang, F., Forster, O., Meboldt, M. & Schmid Daners, M. CARD9: Cardiac Contractility Estimation Based on Left Ventricular Pressure: Comparison of Time Series Classifiers and Graph-based Neural Networks. *ASAIO J.* 68, 48–48 (2022).

After developing the necessary technology and algorithms in studies I and II to allow continuous monitoring of the hemodynamics of the cardiovascular system and its time-varying properties, the third study aimed to fulfill the fourth objective of this work. Based on Section 1.4, a plethora of physiological controllers have been investigated, including simple and complex strategies, as well as single and multi-objective strategies. However, the majority of these controllers are affected by the changes in cardiac contractility and in patient's frailty-level, while they do not account for the lack of pulsatility. These shortcomings constitute their long-term performance and stability questionable, limiting their implementation in the clinical setting. Based on these shortcomings, the following research questions were formulated:



**RQ VI:**

What is the most appropriate control approach to enable adaptive control output based on the time-varying properties of the cardiovascular system?

**RQ VII:**

How can treatment-based pulsatile pump flow trajectories be designed, implemented and accurately tracked while physiological response of the VAD is achieved?

These research questions were addressed in the third study of this thesis. Specifically, in Study III, a physiological data-driven iterative learning controller (PDD-ILC) was presented. This controller accurately tracked predefined pump flow trajectories, aiming to achieve physiological, pulsatile and treatment-driven response of continuous flow VADs. The controller has been extensively tested in an in-silico environment under various physiological conditions, and compared with a physiological pump flow proportional-integrative-derivative controller (PF-PIDC) (developed in this study too) as well as the constant speed (CS) control that is the current state-of-the-art in clinical practice. Additionally, two treatment objectives were investigated to achieve pulsatility maximization and left ventricular stroke work (LVSW) minimization by implementing copulsation and counterpulsation pump modes, respectively. Under all experimental conditions, the PDD-ILC as well as the PF-PIDC demonstrated highly accurate tracking of the reference pump flow trajectories, outperforming existing model-based iterative learning control approaches. Additionally, the developed controllers achieved the predefined treatment objectives and resulted in improved hemodynamics and preload sensitivities compared to the CS support.

**Study III:**

<sup>101</sup> **Magkoutas, K.**, Arm, P., Meboldt, M. & Schmid Daners, M. Physiologic Data-Driven Iterative Learning Control for Left Ventricular Assist Devices. *Front. Cardiovasc. Med.* **9**, (2022).

The last study of this thesis aimed to address the fifth objective described in section 1.6. Specifically, based on information that is provided in Section 1.4, the interpatient variability with respect to metabolic needs, disease status and progression, and treatment goals, constitutes a notable obstacle towards the identification of universal control parameters that result in the optimum controller performance. Considering also that the identification process is currently conducted with non-intuitive trial-and-error approaches, the achievement of physiological controllers that perform optimally to all patients becomes infeasible. As a result, the following research question was raised:

**RQ VIII:**

How can we optimize intuitively the control parameters of physiological controllers to improve their performance and incorporate treatment- and patient-specific parameters?

This study describes the development and evaluation of a novel, genetic algorithm-based optimization framework (GAOF) that could be deployed to optimize the control parameters of ventricular assist devices (VADs). This framework enables the optimization of complex control structures based on VAD- and patient-specific characteristics by allowing the selection of the

numerical model of the human cardiovascular system and the VAD to represent the patient scenario of interest accurately. Additionally, the GAOF could incorporate treatment-specific goals during the definition of the objective functions of the optimization problem and, consequently, promoted the development of treatment-specific VAD controllers. The efficacy of the GAOF was assessed with one- and two-degree-of-freedom physiologic proportional-integral-derivative controllers and a physiologic data-driven iterative learning controller. Two VAD designs and various patient disease scenarios were used to further explore and evaluate the capabilities of the GAOF. The optimized controllers outperformed substantially the hand-tuned controller, which was used as the benchmark, in all the investigated cases. This highlighted the potential improvement in the performance of any VAD controller by deploying the GAOF and, consequently, the possibility to increase the survival rates and enhance the quality of life of VAD patients.

#### Study IV:

<sup>102</sup> **Magkoutas, K.**, Nunes Rossato, L., Heim, M. & Schmid Daners, M. Genetic Algorithm-Based Optimization Framework for Control Parameters of Ventricular Assist Devices Introduction (under preparation). *Biomed. Signal Process. Control* (2023).

Alongside the contributions that shaped this thesis, the author had the chance to collaborate with other colleagues of the Zurich Heart consortium and contribute to their work. In detail, Chala N., Wu X., and the author collaborated with the aim to enable the integration of various technologies that have been developed under the umbrella of the Zurich Heart project. Within this project the author developed and operated the mock loop to allow the investigation of endothelial monolayer retention on an inflow VAD cannula under the physiologic conditions of a beating heart phantom.<sup>103</sup> Along with Rebholz M., the author investigated in an in-vivo experimental setting the ability to control the ventricular unloading by manipulating the stroke ratio of an electrocardiogram-synchronized pulsatile ventricular assist device.<sup>104</sup> An important collaboration for the author was developed with von Petersdorff-Campen, K. and Dupuch, M. During this collaboration, the design benefits of additive manufacturing were exploited to allow the integration of pressure sensors on the tapered surface of an inflow canula of an implantable VAD. Based on the configuration of the sensors on the tapered surface, accurate pressure measurement and flow estimation were enabled.<sup>88,105</sup> Along with his predecessor Petrou A., the author worked on a novel framework that enables the estimation of the total cardiac output of a VAD-supported HF patient and it holds promises for an online implementation in physiological controllers.<sup>98</sup> Dual S. collaborated with the author to perform the in-silico validation of an implantable strain sensor that is offering continuous monitoring of ventricular volume. Finally, along with a number of colleagues, supported the preparation of the backstory of the building process of an interdisciplinary program of cardiovascular research. The studies conducted with the aforementioned collaborators are not part of this work, however, further information can be found in the following references.

<sup>103</sup> **Magkoutas, K.** *et al.* In-vitro Investigation of Endothelial Monolayer Retention on an Inflow VAD Cannula Inside a Beating Heart Phantom. (2023)

<sup>104</sup> Magkoutas, K. *et al.* Control of ventricular unloading using an electrocardiogram-synchronized pulsatile ventricular assist device under high stroke ratios. *Artif. Organs* **44**, E394–E405 (2020).

<sup>88</sup> von Petersdorff-Campen, K., Dupuch, M. A., Magkoutas, K., Hierold, C. & Schmid Daners, M. Pressure and Bernoulli-based Flow Measurement via a Tapered Inflow VAD Cannula. *IEEE Trans. Biomed. Eng.* **9294**, 1–1 (2021).

<sup>105</sup> von Petersdorff-Campen, K., Dupuch, M. A., Magkoutas, K., Hierold, C. & Schmid Daners, M. BIO8: Cannula Add-On For Pressure And Flow Measurement In VADs. *ASAIO J.* **68**, 13–13 (2022).

<sup>98</sup> Petrou, A. *et al.* Cardiac Output Estimation: Online Implementation for Left Ventricular Assist Device Support. *IEEE Trans. Biomed. Eng.* **68**, 1990–1998 (2021).

<sup>86</sup> Dual, S. A. *et al.* Continuous Heart Volume Monitoring by Fully Implantable Soft Strain Sensor. *Adv. Healthc. Mater.* **9**, 1–11 (2020).

<sup>106</sup> Kourouklis, A. P. *et al.* Building an interdisciplinary program of cardiovascular research at the Swiss Federal Institute of Technology– the ETHHeart story. *iScience* **25**, 105157 (2022).



## ***2 Continuous Monitoring of Blood Pressure and Vascular Hemodynamic Properties with Miniature Extravascular Hall-Based Magnetic Sensor***

### **2.1 Introduction**

Cardiovascular diseases (CVDs) affect a large proportion of the western population and constitute the dominant cause of mortality, accounting for more than 17 million deaths worldwide on a yearly basis.<sup>107</sup> In this context, continuous, long-term monitoring of arterial blood pressure (ABP) and properties that reflect changes in the vascular system can provide useful information on disease progression, and enable surveillance of patient-compliance and assessment of treatment efficacy.<sup>108–110</sup>

Over the last years, the advent and rapid evolution of stretchable electronics enabled the development of devices that accurately monitor vascular biomechanical properties.<sup>86,111–113</sup> These properties include pulse wave velocity, as well as arterial compliance, distensibility, strain, stress, stiffness, and elasticity.<sup>114–116</sup> However, the most valuable and most easily derived variable that reflects the changes in the overall cardiovascular system is the ABP.<sup>108,117</sup> The waveform of the ABP is affected by left ventricular stroke volume, the biomechanical properties of the aorta, as well as the compliance and resistance of the entire vascular system. Hence, various underlying CVDs alter the ABP waveform (Fig. 2.1a-b), the analysis of which provides remarkable insights into the dynamic cardiovascular status.<sup>118</sup>

The gold standard method for monitoring ABP is through invasive arterial catheterization, typically using the radial or femoral artery.<sup>119</sup> Although this method enables accurate acquisition of the entire ABP waveform, it cannot be applied long-term or in an ambulatory setting. Invasive ABP measurement limits mobilization, bears a risk of vascular thrombosis with downstream occlusion, and is associated with infections and bleeding complications at the access site.<sup>120</sup> To overcome these limitations, new invasive approaches have been investigated that exploit the arterial distension and properties of stretchable electronics to provide monitoring of the ABP.<sup>79–83</sup> While these sensing approaches offer accurate measurements of the entire ABP waveform, their long-term usage is still complicated by drift, a phenomenon of changing sensor output over time, and the need of a tight fixation on the circumference of the aortic wall which may lead to unwanted interference with vascular movement and compliance.

Non-invasive measurement of the ABP by cuff-type sphygmomanometer or wearable devices that are directly attached to the skin provide only incremental values.<sup>121–126</sup> Although the wearable devices have significantly improved the stability of the sensing device, the measurement accuracy and reproducibility are highly affected by body posture, movement of the measuring device during use, and often by increased ABP at the time of measurement at the clinic (i.e. white coat hypertension).<sup>127</sup> Additionally, these devices typically estimate the ABP by using the peripheral blood pressure and generalized mathematical models that are associated with high inaccuracies<sup>128,129</sup> and, hence, can increase the risk of potential misdiagnosis and mistreatment<sup>116</sup>.

We present an improved invasive sensing approach for continuous monitoring of ABP as well as arterial wall diameter (AD) and arterial circumferential strain (ACS). The waveforms of the latter variables constitute the basis to further deduce pulse wave velocity, respiration frequency, and duration of the systolic phase of the cardiac cycle, which can offer new capabilities in CVD treatment management. In detail, similar to the work of Ruhhammer et al.<sup>81</sup>, an extravascular sensing device is proposed, which is attached to the outer vascular wall. The device comprises a

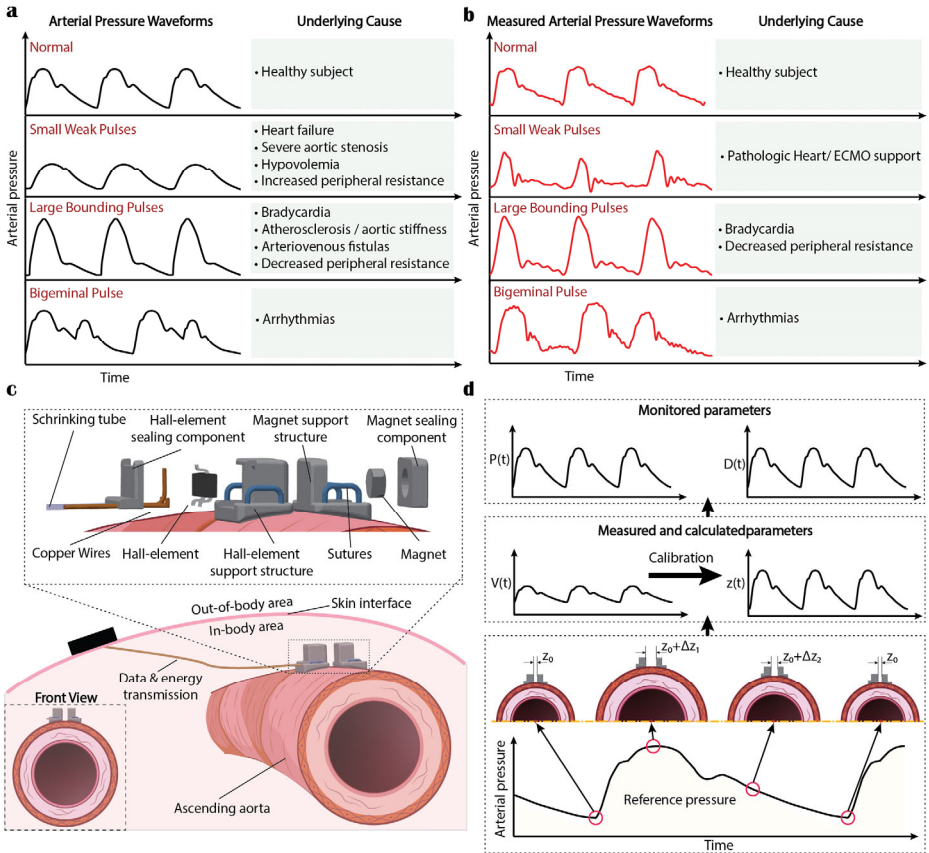


**Figure 2.1. Sensing approach of the hall-based sensing device (HBSD) for cardiovascular disease patient management.** **a**) Schematic of the most common CVDs and their influence on the blood pressure (BP) waveform. The analysis of the BP waveform contains significant information, which could be used to guide the treatment. **b**) BP waveforms captured with the sensing device during the in-vivo validation. **c**) Illustration of the HBSD attachment and a detailed view showing the components comprising the sensing device. The hall-effect sensor (HES) and magnet are completely separated and they are sutured at a predefined distance on the outer arterial wall. **d**) The contraction of the heart creates a pulsating pressure profile  $P(t)$  that travels through the arterial vessels. Depending on the vascular compliance, this pulsating pressure results in a varying vessel diameter  $D(t)$  which changes the position of the two sensing components. During systole, the distance between the components increases, resulting in a weakened magnetic-flux at the measurement surface of the HES and, hence, an increased voltage output  $V(t)$  (negative sensitivity selected for the HES). The voltage variation is translated to distance changes  $z(t)$  via the operation map produced during the calibration of the sensor. The distance between the sensing components is used to deduce the arterial diameter, the arterial circumferential strain and the pressure waveforms in a continuous manner. *ECMO, extracorporeal membrane oxygenation.*

magnetic-flux sensor (hall-effect sensor) and a miniature magnet, both fully encapsulated in 3D-printed biocompatible housings. By eliminating the elastic interconnection between the hall-effect sensor (HES) and magnet assemblies, the sensing device not only avoids vascular restriction, but also unwanted drift phenomena. The performance of the hall-based sensing device (HBSD) was

first evaluated in-vitro using an artificial silicone artery. As a next step, in a proof-of-concept study, the translational capabilities of the HBSD were validated in-vivo. In detail, the HBSD was tested in a porcine model under physiologic and pathologic hemodynamic conditions, demonstrating high accuracy in monitoring the ABP and the vascular properties in all experimental settings.

## 2.2 Methods

### 2.2.1 *Design and fabrication*

The proposed HBSD sensor is an extravascular sensing system that enables continuous measurement of the ABP, the AD and the ACS. The sensor has been optimized to allow the acquisition of changes in the diameter of large vessels such as the ascending aorta (diameter of 27.2 – 36.6 mm); however, its parametric design would also allow the adaptation of the sensor to function accurately even when smaller vessels (minimum diameter of 10 mm) need to be monitored. The sensing approach and the device structure are presented in Fig. 2.1c-d. In short, the device consists of two distinct components, namely the magnet component and the HES component, which are attached to the outer wall of the aorta. With no physical interconnection of the components, any vessel constriction and restraint is avoided, while, at the same time, drift phenomena due to material fatigue are eliminated.

The fabrication procedure of the HBSD is presented in more detail in Appendix A2 as well as Fig. A2 in the Supplemental appendix, while in Appendix A8 in the Supplemental appendix the considerations for the material selection can be found. Briefly, the magnetic component embodied a miniature Nickel-plated, Neodymium (N48) permanent magnet (Diameter =  $2\pm 0.1$  mm, Height =  $1\pm 0.1$  mm, Weight = 0.024 g), which was coated with Parylene-C by chemical vapor deposition to improve the temperature stability, as well as to ensure chemical and moisture resistance. For the HES component, an analog-bipolar HES with a SOT-23 packaging and a sensitivity of -45 mV/mT was selected (Length x Height x Thickness = 2.92 mm  $\times$  1.30 mm  $\times$  1.15 mm, Weight =  $0.3 \pm 0.01$  g). Both components were encapsulated in 3D printed and UV-cured housings made of Class-I biocompatible resin, which enabled exact positioning of the components on the arterial wall. The encapsulated assemblies, along with the copper wires for energy and data transmission, were coated with a 3 $\mu$ m layer of Parylene-C via chemical vapor deposition to ensure adequate insulation and biocompatibility. By accounting both components of the HBSD, the total weight was  $1.38\pm 0.02$  g, the height was  $3.22\pm 0.01$  mm, while the footprint on the vessel wall was  $7\pm 0.02$  mm  $\times$   $8\pm 0.4$  mm (longitudinal length  $\times$  circumferential length). The weight distribution of the HBSD on the aortic wall is given in a qualitative form in the Supplemental Fig. A9.

### 2.2.2 *Working principle*

The pulsatile nature of the native heart results in a pulsatile blood flow and, hence, the aorta experiences an altering diameter within each cardiac cycle. As illustrated in Fig. 2.1d, the variation in the AD, results in a varying distance between the magnet component and the HES component of the sensing device. Hence, a varying magnetic field is applied on the HES and, consequently, a varying output voltage is measured. By measuring the voltage output of the HES, the AD, the ACS, as well as the ABP are calculated. Based on the ABP waveform, the respiration frequency and the systolic period of the cardiac cycle can be deduced. When a second sensing device is implanted in the proximity of the first sensor, the pulse wave velocity (PWV) can also be measured.

A thorough description of the steps required to obtain the aforementioned properties is given in Fig. 2.2. Specifically, the deduction of the AD is based on the working principle of the HES since the latter responds linearly to the magnetic-flux induced perpendicular to the measurement

surface. Any translation of the permanent magnet, results in alterations of the magnetic-flux sensed by the HES and, hence, an alteration in the measured voltage output. Based on the predefined and constant sensitivity ( $S$ ) of the HES, the applied magnetic-flux perpendicular to the measuring surface ( $B_z$ ) can be calculated by the measured output voltage ( $V_m$ ):

$$B_z = \frac{V_m}{S} \quad (T) \quad (1)$$

By using the “current model” for the analysis of a permanent magnet polarized along its symmetry axis with a uniform magnetization  $M_s^{130}$  (Appendix A1 and Fig. A1, Supplemental appendix), the distance between the centers of the magnet component and the HES component of the sensing device can be calculated from the magnetic-flux. This approach results in highly accurate calculation of the distance and accounts for any misalignment between the centers of the components induced by the imprecision of the implantation. Misalignment induced during the manufacturing process, or any inherent deviation in the residual flux density of the permanent magnet however, could drastically deteriorate the accuracy of the mathematically calculated distance. To eliminate the risk for inaccuracies, we conducted a calibration procedure for each sensing device (Appendix A6 in Supplemental appendix). Based on the calibration procedure, the voltage output to distance relation was acquired for all possible orientations and misalignments of the sensing components (Fig. 2.2a), resulting in a “calibration space” for each sensing device (Fig. 2.2c). This calibration space is defined by second order exponential equations:

$$z(t) = a \cdot e^{b \cdot V_m(t)} + c \cdot e^{d \cdot V_m(t)} \quad (mm), \quad (2)$$

*with  $a, b, c, d \equiv f(\varphi, \gamma, r)$*

where  $z$  is the distance between the center of the magnet component and the HES component,  $\varphi$  the misalignment angle in the yaw plane,  $\gamma$  the misalignment angle in the pitch plane,  $r$  the misalignment of the magnet and HES centers in the x-y plane expressed as a radius, and  $V_m$  the measured voltage output.  $a$ ,  $b$ ,  $c$ , and  $d$  are exponential coefficients that depend on the misalignment parameters.

In Fig. 2.2d, the usage of the calibration space and the necessary steps to derive the monitored variables are depicted. More precisely, during the implantation procedure of the sensing device the misalignment angles  $\varphi$  and  $\gamma$ , as well as the misalignment radius  $r$  are measured. These quantities are then set as input parameters in the calibration space to acquire the appropriate voltage output to distance relation, termed the operating map. In case the measured values of  $\varphi$ ,  $\gamma$  and  $r$  do not coincide with the calibration values, a spline-based multivariate interpolation is conducted. As a next step, based on Fig. 2.2b, the AD can be calculated directly from the distance between the magnet component and the HES component by:

$$D(t) = D_0 + \frac{z(t) - z_0}{\sin(k/2)} \quad (mm) \quad (3)$$

where  $z(t)$  is the distance between the magnet component and the HES component calculated by (2),  $z_0$  is the initial distance between the magnet component and the HES component,  $k$  is the angle between the magnet component and the HES component with respect to the center of the aorta in the x-y plane, and  $D_0$  is the initial aortic diameter.

The circumferential arterial strain can be calculated from the arterial diameter as:

$$\varepsilon_c = \frac{D(t) - D_0}{D_0} \quad (4)$$



The calculation of the ABP is based on the Young-Laplace equation defined for thin-walled vessels<sup>131</sup>, given as:

$$\sigma_c = P \frac{R}{\delta} \quad (5)$$

with  $\sigma_c$  being the circumferential stress,  $P$  the arterial pressure,  $R$  the arterial wall radius and  $\delta$  the arterial wall thickness. When the arterial wall is considered as non-viscous and inertialess material with a linear elastic response, the circumferential stress is linearly related to the strain  $\varepsilon_c$  with the elastic Young modulus  $E_Y$  ( $\sigma_c = E_Y \varepsilon_c$ ). However, studies have shown that the arterial wall is characterized by a visco-elastic behavior<sup>115</sup>. In this work, the visco-elastic behavior of the arterial wall is taken into consideration by incorporating the effect of the rate of change of strain in the stress-strain relation, as proposed by Peterson et al.<sup>132</sup> and given by:

$$\sigma_c = E \varepsilon_c + R_m \frac{d\varepsilon_c}{dt} \quad (6)$$

By substituting equation (6) to (1), the arterial pressure is calculated by:

$$P = \frac{\delta}{R} (E \varepsilon_c + R_m \frac{d\varepsilon_c}{dt}) \quad (7)$$

with  $E$  and  $R_m$  being subject-specific elastic moduli that are identified with in-situ calibration during the implantation process.

The respiratory activity influences the transmural pressure (pressure inside the heart chamber minus the intrapleural pressure), resulting in increased or decreased preload and ventricular stroke volume during inspiration or expiration, respectively. These alterations in preload and stroke volume during the respiration cycles affect the ABP, allowing the deduction of the respiratory frequency by the ABP waveform. The latter deduction requires accurate identification of the onset of each cardiac cycle. In this study, we identified the cardiac cycle onsets based on the maxima of the first derivative of the ABP waveform, when the latter is low-pass filtered with an 18<sup>th</sup> order, zero-phase finite impulse response (FIR) filter with a cut-off frequency of 8 Hz (Appendix A3, Fig. A3, Supplemental appendix). The cardiac cycle onsets enable the extraction of the systolic pressure (SP). The SP points of the ABP result in a new waveform. By identifying the minima of this waveform, the respiration period can be calculated as the time interval between two consecutive minima. Consequently, the respiration frequency is deduced as the inverse of the respiration period. A detailed flowchart of the described process is given in Fig. A5 in the Supplemental appendix.

For the calculation of the systolic phase of the cardiac cycle, the cycle onset along with the dicrotic notch are prerequisites. However, the identification of the dicrotic notch is not trivial. In this work, we followed the process described in Fig. A4 in the Supplemental appendix. In short, the maxima of the first derivative of the low-pass filtered ABP waveform, which do not correspond to the cardiac cycle onsets and the index of which exceeds the SP index, are identified. The indexes of these maxima are then used as pivot points to search and identify the regional maxima of the original ABP waveform. The regional maxima correspond to the dicrotic notch of each cardiac cycle. By calculating the time interval between the onset and the dicrotic notch of each cycle, the systolic phase of the cardiac cycle is deduced (Fig. A4, Supplemental appendix).

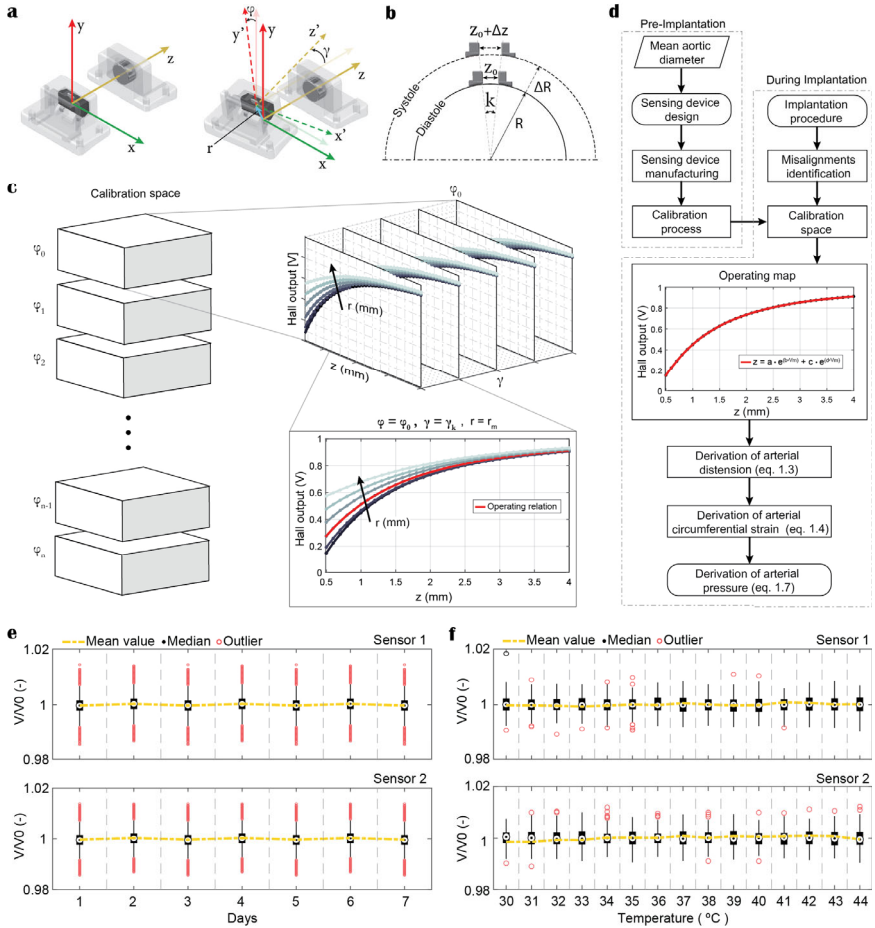


**Figure 2.2. Working principle and characterization of the hall-based sensing device (HBSD).** **a**) misalignment between the centers of the sensing components during the implantation procedure.  $\varphi$  is the angle in the yaw plane ( $x' - y'$ ),  $\gamma$  is the angle in the pitch plane ( $x' - z'$ ),  $r$  is the misalignment of the magnet and hall-effect sensor (HES) centers in the yaw plane expressed as a radius. **b**) schematic of the changing distance between the sensing components within a cardiac cycle.  $z_0$  is the initial distance between the magnet component and the HES component,  $k$  is the angle between the magnet and the HES with respect to the center of the aorta in the yaw plane,  $R$  is the arterial radius during diastole, while  $\Delta R$  and  $\Delta z$  are the change in arterial radius and distance, respectively. **c**) each HBSD is calibrated for a set of  $\varphi, \gamma$  and  $r$  combinations, resulting on the depicted calibration space. The measured misalignment values are used as driving parameters in the calibration space to identify the operating relation between the sensor output and the distance between the sensing components. **d**) flowchart of the steps necessary to derive the arterial distension, the arterial circumferential strain (ACS) and the arterial blood pressure (ABP). **e**), HBSDs evaluated for their operation robustness when they are immersed in a 0.9% saline bath at 37 °C for seven days. Both sensors show great stability with the change in their response being within the initial deviation of the sensor. **f**) The performance of two sensors was evaluated in a temperature ramp test. Temperature changes within the range of 30°C to 44 °C had no effect on the sensor's response.

The PWV can be measured by attaching a second sensor in the proximity of the first sensor. More precisely, the PWV is calculated by the division of the distance between the two sensors and the time interval between the cardiac cycle onset on the first sensor and the same cardiac cycle onset of the second sensor.

### **2.2.3 Characterization of hall-based sensing device**

The HBSD was tested and characterized with respect to its robustness to sterilization, immersion into liquid, temperature changes, dynamic cyclic loading, as well as, to misalignment effects induced by imprecision of the implantation. In detail, five HBSDs were sterilized by autoclaving (121 °C for 20 min) to ensure their robustness in common sterilization procedures. The autoclaved sensing devices were mounted on a holding structure that ensured fixed distance between the magnet and the HES components. The holding structure with the sensing devices attached was immersed in a 0.9% saline solution bath that was kept at 37 °C via a heating element (Corio™, JULABO GmbH, Seelbach, Germany). The sensing devices were directly connected to an NI-DAQ-USB6210 (National Instruments (NI), 1 kHz sampling frequency) and the data was continuously registered in a desktop PC for 7 days. After this period, all sensors were retrieved to be examined for swelling. Based on Dual et al.<sup>86</sup>, the weight of each sensor was measured on a precision scale (ALJ 500-4A, KERN & SOHN GmbH, Balingen, Germany). After applying vacuum and heat (100 °C) for 2 hours, the weight of each sensor was measured again on the same precision scale.

The temperature experiments were conducted with the HBSDs (n = 5) being mounted on a holding structure and immersed in a 0.9% saline solution bath. The temperature of the bath ranged from 30 – 44 °C, in steps of 1 °C and it was measured with a thermistor (MA-100, Amphenol Advanced Sensors, St. Marys, PA, USA). The response of the sensing devices, as well as, the temperature of the bath, were acquired via an NI-DAQ-USB6210 (NI, 1 kHz sampling frequency). For each temperature setting, after the temperature in the bath had stabilized at the required level, the data was measured and collected in 30-minutes windows and registered to a desktop PC.

To evaluate the robustness of the sensing devices in long-term cyclic loading, tests were performed on a tensile testing machine (AGS-X, Shimadzu Schweiz GmbH, Reinach BL, Switzerland). The clamping of the sensing devices on the tensile device required specific mountings that have been designed and manufactured out of polylactic acid (PLA) with fused deposition modelling (FDM) 3D printing. The cyclic loading emulated the maximum distension of 2 mm that the sensing device could measure when implanted on an ascending aorta with a diameter of 30 mm. The moving velocity was 4 mm·s<sup>-1</sup>, emulating a heart rate of 60 bpm and symmetric systolic and diastolic periods.

Finally, the assessment of the misalignment effects on the response and accuracy of the HBSD was based on the calibration space developed during the HBSD calibration procedure (Appendix A6 in Supplemental appendix).

### **2.2.4 In-vitro setup and experiments**

The performance of the HBSD in measuring the AD, the ACS and the ABP was first evaluated in-vitro. The testbench for the in-vitro tests (shown in Fig. 2.3a) consisted of a linear motor (P01-37x120F, Linmot, NTI AG LinMot & MagSpring, Spreitenbach, Switzerland), a bellows, two unidirectional valves, a waterproof tank made of Plexiglass, an artificial artery molded with RTV3040 silicone, two mountings for the artificial artery with pressure measurement ports, two pressure sensors (TruWave, Edwards Lifesciences), a laser optical displacement sensor (optoNCDT, Micro-Epsilon Messtechnik GmbH & Co. KG, Wittenbach, Switzerland), a flow meter (Sonoflow CO.55/190, Sonotec GmbH, Halle, Germany) a thermistor (MA-100, Amphenol

Advanced Sensors, St. Marys, PA, USA) and a heating element (Corio™, JULABO GmbH, Seelbach, Germany).

To adequately mimic the typical expansion and pulsatile nature of the native aorta in the ascending region, the artificial artery had an outer diameter of 30 mm (the typical outer diameter of the ascending aorta in adults is 27.2 – 36.6 mm)<sup>128</sup> and a wall thickness of 2 mm. The silicone artery was fabricated based on the process described by Zimmermann et al.<sup>133</sup> Five HBSDs were attached on the artificial artery with instant adhesive and the artificial artery was mounted on the testbench to form a closed loop system. During the in-vitro experiments, the tank was filled with a physiologic saline solution and the temperature was controlled at 37 °C. The closed loop system was also filled with saline solution; however, its temperature was not controlled. By manipulating the stroke length and the velocity of the linear motor, various sinusoidal pressure curves could be achieved, accounting for different pressure conditions and various physiologic heart rates. The intravascular pressure (measured through the pressure ports before and after the artificial artery) and the displacement of the arterial wall (measured with the laser optical displacement sensor) were used as reference signals for the evaluation of the performance of the HBSDs.

### **2.2.5 *In-vivo setup and experiments***

The feasibility of HBSD and its performance were further assessed in-vivo, in a porcine model, mimicking more accurately the environment and the arterial motions encountered under clinical conditions. In addition, to evaluate the translational readiness, the HBSD was tested under physiologic and pathologic hemodynamic conditions, with the latter being mimicked by implementing cardiopulmonary bypass (CPB) support. All experiments were conducted on adult pigs (n = 12, Swiss large white, female, 96.9± 8.7 kg body weight (BW)) with a diameter of the ascending aorta of 23.4±3.3 mm. The experiments were divided into three phases. In detail, the first four experiments facilitated the model and device establishment, wherein the design and electronics of the HBSDs were iteratively optimized and the experimental protocol was established. The second phase, comprised two experiments, dedicated to the optimization of the physiologic and hemodynamically deviated animal models as well as to the optimization of the overall experimental protocol. Finally, a device validation phase followed, wherein the standardized assessment of the optimized device was performed in six animals. The animal housing and all procedures and protocols were performed with the ethical approval of the local committee for experimental animal research (Cantonal Veterinary Office Zurich) under the license number ZH213/2019.

The experimental procedure of the in-vivo experiments is shown in Fig. 2.4a-b. In detail, after the loss of postural reflexes following premedication with ketamine (Ketasol®-100 ad us. vet.; Dr. E. Graeub AG, Berne, Switzerland, 15 mg/kg), azaperone (Stresnil®, Elanco Tiergesundheit AG, Basel Switzerland 2 mg/kg) and atropine (Atropin 1% Kantonsapotheke, Zurich Switzerland 0.05 mg/kg), anesthesia was induced by a bolus injection of propofol (Propofol®- Lipuro 1%, B. Braun Medical AG; Sempach, Switzerland, 1–2 mg/kg BW), and the animals were intubated. Anesthesia was then maintained with 2–3% isoflurane and propofol (2–5 mg/kg/h). Amiodarone (Cordarone, Sanofi-Aventis (Suisse) SA, Vernier, Switzerland, 150 mg bolus iv) was administered to stabilize the heart rhythm, while administration of buprenorphine (0.01 mg/kg) every 4 hours for the duration of the procedure was included for the pain management.

Once the animal was anesthetized, as it is depicted in Fig. 2.4a-b, a left thoracotomy was performed to provide access to the ascending and descending aorta. A perivascular flowmeter (T400, Transonic Systems Inc, Ithaca, NY, USA) was implanted at the base of the ascending aorta to provide reference measurements of the cardiac output. Specifically designed paper-stencil representing the sensors' exact foot-print was placed at the predetermined site of sensor implantation on the aorta and served as a guide for the precise placement of 5-0 Prolene surgical sutures (Ethicon, Puerto Rico, USA). Following the suture placement, the needles were cut and

sutures threaded through pre-fabricated holes on the HBSD components. The two components of each HBSD were then 'sided' along their corresponding sutures into the thoracic cavity and then fixed onto the aortic wall by knotting the suture's free ends. The position of the HBSD components was radial (perpendicular to the longitudinal axis of the aortic wall), allowing the distance between the two components to freely follow the pulsatile changes of the aortic diameter (the implantation process is demonstrated in the Supplemental video "ImplantationHBSD.mp4"). After fixing the HBSD components, as shown in Supplemental Figure A7, a fluoroscopy image in latero-lateral projection was taken and the alignment of the two components was assessed. When the HBSD alignment met the acceptance criteria (Appendix 7, Supplemental Figure A8, Supplemental appendix), the voltage output of the sensor was measured for 20 s, otherwise one of the HBSD components was repositioned and the process was repeated. The mean value of the 20-second measurement was compared to the voltage output identified during the calibration process for the same distance and alignment. In case the voltage deviation exceeded 5% (Appendix A7, Supplemental Figure A8, Supplemental appendix), the HBSD was replaced. In a next step, an intravascular fluid-filled blood pressure measuring catheter (Infiniti 5F PIG 145 .038 125cm, Cordis Corporation, Miami Lakes, USA) was inserted through the femoral artery and under fluoroscopic guidance carefully positioned at the height of the HBSD at the ascending aorta, and connected to a commercial blood pressure sensor to provide the necessary reference signal. All the reference sensors and the HBSDs were connected directly to a data acquisition card and the data was continuously recorded.

To demonstrate the full capabilities of the HBSD, a number of different hemodynamic conditions were emulated during all animal experiments. Specifically, after a baseline measurement at stable resting conditions, adrenergic stimulation using Dobutamine (0.5 mg/mL) was performed to achieve a systolic pressure (SP) of approximately 130 mmHg for a pre-specified period of 5 minutes. These settings allowed the evaluation of the HBSD under increased blood pressure levels (up to 150 mmHg), as well as, increased heart rates (up to 130 beats-per-minute). Additionally, to investigate the effect of the respiration induced movement on the HBSD performance, 15-20 seconds of apnea conditions were conducted.

To test the capabilities of the HBSD in hemodynamic conditions present in patients with heart failure (e.g. volume overload) or in case of low pulse pressures (e.g. heart failure patients supported with ventricular assist devices), the animals were connected to a cardiopulmonary bypass (CPB) circuit. To achieve this, after heparinization (ACT>300s), cannulation of the aortic arch (inflow) and the pulmonary artery (outflow) was performed and the pig was connected to the CPB circuit (Fig. 2.4c). The performance of the HBSD was assessed under various CPB support levels, with and without pharmacological stimulation (Dobutamine).

During the in-vivo experiments, the intravascular pressure, the voltage output of the HBSD and the aortic flow were acquired with an NI-DAQ-USB6210 (2 kHz sampling frequency), driven by a MATLAB 2020b (The MathWorks, Natick, USA) script.

On the completion of the study procedure, all animals were euthanized by the administration of an overdose of pentobarbital while still under general anesthesia according to the animal study protocol.

### **2.2.6 Data post-processing.**

The data collected during the in-vitro and in-vivo experiments was filtered with an 18<sup>th</sup> order, zero-phase finite impulse response (FIR) filter with cut-off frequency of 30 Hz and 14 Hz, respectively. Post-processing was conducted with MATLAB 2020b (The MathWorks, Natick, USA) scripts.

### **2.2.7 Statistical analysis.**

The data are presented as time sequences, as well as with the mean  $\pm$  standard deviation (SD) of the difference between the reference measurements and the measurements conducted with the

HBSD. The comparison of the reference and HBSD measurement approaches is based on the intraclass correlation coefficient (ICC) with its 95% confidence intervals (CIs), using the model of absolute agreement with single measurements (A-1)<sup>134</sup> implemented by Salarian.<sup>135</sup> Additionally, the data are compared with the Bland-Altman plots of differences with the representation of the mean difference, the limits of agreement from -1.96 SD to +1.96 SD, and 95% CI. All statistical analyses were performed in MATLAB R2020b.

## 2.3 Results

### 2.3.1 Characterization of HBSD

The conventional sterilization process, conducted by autoclaving the sensing device at 121 °C for 20 min, had no influence on the operation of the hall-effect-based sensor. The response of two sensors immersed for seven days in a physiologic (0.9%) saline solution bath at 37 °C, simulating the environment within the human body, is shown in Fig. 2.2e. The change in the mean voltage output (MVO) and the standard deviation (STD) with respect to the initial voltage output  $V_0$  was infinitesimal over the course of the experiment. Following the immersion in liquid, the sensors were examined for the presence of swelling of the 3D-printed encapsulation structure. Both sensing devices presented a weight increase of <1%.

In Fig. 2.2f, the effect of temperature changes on the response of the HBSD are presented, by means of the MVO with respect to the initial voltage output  $V_0$ . During the ramp up of the temperature from 30 °C to 44 °C, the MVO was unchanged, while the STD remained in the initial range. This response indicates the robustness of the HBSD to temperature changes in a range much broader than the one expected inside the human body.

The novelty of the proposed HBSD stems from the absence of an elastic interconnecting part between the sensing components. Any elastic component would be prone to cyclic fatigue and, consequently, long-term drift of the sensor. To prove the robust operation of the HBSD over time, long cyclic loading experiments were conducted on a tensile device. As it can be seen in Fig. A6 in the Supplemental appendix, the response of the sensor after 30'000 cycles is identical to the initial response as expected.

In addition, the influence of misalignment among the two sensing components of the HBSD, was examined. The response and resolution of the sensor was adequate as long as  $\phi < 2^\circ$ ,  $\gamma < 2^\circ$  and  $r < 0.5$  mm, while the limit in z-distance for the investigated design was 2.25 mm. In case the induced misalignments exceed the latter limits, the sensor position needs to be adjusted.

### 2.3.2 In-vitro performance validation

By using the in-vitro setup shown in Fig. 2.3a, five HBSD were mounted on the surface of the artificial artery (Fig. 2.3a) and various physiologic conditions (Fig. 2.3b) were emulated by varying the loading range [peak systolic pressure  $\approx$  30-220 mmHg] and the heartrate [60-160 bpm]. In Fig. 2.3c, a comparison of the diameter measured with the HBSD and the reference sensor is shown for the applied operating conditions. The profile of the diameter was almost identical to the reference profile in all conditions. Similarly, the pressure profiles acquired with the HBSD indicated high accuracy when compared to the reference pressure profiles (Fig. 2.3c). In Fig. 2.3d, association between the reference values and the values measured via the HBSD is illustrated. The ICCs for the diameter and pressure measurements were 0.9995 (95% CI: 0.9995-0.9995) and 0.9944 (95% CI: 0.9892-0.9965), respectively. Although the time-sequence data of

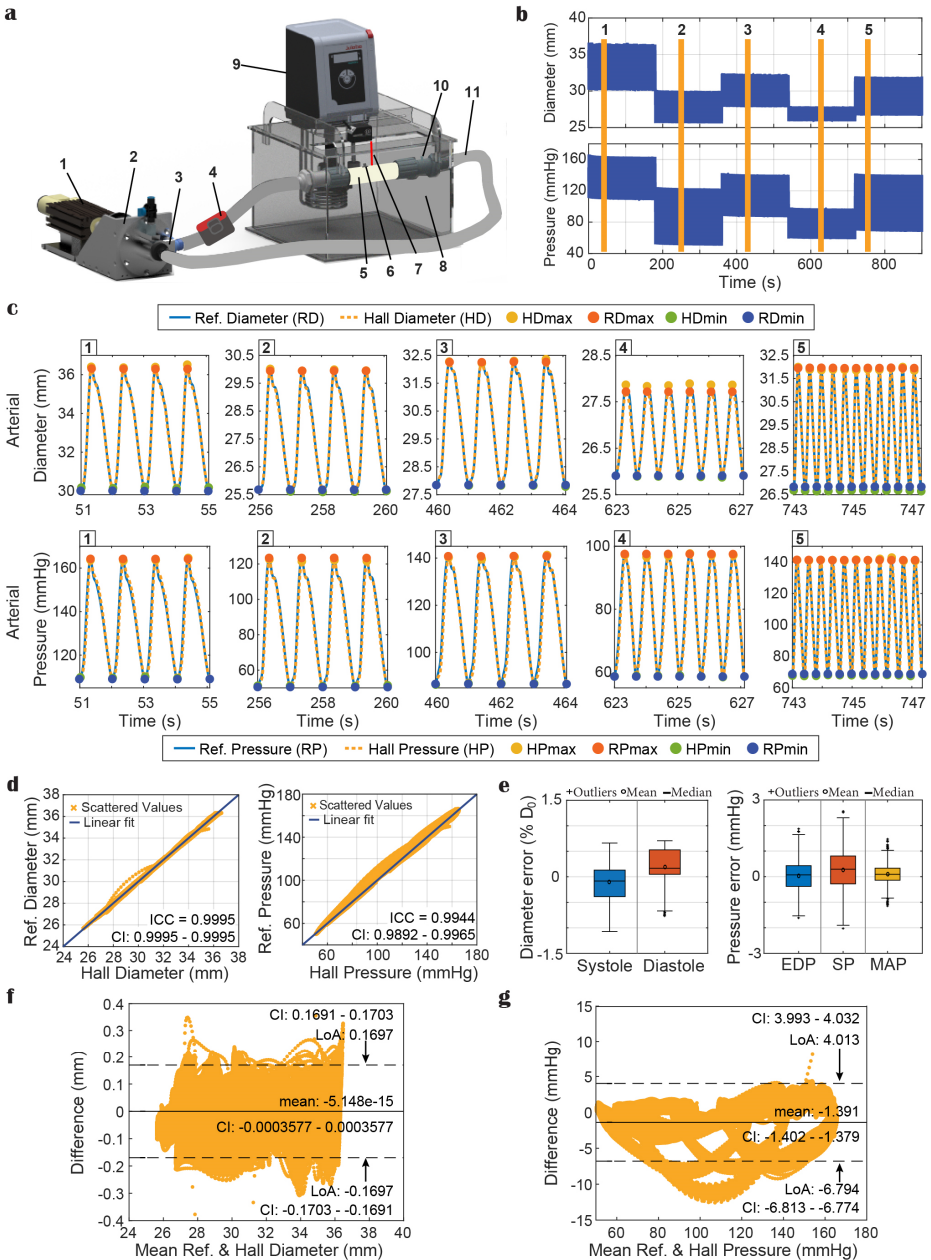


**Figure 2.3. In-vitro setup and performance validation of the hall-based sensing device (HBSD).** **a)** Setup for the in-vitro evaluation of the HBSD, comprised of 1) a linear motor, 2) a bellows that enables a volume change, 3) two unidirectional valves, 4) a flow meter, 5) an artificial silicone artery, 6) five HBSDs, 7) a laser sensor measuring the reference diameter, 8) a waterproof tank, 9) a heating element and a thermometer, 10) a port for reference pressure measurement, and 11) tubing to circulate the saline solution. **b)** The applied

diameter and pressure conditions to emulate different operating scenarios. In time-windows 1-3 the heartrate remained at 60 beats per minute (bpm), with varying loading conditions, while in windows 4 and 5, the heartrate was set to 90 and 160 bpm, respectively. **c**, Detailed depiction of the measurements during the operating conditions 1-5, shown in b. The arterial diameter and pressure measured with the HBSD is compared with the reference diameter and pressure measurements, while the systolic and diastolic values are presented for all signals. **d**) Linear association between the diameter measured with the HBSD and the RD, as well as the pressure measured with the HBSD and the RP. The intraclass correlation coefficients for the diameter and pressure measurements were 0.9995 (95% CI: 0.9995-0.9995) and 0.9944 (95% CI: 0.9892-0.9965), respectively. **e**, Difference of the systolic and diastolic values measured with the HBSD and the reference sensors, including all different operating conditions. The difference in diameter is expressed as a percentage of the initial diastolic aortic diameter. **f**, Bland-Altman plot of differences between the HBSD and the RD, with the representation of the mean difference, the limits of agreement (dashed line) from -1.96 seconds to +1.96 seconds, and 95% CI. **(G)** Bland-Altman plot of differences between the HBSD and RP, with the representation of the mean difference, the limits of agreement (dashed line) from -1.96 seconds to +1.96 seconds, and 95% CI. *EDP*, end-diastolic pressure; *HP*, hall pressure; *MAP*, mean arterial pressure; *SP*, systolic pressure.

diameter and pressure contain crucial information about the condition of a patient, it is of paramount importance to extract the values obtained during systole (SP) and diastole (EDP), as well as the mean ABP (MAP). The mean error between the reference diameter and the diameter measured via the HBSD, expressed as a percentage of the initial diastolic aortic diameter, was  $-0.10\% \pm 0.29\%$  and  $0.19\% \pm 0.34\%$  during diastole and systole, respectively (Fig. 2.3e). The mean error in the EDP, SP, and MAP (Fig. 2.3e) was  $0.03 \pm 0.79$  mmHg,  $0.25 \pm 0.59$  mmHg and  $0.10 \pm 0.38$  mmHg, respectively. Under all conditions examined, the absolute pressure error was below 3 mmHg. The results of the Bland-Altman plot in Fig. 2.3f and 2.3g also indicate that the HBSD has a mean bias of 0 mm, with limits of agreement (LoA) of 0.16 mm, compared to the reference laser sensor, and a mean bias of -1.39 mm Hg, with LoA of -6.79 – 4.01 mm Hg, compared to the reference pressure sensor.

### 2.3.3 *In-vivo performance validation*

To demonstrate the full capabilities of the HBSD and assess its translational readiness an extensive in-vivo experimental protocol has been designed and executed in a porcine model. In Fig. 2.4d, a comparison of the reference pressure and the pressure measured via the HBSD is illustrated for one of the animal experiments. The pressure signal provided by the HBSD accurately captured the highly varying pressure profiles, regardless of the pressure level and the heart rate. In Fig. 2.4f, the linear association between the reference pressure values and the values measured via the HBSD is depicted for the entire experiment. The high association between the two measuring approaches is confirmed by the high ICC that was 0.9856 (95% CI: 0.9855-0.9858). The mean error and the STD in the EDP, SP and MAP (Fig. 2.4g) was  $-2.62 \pm 3.17$  mmHg,  $0.43 \pm 2.39$  mmHg, and  $-1.60 \pm 2.28$  mmHg, respectively. Additionally, in the Bland-Altman plot (Fig. 2.4j) it is indicated that the HBSD has a mean bias of 0 mmHg, with LoA of 4.08 mmHg, compared to the reference pressure sensor.

A cumulative analysis of the entire in-vivo dataset, is provided in Fig. 2.5a-c. From the 24 sensors implanted in all in-vivo experiments, 15 were eligible for further evaluation. The rest of the sensors were excluded due to corrupted reference measurements (2 sensors), animal complications (2 sensors), or sensor malfunction including sensor detachment or wire breakage (5 sensors). In Fig. 2.5a, boxplots with the difference between the EDP, SP and MAP values measured with the HBSDs and the reference sensors are depicted for stable resting conditions. All sensors demonstrated accurate measurement of EDP, SP and MAP, with the mean absolute



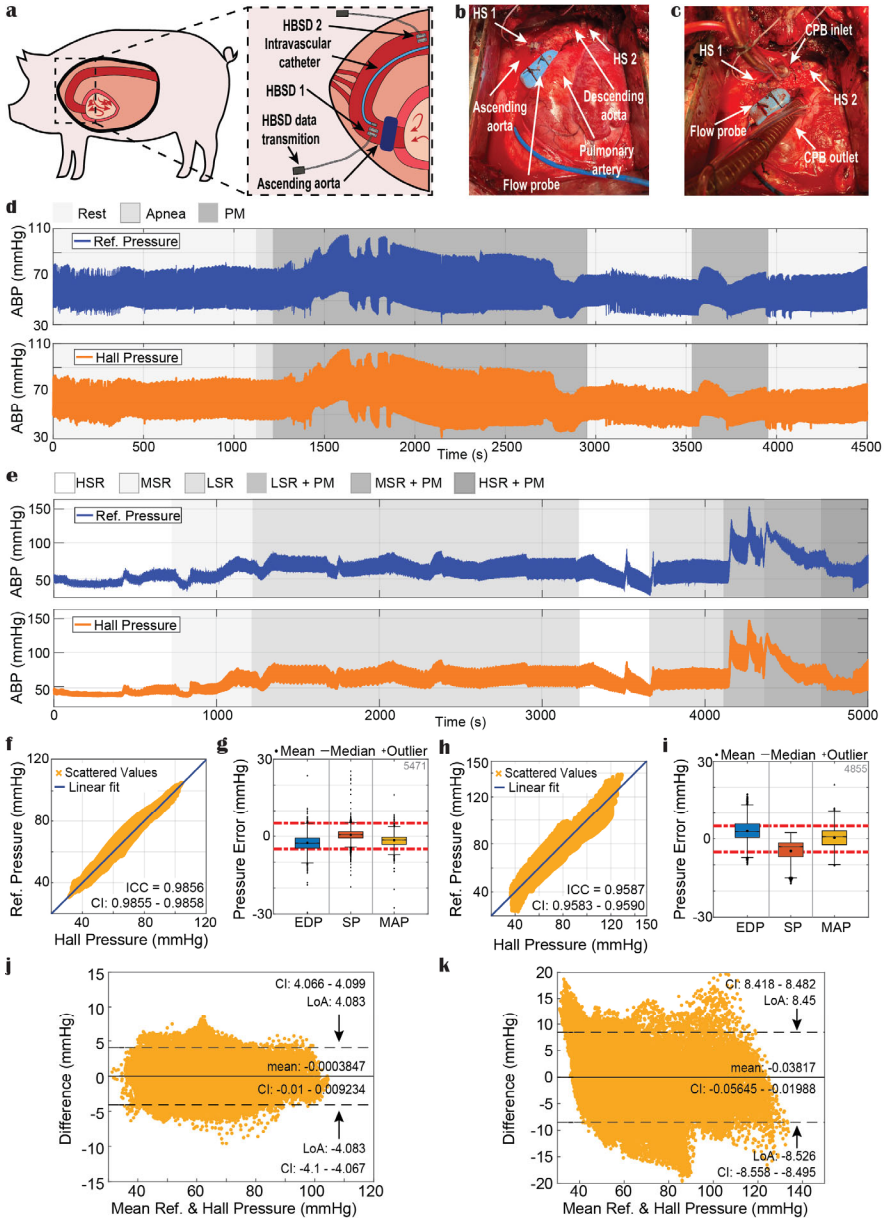


**Figure 2.4. In-vivo setup and performance validation of the HBSD.** **a)** Setup for the in-vivo evaluation of HBSD. Under general anesthesia, the ascending aorta was surgically accessed through a left thoracotomy. Further, the two components of the HBSD were carefully fixed on the vessel, in a transversal direction, with surgical sutures. Through a femoral access, an intravascular catheter was placed in the ascending aorta to provide the reference pressure values. **b)** Image of the in-vivo setup with the HBSD 1 and HBSD 2 being sutured on the ascending and descending aorta, respectively. **c)** Image of the in-vivo setup after the insertion

of the inlet and outlet CPB tubing. **d)** Comparison of the ABP measured via the HBSD and the reference intravascular pigtail catheter during the in-vivo experiment. The HBSD was able to accurately capture the varying loading conditions, which were achieved by administering adrenergic medical stimulation. **e)** Comparison of the ABP measured via the HBSD and the reference intravascular pigtail catheter during the CPB support. The HBSD was able to accurately capture the varying loading conditions, which were achieved by administering boluses of Dobutamine and different support ratios. **f)** The intraclass correlation coefficient for the ABP measured with the HBSD and the reference ABP was 0.9856 (95% CI: 0.9855-0.9858). **g,** Difference of the EDP, SP, and MAP values measured with the HBSD and the reference sensor, including all different operating conditions. **h,** The intraclass correlation coefficient for the ABP measured with the HBSD and the reference ABP during the CPB support was 0.9587 (95% CI: 0.9583-0.9590). **i,** Difference of the EDP, SP, and MAP values measured with the HBSD and the reference sensor, including all different CPB support ratios and pressure conditions. **j,** Bland-Altman plot of differences between the HBSD and the reference pressure, with the representation of the mean difference, the limits of agreement (dashed line) from -1.96 seconds to +1.96 seconds, and 95% CI. **k,** Bland-Altman plot of differences between the HBSD and the reference pressure during CPB, with the representation of the mean difference, the limits of agreement (dashed line) from -1.96 seconds to +1.96 seconds, and 95% CIs. *CPB, cardiopulmonary bypass; HBSD, hall-based sensing device; HSR, high support ratio; LSR, low support ratio; MSR, medium support ratio; PM, pressure manipulation; other abbreviations as in Fig. 2.3.*

error (MAE) being below 5 mmHg compared to reference. Overall, HBSDs showed slightly lower accuracy in SP measurements, with increased MAE and STD values. The same boxplots are given in Fig. 2.5b for the experimental section where blood pressure and heart rate stimulation were performed. During these conditions, although all HBSDs demonstrated a MAE below 5 mmHg in EDP and MAP measurements, five HBSDs showed MAE above 5 mmHg in SP measurement. In addition, during the blood pressure stimulation the STD was increased for all HBSDs. In Fig. 2.5c, boxplots of the difference between the EDP, SP and MAP values measured with the HBSDs and the reference sensors during apnea are depicted. Under apnea, a significant reduction in both MAE and STD is demonstrated for all of the examined HBSDs. However, the samples size (given on the lower right corner of each boxplot) was significantly lower compared to the other sections. Furthermore, for HBSD 5 and 6, the apnea section was not completed due to animal complications.

In Fig. 2.4e, a comparison of the reference pressure and the pressure measured via the HBSD is illustrated during the CPB support. Independent of the pressure level, the CPB support level and, hence, the effective pulse pressure, the pressure signal provided by the HBSD captured accurately the highly varying pressure profiles. In Fig. 2.4h, the linear association between the reference pressure values and the values measured via the HBSD is depicted for the entire experiment under CPB support. The ICC for the ABP measured with the HBSD and the reference ABP during the CPB support was 0.9587 (95% CI: 0.9583-0.9590), confirming the high association between the two measuring approaches. The mean error in the EDP, SP and MAP (Fig. 2.4i) was  $3.0 \pm 4.75$  mmHg,  $-4.65 \pm 4.4$  mmHg, and  $0.46 \pm 3.92$  mmHg, respectively. Additionally, in the Bland-Altman plot (Fig. 2.4k) it is indicated that during the CPB support, the HBSD has a mean bias of 0.03 mmHg, with LoA of 8.50 mmHg, compared to the reference pressure sensor. In Fig. 2.5d, the boxplots showing the difference between the EDP, SP and MAP values measured with the HBSDs and the reference sensors during the CPB support are illustrated. A total of eleven sensors were assessed during this experimental section, four sensors were again excluded due to animal complications or sensor malfunctions (sensor detachment or wire breakage) after the CPB implantation. The examined sensors demonstrated high accuracy in EDP, SP and MAP measurement regardless of the CPB support level. Except for two HBSDs, the analyzed HBSDs showed a MAE lower than 5 mmHg for all measurement; however, in some

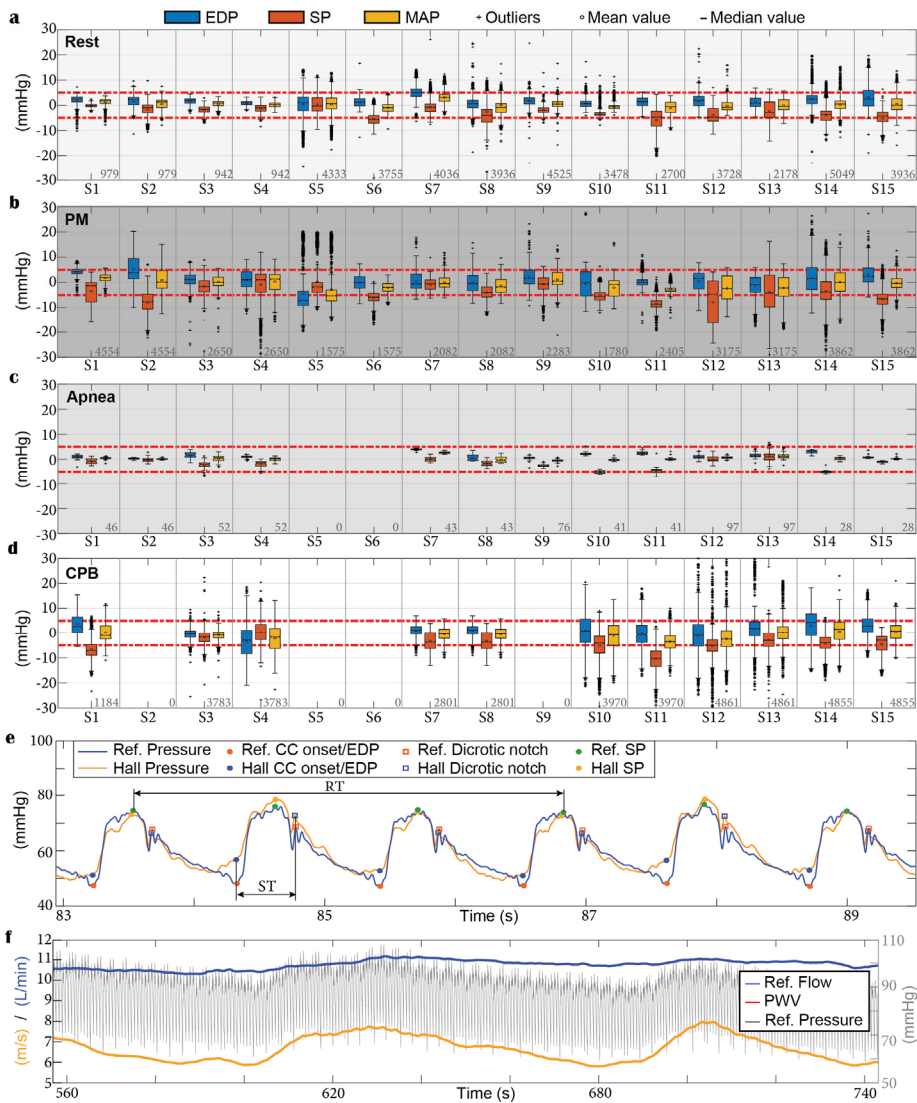


**Figure 2.5. Cumulative analysis of HBSD performance in-vivo, identification of cycle critical components and PWV calculation.** Difference of the EDP, SP and MAP values measured with 15 HBSDs and the reference sensor during the in vivo experiments: **a)** rest/stable animal condition. **b)** apnea. **c)** pressure manipulation, **d)** CPB support. At the bottom-right corner of each sensor block the number of evaluated samples is given. The patch colors correspond to Fig. 2.4d. The dashed red lines show the boundaries for pressure measurement device certification. **e)** identification of cardiac cycle onset/EDP, dicotic notch and SP from the ABP waveform provided from the HBSD and the reference sensor. The systolic phase of the cardiac cycle is calculated as the time interval between the onset and the dicotic notch of each cardiac cycle. The respiration period and, hence the respiration frequency is calculated by the time interval between the minim of the SP values (Appendix 3-5, Fig. A3-5 in Supplemental appendix). **f)** PWV calculation based on the ABP waveforms of two consecutive HBSDs. The reference flow and pressure are also depicted to validate the changes in the PWV. CC, cardiac cycle; CPB, cardiopulmonary bypass machine; EDP, end diastolic

pressure; HBSD, hall-based sensing device; MAP, mean arterial pressure; PM, pressure manipulation; PWV, pulse wave velocity; RT, respiration time; SP, systolic pressure; ST, systolic phase duration.

cases the number of outliers has been increased due to misdetections during the identification of the EDP value.

By capturing the entire ABP waveform, as shown in Fig. 2.5e, the HBSD enables the identification of the cardiac cycle onsets, EDP, SP, and dicrotic notch through post-processing. Based on the time-index of the dicrotic notch and the onset of a specific cardiac cycle, the systolic phase of the cardiac cycle can be determined. In the same figure, the points used for the calculation of the respiration frequency are showed; however, a detailed flowchart of the calculation is given in the Supplemental appendix (Appendix A5 and Fig A5, Supplemental appendix). In Fig A5, the calculated respiration frequency is compared with the reference respiration frequency which was set as default value on the ventilator used during the experiments (20 breaths/min).

In Fig. 2.5f, the calculated PWV along with the reference flowrate and ABP is illustrated. Although there was not a reference measurement for the PWV, the calculated PWV was in the physiologic range of the animal model used<sup>129</sup>. Additionally, as it is illustrated in Fig. 2.5f, the PWV followed correctly the pressure and flow variations, confirming its accuracy.

## 2.4 Discussion

In this work, the design, characterization as well as in-vitro and in-vivo performance of an implantable HBSD for continuous monitoring of ABP, AD, and ACS have been demonstrated under various hemodynamic conditions. The HBSD consists of a HES and a miniature magnet, which are both embedded in 3D printed biocompatible housings and then coated with Parylene-C. The design of the sensing device allows for optimization of the housings based on the vascular diameter, ensuring safe attachment and accurate measuring capabilities.

The extravascular nature of the HBSD diminishes the risk of thrombosis, blood cell damage and flow obstruction, which constitute common problems that current intravascular sensors encounter.<sup>136</sup> The lack of connective material between the components of the HBSD, along with the minimal footprint and weight (<1.4 g) of the HBSD, ensure that neither relevant restriction on the distension, nor gravitational forces due to the device's mass are applied on the arterial wall. Hence, compared to the majority of extravascular sensors that have been proposed for the measurement of vascular and hemodynamic properties,<sup>79–82,86,111–113</sup> the HBSD may substantially reduce the risk of adverse events.

The robustness of the HBSD was demonstrated during autoclaving procedures, immersion in liquid environment, and temperature changes. Additionally, the sensing device showed excellent response under dynamic cyclic loading. The latter characteristic stems from the avoidance of any elastic connective material, which are prone to fatigue and often the main source of sensor drift. Eliminating drift is a major step towards the achievement of long-term monitoring of CVD patients and constitutes a fundamental benefit compared to the majority of other extravascular or wearable sensing technologies.<sup>137</sup>

The in-vitro tests of the HBSD demonstrated its capabilities to monitor the AD, the ACS and the ABP. The HBSD was able to accurately capture all applied changes in diameter and pressure of the artificial artery. Comparison of the data produced by the HBSD with the reference data showed high association and agreement, independent of the emulated hemodynamic state. Compared to published data, the HBSD outperforms the existing extravascular sensing approaches in regards of accuracy.<sup>81,83,112</sup>

The performance of the HBSD was further evaluated in-vivo under various hemodynamic conditions (e.g. physiologic, pathologic) in a pig model. The pressure waveforms provided by the HBSD demonstrated high association and agreement with the reference pressure waveforms measured by the intravascular catheter during the entire experiment and, independent of the

pressure range and the heartrate changes. For the sensors analyzed in this work, the mean error between the EDP, SP and MAP values provided by the two sensing approaches was in all cases significantly smaller than in existing, similar sensing approaches.<sup>81,83</sup> Additionally, the mean error was comparable or smaller than for the only FDA approved implantable sensor,<sup>91</sup> applicable only in the pulmonary artery.

In eight of the twelve animals, the hemodynamic conditions were altered by CPB in order to mimic deviation from physiologic hemodynamic properties. In this context, the performance of the HBSD was assessed under low pulse pressure and various loading conditions similar to those of end-stage heart failure patients supported by ventricular assist devices (VADs). The comparison of the ABP waveforms provided by the HBSD demonstrated high association and agreement with the reference pressure waveforms during the entire experiment, independent of the level of CPB support. Considering that the HBSD design was optimized for higher pressure and distension levels, further improvement in the measurement accuracy could be achieved with HBSDs specifically designed for CPB conditions. In this setting, the HBSD could provide the necessary hemodynamic input parameters for the clinical implementation of physiologic control algorithms developed for VADs and, hence, improve the performance of such systems and the management of end-stage heart failure patients.<sup>15,64,138</sup>

In addition, it has been shown that the ABP waveforms captured by HBSD enable the accurate extraction of the cardiac cycle onset/EDP, SP and dicrotic notch. Based on these quantities, the duration of the systole and the respiration frequency can be calculated. The continuous monitoring of the systolic period of the cardiac cycle can support the calculation of the ejection fraction<sup>139</sup> and, hence assist in heart failure therapy guidance. Continuous monitoring of the respiration frequency could be used as an input in the prediction of progressive heart failure.<sup>140,141</sup>

The calculation of the PWV when two HBSD are implanted has been also demonstrated. Although the lack of reference values during the experiments, the PWV was in physiologic range and followed the pressure and flowrate variations. The acquisition of the PWV, could enable the monitoring of biomechanical properties of the vessel that the HBSD is attached and, hence, support the surveillance of CVD patients. In addition, the PWV, combined with the calculated AD, can offer new possibilities for indirect estimation of the cardiac output. The latter, could further facilitate the clinical implementation of physiologic control algorithms developed for VADs.<sup>15,64,101</sup>

We recognize that the deviation between the HBSD and the reference pressure measurements is higher in the in-vivo than in the in-vitro experiments, especially in systole. Based on the results obtained during apnea, the main attributor to this discrepancy is the respiration induced movement of the aortic wall, which was not simulated in-vitro. This behavior shows that the HBSD lacks in selectivity and, hence, the measured signal is prone to respiratory artifacts. Although these artifacts can be used to deduce the respiration frequency as described before, due to the distinct difference between respiration and heart frequency, a correction against these artifacts could be implemented if necessary.

The proper function of HBSD requires highly accurate surgical placement of the two sensing components since implantation induced misalignment can affect the sensing accuracy. Hence, a delivery tool that allows for automatic fixation of the sensing components at predefined positions on the vascular wall and minimizes the invasiveness of the implantation procedure is currently under development. Moreover, data and energy transmission of the presented HBSD was achieved through copper wires. Being aware that this approach may increase the risk of infections at the skin exiting site and device malfunctions, a wireless transmission unit is under development. In this unit, a Bluetooth Low Energy (BLE) communication protocol is used to transfer data from the sensor to an external receiver. The sensor and the BLE module are powered through a rechargeable lithium-ion coin-cell battery, with the battery being recharged every 72 hours through inductive coils. This system is currently tested in an in-vitro setting and we envision

its usage to achieve a fully implantable version of the HBSD with transcutaneous energy and data transmission.

The HBSD in its current design can be exclusively used during open heart procedures, requiring a sternotomy or lateral thoracotomy for surgical access like left ventricular assist device implantation, coronary artery bypass graft surgery, etc. Hence, considering that the fixation of the sensor requires only routine placement of non-resorbable superficial sutures to the adventitia of the aorta, the implantation of HBSD would not affect greatly the invasiveness of the existing surgical procedures. After such a cardiac surgical procedure, the pericardium is (at least partially) closed and the epicardial fat layer lands itself on top. Within a few weeks after the index procedure adhesions will be formed between the aorta and the covering layer. These adhesions would possibly lead to sensor encapsulation, which along with the non-resorbable sutures, should enhance the positional stability of the HBSD and render its detachment unlikely. Although the aforementioned encapsulation and the possible vascular scar formation or tissue ingrowth may impact the HBSD's long term performance, considering that the strength of the magnetic field is not influenced by tissue, the response of the sensor should not be affected. Despite the validation of the HBSD with an extensive in-vitro and in-vivo experimental protocol, the performance in closed chest setting that would allow the assessment of the latter effects, as well as the potential impact during animal movement have not been investigated yet. In order to evaluate such scenario and assess long-term device performance, chronic animal trials are planned.

Removal of the current HBSD is not envisioned since the risk of a reoperation for the sensor retrieval would not be justifiable, unless this was mandated in the rare event of a device infection. Hence, in case of a failing sensor, the HBSD would be deactivated and it would stay inside the body, similar to the process that is currently followed for the CardioMEMS.

We acknowledge also that the changes in the biomechanical properties of the vasculature might affect the relation between the diameter and the pressure over time and, hence, deteriorate the accuracy of the ABP measurements. However, we have shown that a two-sensor measurement approach enables the PWV derivation, which is highly related with the biomechanical properties.<sup>116,142</sup> We foresee the exploitation of the PWV to implement an online recalibration process.

Finally, it has to be mentioned that although the current hardware implementation is considered sufficient to prove the functionality of the HBSD in an acute setting, the design of the HBSD and the implantation procedure are still in the early developmental phase and further optimization is necessary to allow its use in humans.

## 2.5 Conclusions/Outlook

Continuous measurement of ABP and properties that reflect vascular status have the potential to monitor cardiovascular disease progression and to closely observe and adjust for the treatment effects of antihypertensive and heart failure medications. This proof-of-concept study provides evidence that the ABP, AD, and ACS waveforms can be accurately and continuously monitored via the proposed sensing approach. Based on the ABP waveform, insights about PWV, respiration frequency and the systolic phase of the cardiac cycle can be derived. The HBSD demonstrated unaffected performance after sterilization, immersion in liquid, and temperature changes, while it was able to accurately capture the monitored parameters in-vitro and in-vivo, under various and extreme physiologic and pathologic conditions, induced by cardiopulmonary bypass support. While the current system requires a cable connection for data and energy transmission, a wireless version with remote monitoring capabilities is currently under development to enable the evaluation of the HBSD in long-term in-vivo experiments and allow the translation to the clinical setting.

## 2.6 Competency in Patient Care and Procedural Skills

Revealing the information hidden in the arterial blood pressure waveform, as well as other vascular properties, can constitute the cornerstone to allow better patient-compliance surveillance and treatment management in patients suffering from CVDs. In this study, we demonstrate the development and validation of a miniature extravascular hall-based magnetic sensor that allows continuous measurement of arterial blood pressure waveform, the waveforms of arterial diameter and circumferential strain, allowing to derive also the pulse wave velocity, respiration frequency and duration of the systolic phase of the cardiac cycle. Due to the invasiveness of the implantation procedure of the current device, CVD patients following major cardiovascular surgery such as ventricular assist device implantation could benefit the most. However, after improving the data/power transmission and implantation procedure of the device, its usage in the clinical setting and the insights of the measured properties would allow for monitoring disease progression of various CVDs as well as remote monitoring and adjustment of treatment effects.

## 2.7 Translational Outlook

This proof-of-concept study provides evidence that the proposed HBSD can accurately measure the arterial blood pressure waveform under various physiologic and pathologic conditions, while it enables the acquisition of various vascular and hemodynamic variables. This is an important initial step to allow the translation of the HBSD toward clinical applications; however, to further enhance the translational capabilities of the HBSD, improvements in device design, data/power transmission and implantation procedure have to be considered. Finally, prior to testing the feasibility and safety of the HBSD in humans, chronic animal trials are required to investigate the performance of the sensor in a closed chest environment and to address the consequences of potential tissue ingrowth on the long-term performance of the HBSD.





### ***3 Cardiac Contractility Estimation Based on Left Ventricular Pressure: Comparison of Time Series Classifiers and Graph-based Neural Networks***

#### **3.1 Introduction**

In heart failure therapy, the real-time estimation of remaining cardiac contractility (RCC) can facilitate patient management, as well as, the performance of physiological controllers for ventricular assist devices (VAD). In this study, the real-time estimation of RCC based on time series data (TSD) of the left ventricular pressure (LVP) was investigated by exploiting two traditional time series classifiers (TSC) and two graph-based neural networks (GNN). All classifiers were assessed with respect to their RCC estimation accuracy and their applicability for real-time VAD control.

#### **3.2 Methods and Materials**

For the RCC estimation (Fig. 3.1), LVP TSD was generated using a hybrid mock circulation (HMC).<sup>53</sup> On the HMC instantaneous pressure, volume, and flowrate values were computed by a numerical model of the human cardiovascular system (HMCS) and applied through a hydraulic interface on the inlet and outlet mixed-flow blood pump. The experimental protocol for the acquisition of the LVP TSD included 63 experiments, where preload, afterload, pump speed, and heart rate variations were performed for nine RCC values. The data was pre-processed by segmenting and normalizing the TSD, producing 6300 cardiac cycle samples, which were used for the TSC approaches. The TSCs comprised the dynamic time warping nearest neighbor (DTW-NN) classifier and the support vector (SVM) classifier. Furthermore, the maturity of two GNN approaches was explored, including a simple custom architecture (C-GNN) and a pretrained architecture (P-GNN) provided by the KERAS library (Inception V3). The C-GNN comprised a convolutional layer with 32 filters of size 3x3, a maxpooling layer with filter size 2x2, a dense layer with 128 units, and a dense layer with nine units for the classification output. For the TSD to be used in the GNN frameworks, two different image encoders (IE), namely direct plot and recurrence plot encoders, were used and assessed. The data was split 80/20 for network training and validation.

#### **3.3 Results**

All four classifiers, DTW-NN, SVM, C-GNN (IE: recurrence plot) and the P-GNN (IE: direct plot) achieved an accuracy of at least 98%. The SVM had the highest accuracy (99.9%) and the shortest prediction time (63  $\mu$ s per sample). The prediction time of DTW-NN was on average 4.84 s per sample, prohibiting the implementation in real-time VAD control. Both GNN architectures achieve high accuracy and short prediction time, however, their performance does not reach the benchmark set by the SVM. A comparison of the image encoders showed that both the direct plot and the recurrence plot encoder lead to similar classification performances when using the same GNN, but different performances between the two investigated GNNs.

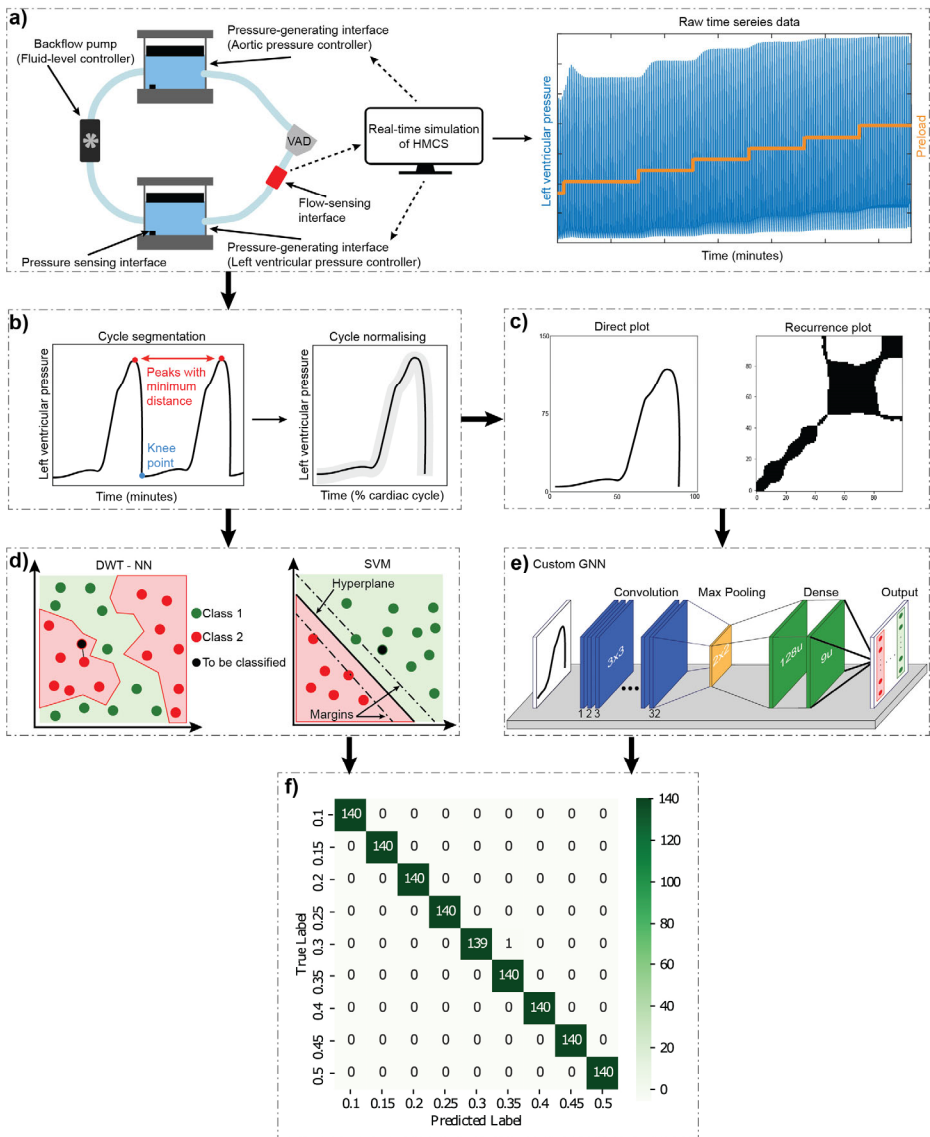


**Figure 3.1.** Schematic of the sequential steps for the estimation of the remaining cardiac contractility from time series data (TSD) of the left ventricular pressure (LVP). **a)** LVP TSD is produced through a hybrid mock circulation, where the human cardiovascular system is simulated and the pressures, volume, and flowrates calculated are applied on the inlet and outlet of a ventricular assist device in real-time via a hydraulic interface. LVP TSD was acquired for various physiologic conditions. **b)** Pre-processing of the data, including cardiac cycle segmentation and time normalization. **c)** Translation of the TSD to images through different image encoders. **d)** Time series classifiers, including dynamic time warping nearest neighbor (DTW-NN) and the support vector (SVM) classifiers. **e)** Graph-based neural networks (GNN). **f)** Classified cardiac contractility.

### 3.4 Conclusions

All classification methods provided accurate RCC estimation with the SVM showing superior performance and being the most promising for real-time clinical implementation. These estimation approaches could substantially support patient surveillance and physiologic VAD control approaches.



## ***4 Physiologic Data-Driven Iterative Learning Control for Left Ventricular Assist Devices***

### **4.1 Introduction**

The prevalence of advanced heart failure (HF), a complex heart syndrome that has long been associated with significant mortality and morbidity rates, has been continuously rising worldwide over the last decades.<sup>6,143,144</sup> For the afflicted patients who account for approximately 1-2% of the general adult population,<sup>6</sup> heart transplantation (HT) is considered the gold standard therapy; however, despite the increased number of heart transplantations performed yearly, the number of recipients continues to significantly outpace the supply of donors.<sup>18</sup>

An alternative surgical treatment to mitigate donors' shortage and allow better management of end-stage HF patients is the implantation of ventricular assist devices (VADs).<sup>22,145</sup> VADs are mechanical pumps that relieve the native heart and restore a fragment of the cardiac output. Their major deployment is complementary, serving as bridge to transplantation or bridge to recovery.<sup>146</sup> However, recent studies have shown that VADs are increasingly used as destination therapy, achieving 1- and 2-year survival rates of 82.3% and 73.1%, respectively, which are comparable to HT.<sup>31,147</sup>

Since their initial approval, VADs have been evolved and matured, with the continuous flow turbodynamic VADs (cfVADs) superseding the bulky and failure-prone volume displacement, pulsatile VADs.<sup>25,148</sup> Despite the notably improved reliability and implantability, cfVADs are still associated with right-heart failure, gastrointestinal bleeding, hemorrhagic strokes, and aortic valve insufficiency, which reduce the survival rates and increase hospital readmissions.<sup>145,149–151</sup> These adverse events are often related to the inability of the currently used cfVADs to respond physiologically to the changing perfusion demands of the patients. To ameliorate this, various research groups have been investigating cfVAD control strategies that restore the physiological response of cfVADs.<sup>15,43</sup> The majority of these strategies aim to imitate the Frank-Starling mechanism<sup>44</sup> by adapting the rotational speed of the cfVAD based on feedback provided by hemodynamic parameters that act as preload surrogates.<sup>57,60,61,152</sup> More complex strategies utilize norm-optimal iterative learning control<sup>62,75</sup> to regulate the end-diastolic volume. They exploit the repetitive nature of the heart and, hence, use information of previous cycles to deduce the control input for the new cycle. These approaches are promising; however, their performance can be restricted by the accuracy of the cardiovascular system and cfVAD models that are integrated in the control structure to allow the prediction of the control function.

All control strategies mentioned above improve the responsiveness of VADs, however, they do not address the diminished blood pulsatility induced by cfVADs support. Whether or not the diminished pulsatility is among the major contributors of adverse events of cfVADs is still a controversial issue.<sup>153</sup> Nonetheless, recent studies have reported strong evidence that the lack of pulsatility can negatively affect the endothelial and peripheral vascular function<sup>38–40</sup> and, hence, increase the risk of nonsurgical bleeding.<sup>41</sup> Additionally, various studies highlight the better control of ventricular unloading and patient's hemodynamics when VADs that effectively resemble the pulsatile flow conditions are deployed.<sup>104,154–156</sup>

In an attempt to imitate the pulsatile blood pressure and flow waveforms, while exploiting the reliability and implantability of cfVADs, various approaches of cfVAD speed modulation have been proposed in literature.<sup>64,157–161</sup> A recent review shows that predefined speed profiles implemented in synchrony with the native heart can systematically manipulate the ventricular

load and the pulsatility in the arterial tree, confirming the positive effect of speed modulation.<sup>162</sup> These approaches focus on the modulation of the speed-profile which is readily available in the clinical setting. However, cfVAD speed-profiles are greatly influenced by the VAD design, hindering the deduction of a direct relation to hemodynamics, as well as, their transferability to different VADs. A more intuitive approach is the modulation of cfVAD speed based on predefined pump flow-profiles. By utilizing an iterative learning control (ILC) scheme, Rüschen et al.<sup>74</sup> provided evidence that accurate tracking of optimized pump flow-profiles can be achieved, resulting in a significant reduction of the left ventricular stroke work (LVSW). For the latter study, a detailed model of the VAD is necessary to enable the accurate flow-profile tracking.

In this study, we introduce a physiologic data-driven iterative learning controller (PDD-ILC) for left ventricular cfVADs. The proposed PDD-ILC enables the generation of preload-adaptive reference pump-flow trajectories based on the Frank-Starling mechanism and treatment objectives, such as pulsatility maximization or LVSW minimization, selected by the clinicians. The tracking of the reference flow trajectories is achieved by measuring left ventricular pressure (LVP) and pump flow (PF), and then implementing the data-driven ILC (DD-ILC). The DD-ILC exploits the recurrent nature of the heart cycle to incorporate the errors identified in previous cycles to the control input of the new cycle and, hence, enhance the tracking performance without requiring a system model. Finally, to enable feedback in the time-domain, a proportional-derivative controller is coupled with the PDD-ILC. The performance of the proposed PDD-ILC was assessed with respect to physiologic responsiveness and trajectory tracking with in-silico experiments that emulated various physiologic conditions, and compared with a constant speed (CS) controller and a newly developed physiological pump flow proportional-integrative-derivative controller (PF-PIDC).

## 4.2 Methods and materials

### 4.2.1 Cardiovascular system model

In this work, the performance of the PDD-ILC was assessed solely with in-silico experiments, wherein the deployed human cardiovascular system (CVS) was modelled based on the lumped-parameter representation proposed by Colacino et al.<sup>52</sup> In this representation, the systemic and pulmonary circulations were divided into the arterial and venous systems. The arterial and venous systems were modelled with five-element and classic Windkessel models, respectively. The CVS model incorporated autoregulatory mechanisms for the adaptation of the flow resistance in the systemic and pulmonary arterial systems, as well as the adaptation of the unstressed volume in the systemic veins. All four chambers of the heart were included as actively contracting elements and they were defined by a nonlinear time-varying elastance model and an energy dissipation term. A detailed description of the model and its validation in physiological and pathological states can be found in the work of Colacino et al.<sup>52</sup> In all simulations, the pathologic conditions defined by Ochsner et al.<sup>53</sup> were used.

### 4.2.2 Numerical models of blood pumps

The conditions of a cfVAD supported patient were imitated by coupling the CVS model described above with a numerical model of a non-implantable mixed-flow turbodynamic blood pump (Deltastream DP2, Medos Medizintechnik AG, Stolberg, Germany). The later model was based on the work of Amacher et al.<sup>160</sup> In detail, the mathematical description includes two differential equations that define the acceleration of fluid (1) and the acceleration of the rotor (2):

$$\frac{dQ}{dt} = \frac{1}{L}(H(Q(t), \omega(t)) - (p_{ds}(t) - p_{us}(t))) \quad (1)$$

$$\frac{d\omega}{dt} = \frac{1}{\theta}(-T(Q(t), \omega(t)) + k \cdot I(t)) \quad (2)$$

where  $Q$ ,  $\omega$ , and  $I$  are the flow-rate, the rotational speed and the current of the pump, respectively.  $p_{ds}$  and  $p_{us}$  are the pressures downstream and upstream of the pump, which correspond to the aortic and left ventricular pressures, respectively.  $L$  and  $\theta$  are the fluid inertance and the rotor inertia, while  $k$  is the torque-constant of the pump motor.  $H$  and  $T$  are matrices containing two-dimensional maps of the pressure across the pump and the hydraulic torque applied on the shaft. The values of these parameters were retrieved from Amacher et al.<sup>160</sup>.

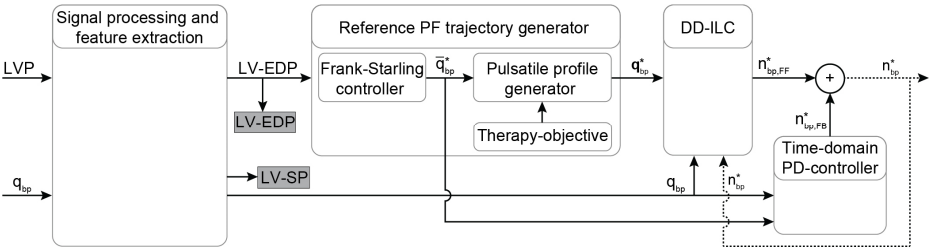


**Figure 4.1.** Schematic overview of the physiological data-driven iterative learning controller. The input signals LVP and PF are filtered and the EDP and SP indices are extracted from the LVP. Based on the Frank-Starling mechanism, the desired average PF is calculated based on the LV-EDP that is used as a preload surrogate, and the reference pulsatile PF trajectory is obtained based on the objectives of the therapy. A data-driven iterative learning controller is implemented to achieve accurate tracking of the reference PF without requiring modelling of the CVS or the pump. Finally, a proportional-derivative (PD) controller and a safety controller are coupled, to enable feedback in the time-domain and prevent suction events, respectively. The desired pump speed is the output of the controller. Bold letters define vectors. *LVP*, left ventricular pressure; *EDP*, end-diastolic pressure; *SP*, systolic pressure; *PF*, pump flow;  $q_{bp}$ , measured pump flow;  $\bar{q}_{bp}^*$ , heart cycle average pump flow,  $q_{bp}^*$ , time vector of the desired pump flow trajectory;  $n_{bp,FF}^*$ , feed forward desired pump speed;  $n_{bp,FB}^*$ , feedback desired pump speed;  $n_{bp}^*$ , desired pump speed output.

### 4.2.3 Overview of PDD-ILC

The proposed PDD-ILC scheme for LVADs aims to provide an accurate reference tracking of predefined, therapy-oriented, PF profiles while it achieves physiological VAD response when preload changes are encountered. A schematic overview of the PDD-ILC structure is depicted in Fig. 4.1 and it can be divided into four main subsystems, namely, signal processing and feature extraction, reference PF trajectory generator, DD-ILC, and time-domain PD-controller.

#### 4.2.3.1 Signal processing and feature extraction

The function of the PDD-ILC is based on the LVP, specifically the end-diastolic (LV-EDP) value, and the PF. The acquisition of these parameters is envisaged by integrating two pressure

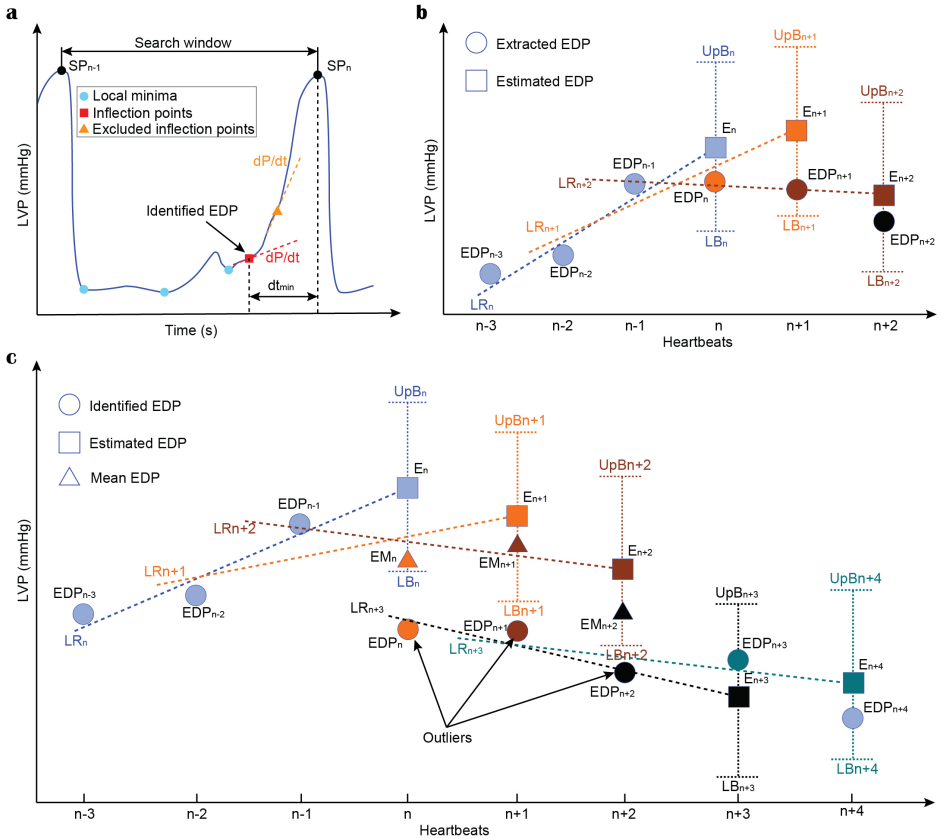


**Figure 4.2.** Schematic representation of the LV-EDP extraction process and the extension for the minimization of misdetections. **a)** Identification of all local minima (cyan circles) and inflection points (yellow rectangles) as LV-EDP candidates. The inflection points with large first LVP derivative ( $dLVP/dt > 40$  mmHg/s) are excluded and the candidate with the smaller distance from the SP index ( $dt_{min}$ ) is identified as the LV-EDP. **b)** Comparison of the identified LV-EDP (filled circles) with the LV-EDP estimated (filled rectangles) based on linear regression of the LV-EDP extracted on the previous three heartbeats. If the identified LV-EDP is within the boundaries, it is extracted as LV-EDP value. **c)** Based on the comparison described in b, if the identified LV-EDP is outside the boundaries it is considered an outlier and the mean value of the last three LV-EDPs is extracted as LV-EDP (filled triangles) of the investigated heartbeat. The outliers are stored in memory and if three consecutive identified LV-EDPs constitute outliers a flag is raised and the new LV-EDP estimate is based on the outliers ( $LR_{n+3}$ ) instead of the extracted LV-EDPs. In this way, physiological rapid changes in preload are not obscured. *LVP*, left ventricular pressure; *EDP*, end-diastolic pressure; *LR*, linear regression; *EM*, extracted mean value; *E*, extracted; *UpB*, upper boundary; *LB*, lower boundary.

sensors into a tapered inflow cannula and exploiting the difference in the dynamic pressure component between the measuring ports to estimate the PF, as proposed by von Petersdorff-Campen et al.<sup>88</sup> However, in this in-silico study, the simulated signals were used instead and white noise was added in specified experiments to emulate a realistic sensor signal and challenge the



PDD-ILC, as described in the section “Experiments for Performance evaluation”. Both LVP and PF signals were low-pass filtered with a first-order filter with cut-off frequency of 25 Hz.

The extraction of the LV-EDP and left ventricular systolic pressure (LV-SP) from the entire time sequence of the LVP was based on the work of Petrou et al.<sup>64</sup> In detail, the LVP was further low-pass filtered with a second-order filter with a cut-off frequency of 8 Hz. From the timeseries data, the indices of the local maxima corresponding to the LV-SP were extracted and the heartbeat was defined as the interval between two consecutive LV-SP indices (Fig. 4.2a). As it is shown in Fig. 4.2a, for each heartbeat, the local minima of the LVP as well as the points of inflection, where the curvature changed from concave to convex, were identified as possible LV-EDP candidates. From the inflection points, only the points where the first derivative of the LVP was below a certain threshold (here 40 mmHg/s) were qualified as possible LV-EDP candidates. From all candidates, the one closest to the LV-SP index was identified as LV-EDP.

Although this approach is accurate, the changes in the LVP waveform due to the in-cycle speed modulation of the cfVAD can increase the LV-EDP misdetections. To address this, an extension for the LV-EDP extraction process was developed in this work. Specifically, as it can be seen in Fig. 4.2, the LV-EDP values identified in the last three heartbeats are used to estimate through linear regression the LV-EDP value of the new heartbeat. The LV-EDP identified for the new heartbeat is compared with the estimate and if it lies within predefined boundaries (here  $\pm 1$  mmHg) it is extracted as the LV-EDP. When the identified LV-EDP lies outside the boundaries (Fig. 4.2c), it is considered an outlier and the mean LV-EDP value of the last three heartbeats is extracted as LV-EDP of the new cycle. The latter value is used along with the LV-EDP of the previous two heartbeats for the estimation of the LV-EDP of the next heartbeat. The outlier is saved in memory and if three consecutive outliers have been identified, a flag is created that the LV-EDP has indeed changed significantly and the new LV-EDP estimate is projected from these three outliers (Fig. 4.2c). The latter step is incorporated to ensure that rapid changes in the LV-EDP are not obscured.

#### 4.2.3.2 Reference pump flow trajectory generator

In this work, reference PF trajectories were used to modulate the pump speed since they provide more intuitive control of the hemodynamics and the interactions between the cfVAD and the CVS,<sup>74,163</sup> while at the same time, they are highly transferable to different cfVAD designs when a sufficiently accurate tracking performance is guaranteed. The generation of these trajectories followed a two-step approach. As a first step, the Frank-Starling mechanism was imitated to obtain a physiological preload response of the cfVAD. More precisely, the LV-EDP extracted at each heartbeat was used as a surrogate of the preload ( $EDP_{LV}$ ) and, by assuming that the flow from the aortic valve is negligible and the PF approximates the cardiac output (CO), the linear part of the starling-relationship between the LV-EDP and the CO was used to provide the necessary average PF ( $\bar{q}_{bp}^*$ ) as follows:

$$\bar{q}_{bp}^* = q_{bp,ref} + k_{FS}(EDP_{LV} - EDP_{LV,ref}) \quad (3)$$

Here  $q_{bp,ref}$  and  $EDP_{LV,ref}$  are reference values for the PF and LV-EDP, respectively, identified from the healthy heart at rest conditions and a CO of 5 L/min during calibration. The parameter  $k_{FS}$  denotes the preload sensitivity which can be selected by the clinician. This ability to directly select the preload sensitivity is paramount to achieve a patient-specific response of the

controller and constitutes a major advantage compared to speed-based controllers, where the control gain needs to be tuned to reach a satisfying preload sensitivity.

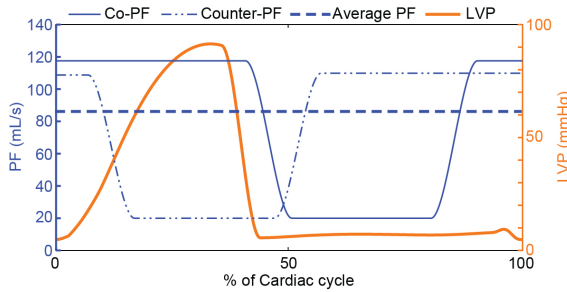


**Figure 4.3.** Reference PF trajectories that incorporate a physiological response to preload changes based on the Frank-Starling mechanism and therapy-oriented pulsatile PF profiles. A copulsation and a counterpulsation PF trajectory along with the LVP for one cardiac cycle are depicted. For both PF trajectories, the minimum PF is  $q_{bp,min}^* = 20 \text{ mL/s}$  and the maximum PF is calculated based on the  $q_{bp,min}^*$  and the necessary average PF provided by the starling-relation ( $\bar{q}_{bp}^*$ ). PF, pump flow; LVP, left ventricular pressure; Co-PF, copulsation pump flow; Counter-PF, counterpulsation pump flow.

The second step to obtain the reference PF trajectories was to incorporate an in-cycle pulsatile profile that enables the accomplishment of treatment-based objectives selected by the clinician. These pulsatile trajectories were based on trapezoidal profiles, wherein the minimum PF was selected to be  $q_{bp,min}^* = 20 \text{ mL/s}$  to provide a safety margin against backflow, and the maximum PF was calculated based on the  $q_{bp,min}^*$  and the necessary average PF provided by the starling-relation ( $\bar{q}_{bp}^*$ ). For each trajectory, the minimum flow was applied for 30% of the cardiac cycle, the maximum flow for 50% of the cardiac cycle, while each transition phase had a duration of 10% of the cardiac cycle. This proportion was chosen to prevent short spikes of desired maximum flow, since such trajectories could not be tracked using cfVADs and would be susceptible to high blood damage. For the pulsatile trajectories, various phase shifts<sup>164</sup> with respect to the onset of cardiac cycle can be applied to achieve different concurrent objectives; however, in this work, only copulsation and counterpulsation trajectories were investigated to achieve maximization of the aortic pulse pressure and minimization of LVSW, respectively, as proposed by Ising et al.<sup>163</sup> The maximum PF was applied during the entire systole for the copulsation trajectory, whereas for the counterpulsation trajectory the maximum PF was applied during diastole. In Fig. 4.3 the reference PF trajectories for an average PF of 85 mL/s are depicted.

#### 4.2.3.3 Data-Driven iterative learning controller (DD-ILC)

To achieve the desired response of the PDD-ILC, accurate reference tracking of the PF trajectory is required. Considering the repeating disturbances applied on the cfVAD in each cardiac cycle by the changes in the head pressure (difference between pressure at the outlet and pressure at the inlet of the cfVAD) from the remaining heart function, as well as the periodic changes in the preload, ILC schemes are suitable for reference trajectory tracking. More precisely, in repetitive process, ILC strategies can exploit the knowledge obtained in previous iterations to produce a feed-forward control input that progressively enhances the tracking performance. In this study, the DD-ILC was developed based on the approach proposed by Chi et al.,<sup>165</sup> wherein a pseudo partial derivative (PPD) computed from the input and output signals serves as system

model in the iteration domain, where one iteration stands for one heartbeat. The model is then used in a quadratic optimization procedure to minimize a cost function subject to input and output constraints.

The implementation of the DD-ILC is illustrated in Fig. 4.4. Initially, a memory block is incorporated to store the per-cycle vectors of the pump speed setpoint  $\mathbf{n}_{bp}^*$  and the PF  $\mathbf{q}_{bp}$ , with varying number of samples  $N$ :

$$\mathbf{n}_{bp,j}^* = [n_{bp,j}^*(0), n_{bp,j}^*(1), \dots, n_{bp,j}^*(N-1), n_{bp,j}^*(N)] \quad (4)$$

$$\mathbf{q}_{bp,j} = [q_{bp,j}(0), q_{bp,j}(1), \dots, q_{bp,j}(N-1), q_{bp,j}(N)] \quad (5)$$

These vectors contain the information of the entire time sequences of the previous cycles (iterations). They are used to obtain a representation of the CVS and the cfVAD system in the iteration domain through dynamic linearization. Specifically, the dynamic linearization model is based on the identification of the PPD  $\Phi_j$  by relating the difference in the output signal  $\mathbf{q}_{bp}$  and the input signal  $\mathbf{n}_{bp}^*$  between consecutive iterations:

$$\Delta \mathbf{q}_{bp,j} = \Phi_j \Delta \mathbf{n}_{bp,j}^* \quad (6)$$

$$\text{with} \quad \Delta \mathbf{q}_{bp,j} = \mathbf{q}_{bp,j} - \mathbf{q}_{bp,j-1}, \quad \Delta \mathbf{n}_{bp,j}^* = \mathbf{n}_{bp,j}^* - \mathbf{n}_{bp,j-1}^*$$

where  $j$  denotes the iteration index. Since the system is causal,  $\Phi_j$  is a lower triangular matrix. To compute an estimate of the PPD, denoted as  $\hat{\Phi}_j$ , the update formula described by Chi et al.<sup>165</sup> was used:

$$\hat{\Phi}_{j+1}^t = \hat{\Phi}_j^t + \frac{\eta(\Delta \mathbf{q}_{bp,j}(k+1) - \hat{\Phi}_j^t \Delta \mathbf{n}_{bp,j}^*(k)) \Delta \mathbf{n}_{bp,j}^{*T}(k)}{\mu + \|\Delta \mathbf{n}_{bp,j}^*(k)\|^2} \quad (7)$$

where  $\hat{\Phi}_{j+1}^t$  denotes the nonzero vector of the  $(t+1)^{th}$  row of  $\hat{\Phi}_{j+1}$ . Accordingly,  $\mathbf{n}_{bp,j}^*(k)$  contains the PF setpoints at iteration  $j$  up to time index  $k$  and based on equation (4) is a varying dimension vector with  $k$  elements. The learning process can be tuned by selecting the normalization value  $\mu$  and the learning gain  $\eta$ . The values of the later parameters were identified through the controller gain optimization described in section 2.6.

For the first iteration, the initial values for the pump speed setpoint, the PF and the PPD required from the algorithm were selected as:

$$\hat{\Phi}_0 = 10^{-4} \begin{pmatrix} 1 & 0 & \dots & 0 \\ 1 & 1 & \dots & 0 \\ \vdots & \ddots & \ddots & 0 \\ 1 & 1 & \dots & 1 \end{pmatrix}, \quad \mathbf{n}_{bp,0}^* = \begin{pmatrix} 0 \\ 0 \\ \vdots \\ 0 \end{pmatrix}, \quad \mathbf{q}_{bp,0} = \begin{pmatrix} 0 \\ 0 \\ \vdots \\ 0 \end{pmatrix} \quad (8)$$

Hence, no model knowledge is required to initialize the controller. none of the previously converged solutions were used in the initialization procedure, and no model knowledge was included.

As a next step, the estimated PPD is used in a quadratic optimization problem to minimize the predicted PF tracking error under actuator constraints. The cost function in this optimization problem comprises two terms, namely the predicted PF tracking error ( $J_q$ ) and the change in the input vector ( $J_u$ ). The  $J_u$  cost component provides robustness against undesirably high changes in the pump speed setpoint during the transient behavior of the learning algorithm. The predicted PF tracking error to be minimized is described as:

$$\mathbf{e}_j = \mathbf{q}_{bp,j+1}^* - \hat{\mathbf{q}}_{bp,j+1}^* \quad (9)$$

where  $\hat{\mathbf{q}}_{bp,j+1}^*$  denotes the predicted PF at cycle  $j + 1$  using the updated PPD given by:

$$\hat{\mathbf{q}}_{bp,j+1}^* = \hat{\mathbf{q}}_{bp,j}^* + \hat{\Phi}_{j+1} \Delta \mathbf{n}_{bp,j}^* \quad (10)$$

Hence, by combining the two cost components, the cost function can be written as:

$$J_{j+1} = J_{q,j+1} + J_{u,j+1} = \mathbf{e}_j^T \mathbf{Q} \mathbf{e}_j + \Delta \mathbf{n}_{bp,j+1}^{*T} \mathbf{R} \Delta \mathbf{n}_{bp,j+1}^* \quad (11)$$

where  $\mathbf{Q}$  and  $\mathbf{R}$  are positive definite weighting matrices that, in this work, are identified during the controller gain optimization described in section 2.6.

Additionally, to avoid unrealistic pump speed setpoints, the pump speed is constrained between a minimum and maximum value defined based on the pump design. Hence, the final optimization problem can be written as:

$$\min_{\Delta \mathbf{n}_{bp,j+1}^*} (J_{j+1}) \quad (12)$$

$$s. t. \quad \Delta \mathbf{n}_{bp,j+1}^* \geq \mathbf{n}_{bp,min} - \mathbf{n}_{bp,j}^* \quad (13)$$

$$\Delta \mathbf{n}_{bp,j+1}^* \leq \mathbf{n}_{bp,max} - \mathbf{n}_{bp,j}^* \quad (14)$$

The optimization problem is solved using MATLAB's quadprog function. The optimized change in the pump speed setpoint vector is added to the speed setpoint vector of the previous iteration to provide the new control input vector as:

$$\mathbf{n}_{bp,j+1} = \mathbf{n}_{bp,j} + \Delta \mathbf{n}_{bp,j+1}^* \quad (15)$$

Finally, since the dynamic linearization and the quadratic optimization are executed only at the beginning of each cycle, an additional module that operates at the full control frequency extracts the feedforward pump speed setpoint  $n_{bp,FF}^*$  at every time index.

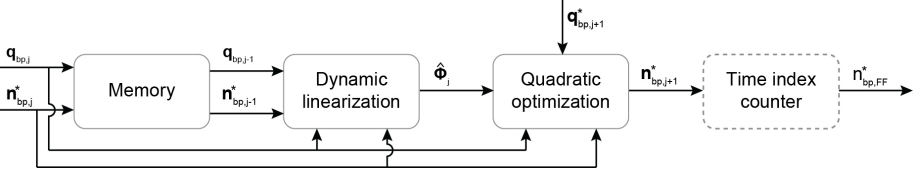


**Figure 4.4.** Schematic overview of the DD-ILC algorithm. The pump speed setpoint and the PF are stored in a memory block. Then, they are used at the beginning of each cycle to update the system model through dynamic linearization. The model is used in a quadratic optimization problem to minimize the PF tracking error under pump speed constraints. The time index counter operates continuously to extract and output the feedforward pump speed setpoint at every time step within an iteration. Bold letters define vectors.  $\mathbf{n}_{bp,j}^*$ , pump speed setpoint vector of the  $j^{\text{th}}$  cycle;  $\mathbf{q}_{bp,j}$ , measured PF vector of the  $j^{\text{th}}$  cycle;  $\hat{\Phi}_j$ , pseudo partial derivative denoting the linearized system model;  $\mathbf{q}_{bp,j+1}^*$ , PF reference trajectory;  $\mathbf{n}_{bp,FF}^*$ , feedforward pump speed setpoint in the time domain.

#### 4.2.3.4 Time-domain proportional-derivative (PD) controller

The DD-ILC incorporates feedback in the iteration domain; however, it is a feedforward controller in the time domain. Therefore, an additional PD controller that operates in parallel to the DD-ILC is introduced (Fig. 4.1). The PD controller showed to deteriorate the convergence speed of the DD-ILC during transient phases. However, it restricts the tracking error to become unbounded when the desired average PF changes rapidly due to changes in LV EDP. Hence, to exploit the latter characteristic without compromising convergence, the time domain PD controller is only activated if the desired average PF changes by at least 1 mL/s and, therefore, it is described as:

$$n_{bp,FB}^*(k) = \begin{cases} k_p(q_{bp}^*(k) - q_{bp}(k)) + k_d \frac{d(q_{bp}^*(k) - q_{bp}(k))}{dk} & \text{if } |\bar{q}_{bp,j+1}^* - \bar{q}_{bp,j}^*| \geq 1 \\ 0 & \text{Otherwise} \end{cases} \quad (16)$$

Finally, by incorporating the feedback in the iteration domain provided by the DD-ILC and the feedback in the time domain provided by the PD controller, the pump speed setpoint at time index  $k$  is given by:

$$n_{bp}^*(k) = n_{bp,FF}^*(k) + n_{bp,FB}^*(k) \quad (17)$$

#### 4.2.4 Physiological flow PID controller

A PID controller was also developed to achieve PF tracking and it was used to further evaluate the performance of the PDD-ILC. This controller uses the LVP and the PF to regulate the pump speed and achieve a physiological response to preload changes while it tracks specific PF profiles. The signal processing and feature extraction blocks, as well as the flow trajectory generator are the same as described for the PDD-ILC. As it can be seen in Fig. 4.5, a time index counter is used after the flow trajectory generator to extract the feedforward PF setpoint at every time step. The measured PF is compared with the PF setpoint and the error is used as feedback to the PID controller. The output of the PID controller corresponds to the desired change in the pump speed. This change is added to a pump speed constant and the desired pump speed is defined. The pump

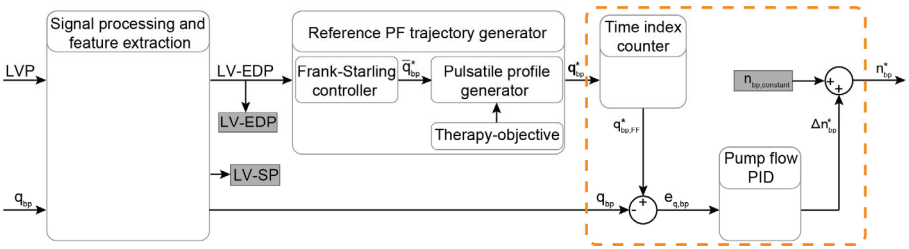


**Figure 4.5.** Schematic overview of the physiological flow PID controller. The input signals LVP and PF are filtered and the EDP and SP indices are extracted from the LVP. Based on the Frank-Starling mechanism, the average PF is calculated based on the LV-EDP that is used as a preload surrogate, and the reference pulsatile PF trajectory is obtained based on the objectives of the therapy. A time index counter operates continuously to extract and output the feedforward PF setpoint at every time step. A PID flow controller (included in the yellow dashed-line box) provides the necessary change in the pump speed setpoint based on the error between the measured and the desired PF. A safety controller is coupled at the end, to prevent suction events. The desired pump speed is the output of the controller. Bold letters define vectors. *LVP*, left ventricular pressure; *EDP*, end-diastolic pressure; *SP*, systolic pressure; *PF*, pump flow;  $q_{bp}$ , measured pump flow;  $\bar{q}_{bp}$ , heart cycle average pump flow,  $\mathbf{q}_{bp}^*$ , time vector of the desired pump flow trajectory;  $\mathbf{q}_{bp,FF}^*$ , feed forward desired pump flow;  $e_{q,bb}$ , feedback error between the measured and the desired PF;  $\Delta n_{bp}^*$ , desired pump speed change;  $n_{bp,constant}$ , pump speed constant;  $n_{bp}^*$ , desired pump speed output.

speed is not constrained between a minimum and maximum value as in the PDD-ILC, however, the step-change in pump speed is constraint to 2500 rotations per minute.

#### 4.2.5 Experiments for performance evaluation

The assessment of the PDD-ILC was based on in-silico experiments that simulate a pathologic CVS supported by a cfVAD, using the numerical models described in sections 2.1 and 2.2. Additionally, to allow a detailed evaluation, several clinical conditions and everyday scenarios emulating resting (Exp0), preload variations (Exp1), afterload variations (Exp2), sleep-to-wake (Exp3), contractility variations (Exp4) as well as rest-to-exercise (Exp5), were tested with the PDD-ILC regulating the cfVAD speed. The parameters of the CVS, as well as the specific values used to simulate the aforementioned conditions are based on the experimental procedure described by Petrou et al.<sup>61</sup> and they are given in Supplemental Table B1-3 of the supplemental material. To test the robustness of the PDD-ILC when real measured signals are used instead of the simulated ones, all experiments were repeated with white noise with a variance of 0.86 mmHg<sup>2</sup> (Exp0n-5n) and 1.72 mmHg<sup>2</sup> (Exp0nn-5nn) on the LVP or/and a variance of 0.86 (mL/s)<sup>2</sup> (Exp0n-5n) and 1.72 (mL/s)<sup>2</sup> (Exp0nn-5nn) PF signals.

To benchmark the performance of the proposed PDD-ILC in comparison to the state-of-the-art, the same experiments have been conducted with a simulated healthy heart (HH), wherein the contractility parameter was set to 1, a constant speed controller (CS), and the developed PF-PIDC. All experiments were executed on MATLAB/Simulink R2020b (The MathWorks Inc., Natick, MA, USA) for 200 s.

#### 4.2.6 Optimization of controller parameters

The performance of the PDD-ILC, as well as the benchmark flow PID controller, is highly dependent on the selection of the control parameters. Although for PID controllers the Ziegler-Nichols approach<sup>166</sup> is most commonly used to fine-tune their parameters ( $K_P$ ,  $K_I$ ,  $K_D$ ), its applicability to non-linear, time-variant systems, such as the CVS system, is prohibited. For the

developed PDD-ILC, which includes six control parameters  $(\mu, \eta, Q, R, k_p, k_d)$ , there is no intuitive method to fine-tune these parameters.

In this work, the genetic algorithm-based optimization framework (GAOF) described by Magkoutas et al.<sup>102</sup> was used to obtain a set of optimal parameters for each controller. In this framework, the user defines the VAD control structure, the numerical model of the CVS coupled with the numerical model of the selected VAD, the objective function (OF) to be evaluated, the experiments for the evaluation of the OF, and the genetic algorithm (GA) parameters. During the execution, each individual, defined as a set of control parameters, is fed to the controller and the numerical model of the VAD-supported heart is simulated. The simulation results are used for the evaluation of the OF and the obtained value is assigned to the respective individual as “score”. As long as the convergence criterion of the optimization problem is not met and the maximum number of generations (each generation includes multiple individuals) is not achieved, the scores of the individuals are fed to the genetic algorithm. Based on those scores, the GA uses genetic operations, namely elitism, crossover, and mutation, to create new individuals for the next generation. The process continues for each individual and each generation until an optimum (or multiple) set of control parameters has been identified.

To enable the execution of the GAOF for the PDD-ILC and the PF-PIDC, the numerical model of the CVS and the cfVAD described in sections 2.1 and 2.2 were used. The contractility parameter of the CVS was set to 34% of the value described for the healthy heart, emulating a pathological circulation. The experiments Exp1-Exp5 described in section 2.5 were used for the evaluation of the OF.

For each controller, a two-objective optimization problem was defined, aiming to minimize the overall error in tracking the reference PF trajectory. For the first objective, the root-mean-square-error (RMSE) of the tracking error was initially calculated for each cardiac cycle by:

$$RMSE_j = \sqrt{\frac{\sum_{k=1}^N (q_{bp,j}(k) - q_{bp,j}^*(k))^2}{N}} \quad (18)$$

where  $j$  denotes the index of the cardiac cycle,  $k$  denotes the time index and  $N$  the total number of time indices within the cardiac cycle  $j$ . As a next step, to ensure that only converged cycles are considered, the last 80 cycles of each experiment ( $m$ ) were obtained and the mean value of  $RMSE$  was calculated as:

$$\overline{RMSE}_m = \sqrt{\frac{\sum_{j=0}^{80} RMSE_j}{80}} \quad (19)$$

Hence, the first objective function including the mean value of the  $RMSE$  for the six experiments was defined as:

$$J_1 = a_1 \overline{RMSE}_1 + a_2 \overline{RMSE}_2 + a_3 \overline{RMSE}_3 + a_4 \overline{RMSE}_4 + a_5 \overline{RMSE}_5 + a_6 \overline{RMSE}_6 \quad (20)$$

where  $a_1 = 0.2, a_2 = 0.2, a_3 = 0.15, a_4 = 0.15, a_5 = 0.15$ , and  $a_6 = 0.15$  are weighting factors corresponding to experiments Exp1-6. The latter factors allow the experiments, which simulated conditions that account for a major fraction of the everyday life of a patient, to have a greater influence on the value of the OF.

The second objective of the optimization problem was developed to evaluate the individuals regarding the convergence of the tracking error. Hence, the standard deviation of the  $RMSE$  in the last 80 cycles of each experiment ( $m$ ) was calculated as:

$$\overline{std}_m = \sqrt{\frac{\sum_{j=1}^{80} (RMSE_j - \overline{RMSE}_m)^2}{80}} \quad (21)$$

Accounting the terms of all experiments and using the weighting factors, the second objective function is defined as:

$$J_2 = a_1 \overline{std}_1 + a_2 \overline{std}_2 + a_3 \overline{std}_3 + a_4 \overline{std}_4 + a_5 \overline{std}_5 + a_6 \overline{std}_6 \quad (22)$$

To avoid unrealistic control parameters, their values were constrained between a minimum and a maximum value given in Supplemental Table B4 in the supplemental material. Hence, the final optimization problem for the PDD-ILC was described as:

$$\min_{\mathbf{x}} (J_1(\mathbf{x}), J_2(\mathbf{x})) \quad (23)$$

$$s. t. \quad \mu_{min} \leq \mu \leq \mu_{max} \quad (24)$$

$$\eta_{min} \leq \eta \leq \eta_{max} \quad (25)$$

$$Q_{min} \leq Q \leq Q_{max} \quad (26)$$

$$R_{min} \leq R \leq R_{max} \quad (27)$$

$$k_{p,min} \leq k_p \leq k_{p,max} \quad (28)$$

$$k_{d,min} \leq k_d \leq k_{d,max} \quad (29)$$

where  $\mathbf{x}$  denotes the set of control parameters ( $\mu, \eta, Q, R, k_p, k_d$ ). The optimization problem for the PF-PIDC, wherein the set of control parameters was  $\mathbf{x} = (K_p, K_I, K_D)$ , was described as:

$$\min_{\mathbf{x}} (J_1(\mathbf{x}), J_2(\mathbf{x})) \quad (30)$$

$$s. t. \quad K_{p,min} \leq K_p \leq K_{p,max} \quad (31)$$

$$K_{I,min} \leq K_I \leq K_{I,max} \quad (32)$$

$$K_{D,min} \leq K_D \leq K_{D,max} \quad (33)$$

where the a minimum and a maximum constraint values are given in Supplemental Table B4 in the supplemental material.

The solution of the described two-objective optimization problem did not provide a single optimum solution, but a set of nondominated solutions (pareto front) that were chosen as optimal



if any of the objectives could not be improved without sacrificing the other objective. Hence, from the several individuals included in the pareto front of each controller, the final control parameters (Table 4.1) were selected after evaluating the overall performance of several sets of optimum parameters under the dynamic tests described in section 2.5.

For both controllers, the optimization problem was solved by using the multi-objective genetic algorithm provided in the global optimization toolbox of MATLAB. The default parameters of the genetic algorithm were applied for the genetic operations, while the initial population and the size of each generation was 500 individuals. The convergence criteria were met when for 15 consecutive generations any new individual was included in the pareto front, or when a maximum number of 50 generations was reached

**Table 4.1.** Optimized control parameters for PDD-ILC and flow PID controllers

PDD-ILC		Flow PID	
$\mu$	0.7315	$K_P$	401.23
$\eta$	0.7859	$K_I$	67.51
$Q$	120.7388	$K_D$	19.15
$R$	0.1365		
$k_p$	3.2155		
$k_d$	3.1926		

## 4.3 Results

### 4.3.1 Trajectory tracking and convergence

The performance of the PDD-ILC and the PF-PIDC in tracking the PF reference trajectories was evaluated under all physiological conditions simulated with the experiments described in section 2.5 for copulsation and counterpulsation modes (Fig. 4.6-8). In Fig. 4.6, the tracking performance during rest conditions (Exp0, Supplemental Table B1, supplemental material) is shown for one cardiac cycle with both controllers being converged. When the copulsation mode is selected (Fig. 4.6a), both controllers show excellent performance with the minimum and maximum PF values being achieved without overshoot and time delay. During the counterpulsation mode the tracking is accurate and without time delays in the transition phases (Fig. 4.6b). However, the highly changing pressure conditions applied on the cfVAD during the contraction of the LV deteriorate the tracking performance in the region of low PF of both controllers.

In Fig. 4.7, the RMSE calculated based on (18) as well as the maximum instantaneous tracking error computed for each cardiac cycle are depicted for all physiological experiments (Ex0-5, Supplemental Table B1, supplemental material) under copulsation mode. During the rest-conditions experiment (Exp0), the PDD-ILC obtained an RMSE below  $0.33 L \min^{-1}$  after 30

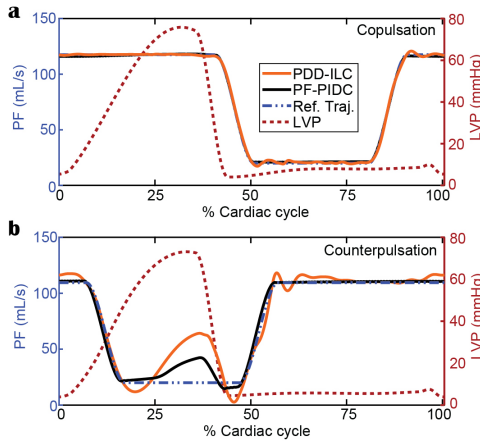


**Figure 4.6.** Reference trajectory tracking performance of the PDD-ILC and the PF-PIDC during one cardiac cycle of the rest-conditions experiment (Exp0, Supplemental Table B1, supplemental material) under **a)** copulsation and **b)** counterpulsation. The reference trajectories, along with the left ventricular pressure profile that corresponds to the main source of disturbance are given for both modes. Both controllers are able to track accurately the reference trajectory during copulsation, reaching the maximum and minimum PF values without time lag. During the counterpulsation, the high disturbance of the fast change in LVP cannot be compensated completely from any of the controllers, however, the overall tracking is adequate. *PDD-ILC*, physiologic data-driven iterative learning controller; *PF-PIDC*, pump flow proportional-integrative-derivative controller; *Ref. Traj.*, reference trajectory; *LVP*, left ventricular pressure.

iterations and converged to  $0.07 L \min^{-1}$  after 100 iterations (Fig. 4.7a). Except for the initial 10 iterations, wherein the system was not settled, the maximum tracking error remained below  $1.21 L \min^{-1}$  and reduced continuously to achieve  $0.19 L \min^{-1}$  after convergence. During the same experimental conditions, the PF-PIDC obtained an RMSE of  $0.06 L \min^{-1}$  and a maximum error of  $0.11 L \min^{-1}$ . During the preload variations (Exp1), the controllers showed an increase in both the RMSE and the maximum error during the transition phases of the experiment, however after the last transition (at about 75 s) both reached the error values achieved in Exp0, with the PDD-ILC converging in less than 60 iterations to. As depicted in Fig. 4.7c, the PF-PIDC showed a slightly increased RMSE of  $0.24 L \min^{-1}$  during the afterload experiment (Exp2). In this setting, the PDD-ILC also presented higher RMSE and maximum error throughout the entire experiment, achieving an RMSE of  $0.87 L \min^{-1}$  at the end of the experiment. During the sleep-to-wake (Exp3) and contractility variation (Exp4) settings both controllers showed excellent tracking performance, resulting in RMSE and maximum error values similar to the rest-conditions experiment (Fig. 4.7d-e). In Fig. 4.7f, the tracking performance during the rest-to-exercise experiment is illustrated for both controllers. During this experiment, wherein the pump has to provide the major fraction of the CO, the RMSE obtained with the PF-PIDC remained at a level of  $1.56 L \min^{-1}$ , while the maximum error converged to  $4.63 L \min^{-1}$ . The PDD-ILC although showed a reduction in the tracking accuracy, it considerably outperformed the PF-PIDC. More precisely, the RMSE and the maximum error obtained by the PDD-ILC after convergence was  $0.68 L \min^{-1}$  and  $2.46 L \min^{-1}$ , respectively.

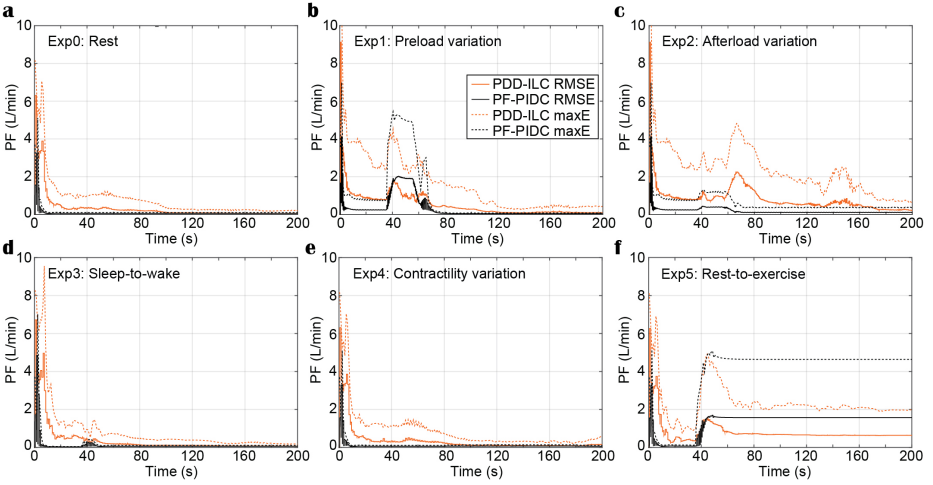


**Figure 4.7.** Transient performance of the PDD-ILC and the PF-PIDC in terms of RMSE and maximum instantaneous error in tracking the reference trajectory under all physiological conditions and scenarios executed with the copulation mode. **a)** Rest-conditions (Exp0): The PDD-ILC converged after 100 iterations, obtaining an RMSE of  $0.07 L min^{-1}$  and maximum error of  $0.19 L min^{-1}$ . The PF-PIDC obtained an RMSE of  $0.06 L min^{-1}$  and maximum error of  $0.11 L min^{-1}$ . **b)** Preload variation (Exp1): Last variation at 85 seconds. The converged RMSE and maximum error for the PDD-ILC was  $0.07 L min^{-1}$  and  $0.23 L min^{-1}$ , respectively. The RMSE and maximum error for the PF-PIDC was  $0.05 L min^{-1}$  and  $0.08 L min^{-1}$ , respectively. **c)** Afterload variation (Exp2): Last variation at 85 seconds. The converged RMSE and maximum error for the PDD-ILC was  $0.20 L min^{-1}$  and  $0.73 L min^{-1}$ , respectively. The RMSE and maximum error for the PF-PIDC was  $0.11 L min^{-1}$  and  $0.38 L min^{-1}$ , respectively. **d)** Sleep-to-wake (Exp3): Last variation at 85 seconds. The converged RMSE and maximum error for the PDD-ILC was  $0.05 L min^{-1}$  and  $0.21 L min^{-1}$ , respectively. The RMSE and maximum error for the PF-PIDC was  $0.06 L min^{-1}$  and  $0.11 L min^{-1}$ , respectively. **e)** Contractility variation (Exp4): Last variation at 85 seconds. The converged RMSE and maximum error for the PDD-ILC was  $0.05 L min^{-1}$  and  $0.18 L min^{-1}$ , respectively. The RMSE and maximum error for the PF-PIDC was  $0.06 L min^{-1}$  and  $0.10 L min^{-1}$ , respectively. **f)** Rest-to-exercise (Exp5): Last variation at 85 seconds. The converged RMSE and maximum error for the PDD-ILC was  $0.68 L min^{-1}$  and  $2.46 L min^{-1}$ , respectively. The RMSE and maximum error for the PF-PIDC was  $1.56 L min^{-1}$  and  $4.63 L min^{-1}$ , respectively. *RMSE, root mean square error; maxE, maximum error; PDD-ILC, physiologic data-driven iterative learning controller; PF-PIDC, pump flow proportional-integrative-derivative controller.*

The tracking performance of the controllers under counterpulsation mode is illustrated in Fig. 4.8 for the conducted simulations. During Exp0 (Fig. 4.8a), the PF-PIDC reached an RMSE and maximum error of  $0.42 L min^{-1}$  and  $1.32 L min^{-1}$ , respectively. In this setting, the PDD-ILC required 50 iterations to converge at an RMSE and maximum error of  $0.88 L min^{-1}$  and  $2.64 L min^{-1}$ , although it obtained similar error values already after the thirtieth iteration. During Exp1 (Fig. 4.8b), Exp3 (Fig. 4.8d), and Exp4 (Fig. 4.8e) both controllers obtained tracking errors similar to those in Exp0 after convergence, however, the tracking error was increased during the transition phases of the experiments. During Exp2 both controllers converged to error values lower than Exp0 (Fig. 4.8c). More precisely, the PDD-ILC converged to an RMSE and maximum error of  $0.50 L min^{-1}$  and  $1.67 L min^{-1}$  and the PF-PIDC to  $0.19 L min^{-1}$  and  $0.50 L min^{-1}$ ,

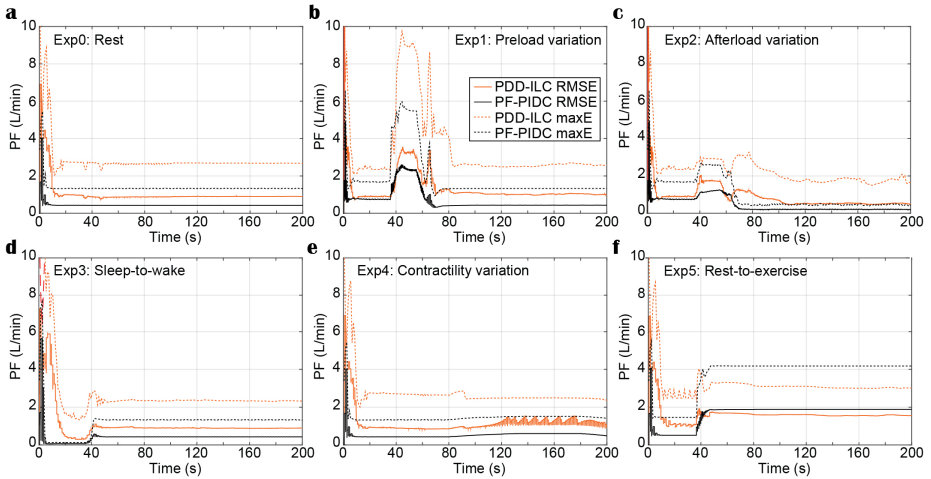


**Figure 4.8.** Transient performance of the PDD-ILC and the PF-PIDC in terms of RMSE and maximum instantaneous error in tracking the reference trajectory under all physiological conditions and scenarios executed with the counterpulsation mode selected. **a)** Rest-conditions (Exp0): The PDD-ILC converged after 50 iterations, obtaining an RMSE of  $0.88 L min^{-1}$  and maximum error of  $2.64 L min^{-1}$ . The PF-PIDC obtained an RMSE of  $0.42 L min^{-1}$  and maximum error of  $1.32 L min^{-1}$ . **b)** Preload variation (Exp1): Last variation at 85 seconds. The converged RMSE and maximum error for the PDD-ILC was  $0.94 L min^{-1}$  and  $2.60 L min^{-1}$ , respectively. The RMSE and maximum error for the PF-PIDC was  $0.43 L min^{-1}$  and  $1.32 L min^{-1}$ , respectively. **c)** Afterload variation (Exp2): Last variation at 85 seconds. The converged RMSE and maximum error for the PDD-ILC was  $0.50 L min^{-1}$  and  $1.67 L min^{-1}$ , respectively. The RMSE and maximum error for the PF-PIDC was  $0.19 L min^{-1}$  and  $0.50 L min^{-1}$ , respectively. **d)** Sleep-to-wake (Exp3): Last variation at 85 seconds. The converged RMSE and maximum error for the PDD-ILC was  $0.90 L min^{-1}$  and  $2.30 L min^{-1}$ , respectively. The RMSE and maximum error for the PF-PIDC was  $0.43 L min^{-1}$  and  $1.34 L min^{-1}$ , respectively. **e)** Contractility variation (Exp4): Last variation at 85 seconds. The converged RMSE and maximum error for the PDD-ILC was  $1.08 L min^{-1}$  and  $2.36 L min^{-1}$ , respectively. The RMSE and maximum error for the PF-PIDC was  $0.48 L min^{-1}$  and  $1.41 L min^{-1}$ , respectively. **f)** Rest-to-exercise (Exp5): Last variation at 85 seconds. The converged RMSE and maximum error for the PDD-ILC was  $1.61 L min^{-1}$  and  $3.06 L min^{-1}$ , respectively. The RMSE and maximum error for the PF-PIDC was  $1.88 L min^{-1}$  and  $4.18 L min^{-1}$ , respectively. RMSE, root mean square error; maxE, maximum error; PDD-ILC, physiologic data-driven iterative learning controller; PF-PIDC, pump flow proportional-integrative-derivative controller.

respectively. Similar to the copulsation mode, during the rest-to-exercise experiment (Exp5), the tracking error was increased for both controllers. As it can be seen in Fig. 4.8f, the PDD-ILC obtained an RMSE and maximum error of  $1.61 L min^{-1}$  and  $3.06 L min^{-1}$ , outperforming the PF-PIDC that converged to  $1.88 L min^{-1}$  and  $4.18 L min^{-1}$ , respectively.

The addition of noise in the simulated LVP and PF signals had infinitesimal effect on the reference trajectory tracking. In the supplemental material, the detailed results for white noise of 0.86 variance can be found in Fig. B1 for all experiments under copulsation and Fig. B2 under counterpulsation, while for white noise of 1.72 variance can be found in Fig. B3 for all experiments under copulsation and Fig. B4 under counterpulsation.

### 4.3.2 Ventricular unloading, pulsatility and hemodynamic response

In this study, the reference PF trajectories were obtained by using copulsation and counterpulsation as support modes, aiming to increase the pulsatility or reduce the LVSW, respectively. The influence of both modes on the LVSW is illustrated in Fig. 4.9 for the executed experiments and is compared with the LVSW produced by the simulated diseased heart (DH) and the DH supported with a cfVAD with a constant speed controller (CS). During the experiments Exp0 (Fig. 4.9a), Exp3 (Fig. 4.9d), Exp4 (Fig. 4.9e) and Exp5 (Fig. 4.9f), using copulsation mode, both the PDD-ILC and the PF-PIDC controller followed the LVSW values obtained with the CS controller. In the same experiments, under counterpulsation, both the PDD-ILC and the PF-PIDC controller reduced the LVSW by 54.3%, 55.9%, 69.8% and 24% compared to the CS support. During the preload variation (Fig. 4.9b), the PDD-ILC and the PF-PIDC controller showed similar responses, reducing the LVSW by 56% compared to the CS and by 57.2% compared to the copulsation modes. However, during the low preload conditions, applied after the last transition point of Exp1, the CS reduced the LVSW by 26.3% compared to the PDD-ILC and PF-PIDC controller under counterpulsation. As it can be seen in Fig. 4.9c, during low afterload conditions (between 40 and 80 seconds), the PDD-ILC and the PF-PIDC controller under counterpulsation, as well as the CS controller, obtained similar LVSW values, while the copulsation modes resulted in 31.2% higher LVSW values. However, during the high afterload conditions in Exp 2 (after 80s in Fig. 4.9c), the PDD-ILC and the PF-PIDC controller under counterpulsation resulted in 75.7% and 72.7%, respectively, compared to CS support. Overall, both the PDD-ILC and the PF-PIDC achieved the intended LVSW reduction during counterpulsation modes.

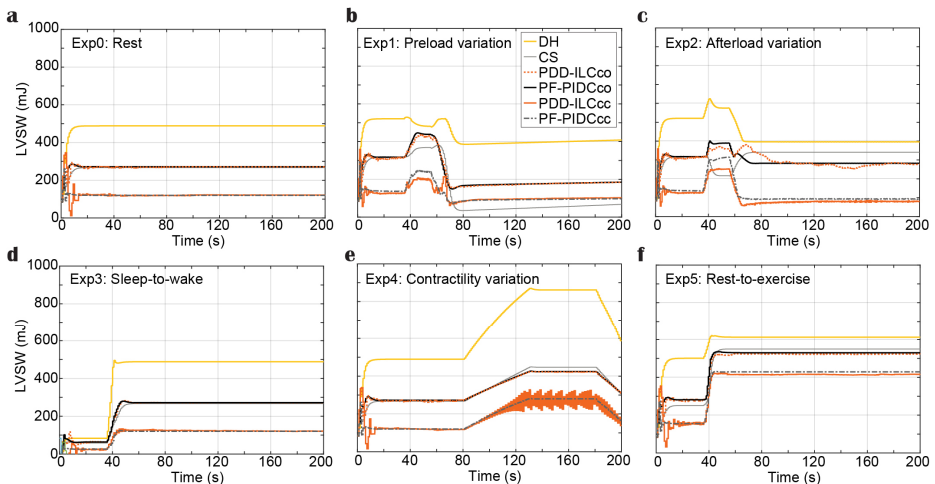


**Figure 4.9.** Influence of the copulsation and counterpulsation modes on the left ventricular stroke work (LVSW) of the diseased heart (DH) during: **a)** Rest-conditions (Exp0), **b)** Preload variation (Exp1) **c)** Afterload variation (Exp2) **d)** Sleep-to-wake (Exp3) **e)** Contractility variation (Exp4) **f)** Rest-to-exercise (Exp5). *DH*, diseased heart; *CS*, constant speed control; *PDD-ILCco*, physiologic data-driven iterative learning controller copulsation; *PF-PIDCco*, pump flow proportional-integrative-derivative controller copulsation; *PDD-ILCcc*, physiologic data-driven iterative learning controller counterpulsation; *PF-PIDCcc*, pump flow proportional-integrative-derivative controller counterpulsation.

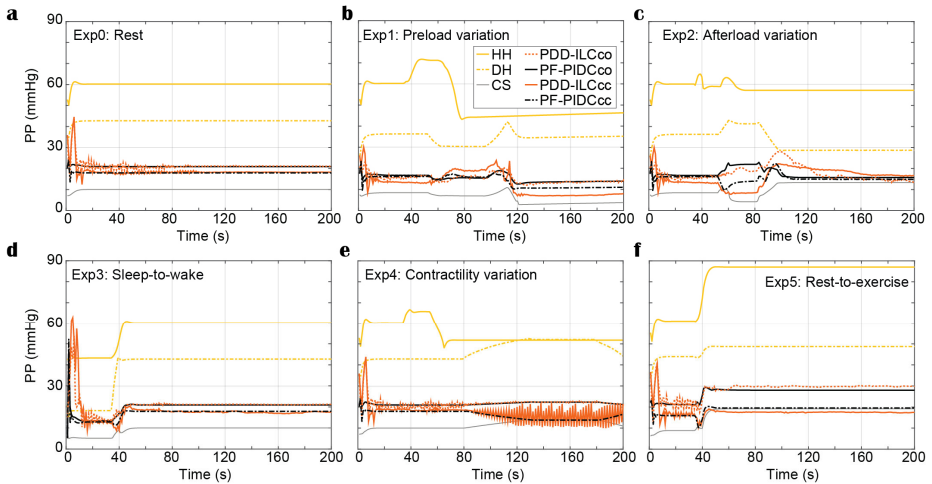


**Figure 4.10.** Influence of the copulsation and counterpulsation modes on the aortic pulse pressure (PP) of the diseased heart (DH) during: **a)** Rest-conditions (Exp0), **b)** Preload variation (Exp1) **c)** Afterload variation (Exp2) **d)** Sleep-to-wake (Exp3) **e)** Contractility variation (Exp4) **f)** Rest-to-exercise (Exp5). *HH*, healthy heart; *DH*, diseased heart; *CS*, constant speed control; *PF-PIDCco*, pump flow proportional-integrative-derivative controller copulsation; *PDD-ILCcc*, physiologic data-driven iterative learning controller counterpulsation; *PF-PIDCcc*, pump flow proportional-integrative-derivative controller counterpulsation.

The influence of the copulsation and the counterpulsation modes on the pulsatility is evaluated based on the aortic pulse pressure (PP = systolic aortic pressure – diastolic aortic pressure) and is illustrated in Fig. 4.10 for all experiments. During Exp0 (Fig. 4.10a) and Exp3 (Fig. 4.10d) the CS diminishes significantly the pulsatility, obtaining a PP of only 10.1 mmHg. Both the PDD-ILC and the PF-PIDC under the counterpulsation mode increased the PP to 16.2 and 17.9 mmHg for Exp0 and Exp3, respectively, while under copulsation, the PDD-ILC and the PF-PIDC further increased the PP to 21.1 and 20.9 mmHg for Exp0 and Exp3, respectively. During the preload experiment (Fig. 4.10b) and after the convergence of all controllers, the CS resulted in the lowest PP of 4.0 mmHg, the PDD-ILC resulted in 14.6 and 15.2 mmHg for counterpulsation and copulsation, respectively, while the PF-PIDC resulted in 9.4 and 11.6 mmHg for counterpulsation and copulsation. During the transition phases of the afterload experiment (Fig. 4.10c), the CS reduced the PP to only 4.1 mmHg, however, the PDD-ILC resulted in significantly increased PP values of 8.4 and 18.7 mmHg with counterpulsation and copulsation, respectively. During the same settings, the PF-PIDC increased further the PP with respect to CS and PDD-ILC, achieving a PP of 13.8 and 29.9 mmHg under counterpulsation and copulsation, respectively. At high afterload conditions in Exp2 (after 110 s in Fig. 4.10c), all controllers resulted in similar PP value of approximately 14.9 mmHg. During the Exp4 (Fig. 4.10e) both the PDD-ILC and the PF-PIDC with copulsating mode resulted in PP of 19.8 mmHg, while the CS, as well as the PDD-ILC and the PF-PIDC under counterpulsation showed reduced pulsatility, obtaining a PP of 10.5, 20.0 and 18.9 mmHg, respectively. The PDD-ILC presented an oscillating PP when the contractility reached 17% of that of the HH. During the rest-to-exercise experiment (Fig. 4.10f), the PDD-ILC with counterpulsation resulted in the lowest PP of 17.5 mmHg, while the CS and the PF-PIDC resulted in 19.5 and 19.1 mmHg. Under the same settings, the PID-controller and the PDD-ILC under copulsation increased significantly the PP achieving 28.0 and 30.0 mmHg, respectively.

### 4.3.3 Preload and afterload sensitivity

The sensitivity of the developed controllers in preload and afterload changes was evaluated in Exp1 and Exp2, respectively, and it was compared with the sensitivities of the CS controller and the HH. Based on the equations given in Appendix B1 in the supplemental material, the end-diastolic LV pressure and the mean aortic pressure (MAP) were used as surrogates of the preload and the afterload, respectively, and a summary of all sensitivities is provided in Table 4.2. As it can be seen in Table 4.2, both the PDD-ILC and the PF-PIDC showed physiological sensitivities compared to the HH, while the CS support resulted in highly non-physiological sensitivities in all cases. More precisely, during preload increase the HH showed a sensitivity of  $0.502 \text{ Lmin}^{-1}/\text{mmHg}$ . The PDD-ILC in copulsation mode followed closely this value, resulting in  $0.496 \text{ Lmin}^{-1}/\text{mmHg}$ , while the PF-PIDC showed  $0.488 \text{ Lmin}^{-1}/\text{mmHg}$  and  $0.470 \text{ Lmin}^{-1}/\text{mmHg}$  under copulsation and counterpulsation, respectively. The PDD-ILC in counterpulsation mode had a lower preload sensitivity of  $0.177 \text{ Lmin}^{-1}/\text{mmHg}$  and the CS showed a highly non-physiologic sensitivity of  $0.039 \text{ Lmin}^{-1}/\text{mmHg}$ . Similar to preload increase, during preload decrease the developed controllers followed closely the sensitivity of the HH, while the CS showed again a sensitivity of  $0.040 \text{ Lmin}^{-1}/\text{mmHg}$ . The sensitivity of the HH was  $-0.015 \text{ Lmin}^{-1}/\text{mmHg}$  and  $-0.016 \text{ Lmin}^{-1}/\text{mmHg}$  during afterload increase and decrease, respectively. The PDD-ILC in copulsation mode showed a sensitivity of  $-0.019 \text{ Lmin}^{-1}/\text{mmHg}$  and  $-0.024 \text{ Lmin}^{-1}/\text{mmHg}$  during afterload increase and decrease, while in counterpulsation showed high sensitivity values of  $-0.030 \text{ Lmin}^{-1}/\text{mmHg}$  in all afterload changes. The PF-PIDC in copulsation and counterpulsation modes responded with a sensitivity of  $-0.018 \text{ Lmin}^{-1}/\text{mmHg}$  and  $-0.011 \text{ Lmin}^{-1}/\text{mmHg}$  to afterload increase, and with a sensitivity of  $-0.026 \text{ Lmin}^{-1}/\text{mmHg}$  and  $-0.019 \text{ Lmin}^{-1}/\text{mmHg}$  to afterload decrease. The CS controller showed more than three times higher afterload response than the HH, resulting in sensitivities of  $-0.046 \text{ Lmin}^{-1}/\text{mmHg}$  and  $-0.057 \text{ Lmin}^{-1}/\text{mmHg}$  to afterload increase and decrease, respectively.

**Table 4.2.** Preload and afterload sensitivity of the healthy heart (HH), the constant speed (CS) controller, the PDD-ILC, and the PF-PIDC calculated in experiments Exp1 and Exp2.

System	Preload (increase) ( $\text{Lmin}^{-1}/\text{mmHg}$ )	Preload (decrease) ( $\text{Lmin}^{-1}/\text{mmHg}$ )	Afterload (increase) ( $\text{Lmin}^{-1}/\text{mmHg}$ )	Afterload (decrease) ( $\text{Lmin}^{-1}/\text{mmHg}$ )
Healthy heart	0.502	0.481	-0.015	-0.016
CS controller	0.039	0.040	-0.046	-0.057
PDD-ILC <sub>co</sub>	0.496	0.466	-0.019	-0.024
PDD-ILC <sub>cc</sub>	0.177	0.386	-0.030	-0.030
PF-PIDC <sub>co</sub>	0.488	0.377	-0.018	-0.011
PF-PIDC <sub>cc</sub>	0.470	0.411	-0.026	-0.019

## 4.4 Discussion

In the current work, we presented a data-driven iterative learning physiological controller and a pump flow PID-controller that accurately track predefined pump flow trajectories, aiming to

achieve physiological, pulsatile and treatment-driven response of cfVADs. A trajectory generator, which can be incorporated as a standalone block in other cfVAD control approaches, was also developed and by exploiting the LV-EDP it provided preload adaptive reference trajectories. In the case of the PDD-ILC, the reference PF trajectories were tracked by a model-free, data-driven ILC that used the time-sequences of LVP and PF to obtain a model. To the best of our knowledge, this is the first application of such a DD-ILC for cfVAD control. Both control approaches have been extensively tested in an in-silico environment under various physiological conditions, including rest, pre- and afterload variations, contractility variations, as well as everyday scenarios like sleep-to-wake and rest-to-exercise. Additionally, two treatment objectives were investigated, termed minimization of LVSW (counterpulsation) and maximization of pulsatility (copulsation). Under all experimental conditions, the PDD-ILC and the PF-PIDC demonstrated highly accurate tracking of the reference PF trajectories, outperforming existing model-based iterative ILC approaches,<sup>74</sup> while they also achieved the predefined treatment objectives and resulted in improved hemodynamics and preload sensitivities compared to a CS controller that is the current state-of-the-art in the clinical practice (Table 4.2).<sup>47</sup>

The reference trajectories constituted a critical component of the DD-IILPC and the PF-PIDC since they were responsible to provide preload adaptivity and incorporate the treatment objectives. To obtain preload adaptivity, the Frank-Starling mechanism was imitated by selecting the preload sensitivity of the controller in equation (3). To our knowledge, this is the first time that the preload sensitivity can be directly selected based on clinical input, constituting a great improvement compared to CS controllers and speed-based controllers, where fine-tuning of the control gains is necessary to achieve adequate sensitivity.<sup>61,64,167</sup> Based on the results in section 3.3, the PDD-ILC and the PF-PIDC were able to follow the set value and provide preload sensitivities similar to the healthy heart, while the CS controller showed infinitesimal sensitivity. Hence, based on our approach, a patient-specific preload sensitivity is feasible for both controllers, offering new opportunities in cfVAD treatment management.

The treatment objectives incorporated in the reference trajectories were the minimization of LVSW and the maximization of pulsatility. To minimize the LVSW, a counterpulsating pump modulation with respect to the native heart has been applied as proposed in the literature.<sup>158,160,163</sup> By accurately tracking the counterpulsation PF trajectories developed in section 2.3.2, the PDD-ILC and the PF-PIDC were able to substantially reduce the LVSW by more than 50% compared to the CS support in the majority of the investigated physiological conditions. This is important when treatment approaches for LV training are considered. To maximize the pulsatility, a copulsation trajectory was developed and tracked by the PDD-ILC and the PF-PIDC controller. During all physiological conditions studied, both controllers increased drastically the PP compared to the CS support. These results agree with the literature<sup>158,160,163</sup> and, consequently, they can be implemented to enhance the pulsatility and investigate its effects and its necessity on cfVAD supported patients. It is important to mention that the effectiveness of our pipeline in reducing the LVSW and increasing the PP is mainly dependent on the developed PF reference trajectories. The difference in LVSW reduction and PP increase between the PDD-ILC and the PFPIDC are a result of their slightly different tracking performance. By exploiting the accurate trajectory tracking achieved from both the PDD-ILC and the PF-PIDC, various phase shifts can be investigated to deduce a better understanding of the interactions between the cfVAD and the native heart to improve the treatment of heart failure patients.

The tracking performance of the DD-ILC and the PF-PIDC was excellent for the copulsation mode, regardless of the physiological conditions applied and the rapid changes in the



hemodynamics and the heartbeat. During the counterpulsation, both controllers demonstrated lower tracking accuracy in all experiments compared to the copulsation. However, they significantly outperformed existing ILC approaches.<sup>74</sup> The inferior tracking performance of the controllers under counterpulsation can be attributed to two reasons. Firstly, during the counterpulsation, a rapid change of head pressure is applied on the pump from the heart contraction, which cannot be counteracted by the slower dynamic response of the pump. Secondly, the controller parameters were optimized for the copulsation mode, hence better tracking performance during counterpulsation could be achieved with the further optimization of the control parameters.

The control parameters have a strong influence on the stability and the tracking performance of both the PDD-ILC and the PF-PIDC; hence, their selection is of high importance. In this work, we implemented the genetic-algorithm-based optimization framework proposed by Magkoutas et al.<sup>102</sup> to obtain the optimum parameter sets for our control approaches. By using the latter optimization framework, intuitive tuning of the control parameters can be achieved based on the selection of the objective functions to be minimized. Hence, by exploiting the GAOF, the gains of the PDD-ILC and the PF-PIDC controller can be further optimized to facilitate patient-specific treatment goals and, consequently, enhance the prognosis of cVAD supported patients. However, it has to be mentioned that, depending on the selected objective functions and the experiments in the optimization process, the development phase of the controller can be prolonged since the completion of the optimization might take up to 20 days.

Although the superiority of the PDD-ILC and the PF-PIDC over the CS controller with respect to hemodynamics and pre- and afterload sensitivities has been demonstrated, the proposed control approaches have also limitations. The development of the reference trajectories assumes negligible flow through the aortic valve, however, when a phase shift between the pump pulsation and the native heart has to be incorporated in the reference trajectory (e.g. counterpulsation) the assumption of negligible flow through the aortic valve is violated. This affects the development of a feasible PF trajectory. Additionally, the assumption of negligible aortic valve flow results in reference trajectories that aim to achieve the necessary CO only through the cVAD operation. Consequently, the flow through the aortic valve is minimized and the risk of aortic valve insufficiency increases. Although such pathological consequences were not within the scope of this study, to ameliorate the risk of aortic valve insufficiency we envisage the addition of a support level parameter to manipulate the percentage of the CO delivered by the pump and the CO expected from the remaining contraction of the native heart.

The excellent tracking performance of both the PDD-ILC and the PF-PIDC necessitates the accurate measurement of LVP and PF signals. We are aware that no reliable, long-term blood pressure and flow sensors are currently available for cVADs; however, the approach developed by von Petersdorff-Campen et al.<sup>88</sup> is promising and could pave the way towards the realization of LVP and PF measurements. In this study, we have accounted for the inherent noise of real measurement and its effect on the tracking performance by assessing the PDD-ILC and the PF-PIDC tracking ability when white noise was added on the LVP and the PF signals. Additionally, the overall performance of the proposed control approaches has been evaluated only in an in-silico environment with a numerical model of a non-implantable mixed-flow turbodynamic blood pump. In-silico, studies with the numerical model of the current state-of-the-art blood pump HeartMate 3 have to be also performed. Furthermore, to prove the performance of the controllers in the real-time setting and allow the translation of the controllers into the clinical practice, in-vitro and in-vivo studies have to be conducted.

Finally, considering the high complexity of the presented control schemes, suction prevention features were not included in the main control structures. Although no suction events were identified in the executed experiments, safety controllers similar to those proposed by Petrou et al.<sup>64</sup> could be incorporated.

## 5 Genetic Algorithm-Based Optimization Framework for Control Parameters of Ventricular Assist Devices

### 5.1 Introduction

Ventricular assist devices (VADs) have been established as an important option in severe acute and chronic heart failure treatment,<sup>168</sup> complementing the cardiac output produced by the native heart. Their deployment most often aims to support end-stage heart failure patients as bridge-to-transplantation or bridge-to-recovery,<sup>146</sup> however, the increasing pool of patients in need of transplantation along with the scarcity of available organs have progressively expanded the usage of VADs as destination therapy.<sup>169</sup>

The progress of VADs in size, reliability, and implantability is substantial since their advent,<sup>25,168</sup> with the patients supported by third-generation continuous-flow VADs (cfVADs) appreciating nowadays significant improvement in their quality of life<sup>170</sup> and 1- and 2-year post-implantation survival rates of 82.3% and 73.1%, respectively.<sup>31,147</sup> Nonetheless, the burden of cfVAD-related adverse events (AE) remains significant,<sup>171</sup> resulting in hospital readmission of 38.6% and 72.2% of the patients in 90 days and 12 months after the VAD implantation, respectively.<sup>31</sup> These AE include gastrointestinal bleeding, right-heart failure, hemorrhagic/ischaemic strokes, and aortic valve insufficiency.<sup>29,84</sup> The exact mechanisms triggering the AE are not fully understood. However, the flow balancing issues between the left and right ventricles as well as the diminished flow pulsatility provoked by the fixed pump-speed operation and the continuous flow of the state-of-the-art cfVADs, are among the major contributors.<sup>29,84,151,172</sup>

To pave the way for a VAD therapy free of cfVAD-related AE, the integration of physiological controllers that automatically adapt the pump speed based on the perfusion demand of the patient can constitute the cornerstone.<sup>173</sup> In this context, numerous research groups have been developing control strategies that exploit hemodynamic parameters and intrinsic signals of the pump to improve the physiological response of VADs.<sup>15,61,174–176</sup> These strategies include proportional (P), proportional-integral (PI), and proportional-integral-derivative (PID) controllers,<sup>56–58,66</sup> as well as more complex, multi-objective<sup>64,73</sup> and iterative-learning controllers.<sup>74,75,101</sup>

Although the aforementioned controllers improve notably the responsiveness of VADs, their performance is highly dependent on the selection of their control parameters. The identification of the optimal control parameters for PID controllers is often conducted with the Ziegler-Nichols approach,<sup>166</sup> however, the latter approach is not applicable to complex control strategies and, most importantly, to non-linear and time-variant systems such as the human cardiovascular system (CVS). Hence, the control parameters of VAD controllers are selected through non-intuitive, trial and error methods, resulting in suboptimal controllers that are strongly dependent on the patient characteristics and the conditions that have been used during the selection process. To allow an intuitive optimization of the control parameters based on specific criteria and multi-objective goals, metaheuristic optimization approaches<sup>177</sup> can be used. For instance, the swarm-based optimization approach has been successfully used to identify the optimal PID parameters and, hence, improve the dynamic response of a pressure-based PID controller for artificially ventilated human respiratory systems.<sup>178</sup> Similarly, genetic algorithm (GA) optimization has been implemented to improve the performance of an electrohydraulic servo control system<sup>179</sup> or a robotic manipulator<sup>180</sup> by identifying the optimum control parameters of their PID controllers.

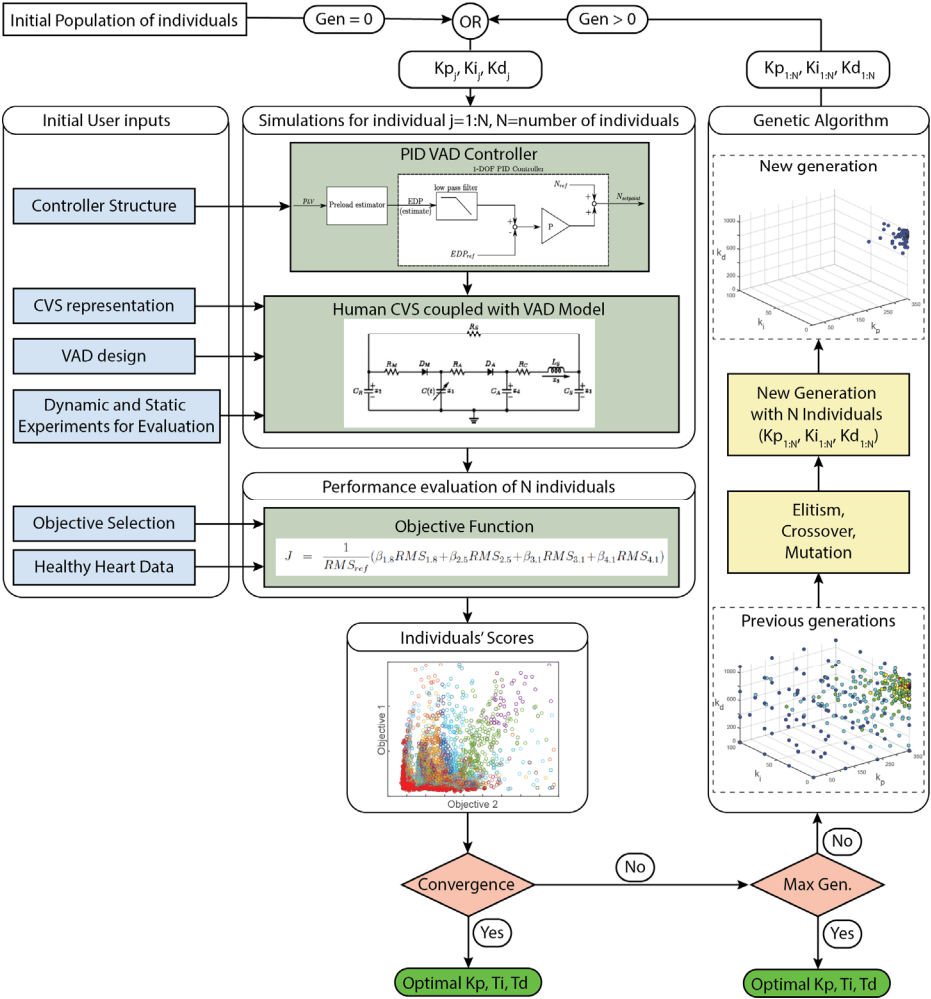


**Figure 5.1.** Overview of the genetic algorithm-based optimization framework (GAOF). \*This is an exemplary electrical analog of the CVS retrieved from Simaan et al.<sup>181</sup>. The CVS used in the current study is from Colacino et al.<sup>52</sup> and it is described in section 5.2.2. *CVS*, cardiovascular system; *VAD*, ventricular assist device; *Gen*, generation; *PID*, proportional-integral-derivative; *Kp*, proportional gain; *Ki*, integral gain; *Kd*, derivative gain.

In this work, we present a genetic algorithm-based optimization framework (GAOF) that allows the identification of optimal control parameters of VAD controllers based on pump-, patient-, and treatment-specific characteristics. The GAOF incorporates the numerical model of the CVS, the numerical model of a VAD, the control strategy, the objective function (OF) to evaluate the performance of the controllers, the experiments for the evaluation of the OF, and the genetic algorithm (GA) that provides the set of optimal parameters for each controller. The performance of the GAOF has been assessed in an in-silico environment, with the optimization of one- and two-degree-of-freedom physiologic PID controllers, as well as a physiologic data-

driven iterative learning controller (PDD-ILC). Additionally, the GAOF has been deployed for the optimization of the one- and two-degree-of-freedom physiologic PID controller, when different VAD designs, patient characteristics, and OF are selected to assess the performance of the GAOF in achieving patient-specific control strategies.

## 5.2 Materials and Methods

### 5.2.1 *Framework overview*

The GAOF constitutes an optimization framework that improves the performance of VAD controllers by identifying optimum sets of control parameters based on pump, patient, and treatment characteristics. To achieve this, as shown in Fig. 5.1, the GAOF-user (e.g. the control engineer or the VAD specialist) has to provide the control structure along with the control parameters to be optimized.

Based on the allowable range of each control parameter, a design space is formed for the controller. Considering each set of control parameters as an “individual”, an initial population of  $N$  individuals is produced (generation 0), aiming to cover all the areas of the design space. As a next step, each individual is tested in an in-silico environment, where the GAOF-user has to select the numerical model of the CVS and the VAD that are coupled to allow the simulation of a diseased heart supported by the controlled VAD. The in-silico experiments include various hemodynamic conditions, such as preload or afterload manipulations, and daily scenarios, such as wake-to-sleep or rest-to-exercise, based on the selection of the GAOF-user. At the end of each round of simulations, a “score” is assigned to each individual by computing the OF defined by the GAOF-user. The individual scores serve as input for the genetic algorithm, which aims to identify the optimal set of control parameters by using genetic operations (elitism, crossover, and mutation) to propagate the features of the best individuals, and eliminate or mutate the poor ones. Based on the genetic operations, a new, optimized generation of individuals is produced and the in-silico experimentation is initiated again for each individual. This process is repeated until the convergence criterion or the maximum number of generations has been reached, concluding the optimal individual.

### 5.2.2 *Numerical model of the human cardiovascular system*

The mathematical representation and the complexity of the numerical model of the CVS in the GAOF can be chosen arbitrarily by the GAOF-user. In this work, the lumped-parameter model originally described and validated by Colacino et al.<sup>52</sup> was used to simulate realistic physiologic and pathological conditions of the human heart, based on the MATLAB/Simulink (The MathWorks, Natick, MA, USA) implementation presented by Ochsner et al.<sup>53</sup> The model, which is elaborated also in Appendix C3 “Numerical Model of the Cardiovascular System”, comprises the systemic and pulmonary circulations, a fully contracting heart as well as an extension to allow the simulation of ventricular suction.<sup>182</sup> Each of the systemic and pulmonary circulations is segmented into an arterial and venous system, modeled with five-element and classic Windkessel models, respectively. The contracting heart consists of two active atria and two active ventricles modeled based on the principle of time-varying elastance. Additionally, the model incorporates three independent autoregulatory mechanisms to regulate arterial pressure, pulmonary pressure, and cardiac output.

### 5.2.3 *Numerical model of ventricular assist devices*

The design and the dynamic response of the VAD have a strong influence on the VAD-heart interactions, necessitating the optimization of the control parameters based on the VAD

characteristics. In the GAOF, the emulation of a VAD-supported heart has been achieved by coupling the CVS model with the numerical model of a VAD that operates in parallel with the left ventricle. The GAOF-user can select the numerical model of any VAD, however, in this study, two blood pump designs have been investigated. Specifically, the numerical model of a non-implantable mixed-flow turbodynamic blood pump (Deltastream DP2, Medos Medizintechnik AG, Stolberg, Germany) and the numerical model of the state-of-the-art implantable centrifugal turbodynamic blood pump (HeartMate 3 (HM3), Abbott, Abbott Park, IL, USA). The mathematical representation of the Deltastream and the HM3 were retrieved from the work conducted by Amacher et al.<sup>160</sup> and Boës et al.<sup>183</sup>, respectively, and they were implemented in MATLAB/Simulink. Both models are elaborated in the Supplemental material (Appendix C1, Appendix C2)

#### **5.2.4 Control strategies for ventricular assist devices**

The efficacy of the GAOF in identifying the optimum set of control parameters was investigated by optimizing three physiologic controllers of different complexity. More precisely, the optimized control schemes included a physiologic one-degree-of-freedom PID (1DOF-PID), a physiologic two-degree-of-freedom PID (2DOF-PID), and a physiologic data-driven iterative learning controller<sup>101</sup> (PDD-ILC). All control schemes aimed to improve the response of the VAD and avoid over- and under-pumping during manipulations of the hemodynamic conditions of the patient.

##### **5.2.4.1 Proportional-integral-derivative (PID) controllers**

The 1DOF-PID controller aims at imitating the Frank-Starling mechanism and, hence, achieving a physiologic response of the VAD during preload changes. To monitor the preload, the left-ventricular end-diastolic pressure (LV-EDP) extracted via the feature extraction algorithm presented by Magkoutas et al.<sup>101</sup> is used as a surrogate. As depicted in Fig. 5.2a, the difference between the extracted LV-EDP and the reference LV-EDP is calculated and it serves as input in the PID controller. Based on the proportional ( $K_p$ ), integral ( $K_I$ ), and derivative ( $K_D$ ) gains of the PID controller, the necessary change in the rotational speed of the VAD is computed and added to the reference VAD speed to identify the setpoint speed for the VAD. Hence, the overall performance of the 1DOF-PID depends on the selection of the three gains, which in this work were optimized by using the GAOF.

The 2DOF-PID controller, in addition to the Frank-Starling mechanism, aims at imitating the systemic arterial baroreflex to allow an improved afterload response of the VAD. The preload component of the 2DOF-PID controller is the same as in the 1DOF-PID controller, where the LV-EDP is used as input in the first PID; however, a second component that is using the mean arterial pressure (MAP) is added to account for the afterload changes. In the latter component of the control structure, as is shown in Fig. 5.2b, the difference between the extracted MAP and the reference MAP is used as input in the second proportion-derivate (PD) controller, and based on the selected gains a change in the VAD speed is calculated. The changes in the VAD speed proposed by the preload PID and the afterload PD are added to the reference speed, defining the setpoint speed for the VAD. Based on the structure of the 2DOF-PID, the five gains of the PID and PD controllers constitute the parameters to be optimized with the GAOF.

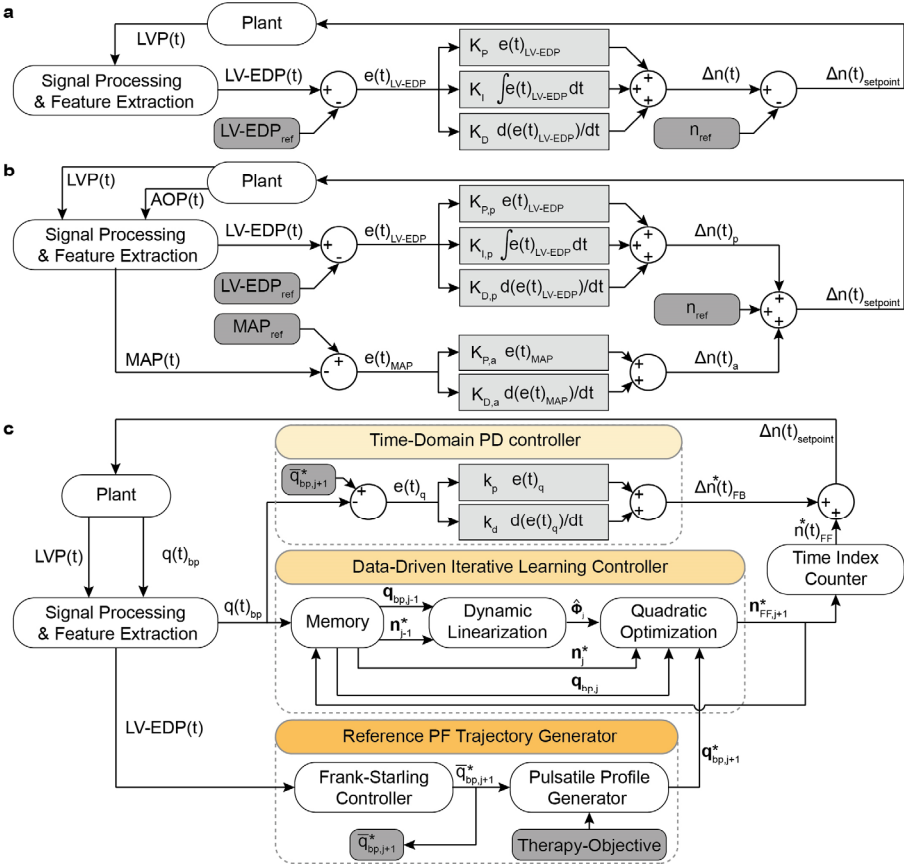


**Figure 5.2.** Overview of the control structures. **a**) One-degree of freedom proportional-integral-derivative (1DOF-PID) controller. The end diastolic left ventricular pressure (LV-EDP), extracted from the left ventricular pressure (LVP) that is the only measured variable, constitutes the input parameter of the 1DOF-PID. Based on the instantaneous LV-EDP and the reference LV-EDP, an error term is calculated that is used by the 1DOF-PID to regulate the rotational speed of the blood pump ( $n(t)$ ) and, hence, achieve physiologic preload response of the blood pump. **b**) Two-degree of freedom proportional-integral-derivative (2DOF-PID) controller. The 2DOF-PID incorporates a PID and a PD controller which aim to achieve physiologic preload and afterload response of the blood pump. The PID controller of the 2DOF-PID operates similar to the 1DOF-PID, while the PD component of the 2DOF-PID uses the mean arterial pressure (MAP) as input to regulate the speed  $n(t)$  with regards to the afterload changes. The changes in  $n(t)$  suggested from the two PIDs are added to the reference speed to calculate the setpoint speed. **c**) Physiologic data-driven iterative learning controller (PDD-ILC). In the PDD-ILC the LV-EDP extracted from the LVP is used to calculate the desired average pump flow (PF) based on the Frank-starling mechanism. Based on the objectives of the therapy a reference pulsatile PF trajectory is formulated and stored as a vector in the memory block of the DD-ILC along with the pump speed setpoint vector. These vectors are used to update the system model at each cardiac cycle (iteration) through dynamic linearization. The model is used in a constrained quadratic optimization problem to minimize the PF tracking error. The time index counter extracts and outputs the feedforward pump speed setpoint at every time step within a cardiac cycle. To enable feedback in the time domain the PD component is added in the controller structure. The desired instantaneous pump speed is the output of the PDD-ILC. *AOP*, aortic pressure; *e*, error; *n*, blood pump speed; *ref*, reference; *p*, preload; *a*, afterload; *j*,

iteration (cardiac cycle);  $q_{bp}$ , measured blood pump flow;  $\bar{q}_{bp}^*$ , desired average blood pump flow;  $\mathbf{q}_{bp}^*$  desired blood pump flow trajectory vector;  $\hat{\Phi}$ , pseudo partial derivative denoting the linearized system model;  $\mathbf{n}_{FF}^*$ , feed forward desired pump speed vector;  $n_{FF}^*$ , feed forward desired pump speed in the time domain;  $\Delta n_{FB}^*$ , feedback desired pump speed change.

The reference values of the LV-EDP ( $LV - EDP_{ref}$ ), MAP ( $MAP_{ref}$ ) and the VAD speed ( $N_{ref}$ ) used in the 1DOF-PID and 2DOF-PID are obtained by a calibration process. In the latter process, the pump speed that results in a total cardiac output of 5 L/min under rest conditions of the simulated patient is identified as  $N_{ref}$ , while the LV-EDP and MAP values observed during this setting serve as  $LVEDP_{ref}$  and  $MAP_{ref}$ , respectively.

#### 5.2.4.2 *Physiologic data-driven iterative learning controller (PDD-ILC)*

The physiologic data-driven iterative learning controller (PDD-ILC) used in this work aims at achieving physiologic, pulsatile, and treatment-driven response of VADs. A detailed description of the PDD-ILC structure and assessment has been given by Magkoutas et al<sup>101</sup>, however, in brief, the PDD-ILC (Fig. 5.2c) imitates the Frank-Starling mechanism by calculating the necessary average pump flow based on the LV-EDP that is used as a preload surrogate. In the next step, considering treatment objectives selected by the clinicians, a reference pulsatile pump flow trajectory is obtained. The accurate tracking of this reference pump flow trajectory is achieved by implementing a data-driven iterative learning controller, which eliminates the need for a model of the CVS and the pump. Finally, a proportional-derivative (PD) controller is coupled to enable feedback in the time domain and provide the pump speed as the output of the controller. Due to the higher complexity of the PDD-ILC, its performance is dependent on the selection of six parameters, four for the iterative learning controller and two for the PD controller.

#### 5.2.5 *Dynamic experiments*

The process of identifying the optimum set of control parameters for a given control structure in the GAOF requires an extensive evaluation of each control individual. To allow this, a series of in-silico experiments that simulate a pathological CVS supported by a VAD is conducted. The in-silico experiments include several hemodynamic conditions emulating resting ( $S_0$ ), contractility variations ( $S_1$ ), preload variations ( $S_2$ ), and afterload variations ( $S_3$ ), as well as everyday scenarios that change the perfusion need of the patient, such as sleep-to-wake ( $S_4$ ) and rest-to-exercise ( $S_5$ ). Based on the work of Petrou et al.<sup>61</sup>, to simulate the various experimental conditions, the unstressed venous volume (UVV), the systemic vascular resistance (SVR), and the heartrate (HR) of the CVS were manipulated, with the specific values for each experiment given in Supplemental Table C1 in Supplemental material. For the 1DOF-PID and 2DOF-PID controllers, the duration of each simulation ranged between 60 and 120 seconds, while for the PDD-ILC the duration was 200 seconds. The difference in the duration of the simulations stems from the fact that the PDD-ILC requires more cycles to achieve initial convergence.

#### 5.2.6 *Controller optimization*

##### 5.2.6.1 *Genetic algorithm configuration*

To allow the identification of the optimum set of control parameters, regardless of the complexity of the VAD control structure, the GAOF uses the genetic algorithm (GA) provided by the ‘‘Global Optimization Toolbox’’ in MATLAB/Simulink. By considering a set of parameters as a candidate solution (individual) for the given optimization problem, and evaluating the individuals according to their fitness, the GA starts from an initial generation of individuals,



simulates the biological evolution process by employing genetic operations to generate increasingly better candidate solutions, and terminates when the convergence criteria are met.<sup>177</sup> The genetic operations include a) *elitism*, where a fixed, small number of the fittest individuals advances unchanged to the next generation of candidate solutions, b) *crossover*, where random parameters of two “parent” individuals, which are selected with a probability increasing with their fitness, are exchanged to form a new individual in the next generation of candidate solutions, and c) *mutation*, where individuals advance to the next generation of candidate solutions with random portions of their parameter representation replaced with random new values.<sup>184</sup> The evaluation of the individuals with respect to their fitness is based on the computation of OFs that incorporate the aims of the optimization problem. The OFs used in this work vary depending on the control structure and the optimization problem, and they are elaborated in following subsections.

For the genetic operations, the default parameters of MATLAB’s GA were applied with elitism being 5% of the population size, crossover being 80% of the remaining population, and the mutation probability being 1%, while the optimization configuration for each controller is given in Table 5.1. The convergence criteria were met when any new individual was included in the family of the fittest individuals (Pareto front) for a number of consecutive generations, or the maximum number of generations was reached. The number of consecutive and maximum generations are provided in Table 5.1 for each optimization problem.

**Table 5.1:** Setup of the genetic-algorithm framework to optimize the VAD controller parameters. *so*, single objective; *mo*, multi-objective

Parameter	1DOF-PID <sub>so</sub>	1DOF-PID <sub>mo</sub>	2DOF-PID <sub>so</sub>	2DOF-PID <sub>mo</sub>	PDD-ILC
Simulation Time Step (s)	0.0001	0.0001	0.0001	0.0001	0.0001
Number of Parameters (-)	3	3	5	5	6
Initial Population (-)	400	400	400	400	500
Generation Size (-)	400	400	400	400	500
Consecutive Generations (-)	5	5	5	5	15
Maximum Generations (-)	30	30	30	30	50

### 5.2.6.2 Definition of optimization problems and objective functions (OFs)

The main component of the optimization problem is the OF that is used to evaluate the fitness of the individuals and, hence, its definition drastically affects the results of the optimization process. For the VAD controllers, the definition of the OF and, hence, the optimization problem is not trivial and it can be adapted based on the structure of the controller and, most importantly, the aims of the treatment. In this study, depending on the controller at hand, single- and multi-objective optimization problems have been defined and investigated within the GAOF.

In detail, for the 1DOF-PID and 2DOF-PID controllers, the optimization problem aimed to minimize under varying hemodynamic conditions the deviation between the CO produced by the diseased heart supported by the controlled VAD ( $CO_{SH}$ ) and the CO produced by the healthy heart

( $CO_{HH}$ ), as well as the CO oscillations. To achieve this, the dynamic experiments  $S_2$ - $S_5$  were conducted and the CO data were retrieved from the simulation results. In the next step, the CO data from each experiment were classified into steady-state (*ss*) data and transition-state (*ts*) data to consider the distinct characteristics of each state.

The assessment of the CO deviation was based on the root-mean-square-error (RMSE) of the  $CO_{SH}$  and  $CO_{HH}$ , calculated by:

$$RMSE = \sqrt{\frac{\sum_{i=1}^N (CO_{SH,i} - CO_{HH,i})^2}{N}} \quad (1)$$

where  $i$  is the time index of the simulation and  $N$  is the total number of time indices for each experiment and state. Hence, by considering the dynamic experiments  $S_2$ - $S_5$  and the different states, the two OFs to be satisfied for the minimization of the CO deviation are formulated as:

$$J_1 = \sum_{j=2}^5 (b_j \cdot RMSE_{ss,j}) \quad (2)$$

$$J_2 = \sum_{j=2}^5 (b_j \cdot RMSE_{ts,j}) \quad (3)$$

with  $j$  denoting the number of the dynamic experiment and  $b_j$  being the weighting factor for each dynamic experiment that aim to increase the influence of the experiments that the patient encounters more frequently in the everyday life in the optimization process. The values of the weighting factors are provided in Supplemental Table C2 in the Supplemental material.

The second aim of the optimization problem for the 1DOF-PID and 2DOF-PID controllers was the minimization of the CO oscillations, which are evaluated differently based on the state of the experiment. More precisely, during the steady-state phases of the dynamic experiments, the CO oscillations are quantified by the standard deviation (*STD*) of the CO, while during the transition-state phases by the summation of the cardiac output finite difference (*SCOFD*). The latter is calculated as:

$$SCOFD = 1 - \frac{\sum_{i=1}^{N-1} |CO_{SH,i} - CO_{SH,i+1}|}{\sum_{i=1}^{N-1} |CO_{HH,i} - CO_{HH,i+1}|} \quad (4)$$

where  $i$  is the time index of the simulation and  $N$  is the total number of time indices for each experiment and state. Hence, the OFs for the minimization of the CO oscillations were formulated as:

$$J_3 = \sum_{j=2}^5 (b_j \cdot STD_j) \quad (5)$$

$$J_4 = \sum_{j=2}^5 (b_j \cdot SCOFD_j) \quad (6)$$

where  $j$  denotes the number of the dynamic experiment and  $b_j$ , as explained above, is the weighting factor of each dynamic experiment.

By considering the described OFs, the multi-objective optimization problem for the 1DOF-PID and 2DOF-PID controllers can be defined as:

$$\min_{\bar{x}}(J_1(\bar{x}), J_2(\bar{x}), J_3(\bar{x}), J_4(\bar{x})) \quad (7)$$

$$s. t. \bar{x}_{min} \leq \bar{x} \leq \bar{x}_{max} \quad (8)$$

where  $\bar{x}$  denotes the vector of control parameters for each controller, hence, being  $\bar{x} = (K_P, K_I, K_D)$  for the 1DOF-PID and  $\bar{x} = (K_{P,p}, K_{I,p}, K_{D,p}, K_{P,a}, K_{D,a})$  for the 2DOF-PID. The vectors  $\bar{x}_{min}$  and  $\bar{x}_{max}$  correspond to the constraint vectors that were used to reduce the search space and avoid unrealistic values for the control parameters. The specific constraint values for each controller are given in Supplemental Table C3 in the Supplemental material.

The solution of the optimization problem defined in equations (7-8), provides a family of optimal individuals, termed the Pareto front. Hence, the GAOF-user has the flexibility to select and test several of the individuals included in the Pareto to conclude the optimal one, based on their preferences.

To reduce the involvement of the GAOF-user in the selection of the optimal individual, the multi-objective optimization problem defined in equations (7-8) was formulated as a single-objective optimization problem by considering a weighting factor for each OF. Hence, the second optimization problem for the 1DOF-PID and 2DOF-PID controllers is defined as:

$$\min_{\bar{x}}(a_1 \cdot J_1(\bar{x}) + a_2 \cdot J_2(\bar{x}) + a_3 \cdot J_3(\bar{x}) + a_4 \cdot J_4(\bar{x})) \quad (9)$$

$$s. t. \bar{x}_{min} \leq \bar{x} \leq \bar{x}_{max} \quad (10)$$

with  $\bar{x}$ ,  $\bar{x}_{min}$ , and  $\bar{x}_{max}$  denoting the vector of control parameters and the constraint vectors for each controller, while the weighting factors are  $a_1 = 0.5$ ,  $a_2 = 0.3$ ,  $a_3 = 0.1$ , and  $a_4 = 0.1$ . The selection of the aforementioned weighting factors was based on the importance of each OF.

For the PDD-ILC, the aim of the optimization problem was the minimization of the overall error in tracking the desired pump flow trajectory under varying hemodynamic conditions. To achieve this, two OFs were defined, with the first objective evaluating the mean root-mean-square-error ( $\overline{RMSE}$ ) of each PDD-ILC individual. In detail, the simulation results from the dynamic experiments  $S_0$ - $S_5$  were retrieved and split into cardiac cycles. For each cardiac cycle, the root-mean-square-error ( $RMSE$ ) of the measured pump flow ( $q_{bp}$ ) and the desired pump flow ( $q_{bp}^*$ ) were calculated and then, by using the last 80 cardiac cycles of each experiment to ensure that the PDD-ILC convergence has been achieved, the mean RMSE for each experiment was calculated as:

$$\overline{RMSE}_j = \sqrt{\frac{\sum_{k=1}^{80} \sqrt{\frac{\sum_{i=1}^N (q_{bp,k}(i) - q_{bp,k}^*(i))^2}{N}}}{80}} \quad (11)$$

where  $j$  is the number of the dynamic experiment,  $k$  is the index of the cardiac cycle,  $i$  is the time index, and  $N$  is the total number of time indices within the cardiac cycle  $k$ . By considering the six dynamic experiments, the first OF of the optimization problem for the PDD-ILC can be defined as:

$$J_a = \sum_{j=0}^5 (b_j \cdot \overline{RMSE}_j) \quad (12)$$

with  $j$  denoting the number of the dynamic experiment and  $b_j$  the weighting factor of each dynamic experiment provided in Supplemental Table C2 in the Supplemental material.

The second objective for the optimization problem of the PDD-ILC aimed to assess the convergence of the tracking error for each PDD-ILC individual by quantifying the standard deviation ( $STD$ ) of the  $RMSE$  of the last 80 cycles of each dynamic experiment. Hence, by accounting for all dynamic experiments, the second OF can be formulated as:

$$J_b = \sum_{j=0}^5 (b_j \cdot STD_j) \quad (13)$$

with  $j$  denoting the number of the dynamic experiment and  $b_j$  the weighting factor of each dynamic experiment as described above.

Finally, by considering the two objectives, the optimization problem for the PDD-ILC can be described as:

$$\min_{\bar{x}} (J_a(\bar{x}), J_b(\bar{x})) \quad (7)$$

$$s. t. \bar{x}_{min} \leq \bar{x} \leq \bar{x}_{max} \quad (8)$$

where  $\bar{x}$  denotes the vector of control parameters, hence, being  $\bar{x} = (\mu, \eta, Q, R, k_p, k_D)$ , while  $\bar{x}_{min}$  and  $\bar{x}_{max}$  correspond to the minimum and maximum constraint vectors, respectively, given in Supplemental Table C3 in the Supplemental material.

The execution of the GAOF for all the optimization problems was performed on a high-performance computer cluster (Euler cluster ETH).

### 5.2.7 Interpatient variability

The capabilities of the GAOF in achieving patient-specific control strategies were further explored with the 2DOF-PID controller, by comparing the performance of a “generic” optimized controller and a patient-specific optimized controller when interpatient variability is considered. More precisely, by extracting information from literature, a database with the physiological range of the CVS model parameters was developed. By manipulating these parameters within the physiological range, artificial patients emulating different pathologies associated with heart failure, such as coronary artery disease (CAD), high blood pressure (HBP), and heart valve insufficiency (HVI) were generated. Each pathology was modeled with different severity levels, termed low, mild, and high, while artificial patients with combined diseases were also developed. The manipulated parameters and their specific values used for each artificial patient in this work are given in Supplemental Tables C4-7 in the Supplemental material.

The “generic” optimized controller constitutes a controller that has been optimized with the GAOF, based on the multi-objective problem described in (9)-(10), with the contractility parameter of the CVS being set to 34% of the value described for the healthy heart to emulate a pathological circulation as described by Ochsner et al.<sup>53</sup> In contrary, the patient-specific optimized controllers were identified by using the parameters of each artificial patient in the CVS model of the GAOF. Hence, by comparing the performance of the “generic” optimized controller when it operates on a different artificial patient with the performance of the controller optimized specifically for this patient, the assessment of the GAOF usage in achieving patient-specific control strategies is enabled.

### 5.2.8 Characterization of optimum controllers

The comparison and characterization of the optimum controllers were based on the previously elaborated cost components, termed *RMSE*, *STD*, and *SCOFD*, depending on the investigated control structure. Furthermore, the response of all controllers was assessed when two magnitudes of white noise variance were added to the signals that are used as input parameters of the controllers, namely LV-EDP, MAP, and  $q_{bp}$  to simulate real measured signals ( $0.86 \text{ mmHg}^2$  and  $1.72 \text{ mmHg}^2$  for the pressure signals and  $0.86 \text{ (mL/s)}^2$  and  $1.72 \text{ (mL/s)}^2$  for the flow signals).

## 5.3 Results

### 5.3.1 1DOF-PID and 2DOF-PID controllers

#### 5.3.1.1 Single-objective optimization problems

The optimization problem defined in equations (9-10) for the 1DOF-PID and 2DOF-PID aimed to improve the response of the controllers with regards to the total CO produced by the controlled VAD and the diseased heart, by minimizing a single OF. The execution of the GAOF for both controllers was terminated when the maximum number of 30 generations was reached and the total duration was approximately 2 days.

The evolution of the control parameters for the 1DOF-PID is provided in Fig. 5.3a, where the initial generation, the 15<sup>th</sup> generation, and the final generation are depicted. Over the progression of the optimization process the space occupied by the individuals of the new generations reduces significantly, with the individuals forming the final generation to be squeezed in an infinitesimal area. In Fig. 5.3b, a parallel coordinate plot with the control parameters of all the generations and their nondimensionalized value is provided. Fig. 5.3b shows that the control parameters explored during the entire optimization process (grey lines), cover the majority of the design space, however, in each successive generation they converge to specific values that result in the minimum value of the OF. Based on the last generation (black lines), the “good” individuals tend to have high values of  $K_p$  and  $K_D$ , while they have infinitesimal values of  $K_I$ . The optimum control parameters are given in Table 5.2.

The progression of the nondimensionalized value of the OF retrieved from the best individual of each generation is depicted in Fig. 5.3c. In this figure, it is evident that the value of the OF reduces excessively in the first 10 generations and then approaches with reduced speed the minimum value.

The performance of the optimized 1DOF-PID is evaluated against the performance of the constant speed controller (CS), a hand-tuned proportional controller (benchmark) adapted from the work of Petrou et. al<sup>64</sup>, and the response of a healthy heart (HH) (Fig. 5.3d). The optimized 1DOF-PID is able to accurately follow the response of the HH during the dynamic experiments  $S_2 - S_5$ , outperforming notably the CS controller. During the preload variation ( $S_2$ ) and the rest-to-exercise ( $S_5$ ) experiments, the 1DOF-PID outperforms also the benchmark controller, by reducing the CO error by 42% and 23%, respectively. However, during the afterload variation ( $S_3$ ) and the sleep-to-wake ( $S_4$ ) experiments the two controllers have similar behaviour.

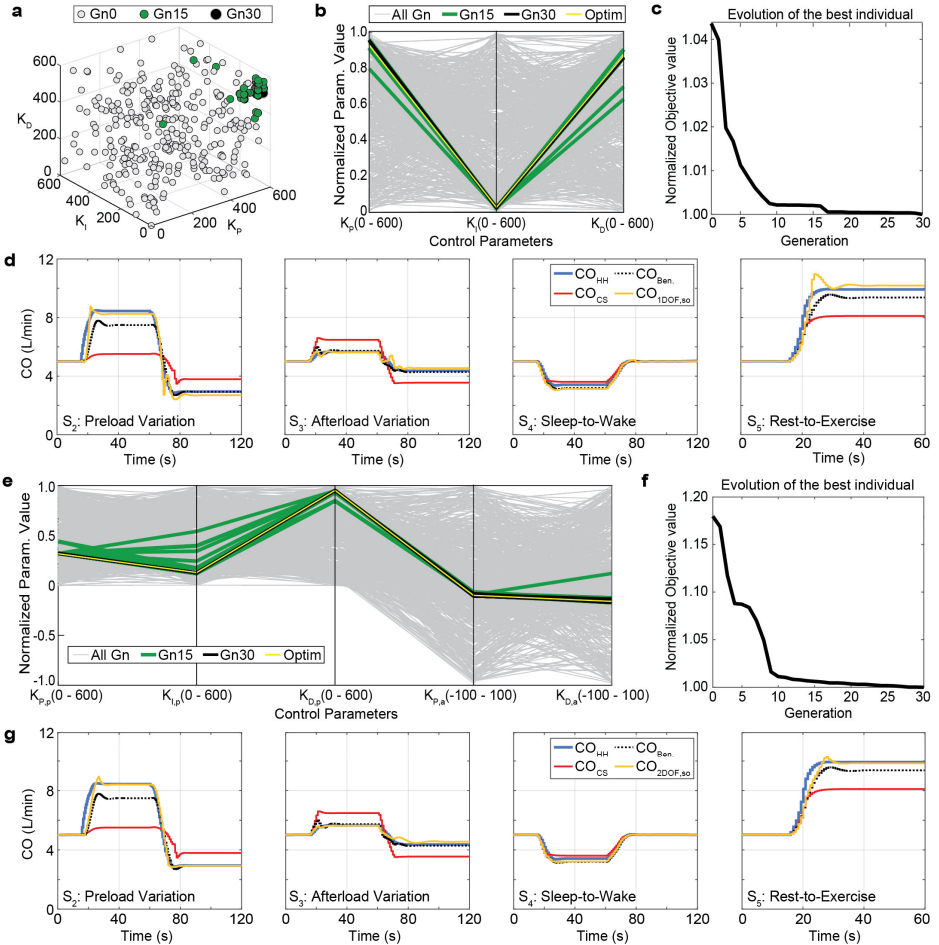


**Figure 5.3.** Performance of GAO in optimizing the 1DOF-PID and the 2DOF-PID when a single-objective optimization problem is formulated. **a)** Evolution of the individuals of the 1DOF-PID. In the last generation, the values of the control parameters converge to an infinitesimal area. **b)** Parallel coordinate plot of the control parameters of the 1DOF-PID, normalized with the respective maximum value of the parameter (the range of each parameter is given in parenthesis). The gray lines correspond to the entire population of individuals, while the individuals of the 15<sup>th</sup> generation are depicted with green lines. The last generation and the optimum controller are depicted with black and yellow lines, respectively. **c)** Evolution of the value of the objective function (OF) based on the score of the best individual of each generation for the 1DOF-PID. **d)** Comparison of the performance of the optimized 1DOF-PID against the constant speed controller, the benchmark controller and the physiological response of a healthy heart during the dynamic experiments  $S_2 - S_5$ . **e)** Parallel coordinate plot of the 2DOF-PID control parameters, normalized with the respective maximum value of the parameter (the range of each parameter is given in parenthesis). The colors of the lines correspond to the ones of the caption of plot B. **f)** Evolution of the value of the OF based on the score of the best individual of each generation for the 2DOF-PID. **g)** Comparison of the performance of the optimized 2DOF-PID against the constant speed controller, the benchmark controller and the physiological response of a healthy heart during the dynamic experiments  $S_2 - S_5$ . *Gn*, generation; *Param*, parameter; *CO*, cardiac output; *HH*,

healthy heart; CS, constant speed controller; Ben, benchmark controller (P-controller not optimized); so, single objective.

In Fig.5.3e, a parallel coordinate plot with the entire population of the control parameters of the 2DOF-PID is provided. Similar to the 1DOF-PID, the design space of the 2DOF-PID is adequately explored by the GAOF. Following the progression of the optimization process, in the final generation (black lines) the control parameters converge to certain values. Based on these lines and the ranges given for each parameter, it can be deduced that the best individuals share  $K_{P,p}$  values of 185-200 rpm/mmHg, high values of  $K_{P,D}$  in the range of 550-600 rpm·s/mmHg, and low values for the rest of the parameters.

**Table 5.2:** Optimized sets of control parameters identified by solving the single- and multi-objective optimization problems for the 1DOF-PID and 2DOF-PID. *so*, single objective; *mo*, multi-objective; *P*, proportional; *I*, integral; *D*, derivative; *p*, preload; *a*, afterload.

Controllers	Parameters				
	$K_P$	$K_I$	$K_D$	-	-
Benchmark	300	-	-	-	-
1DOF-PID <sub>so</sub>	572	14	517	-	-
1DOF-PID <sub>mo</sub>	558	15	523	-	-
	$K_{P,p}$	$K_{I,p}$	$K_{D,p}$	$K_{P,a}$	$K_{D,a}$
2DOF-PID <sub>so</sub>	190	77	571	-10	-16
2DOF-PID <sub>mo</sub>	226	106	530	-8	-17

The OF, as it can be observed by the nondimensional values in Fig. 5.3f, reduces rapidly in the nine first generations and then reduces incrementally until its minimum value that it is achieved in the final generation. The control parameters resulting in the minimization of the OF are given in Table 5.2. By implementing these optimum control parameters, as it can be seen in Fig. 5.3g, the response of the 2DOF-PID compared to the HH is excellent under all the hemodynamic conditions. During the experiments  $S_2$  and  $S_5$ , the optimized 2DOF-PID reduces the CO error by 49% and 36%, respectively, compared to the benchmark controller. During the same experiments, the CO error reduces by 82% and 75%, respectively, when the optimized 2DOF-PID is compared against the CS controller. The response of the 2DOF-PID and the benchmark controller is similar during the experiments  $S_3$  and  $S_4$ , however, both controllers outperform notably the CS controller.

### 5.3.1.2 Multi-objective optimization problems

The multi-objective optimization problem defined in equations (7-8) for the 1DOF-PID and 2DOF-PID had the same aim as the single-objective problem, however, instead of a single optimum controller, the multi-objective optimization problem provides a set of optimum solutions, allowing the GAOF-users to specify the final controller based on their decision. The execution of the GAOF for the 1DOF-PID was terminated when the maximum number of 30 generations was reached, while for 2DOF-PID after 20 generations due to unaltered Pareto for

five consecutive generations. The total duration of the execution was approximately 2 days for the 1DOF-PID and 1.5 days for the 2DOF-PID.

The sets of control parameters explored by the GAOF are depicted in Fig. 5.4a (grey lines), where the maximum value of the design space for each parameter has been used to nondimensionalize the respective parameter. In addition, the same figure presents the 10 individuals achieving the best value for each one of the OFs  $J_1 - J_4$ . It can be observed that, although in the initial generation the best individuals of each OF show high discrepancy, in the final generation the individuals minimizing each of the OFs follow a clear pattern. Specifically, all OFs to be minimized require a high value for the proportional parameter  $K_p$ , ranging between 419 and 600 rpm/mmHg, and a minimal value for the integral parameter  $K_I$ , ranging between 6 and 33 rpm/(mmHg·s). The  $K_D$  parameter contributes to the minimization of  $J_4$  when a value between 550 and 600 rpm·s/mmHg is selected, while for the minimization of the other three OFs, a value between 320 and 420 rpm·s/mmHg is more preferable. Following these patterns, the optimum control parameters selected for the 1DOF-PID are given in Table 5.2.

In Fig. 5.4b, the values of the four OFs, normalized with the respective maximum value, are presented for the entire population, as well as, for the 15<sup>th</sup> generation, the 30<sup>th</sup> generation, and the set of optimum control parameters. This parallel coordinate plot shows that although all the objectives are significantly minimized with the progression of the optimization process, the CO RMSE during the transition phases (OF  $J_2$ ) remains at relatively high values and, hence, deteriorates the performance of the controllers.

The response of the optimized 1DOF-PID during the dynamic experiments  $S_2 - S_5$  is illustrated in Fig. 5.4c and it is compared to the CS controller, the benchmark controller and the response of a HH. During the experiments  $S_2$ ,  $S_3$ , and  $S_5$ , the optimized 1DOF-PID reduces the CO error more than 80% with respect to the CO error of the CS controller, while compared to the benchmark controller, the optimized 1DOF-PID reduces the CO error more than 42%. During the experiment  $S_4$ , the optimized 1DOF-PID results in a reduction of 31% in CO error compared to the benchmark controller and 38% compared to the CS controller.

For the 2DOF-PID, the distribution of the entire population of control parameters is illustrated in Fig. 5.4d (grey lines), along with the 10 best individuals for each one of the OFs  $J_1 - J_4$ , retrieved from the final generation of the optimization process. Based on this figure, to achieve a “good” individual for the 2DOF-PID controller, the pattern of low  $K_{I,p}$ , low  $K_{p,a}$ , and high  $K_{D,p}$  values should be followed. For the  $K_{p,p}$  and  $K_{D,a}$ , there is a big range of values that result in the minimization of different OFs and, hence, there is not a clear pattern to support the selection of their value. The optimum control parameters selected for the 2DOF-PID comply with the aforementioned pattern and they are given in Table 5.2.

The values of the four OFs, normalized with the respective maximum value, are depicted for the entire population, the 10<sup>th</sup> generation, the 20<sup>th</sup> generation, and the optimum control parameters in Fig. 5.4e in a parallel coordinate plot. As it can be seen in this figure, the optimized controller achieves sufficiently low values for all OFs, except for OF  $J_2$ . Additionally, it can be observed that, in contrary to the optimization of the 1DOF-PID, in the case of the 2DOF-PID the values of the OFs achieved by the individuals of the last generation (black lines) vary enormously and a significant number of individuals cannot be considered as “good” candidates.



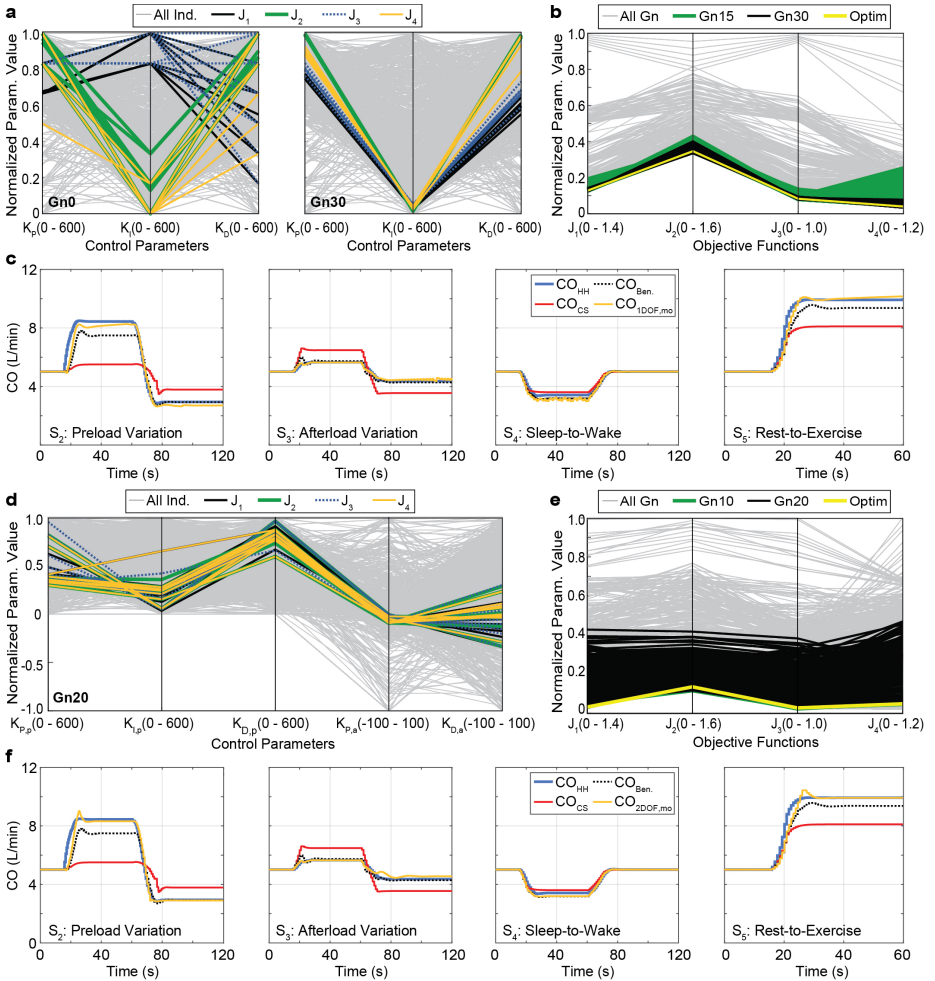


**Figure 5.4.** Performance of GAO in optimizing the 1DOF-PID and the 2DOF-PID when a multi-objective optimization problem is formulated. **a)** Parallel coordinate plot of the control parameters of the 1DOF-PID in the initial and the last generation, normalized with the respective maximum value of the parameter (the range of each parameter is given in parenthesis). The gray lines represent the entire population of individuals, while the other lines correspond to the 10 best individuals for the objective function (OF)  $J_1$  (black lines),  $J_2$  (green lines),  $J_3$  (blue dashed-lines), and  $J_4$  (yellow lines), as they formulated in equations (2-3) and (5-6). **b)** Parallel coordinate plot of the values of the four OFs, normalized with the respective maximum value (the range of each parameter is given in parenthesis). The gray lines correspond to values achieved from the entire population of individuals, while the values of the OFs achieved in the 15<sup>th</sup> and 30<sup>th</sup> generation, as well as the optimum controller are depicted with green, black and yellow lines, respectively. **c)** Comparison of the performance of the optimized 1DOF-PID against the constant speed controller, the benchmark controller and the physiological response of a healthy heart during the dynamic experiments  $S_2 - S_5$ . **d)** Parallel coordinate plot of the control parameters of the 2DOF-PID of the last generation, normalized with the respective maximum value of the parameter (the range of each parameter is given in parenthesis). The different color lines correspond to subfigure a. **e)** Parallel coordinate plot of the values of the four OFs, normalized with the

respective maximum value (the range of each parameter is given in parenthesis). The different color lines correspond to subfigure b. **f)** Comparison of the performance of the optimized 2DOF-PID against the constant speed controller, the benchmark controller and the physiological response of a healthy heart during the dynamic experiments  $S_2 - S_5$ . *Gn*, generation; *Param*, parameter; *Optim*, set of optimum control parameters; *CO*, cardiac output; *HH*, healthy heart; *CS*, constant speed controller; *Ben*, benchmark controller (*P*-controller not optimized); *so*, single objective.

In Fig. 5.4f, the performance of the optimized 2DOF-PID is assessed based on the response of the CS controller, the benchmark controller and the HH. In this figure, it can be noticed that the optimized controller follows accurately the response of the healthy heart, independent of the hemodynamic changes emulated during the experiments  $S_2 - S_5$ . Additionally, when compared to the CS controller and the benchmark controller, the optimized 2DOF-PID is able to reduce the CO error during the preload variation by 80% and 50%, respectively, while during the rest-to-exercise experiment the same comparison shows a reduction of 76% and 38% in the CO error. During the experiments  $S_3$  and  $S_4$  the optimized 2DOF-PID and the benchmark controller present similar behavior, while they both outperform the CS controller.

### 5.3.2 Optimization of PDD-ILC

The optimization problem for the PDD-ILC incorporated two OFs that aimed to minimize the error in tracking the desired reference trajectory and ensure the convergence of the ILC component. The execution of the GAOF was terminated when the maximum number of 50 generations was reached and the total duration was 25 days.

In Fig. 5.5a, it can be seen that the initial population ( $Gn_0$ ) resulted in high scores for both OFs with only 11 out of 500 individuals showing acceptable behaviour (individuals inside the “zoom-in” window). However, over the progression of the optimization process the number of “good” individuals with minimal scores for both  $J_a$  and  $J_b$  increased substantially, with only few individuals remaining outside the “zoom-in” window mainly due to the mutation applied on the individuals. A cumulative representation of all the combinations of scores for  $J_a$  and  $J_b$  achieved by the entire population of individuals is given in Fig. 5.5b (grey circles). In the same figure, the final generation ( $Gn_{50}$ ) is superimposed (black dots) to emphasize the improvement of the individuals along the progression of the optimization process.

To understand the behavior of each control parameter towards the minimization of both OFs, a parallel coordinate plot with the nondimensionalized value of each control parameter is given in Fig. 5.5c. In this figure, the grey lines, corresponding to the entire population of individuals, range among all possible parameter combinations and, hence, the exploration of the vast majority of the design space has been achieved by the GAOF. The individuals included in the Pareto front, depicted with black lines, show that the “good” individuals are more probable to have high values of  $\eta$  and low values of  $R$  and  $k_p$ . The remaining control parameters do not show an evident pattern. The optimum controller, depicted with yellow, follows the pattern of the “good” individuals, while the hand-tuned controller, shown with blue, shows extremely different pattern. The values of the optimum control parameters are  $\mu = 0.7315$ ,  $\eta = 0.7859$ ,  $Q = 120.7388$ ,  $R = 0.1365$ ,  $k_p = 3.2155$ , and  $k_D = 3.1926$ , while for the hand-tuned controller they are  $\mu = 1.0$ ,  $\eta = 7 \cdot 10^{-5}$ ,  $Q = 100$ ,  $R = 0.5$ ,  $k_p = 1.0$ , and  $k_D = 0$ .

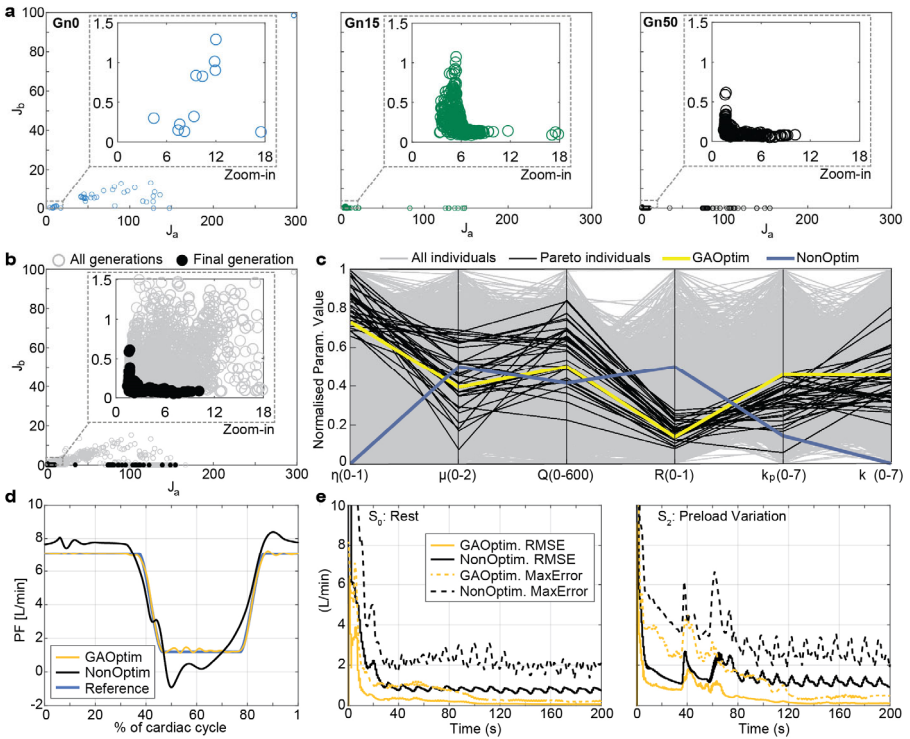


**Figure 5.5.** Performance of GAOF in optimizing the control parameters of the PDD-ILC. **a)** Evolution of the individuals towards the minimization of the objective functions  $J_a$  and  $J_b$  over the successive generations. Within the plot of each generation, a “zoom-in” view is given to highlight the transition of the individuals in the area of minimal  $J_a$  and  $J_b$ . **b)** Cumulative representation of the “scores” achieved by all the individuals being explored by the optimizer. In the “zoom-in” view the significant improvement of the individuals of the last generation (black dots) over the entire population (grey circles) is highlighted. **c)** Parallel coordinate plot of the control parameters, normalized with the respective maximum value of the parameter (the range of each parameter is given in parenthesis). The gray lines, correspond to the entire population of individuals, while the individuals included in the Pareto front are depicted with black lines. The optimum controller is depicted with a yellow line, while the hand-tuned controller is depicted with the blue line. **d)** Comparison of the reference tracking performance of the optimized (orange line) and the hand-tuned (black line) PDD-ILC after the convergence of the ILC component. The depicted tracking performance is achieved during the  $S_0$ (rest) experiment under copulation mode of the controller. The optimized controller parameters result in significant improvement of the PDD-ILC. **e)** Comparison of the tracking error of the optimized and the hand-tuned PDD-ILC over the entire duration of the dynamic experiments  $S_0$  (rest) and  $S_2$  (preload variation). *Gn*, generation; *GAOptim*, optimum PDD-ILC identified with the GAOF; *NonOptim*, hand-tuned PDD-ILC.

In Fig. 5.5d, the desired reference trajectory of the pump flow for one cardiac cycle (blue line) is depicted along with the pump flow trajectory achieved by the VAD controlled with the optimized PDD-ILC (orange line) and the hand-tuned PDD-ILC (black line). The trajectories were retrieved from the dynamic experiment simulating rest conditions ( $S_0$ ) after the convergence of the ILC component of both controllers. The optimized PDD-ILC follows excellent the reference trajectory throughout the entire cardiac cycle, outperforming significantly the hand-

tuned PDD-ILC that shows slow dynamic behavior that results in excessive overshoot and undershoot. Additionally, as it can be seen in Fig. 5.5e, after the convergence of the ILC component, the optimized PDD-ILC achieves an RMSE of 0.07 L/min and a

**Table 5.3:** Optimized sets of control parameters identified for the 2DOF-PID by solving the multi-objective optimization problem for the generic patient and the disease cases C1(C), C2(HVS<sub>M</sub> + CAD<sub>H</sub>), and-C3(HBP<sub>M</sub> + HVS<sub>M</sub>), explained in Table C7 in the supplemental material. *gOC*, *generic optimized controller*; *Opt*, *optimized*.

Controller	Control parameters				
	$K_{P,p}$	$K_{I,p}$	$K_{D,p}$	$K_{P,a}$	$K_{D,a}$
gOC	226	106	530	-8	-17
C1-Opt	220	1.2	492	-7.8	-24.8
C2-Opt	411	1	585	-1	-17
C3-Opt	279	1	553	-1	-25

max-error of 0.22 L/min during the rest conditions (experiment  $S_0$ ), and an RMSE of 0.11 L/min and a max-error of 0.47 L/min during preload variation (experiment  $S_2$ ). The hand-tuned PDD-ILC achieved an RMSE of 0.78 L/min and a max-error of 1.88 L/min during the  $S_0$  experiment, while during  $S_2$  achieved an RMSE of 1.25 L/min and a max-error of 3.05 L/min. The latter results highlight the significant improvement of the PDD-ILC performance after the optimization of its control parameters.

### 5.3.3 Interpatient variability

The hemodynamic performance of optimized controllers interacting with a diseased heart has been investigated and presented in the Supplementary Figures C3-6 of the Appendix C. The results were compared with the hemodynamics of a HH, an unsupported diseased heart (DH), a continuous CS controller, and a benchmark controller under the various experimental conditions. The results show that compared to the HH, the CS was unable to maintain physiological aortic pressure (AOP) during high preload conditions and resulted in suction events during rapid preload decrease. On the other hand, the benchmark controller and optimized 1DOF and 2DOF controllers achieved physiological responses in both preload increase and decrease. The hand-tuned PDD-ILC also resulted in excessive suction under low preload conditions, but the optimized PDD-ILC successfully avoided suction and emulated the hemodynamics of the HH better. Furthermore, the CS, benchmark, 1DOF, and 2DOF controllers resulted in reduced pulsatility of the AOP due to the continuous VAD operation. However, the hand-tuned PDD-ILC and optimized PDD-ILC significantly increased the pulsatility by incorporating the objective of pulsatility augmentation into their reference trajectories.

### 5.3.4 Interpatient variability

To consider the interpatient variability and evaluate the efficacy of the GAOF in optimizing the 2DOF-PID controller to the patient-specific characteristics, the disease-cases C1-C3, presented in Supplemental Table CS7, were used. By solving the multi-objective optimization problem defined in equations (7-8) for each of the disease-cases, the patient-specific control

parameters given in Table 5.3 were identified as optimum for the 2DOF-PID controller. As it can be seen in the latter table, the patient-specific controllers tend to reduce the  $K_{I,p}$  parameter in all cases investigated.

**Table 5.4:** Cumulative performance analysis of the three patient-specific optimized 2DOF-PID controllers and the generic optimized controller in terms of RMSE, STD, and SCOFD of the CO, MAP and LV-EDP. Each cost component is calculated by the summation of the specific cost component in the dynamic experiments  $S_2 - S_5$ . *Sum*, summation; *Opt*, optimized;

Cost Component	C1: HBP <sub>M</sub> + CAD <sub>H</sub>			C2: HVS <sub>M</sub> + CAD <sub>H</sub>			C3: HBP <sub>M</sub> + HVS <sub>M</sub>		
	Sum. Cost ( $S_2 - S_5$ )		% Red.	Sum. Cost ( $S_2 - S_5$ )		% Red.	Sum. Cost ( $S_2 - S_5$ )		% Red.
	gOC	C1-Opt		gOC	C2-Opt		gOC	C3-Opt	
RMSE CO	5.806	5.188	-10.6	5.844	5.568	-4.7	5.610	5.288	-5.7
RMSE LV-EDP	13.370	10.838	-19.0	14.465	12.705	-12.2	13.337	13.098	-1.8
RMSE MAP	67.237	62.532	-7.0	66.980	64.071	-4.3	64.284	61.807	-3.8
STD CO	1.564	1.467	-6.2	1.554	1.512	-2.7	1.443	1.458	1.0
SCOFD CO	0.977	0.916	-6.2	1.058	0.982	-7.2	0.810	1.029	-5.1

The performance of the patient-specific optimized controllers was evaluated against the generic-optimized controller (gOC) that corresponds to the 2DOF-PID controller presented previously as the optimum solution to the multi-objective optimization problem. In detail, in Table 5.4, a cumulative analysis of the cost components, termed RMSE, STD, and SCOFD of the CO, MAP, and LV-EDP is provided for all the controllers and disease cases. As it can be seen in the latter table, the controllers optimized for the C1 and C2 disease cases, C1-Opt and C2-Opt respectively, outperform the gOC in all cost components, highlighting the benefit of developing patient-specific controllers. In the disease case C3, the optimized controller C3-Opt minimizes all the cost components, except for the STD CO which is slightly increased. This minimal increase stems from the selection of the control parameters of the C3-Opt from the individuals included in the Pareto front, where the minimization of the RMSE CO was the most critical cost component to be minimized. To better understand the effect of the cost components, the response of the patient-specific optimized controllers and the gOC is presented in Supplemental Figure C1 in the Supplemental material for the dynamic experiments  $S_2 - S_5$ .

### 5.3.5 Controller optimization for specific VAD characteristics

The interactions between the diseased heart and the VAD are highly affected by the design and the dynamic response of the VAD. Hence, the VAD controller, depending on the VAD design, has to operate adequately on a plant with different response. In this context, the performance of an optimized controller can be significantly deteriorated if it is applied to a different VAD. This can be seen in Supplemental Figure C2, where the response of the 2DOF-

PID controller optimized for the Deltastream (DTS-Opt), is used to regulate the HM3. In the same figure, the response of the HM3 is shown when the 2DOF-PID controller is specifically optimized for the HM3 (HM3-Opt), along with the response of a HH. The HM3-Opt allows a faster response of the VAD during the hemodynamic manipulations, while it results in the minimization of the CO error with respect to the HH.

In Table 5.5, the sets of optimum parameters for the DTS-Opt and HM3-Opt are provided. In this table, it is evident that the HM3-Opt necessitates an increase of the absolute value for all the control parameters.

**Table 5.5:** Optimized sets of control parameters identified for the 2DOF-PID by solving the multi-objective optimization problem for the generic patient coupled with the blood pump model of the Deltastream and the HeartMate3. *DTS-Opt, optimized controller for Deltastream; HM3-Opt, optimized controller for HeartMate3.*

Controller	Control parameters				
	$K_{P,p}$	$K_{I,p}$	$K_{D,p}$	$K_{P,a}$	$K_{D,a}$
DTS-Opt	226	106	530	-8	-17
HM3-Opt	587	402	550	-12	-25

## 5.4 Discussion

In this work, a novel framework for the optimization of the control parameters of VADs has been developed and evaluated. This genetic-algorithm based framework, allows the selection of the numerical model of the CVS and the VAD that accurately represent the patient scenario of interest and, hence, it enables the optimization of complex control structures based on pump- and patient-specific characteristics. Additionally, the GAOF allows the consideration of treatment-specific goals during the definition of the objective functions of the optimization problem, paving the way for the development of patient- and treatment-specific VAD controllers. The efficacy of the GAOF was assessed with three control structures of different complexities, termed 1DOF-PID, 2DOF-PID and PDD-ILC, as well as with different VAD designs and patient scenarios. The optimized controllers outperformed the hand-tuned controller used as benchmark in all the investigated cases, highlighting the potential improvement in the performance of any VAD controller by deploying the GAOF.

The identification of the control parameters for VADs is a difficult and time-consuming task due to the non-linear and time-varying characteristics of the CVS. Hence, the selection of the control parameters for many of the VAD controllers proposed in literature is conducted with trial and error methods.<sup>56,57,66,74,75,174</sup> By using the GAOF, the selection of the control parameters becomes intuitive not only by allowing the objective function of the optimization problem to be arbitrarily defined based on the goals that the GAOF-user aims to achieve, but also by using the results of the optimization process to assess the effect of the control parameters on the performance of the controller. The importance of the information hidden in the optimization results can be understood by analyzing the parallel coordinate plots (e.g. Fig. 5.4a-b) provided for all the optimization problems of the study that show the distribution of the control parameters among the different generations of the optimization. More precisely, these plots allow the identification of patterns with respect to the values of the control parameters that result in “good” controllers and patterns for the minimization of a specific OF in the case of multi-objective

problems. Hence, by exploiting these patterns, not only decision-based selection of the control parameters can be achieved, but also new optimization procedures with a better-defined design space for the control parameters can be launched. For instance, by considering the patterns revealed from the single- and multi-objective optimization problems for the 1DOF-PID, the integral component of the controller can be omitted without impacting the performance of the 1DOF-PID.

The interpatient variability can substantially affect the performance of the VAD controllers,<sup>63</sup> however, usually this is not considered during the development phase of the controllers. In this study, we showed that different cardiovascular diseases or combinations of them alter the response of the controller. Hence, by using the GAOF, the specific characteristics of the disease can be included in the optimization process and a more suitable controller can be developed. In this way, the potential of a more patient-specific treatment is increased. Similarly, the majority of the VAD controllers available in literature, have been developed and evaluated based on a specific VAD design.<sup>56-58,64,66,74,75,174</sup> However, considering that the controller should perform accurately when it is used with a different pump, the ability to optimize the control parameters for each VAD design is highlighted. More precisely, when the GAOF was used to identify the new, optimum control parameters specifically for the HM3, the performance of the HM3 was enhanced.

The benefit of using the GAOF to improve the performance of any controller and provide pump-, patient-, and treatment-specific controllers has been proven in all the investigated scenarios. However, our system has also limitations. Specifically, the duration of the optimization process was between 1.5 and 2 days for the 1DOF-PID and 2DOF-PID controllers and up to 25 days for the PDD-ILC. This shows that the execution of the GAOF can be computationally expensive. In addition, to allow the usage of the GAOF in a clinical setting, the long execution time should be considered and, hence, data considering the patient characteristics, the disease state, the VAD design and the treatment objectives have to be provided before the VAD implantation. In acute cases where that this is not applicable, the optimized controller could be deployed after the discharge of the patient. One further limitation of the study is the fact that the evaluation of the controllers was based on the experimental conditions that were also used also in the optimization process. This could result in an overestimation of the improvement in the performance of the optimized controllers and, consequently more experiments that are not part of the optimization process should be conducted during the evaluation. Additionally, considering that the GAOF provides optimum parameters based solely on in-silico data, in-vitro and in-vivo evaluations of the optimized and non-optimized should be conducted to assess the achieved improvement in conditions that better emulate the clinical setting. Last but not least, the settings of the genetic algorithm of the GAOF were the default ones given by MATLAB, however, significant reduction of the execution time may be possible with more appropriate settings for the optimizer, usage of hybrid optimization schemes, and different optimization approaches such as swarm optimization. Hence, a study for the optimization of the settings and the exploration of different optimizers should be performed in the future.

## 5.5 Conclusions

In conclusion, this study presents a novel framework for optimizing the control parameters of VADs. The genetic algorithm-based framework, referred to as GAOF, offers a means to select the most appropriate numerical model of the CVS and VAD to reflect the patient's pathology. As a result, it enables the optimization of complex control structures tailored to the unique characteristics of the patient and the VAD design. Furthermore, the GAOF facilitates the

integration of treatment-specific goals into the definition of the optimization problem's objective functions, providing a path towards the development of personalized VAD controllers for individual patients and treatments.



## 6 Conclusion and Outlook

The scope of this thesis was the development of novel technologies that enable continuous outpatient surveillance of HF patients, as well as improved physiological response and adaptability of VADs. Following this line of thought, the focus was laid on monitoring approaches for continuous measurement of patient's hemodynamics, and physiological controllers for VADs. This chapter concludes the four studies comprising this work by reflecting on the main findings and providing an outlook for potential future research to advance the developed technologies.

### 6.1 Conclusion

To realize the continuous outpatient surveillance of HF patients, the first study demonstrated the development of an implantable, extravascular magnetic sensor, named HBSD. This study, provided also evidence that the HBSD can accurately measure the arterial blood pressure waveform under various physiologic and pathologic conditions, while it enables the acquisition of various vascular and hemodynamic properties. In the in-vitro setting, compared to reference data, the HBSD showed high linearity and agreement, with an absolute pressure error below 3 mmHg and independent of the emulated hemodynamic conditions. In the in-vivo setting, the mean error was in the range of 5 mmHg, which was in all cases smaller than in existing, similar sensing approaches, and comparable or smaller than for the only FDA approved implantable sensor. Based on these results, the usage of the HBSD in the clinical setting and the respective insights of the measured properties would allow for monitoring disease progression of various cardiovascular diseases, adjustment of therapeutical protocols, and the acquisition of control parameters for the implementation of physiological control for VADs. However, to enable the translation of the HBSD in the clinical setting, long-term animal experiments, as well as design modifications to ease the implantation process, and wireless data and energy transmission are necessary.

The second study aimed to further enhance the continuous outpatient monitoring of HF patients by focusing on the continuous, real-time estimation of the remaining cardiac contractility of the diseased heart. Hence, in this preliminary study, it was demonstrated that traditional time series classifiers and graph-based neural networks can be applied to estimate the remaining cardiac contractility based on time series data of the left ventricular pressure. The support vector classifier, from the family of time series classifiers, showed superior performance; however, all classification methods provided accurate contractility estimation with real-time implementation capabilities. The usage of these estimation approaches could substantially support patient monitoring and adaptive physiologic VAD control approaches. Further studies, however, are needed to support these findings with animal time series data and data from VAD supported patients.

After fulfilling the need for monitoring technologies with the first two studies, the third study aimed to the development of a responsive and adaptive physiological controller (PDD-ILC) for VADs. Hence, in this study, a data-driven iterative learning physiological controller that accurately tracks predefined pump flow trajectories was demonstrated. The pump flow trajectories are generated based on the Frank-Starling mechanism and treatment objectives. The PDD-ILC tracks these trajectories by a model-free, data-driven iterative learning controller that uses the time-sequences of the left ventricular pressure and the pump flow to obtain a model representation. The controller has been extensively tested in an in-silico environment under various physiological conditions, showing high accuracy in tracking the reference pump flow trajectories, while it outperformed existing model-based iterative learning control approaches.

Additionally, the PDD-ILC achieved the predefined treatment objectives and resulted in improved hemodynamics, pulsatility levels and preload sensitivities compared to the constant speed support that is the current state-of-the-art in the clinical practice. Finally, the PDD-ILC showed excellent robustness against noisy input signals from the pressure and flow sensors. Thus, the PDD-ILC overcomes the majority of the shortcomings of existing controllers and broadens the potential for VAD control in the clinical setting. However, to prove the performance of the PDD-ILC in the real-time setting and allow the final translation of the PDD-ILC into the clinical setting, in-vitro and in-vivo studies have to be conducted.

The last study of this work, demonstrated a novel, genetic algorithm-based optimization framework (GAOF) that enables the optimization of control parameters based on patient characteristics and treatment objectives. The benefit of using the GAOF was evaluated with two different VAD designs, various patient disease scenarios, and three control structures of different complexity, with the PDD-ILC constituting the most challenging with six control parameters. In all the experimental settings, the optimized controllers outperformed the hand-tuned, generic controllers. This is the first time that optimization approaches are used to achieve patient and treatment-specific controllers based on the selection of the control parameters. Hence, the GAOF is considered a valuable tool for potential improvement in the performance of any VAD controller and, consequently, improved survival rates and quality of life of VAD patients.

As an overall conclusion, this thesis contributes two sensory technologies for continuous direct and indirect monitoring of the patient's status in an outpatient setting, an adaptive and physiologically responsive controller for VADs, and an optimization framework for the development of patient and treatment-specific VAD controllers. The implementation in the clinical practice of all the developed technologies together, holds a great potential to overcome the shortcomings of the current management of end-stage HF patients supported with VADs, resulting in improved survival rates and QoL of the patients.

## 6.2 Outlook

Over the last decades, advanced pharmaceutical and device therapies have been developed with the aim to alleviate the symptoms, reduce hospitalization rates and, consequently, improve the QoL and survival of HF patients. However, the diagnosis and management of HF-patients are still heavily based on patient history and physical examination, necessitating regular follow-ups in the hospital. Such periodic in-hospital examinations are a significant limitation for the clinical decision-making and timely intervention, while in the case of VAD-supported patients they also preclude the prevention of adverse events. Hence, to achieve adequate surveillance of the therapy and a better patient management, the development of reliable monitoring technologies and, enabled from these technologies, adaptive physiological controllers are prerequisites. In this work, covering both areas of interest, novel sensory and control strategies have been demonstrated, however, further steps can be investigated in the future to allow the final translation of these strategies in the clinical practice.

Focusing on the HBSD, the main considerations that could be further investigated in the future are the data/power transmission and the long-term reliability of the sensor in the human body. In detail, the energy and data transmission of the HBSD are currently accomplished transcutaneously by copper wires. This approach increases the risk of infections at the access site, as well as, the risk of sensor detachment and malfunction due to contact with the surrounding organs. Hence, future studies should focus on the development of an electronic circuit that is embedded into the body of the HBSD and enables wireless data and energy transmission. The author has conducted the first steps in this direction with an electronic circuit that uses a low energy Bluetooth (BLE)

protocol to transmit the data and is primarily powered with a rechargeable battery that is recharged transcutaneously through inductive coils. To confirm the safety of the HBSD to be implanted in humans, the long-term performance of the sensor should be tested in chronic animal trials to assess the effect of the surrounding organs in a closed-chest environment and to identify any performance degradation due to potential tissue ingrowth.

Based on the information provided in Section 1.5, one of the most useful properties for the assessment of the patient's status, but most importantly, for the implementation of physiological control, is the cardiac output. In Section 2, it was described that the implantation of two HBSD in close proximity allows the calculation of the PWV, which is often used to calculate the blood flow in a vessel. Hence, further investigations should be conducted to enable the estimation of the cardiac output by combining the continuous waveform of the aortic diameter and the PWV that are provided by HBSD.

The estimation of the remaining contractility by applying time series classification approaches on the time series data of the left ventricular pressure (Section 3) demonstrated very promising results. However, the applicability of the times series classification and, hence, the estimation accuracy should be further investigated with artificial data produced for a VAD-supported patient, but most importantly with animal data that provide realistic variability.

The PDD-ILC demonstrated excellent physiological response, adaptiveness, and stability in an extensive experimental protocol (Section 4). However, the experiments have been conducted only in an in-silico environment with one specific combination of VAD design and model of the cardiovascular system. Hence, to ensure the safety of the PDD-ILC its assessment should be extended with different VAD designs and model of the cardiovascular system. Finally, further studies should be conducted in an in-vitro and in-vivo environments, to prove the applicability of the PDD-ILC in real-time settings and assess its performance under conditions that emulate more realistic the human body.



## Appendix

### A. Continuous Monitoring of Blood Pressure and Vascular Hemodynamic Properties with Miniature Extravascular Hall-Based Magnetic Sensor

#### Supplemental methods

##### Appendix A1. Magnetic field expressions

In this work, the magnetic field in the proximity of the cylindrical magnet of the hall-based sensing system constitutes the first step towards the calculation of the distance between the magnet and the hall-element components. The magnetic field inside and outside a cylindrical magnet of finite size and uniform magnetization along its symmetry axis can be obtained by considering the cylindrical body as an ideal solenoid (a collection of current loops). In this case, the total magnetization is  $M \equiv nI$ , with  $I$  being the current per loop and  $n$  being the number of loops per unit length<sup>185</sup>. Derby and Olbert<sup>186</sup>, by applying the Biot–Savart law, provided algebraically convenient derivations of the magnetic field of a cylindrical magnet by using a combination of general elliptic integrals. Those derivations are presented here:

$$B_\rho = B_0 [R_+ C(k_+, 1, 1, -1) - R_- C(k_-, 1, 1, -1)] \quad \text{S1.1}$$

And

$$B_z = \frac{B_0 R}{R + \rho} [\beta_+ C(k_+, j^2, 1, \gamma) - \beta_- C(k_-, j^2, 1, \gamma)] \quad \text{S1.2}$$

With

$$B_0 = \frac{\mu_0}{\pi} M \quad \text{S1.3}$$

where  $B_\rho$  and  $B_z$  are the radial and axial components of the magnetic-flux density, respectively,  $\mu_0$  is the permeability of vacuum and  $R$  is the radius of the cylinder. The generalized complete elliptic integral  $C$  and the supportive variables  $\alpha_\pm, \beta_\pm, k_\pm, z_\pm$  and  $j$  are given by:

$$C(k_c, p, c, s) = \int_0^{\pi/2} \frac{(c \cdot \cos^2 \varphi + c \cdot \sin^2 \varphi) d\varphi}{(\cos^2 \varphi + p \cdot \sin^2 \varphi) \sqrt{\cos^2 \varphi + k_c^2 \cdot \sin^2 \varphi}} \quad \text{S1.4}$$

$$z_\pm = z \pm b \quad \text{S1.5}$$

$$R_{\pm} = \frac{R}{\sqrt{z_{\pm}^2 + (\rho + R)^2}} \quad \text{S1.6}$$

$$\beta_{\pm} = \frac{z_{\pm}}{\sqrt{z_{\pm}^2 + (\rho + R)^2}} \quad \text{S1.7}$$

$$j = \frac{R - \rho}{R + \rho} \quad \text{S1.8}$$

$$k_{\pm} = \sqrt{\frac{z_{\pm}^2 + (\rho - R)^2}{z_{\pm}^2 + (\rho + R)^2}} \quad \text{S1.9}$$

where  $b$  is half the height of the cylinder,  $z$  and  $\rho$  are the axial and radial components of the position where the magnetic field is calculated (Supplemental Figure A1).

Based on the cartesian coordinates of the position where the magnetic field is calculated, the angle  $\theta$  in the x-y plane is calculated by:

$$\theta = \arctan(y/x) \quad \text{S1.10}$$

and the radial components of the magnetic-flux density is analyzed to  $B_x$  and  $B_y$  by:

$$B_x = B_{\rho} \cos \theta, \quad B_y = B_{\rho} \sin \theta \quad \text{S1.11}$$

Hence, the vector of the magnetic field for the position  $A(x,y,z)$  is defined as:

$$\vec{B}_A = [\vec{B}_{Ax}, \vec{B}_{Ay}, \vec{B}_{Az}] \quad \text{S1.12}$$

By implementing the above equations for all possible z-positions, since the x and y is defined during the implantation, the voltage to distance response can be derived. However, the hall-element measures only the component of the magnetic field that is perpendicular to its measurement surface. Hence, based on Supplemental Figure A1, the last step to mathematically derive the magnetic field sensed by the hall element is to rotate the magnetic field vector in the Euclidean space such that its z component is perpendicular to the measurement surface of the hall-sensor for all z-positions. After determining the yaw ( $\varphi$ ), pitch ( $\gamma$ ), and roll ( $\delta$ ) angles in the 3D-space (Supplemental Figure A1), induced during the implantation process, a rotation matrix is defined:

$$R_m = R_z(\delta)R_y(\gamma)R_x(\varphi) \rightarrow \quad \text{S1.13}$$

$$R_m = \begin{bmatrix} \cos \delta & -\sin \delta & 0 \\ \sin \delta & \cos \delta & 0 \\ 0 & 0 & 1 \end{bmatrix} \begin{bmatrix} \cos \gamma & 0 & \sin \gamma \\ 0 & 1 & 0 \\ -\sin \gamma & 0 & \cos \gamma \end{bmatrix} \begin{bmatrix} 1 & 0 & 0 \\ 0 & \cos \varphi & -\sin \varphi \\ 0 & \sin \varphi & \cos \varphi \end{bmatrix} \quad S1.14$$

By applying the rotation matrix  $R_m$  to the vector of the magnetic field  $\vec{B}$ , the vector of the magnetic field expressed on the new coordination system is:

$$\vec{B}_r = R_m \vec{B} = R_m [\vec{B}_x, \vec{B}_y, \vec{B}_z] = [\vec{B}_{rx}, \vec{B}_{ry}, \vec{B}_{rz}] \quad S1.12$$

Finally, the magnetic field measured by the hall sensor is  $B_{rz}$

## Appendix A2. Fabrication procedure of the HBSD

The hall-effect based sensing device (HBSD) proposed in this work, is an extravascular sensing system that consists of two distinct components, namely the magnet component and the hall-sensor (HS) component. These components are not interconnected and they are attached on the outer wall of the aorta. Each of the two components requires the design and manufacturing of housings that facilitate the encapsulation, the implantation procedure, as well as, the robustness and the biocompatibility of the HBSD.

During the project, successive HBSD generations were produced and tested in order to optimize the design, the performance, and the robustness of the HBSD and, finally, reach the translational level for the in-vivo evaluation. In Supplemental Figure A2, two fabrication processes that resulted in the HBSDs used in the final in-vitro and in-vivo evaluation are illustrated. The initial step for both approaches is the identification of the design space of the HBSD (Supplemental Figure A2a). In this step, based on the diameter of the vessel that the sensor is intended to be used, the range of wall distension is estimated. Since the dimensions of the HS are constrained by the SOT-23 packaging protocol we selected, the wall distension range along with the vessel diameter (VD) contribute to the selection of the size of the magnet and the sensitivity of the hall-sensor so that the resolution and the accuracy of the sensor are optimized.

After the selection of the optimum magnet and HS sensitivity, the two components are pre-processed (Supplemental Figure A2b). In detail, to improve the temperature stability, as well as to ensure chemical and moisture resistance, the magnet is coated with a 3 $\mu$ m layer of Parylene-C via chemical vapor deposition (CVD). To allow the energy and data transmission, copper wires are soldered on the hall-sensor under the microscope with the use of soldering paste. At this stage, the magnet and the HS are stored until the assembling process of the HBSD.

The magnet and HS housings of the first generation (G1) of HBSDs, as it can be seen in Supplemental Figure A2c (left), have a simple design with the necessary component-slots, a wide basis and four suturing holes. The wide basis, although increases the HBSD's footprint, it was necessary to allow an accurate and stable sensor attachment. Both housings were 3D-printed (Supplemental Figure A2d) from biocompatible nickel alloy Ti-6Al-4V powder via selective laser melting (SLM). After the printing, the remaining support structures were removed and careful post-processing was conducted under a microscope to clean and polish all surfaces. The polished housings were immersed in deionized water (DW) and dried for 5 minutes at 30 °C in a temperature-controlled oven (Supplemental Figure A2e). As a next step, the coated magnet and the HS were assembled with the magnet and HS housings, respectively (Supplemental Figure A2f). To fully encapsulate and insulate the magnet and the HS, as it is shown in Supplemental Figure A2h, the exposed surfaces of the housings were carefully filled with biocompatible epoxy glue and let to cure for 1.5 hours at 100 °C. In Supplemental Figure A2i (left), the final HBSDs are shown and compared with a 50-cent Swiss franc coin.

The second generation (G2) of HBSDs was improved based on the evaluation of G1. As it can be seen in Supplemental Figure A2c, the design of the contacting area of the housings was rounded, following the exact diameter of the VD. This design change enhanced the attachment of the HBSD on the vessel wall and minimized the misalignment of the two housings, induced by the wall curvature. Additionally, each housing of G2 consisted of a main part and a lit. The addition of the lit aimed to minimize the exposition of the magnet and the HS. The housings of G2 were 3D-printed (Supplemental Figure A2d) from Class-I biocompatible resin DS3000 via selective laser stereolithography (SLA). The new material and 3D-printing method resulted in higher manufacturing precision, reduced printing time, but most importantly, significant



reduction if the weight of the HBSD. The later achievement was crucial for the minimization of the gravitational forces applied on the vessel wall due to the HBSD's mass. After printing, a significantly faster and simpler post-processing face was necessary, wherein the housings were immersed in phosphate buffered saline, dried for 5 minutes at 30 °C in a temperature-controlled oven, immersed in DW and cured under ultraviolet light for 3 minutes (Supplemental Figure A2e). The housings were then assembled with the magnet and the HS (Supplemental Figure A2f). As a next step, the main parts and the lit of the assemblies were carefully glued with biocompatible epoxy and cured for 1.5 hours at 100 °C. As it is shown in Supplemental Figure A2h, the final step of the post-process included the coating of the entire assemblies with a 3 $\mu$ m layer of Parylene-C via CVD to ensure an adequate insulation and biocompatibility. The final HBSDs of G2 are depicted in Supplemental Figure A2i (right), along with a 50-cent Swiss franc coin for size comparison.

### **Appendix A3. Extraction of cardiac cycle onset/EDP and systolic pressure**

In this study, the extraction of onsets, end-diastolic pressure (EDP), and systolic pressure (SP) of the cardiac cycle was performed with the process depicted in Supplemental Figure A3. Specifically, the raw pressure signal derived by the HBSD (Supplemental Figure A3a) was low-pass filtered with an 18<sup>th</sup>-order, zero-phase finite impulse response (FIR) filter and a cut-off frequency of 8 Hz (Supplemental Figure A3b). In a next step, the first derivative of the low-pass filtered pressure waveform was calculated and its maxima were identified (Supplemental Figure A3c). The index of these maxima, laid on the upslope of the pressure waveform and, hence, it was always between the onset (or EDP since they are considered the same point on the pressure waveform) and SP values of each cardiac cycle (Supplemental Figure A3d). By using the index of the later maxima as pivot points, a backward search window with size 10% of the previous cycle-duration was applied and the minimum of the raw pressure signal in this window was identified. This minimum corresponded to the index of the onset and EDP of the cardiac cycle. Similarly, starting from the index of the maxima of the first derivative, a forward search window with size 30% of the previous cycle-duration was applied and the maximum of the raw pressure signal in this window was identified. This maximum corresponded to the index of the SP of the cardiac cycle (Supplemental Figure A3e).

### **Appendix A4. Extraction of dicrotic notch and systolic phase**

The process for the extraction of the dicrotic notch constituted an extension of the extraction approach of the cycle onsets/EDP and SP. More precisely, as it can be seen in Supplemental Figure A4, after applying the zero-phase FIR filtering on the raw pressure signal, all the maxima of the first derivative were identified by changing the thresholds for the maxima selection. From the entire pull of maxima, the indexes used for the extraction of the onset were excluded. The remaining maxima correspond to the middle of the upslope that defines the dicrotic notch (Supplemental Figure A4d). By using the index of the later maxima as pivot point, a forward search window with size 5% of the previous cycle-duration was applied and the maximum of the raw pressure signal in this window was identified (Supplemental Figure A4e). The raw pressure signal along with all the critical components are shown in Supplemental Figure A4f. By

calculating the time interval between the onset and the dicrotic notch of each cycle, the systolic phase of the cardiac cycle is deduced (Supplemental Figure A4e).

## Appendix A5. Calculation of respiration frequency

The transmural pressure (pressure inside the heart chamber minus the intrapleural pressure) is affected from the respiratory activity. In detail, during inspiration or expiration the preload and ventricular stroke volume are increased or decreased, respectively. These alterations in preload and stroke volume during the respiration cycles affect the arterial blood pressure (ABP), allowing the deduction of the respiratory frequency by the ABP waveform.

In this study, to deduce the respiratory frequency, the previously identified SP values (Appendix 3, Supplemental Figure A3 and Supplemental Figure A5a) are exploited. Specifically, by isolating the SP values of the ABP, a new waveform is produced (Supplemental Figure A5b). By identifying the minima of this waveform, the respiration period can be calculated as the time interval between two consecutive minima (Supplemental Figure A5c) by:

$$RP = t_{(SP_{n+1})} - t_{(SP_n)} \quad S1.1$$

Consequently, the respiratory frequency is calculated as the inverse of the RP by:

$$RF = \frac{1}{RP} * 60 [breaths/min] \quad S1.2$$

In Supplemental Figure A5 the flowchart of the described process is given and in Supplemental Figure A5d a comparison with the set respiration value through the ventilation system is given.

## Appendix A6. Calibration procedure of the HBSD

The HBSD was calibrated on a high precision 4-axis sliding table. The angle in the yaw plane ( $\varphi$ ) and the angle in the pitch plane ( $\gamma$ ) (based on their definition in Figure 2 in the main text) were varied between +3 and -3 degrees with steps of 0.2 degrees. Additionally, the radial position was varied from 0 to 1 mm (which was the radius of the magnet) in steps of 0.1 mm. For all combinations of the aforementioned parameters, the response of the sensor (voltage output – V) was register for all z-distances between 0 and 5mm, in steps of 0.1 mm. By combining the data for all calibration points, the a “calibration map” for each sensor was produced.

## Appendix A7. Acceptance criteria

The criteria set to determine sensors' quality are summarized in Supplemental Table A1 and Figure A8 and were focusing on their manufacturing process, their robustness (unaffected performance after sterilization, immersion in liquid, temperature changes) and their resolution of the HBSD. More precisely, all the 3D printed casings were assessed under the microscope to identify any fracture, breakage or incomplete printing events. The casings that showed any of the unwanted events were excluded. The magnets were assessed with respect to their magnetic-flux strength before their integration in the casing. Specifically, by using the calibration station and a simplified version of casing, the magnet was attached on the calibration setup and the magnetic field sensed by the hall sensor was measured when the distance of the magnet was changed from 0.5 mm to 4 mm with steps of 0.1mm. This process was conducted before and after the deposition of Parylene-C and the magnets were accepted if the deviation of the magnetic-flux was smaller than 2% at all measured points. Since the assembling procedure was based on several steps, after mounting the assemblies, each sensor was assessed with respect to its robustness to immersion in water. Similar to the process described in the manuscript, the HBSDs were mounted with a fixed distance between the two sensing components and they were immersed in a 0.9% saline bath at 37 °C for one day with the output voltage of the HBSD being continuously measured. To accept the quality of the HBSD as sufficient, the deviation of the measured mean output voltage compared to the initial mean output voltage should not exceed 2% and the standard deviation should not exceed 5% of the initial standard deviation. Additionally, each sensor underwent a temperature ramp test with the temperature changing within the range of 30 and 44 °C. To accept the HBSD as sufficient, the deviation of the measured mean output voltage at each temperature step compared to the initial mean output voltage at room temperature ( $21\pm 1$ ) should not exceed 2% and the standard deviation should not exceed 5% of the initial standard deviation. Similarly, each sensor underwent autoclave sterilization. The deviation in the measured mean output voltage post-sterilization compared to the initial mean output voltage should not exceed 2% and the standard deviation post-sterilization should not exceed 5% of the initial standard deviation. Finally, the criterion for the resolution of the HBSD was based on the calibration process of the sensor. Specifically, based on the operating line with zero misalignment, the resolution of the HBSD was assessed for a linear distance of 1.5 to 2 mm between the two elements. Since this is the optimal distance for the two components, a resolution of at least 0.6 V/mm was the criterion to accept the sensor. Sensors that failed the above-mentioned steps were excluded from the in-vitro and in-vivo experiments.

During the in-vivo experiments and after the implantation of the sensors, the positioning of the two sensing elements was assessed based on the criteria mentioned in the manuscript ( $\varphi < 2^\circ$ ,  $\gamma < 2^\circ$  and  $r < 0.5$  mm, and limit in z-distance 2.25 mm). Once an alignment that meets the criteria was achieved, the voltage output of the sensor was measured for 20 s and the mean value was compared to the voltage output identified during the calibration process for the same distance and alignment. To qualify the HBSD for analysis, the deviation should not exceed 5%.

After the completion of the experiment, the calibration setup was used to acquire the operating line for a linear distance of 1.5 mm to 2mm between the two elements with zero misalignment. The resolution of the HBSD for this operating line was compared to the resolution that was acquired during the calibration prior to the experiment. A deviation greater than 10% of the pre- and post-operative resolution resulted in disqualification of the sensor.

After the completion of the experiment, the calibration setup was used to acquire the operating line for a linear distance of 1.5 mm to 2mm between the two elements with zero misalignment.

The resolution of the HBSD for this operating line was compared to the resolution that was acquired during the calibration prior to the experiment. A deviation greater than 10% of the pre- and post-operative resolution resulted in disqualification of the sensor.

## **Appendix A8. HBSD material selection**

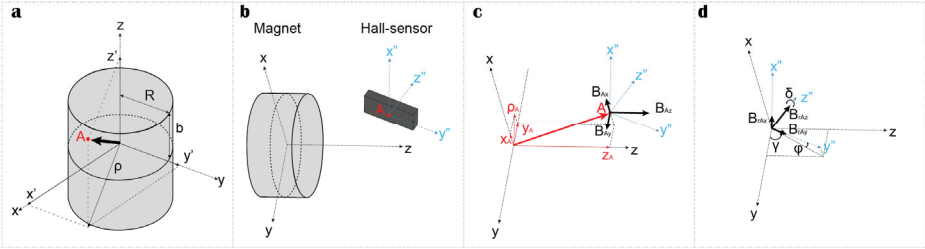
The selection of the materials used for the manufacturing of the sensing components of the sensor was based on tissue compatibility, non-magnetic characteristics, chemical stability, and ability to be produced by rapid prototyping approaches. In detail, to achieve an adequate interaction with the aortic tissue and the surrounding organs the materials for the casings of the sensing elements (biocompatible resin DS-3000) and their coating (Parylene-C) were selected to reduce cytotoxins, toxicological or allergic reactions, as well as the inflammatory processes when in contact with the tissue. The material of the casings (biocompatible resin DS-3000) allows the minimization of the overall weight of the sensor, and hence, it results in reduced effect on the mechanical properties of the host tissue. Additionally, due the non-magnetic characteristics of the biocompatible resin DS-3000 the interference with the magnetic field produced by the magnet (nickel-plated neodymium magnet) is minimized. Although our material selection met all the requirements during the acute in-vivo experiments, it should be considered preliminary and its usage in humans should be avoided.

# Supplemental tables

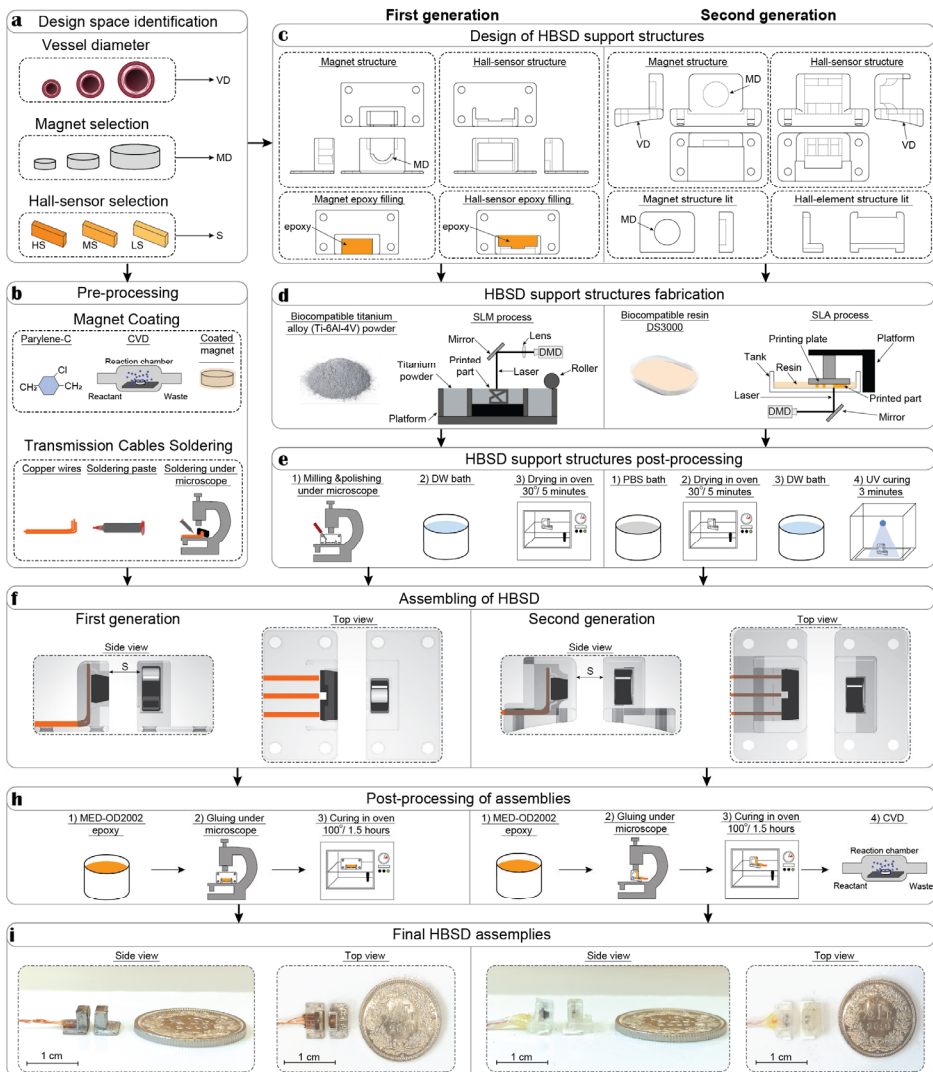
**Supplemental Table A1. HBSD acceptance criteria.**  $V$ , HBSD voltage output;  $V_0$ , initial HBSD voltage output;  $\Delta V\% = |(\bar{V} - \bar{V}_0)/\bar{V}_0| \cdot 100$ ,  $\Delta std\% = |(std(V) - std(V_0))/std(V_0)| \cdot 100$ ;  $S$ , linear distance in z-direction (1.5 mm-2 mm);  $\varphi$ , misalignment angle in yaw plane;  $\gamma$ , misalignment angle in pitch plane;  $r$ , misalignment of the magnet and HES centers in the x-y plane expressed as a radius.

Process	Pass Criteria
<b>Pre-experiment</b>	
Fabrication	No cracks, Complete printing
Autoclave	$\Delta V\% < 2\%$ , $\Delta std\% < 5\%$
Liquid immersion	$\Delta V\% < 2\%$ , $\Delta std\% < 5\%$
Temperature ramp	$\Delta V\% < 2\%$ , $\Delta std\% < 5\%$
Resolution @ zero misalignment	$\Delta V/\Delta S > 0.6$ V/mm
<b>During the Experiment</b>	
Alignment	$\varphi < 2^\circ$ , $\gamma < 2^\circ$ , $r < 0.5$ mm, z-distance $< 2.25$ mm
Response	$\Delta V\% < 5\%$
<b>Post-experiment</b>	
Resolution @ zero misalignment	$ ( (\Delta V/\Delta S)_{post} - (\Delta V/\Delta S)_{pre} ) / (\Delta V/\Delta S)_{pre}   \cdot 100 < 10\%$

# Supplemental figures



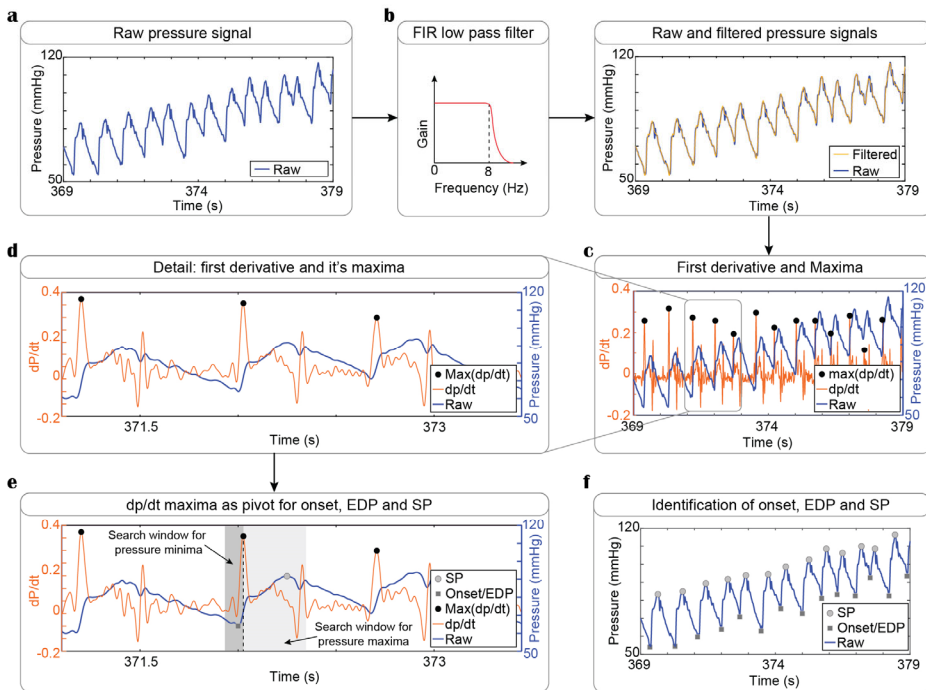
**Supplemental Figure A1. Magnetic field calculation.** **a)** Schematic representation of a cylindrical magnet of finite size and uniform magnetization along its symmetry axis. Point A ( $x'$ ,  $y'$ ,  $z'$ ) corresponds to a random point where the magnetic field is calculated based on the equations S1.1-1.12.  $R$  is the radius of the cylinder and  $b$  is half of its length. **b)** Schematic representation of a magnet and a hall-sensor along with their coordinate systems (CS). The point A corresponds to the center of the measuring surface of the hall-sensor and defines the origin of the CS of the hall-sensor, which has the  $z$ -axis perpendicular to the measuring surface. **c)** Analysis of the origin of the hall-sensor's coordinate system on the CS of the cylinder and calculation of the magnetic field. **d)** Rotate of the magnetic field vector in the Euclidean space such that its  $z$  component is perpendicular to the measurement surface of the hall sensor. The letters  $\varphi$ ,  $\gamma$ , and  $\delta$  define the yaw, pitch, and roll angles in the 3D-space, respectively.



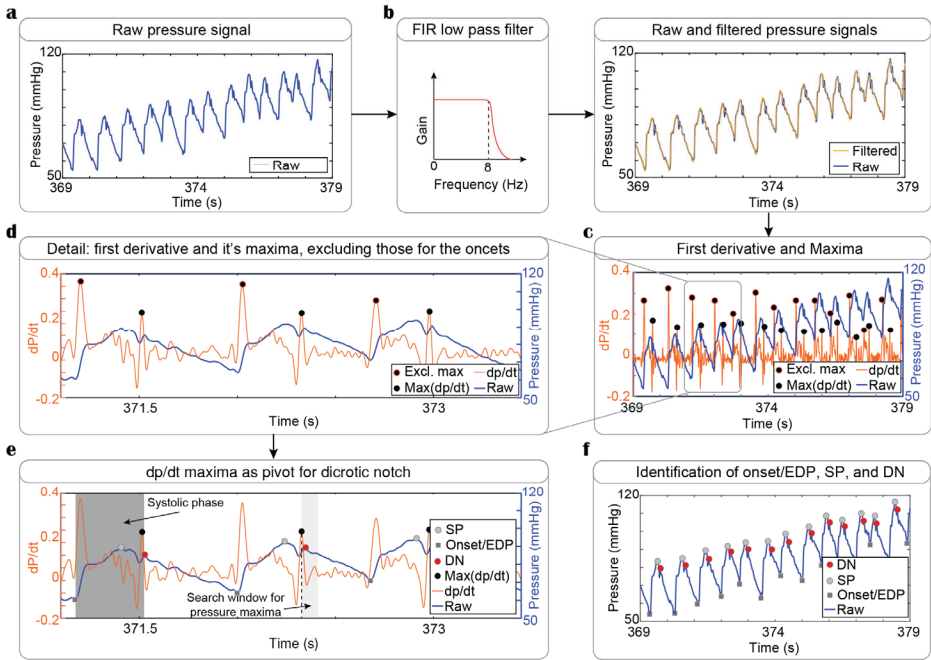
**Supplemental Figure A2. Fabrication procedure of the HBSD.** **a)** Identification of the design space based on the VD, MD and the magnetic-flux sensitivity of the hall sensor. **b)** Magnet coating with Parylene-C via CVD and soldering of the transmission copper cables on the hall-sensor. **c)** Design of the support structures for each HBSD generation. **d)** Fabrication of the HBSD magnet and hall-element structures. For HBSD generation one (G1), SLM printing with Ti-6Al-4V. For the second HBSD generation (G2), SLA printing with biocompatible resin DS-3000. **e)** After the removal of the support structures, the G1 structures were milled and polished under the microscope, cleaned in a bath of DW and dried for 5 minutes at 30° in a temperature-controlled oven. The G2 structures were immersed in a PBS bath, dried for 5 minutes at 30°, immersed in DW and cured under UV-light. **f)** Assembly of all components. **g)** Post-processing of HBSD.

The G1 underwent insulation with MED-OD2002 epoxy glue and curing in a temperature-controlled oven at 100° for 1.5 hours. The G2 included the same process and, further Parylene-C coating via CVD. **i)** Final HBSDs from G1 and G2. HBSD, hall-based sensing device; VD, vessel diameter; MD, magnet diameter; S, axial distance; HS, high sensitivity; MS, medium sensitivity; LS, low sensitivity; SLM, selective laser melting; SLA, selective laser stereolithography; DMD, digital micromirror device; CVD, chemical vapor deposition; PBS, phosphate buffered saline; DW, deionised water, UV, ultraviolet.

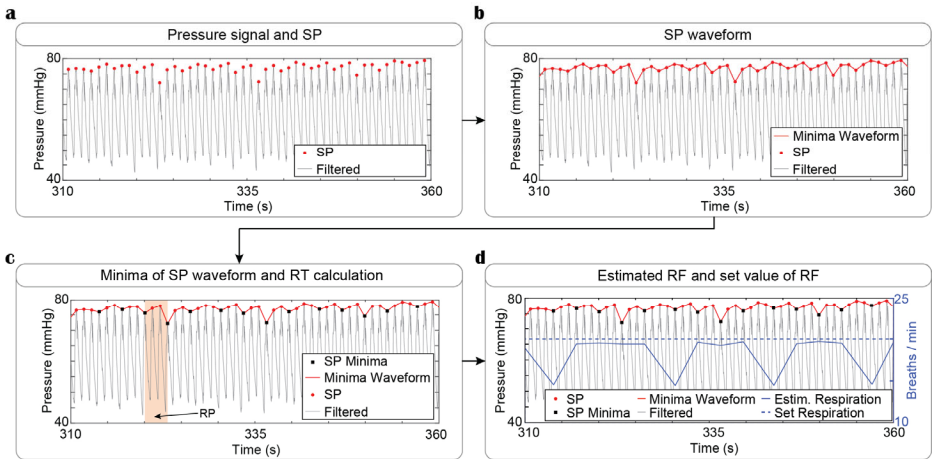




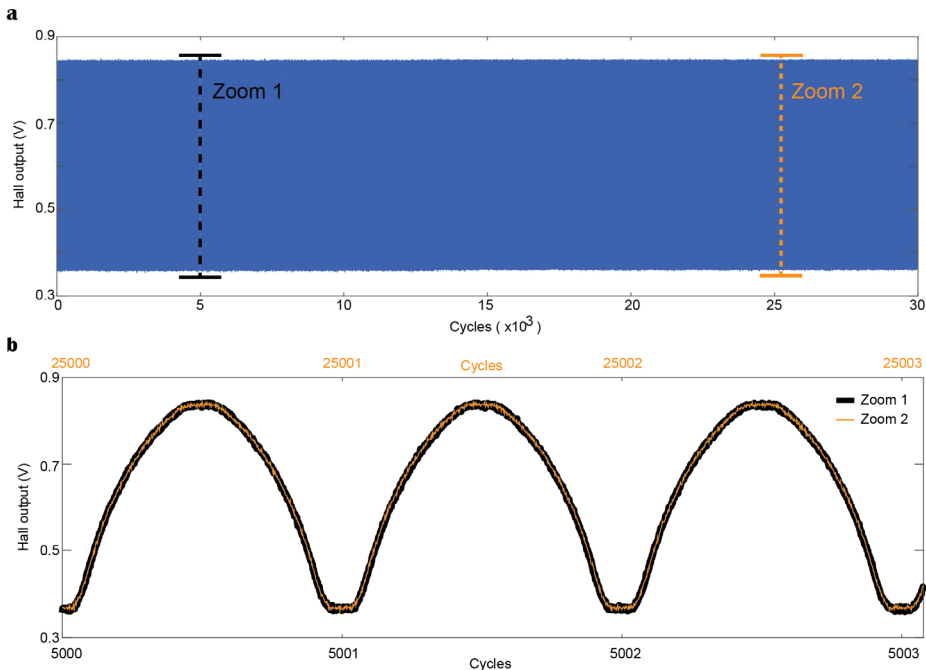
**Supplemental Figure A3. Extraction of cardiac cycle onset/EDP and systolic pressure.** **a)** Raw pressure signal derived by the HBSD. **b)** Pressure signal low-pass filtered with an 18<sup>th</sup>-order, zero-phase finite impulse response (FIR) filter and a cut-off frequency of 8 Hz. The raw signal is also included for comparison. **c)** First derivative of the filtered pressure signal. The black circles correspond to the maxima of the first derivative. **d)** Detailed depiction of the raw pressure, the first derivative and the maxima of the first derivative for three cardiac cycles. **e)** Illustration of the search windows for the extraction of the onset/EDP and the SP based on the index of the maximum of the first derivative. For the onset/EDP, starting from the index of the maximum of the first derivative a backward search window with size 10% of the previous cycle-duration is defined, while for the SP a forward search window with size 30% of the previous cycle-duration is defined. The onset/EDP and the SP extracted are also illustrated. **f)** Raw pressure signal with all the extracted onsets/EDPs and SPs.



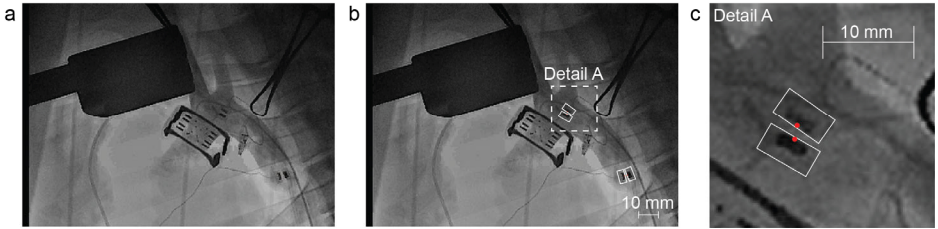
**Supplemental Figure A4. Extraction of dicotic notch and systolic phase.** **a)** Raw pressure signal derived by the HBSD. **b)** Pressure signal low-pass filtered with an 18th order, zero-phase finite impulse response (FIR) filter and a cut-off frequency of 8 Hz. The raw signal is also included for comparison. **c)** First derivative of the filtered pressure signal. The black circles with the red perimeter correspond to the maxima that have been used for the onset extraction and, hence, they are excluded. The black circles with black perimeter correspond to the usable maxima. **d)** Detailed depiction of the raw pressure, the first derivative and the maxima of the first derivative for three cardiac cycles. **e)** Illustration of the search window for the extraction of the DN based on the index of the maximum of the first derivative. For DN a forward search window with size 5% of the previous cycle-duration is defined. The extracted DN along with the calculation of the duration of the systolic phase are also depicted. **f)** Raw pressure signal with all the extracted onsets/EDPs, SPs, and DN.



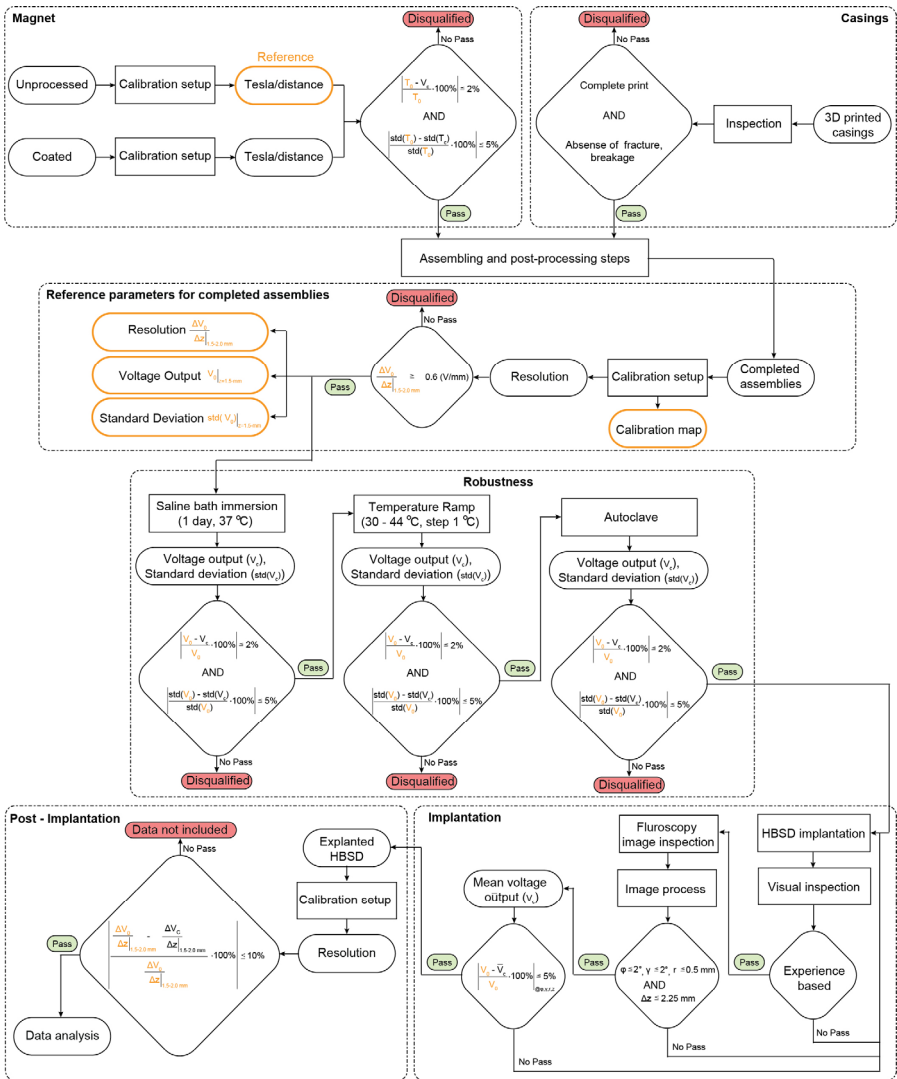
**Supplemental Figure A5. Extraction of respiration frequency.** **a)** Pressure signal derived by the HBSD along with the extracted SP values. **b)** Waveform created from the isolated SP values. **c)** Extraction of the SP-waveform minima. The orange region indicates the RP based on two consecutive SP values. **d)** Superposition of the estimated RF and the set RF value through the ventilation system. SP, systolic pressure; RP, respiration period; Estim, estimated.



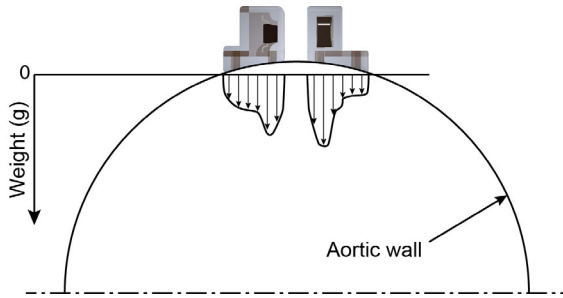
**Supplemental Figure A6. Response of HBSD under cycling loading conditions.** To prove the robust operation of the HBSD over time, cyclic loading experiments were conducted on a tensile device. For the attachment of the HBSD on the tensile device dedicated mounting parts were produced. **a)** Response of a HBSD for 30'000 cycles of loading. The implemented cycles had the same duration for "expansion" and "contraction" phases. No hysteresis between "expansion" and "contraction" was present during the experiment. **b)** Detailed depiction and comparison of three cycles early on the experiment (5000-5003) and three cycles on the at the late experiment (25000-25003). The response of the HBSD is identical to the initial response, verifying the claim of no cyclic fatigue.



**Supplemental Figure A7. Distance and misalignment quantification after implantation. a)** Image under fluoroscopy. **b)** Post processed image for the identification of the position of the sensing components. **c)** Detailed picture of the position of the first sensor. The center of each component, along with the known size of the base of the sensing components, are used to quantify the alignment and the z-distance among the two components.



Supplemental Figure A8. Roadmap of HBSD acceptance.



**Supplemental Figure A9. Qualitative distribution of HBSD weight along the vascular wall surface.**





## B. Physiologic Data-Driven Iterative Learning Control for Left Ventricular Assist Devices

### Supplemental tables

**Supplemental Table B1.** Parameter sets of the experiments used in this Work. SVR, systemic vascular resistance; PVR, pulmonary vascular resistance; UVV, unstressed venous volume; HR, heart rate; LVP, left ventricular pressure; PF, pump flow. The contractility is expressed as a percentage of the healthy heart value.

Experiment	Scenario	Time [s]	SVR [mmHg/s/mL]	PVR [mmHg/s/mL]	UVV [ml]	HR [bpm]	Contractility [%]	Noise LVP	Noise PF
Exp0	Rest	[0 200]	1.11	0.1	2520	60	34	0	0
Exp1	Preload variation	[0, 35, 40, 55, 65, 200]	1.11	0.1	[2520, 2520, 2270, 2270, 2720, 2720]	90	34	0	0
Exp2	Afterload variation	[0, 35, 40, 55, 65, 200]	[1.11, 1.11, 0.51, 0.51, 1.91, 1.19]	0.1	2520	90	34	0	0
Exp3	Sleep to wake	[0, 35, 40, 200]	[1.65, 1.65, 1.11, 1.11]	0.1	[2740, 2740, 2520, 2520]	90	34	0	0
Exp4	Contractility variation	[0, 50, 100, 150, 200]	1.11	0.1	2520	90	[34, 34, 51, 51, 17]	0	0
Exp5	Rest to exercise	[0, 35, 40, 200]	[0.98, 0.98, 0.5, 0.5]	[0.08, 0.08, 0.03, 0.03]	[2520, 2520, 2020, 2020]	[60 60 80 80]	34	0	0

**Supplemental Table B2.** Parameter sets of the experiments used in this Work. SVR, systemic vascular resistance; PVR, pulmonary vascular resistance; UVV, unstressed venous volume; HR, heart rate; LVP, left ventricular pressure; PF, pump flow. The contractility is expressed as a percentage of the healthy heart value.

Experiment	Scenario	Time [s]	SVR [mmHg/s/mL]	PVR [mmHg/s/mL]	UVV [ml]	HR [bpm]	Contractility [%]	Noise LVP	Noise PF
Exp0n	Rest	[0 200]	1.11	0.1	2520	60	34	0.86	0.86
Exp1n	Preload variation	[0, 35, 40, 55, 65, 200]	1.11	0.1	[2520, 2520, 2270, 2270, 2720, 2720]	90	34	0.86	0.86
Exp2n	Afterload variation	[0, 35, 40, 55, 65, 200]	[1.11, 1.11, 0.51, 0.51, 1.91, 1.19]	0.1	2520	90	34	0.86	0.86
Exp3n	Sleep to wake	[0, 35, 40, 200]	[1.65, 1.65, 1.11, 1.11]	0.1	[2740, 2740, 2520, 2520]	90	34	0.86	0.86
Exp4n	Contractility variation	[0, 50, 100, 150, 200]	1.11	0.1	2520	90	[34, 34, 51, 51, 17]	0.86	0.86
Exp5n	Rest to exercise	[0, 35, 40, 200]	[0.98, 0.98, 0.5, 0.5]	[0.08, 0.08, 0.03, 0.03]	[2520, 2520, 2020, 2020]	[60 60 80 80]	34	0.86	0.86

**Supplemental Table B3.** Parameter sets of the experiments used in this Work. SVR, systemic vascular resistance; PVR, pulmonary vascular resistance; UVV, unstressed venous volume; HR, heart rate; LVP, left ventricular pressure; PF, pump flow. The contractility is expressed as a percentage of the healthy heart value.

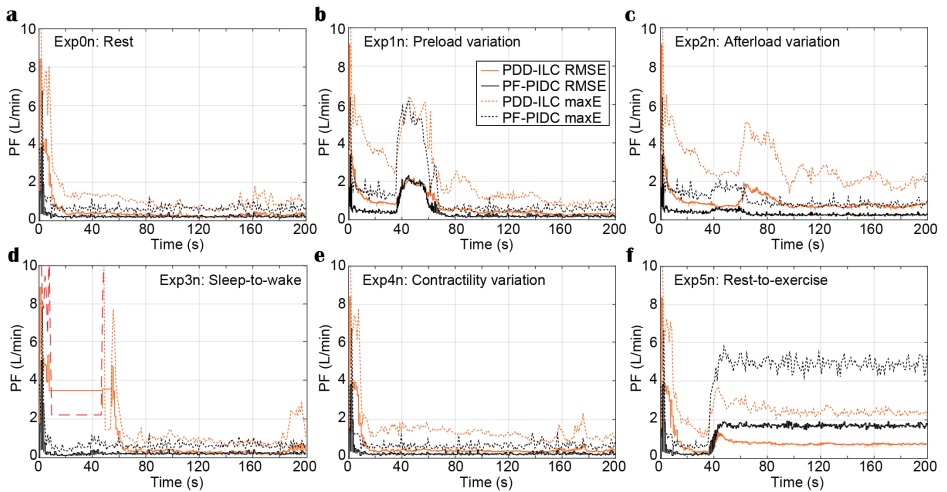
Experiment	Scenario	Time [s]	SVR [mmHg/mL]	PVR [mmHg/mL]	UVV [ml]	HR [bpm]	Contractility [%]	Noise LVP	Noise PF
Exp0nn	Rest	[0 200]	1.11	0.1	2520	60	34	1.72	1.72
Exp1nn	Preload variation	[0, 35, 40, 55, 65, 200]	1.11	0.1	[2520, 2520, 2270, 2270, 2720, 2720]	90	34	1.72	1.72
Exp2nn	Afterload variation	[0, 35, 40, 55, 65, 200]	[1.11, 1.11, 0.51, 0.51, 1.91, 1.19]	0.1	2520	90	34	1.72	1.72
Exp3nn	Sleep to wake	[0, 35, 40, 200]	[1.65, 1.65, 1.11, 1.11]	0.1	[2740, 2740, 2520, 2520]	90	34	1.72	1.72
Exp4nn	Contractility variation	[0, 50, 100, 150, 200]	1.11	0.1	2520	90	[34, 34, 51, 51, 17]	1.72	1.72
Exp5nn	Rest to exercise	[0, 35, 40, 200]	[0.98, 0.98, 0.5, 0.5]	[0.08, 0.08, 0.03, 0.03]	[2520, 2520, 2020, 2020]	[60 60 80 80]	34	1.72	1.72



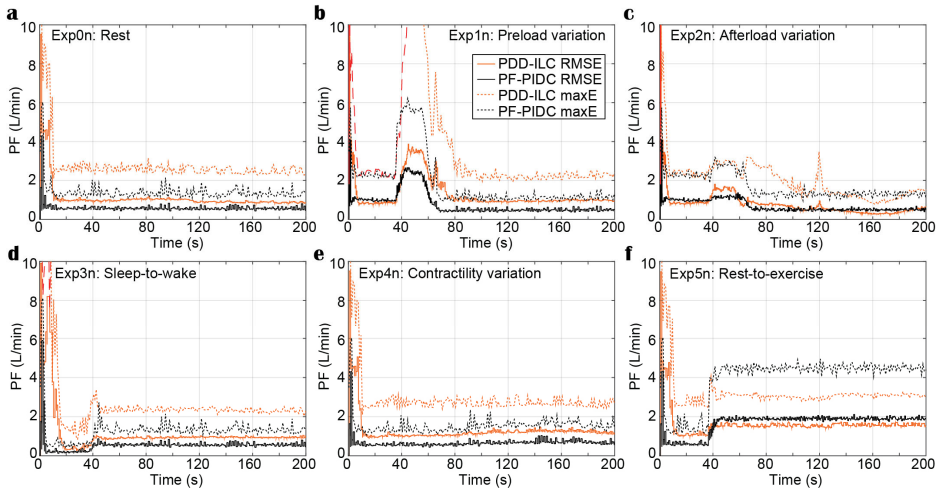
**Supplemental Table B4.** Upper and lower limits of the control parameters of the PDD-ILC and the PF-PIDC used in the minimization problem of the genetic algorithm-based optimization framework.

PDD-ILC			PF-PIDC		
Parameter	Minimum	Maximum	Parameter	Minimum	Maximum
$\mu$	0	2	$K_p$	0	1000
$\eta$	0	1	$K_I$	0	100
$Q$	0	600	$K_D$	0	100
$R$	0	1			
$k_p$	0	7			
$k_d$	0	7			

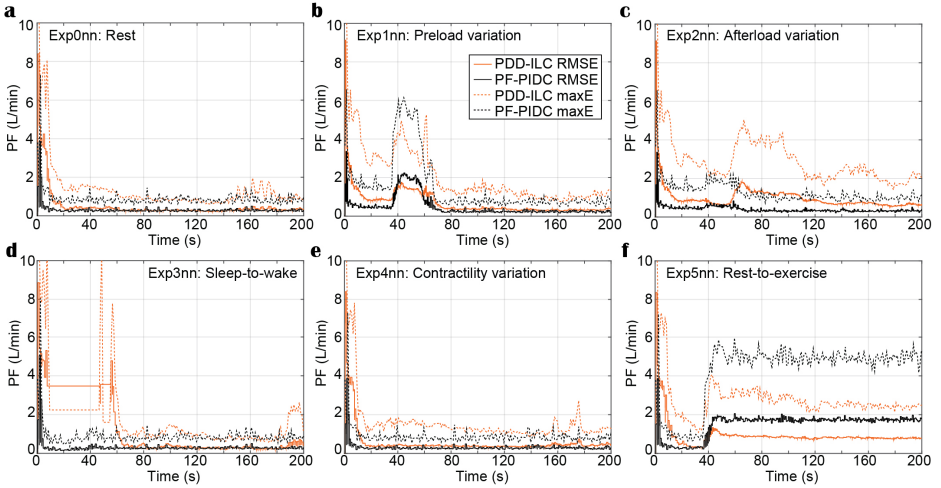
## Supplemental figures



**Supplemental Figure B1.** Transient performance of the PDD-ILC and the PFPIDC in terms of RMSE and maximum instantaneous error in tracking the reference trajectory under all physiological conditions and scenarios executed with the copulation mode and white noise of 0.86 variance added on the left ventricular pressure and pump flow signals. **a)** Rest-conditions (Exp0n) **b)** Preload variation (Exp1n) **c)** Afterload variation (Exp2n) **d)** Sleep-to-wake (Exp3n) **e)** Contractility variation (Exp4n) **f)** Rest-to-exercise (Exp5n). *RMSE*, root mean square error; *maxE*, maximum error; *PDD-ILC*, physiologic data-driven iterative learning controller; *PF-PIDC*, pump flow proportional-integrative-derivative controller.

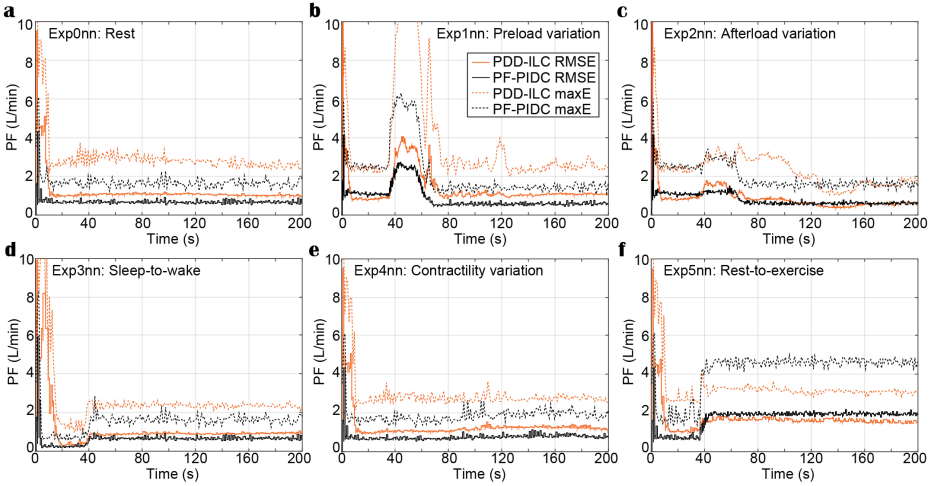


**Supplemental Figure B2.** Transient performance of the PDD-ILC and the PFPIDC in terms of RMSE and maximum instantaneous error in tracking the reference trajectory under all physiological conditions and scenarios executed with the counterpulsation mode and white noise of 0.86 variance added on the left ventricular pressure and pump flow signals. **a)** Rest-conditions (Exp0n) **b)** Preload variation (Exp1n) **c)** Afterload variation (Exp2n) **d)** Sleep-to-wake (Exp3n) **e)** Contractility variation (Exp4n) **f)** Rest-to-exercise (Exp5n). *RMSE*, root mean square error; *maxE*, maximum error; *PDD-ILC*, physiologic data-driven iterative learning controller; *PF-PIDC*, pump flow proportional-integrative-derivative controller.



**Supplemental Figure B3.** Transient performance of the PDD-ILC and the PFPIDC in terms of RMSE and maximum instantaneous error in tracking the reference trajectory under all physiological conditions and scenarios executed with the copulation mode and white noise of 1.72 variance added on the left ventricular pressure and pump flow signals. **a)** Rest-conditions (Exp0n) **b)** Preload variation (Exp1n) **c)** Afterload variation (Exp2n) **d)** Sleep-to-wake (Exp3n) **e)** Contractility variation (Exp4n) **f)** Rest-to-exercise (Exp5n). *RMSE*, root mean square error; *maxE*, maximum error; *PDD-ILC*, physiologic data-driven iterative learning controller; *PF-PIDC*, pump flow proportional-integrative-derivative controller.





**Supplemental Figure B4.** Transient performance of the PDD-ILC and the PFPIDC in terms of RMSE and maximum instantaneous error in tracking the reference trajectory under all physiological conditions and scenarios executed with the counterpulsation mode and white noise of 1.72 variance added on the left ventricular pressure and pump flow signals. **a)** Rest-conditions (Exp0n) **b)** Preload variation (Exp1n) **c)** Afterload variation (Exp2n) **d)** Sleep-to-wake (Exp3n) **e)** Contractility variation (Exp4n) **f)** Rest-to-exercise (Exp5n). *RMSE*, root mean square error; *maxE*, maximum error; *PDD-ILC*, physiologic data-driven iterative learning controller; *PF-PIDC*, pump flow proportional-integrative-derivative controller.

## C. Genetic Algorithm-Based Optimization Framework for Control Parameters of Ventricular Assist Devices

### Appendix C1. Numerical model of Deltastream

The numerical model of the Deltastream (Deltastream DP2, Medos Medizintechnik AG, Stolberg, Germany)VAD was retrieved from the work of Amacher et al.<sup>160</sup> In this model, the pressure upstream ( $p_{us}$ ) and downstream ( $p_{ds}$ ) of the pump, the fluid inertance ( $L$ ), the rotor inertia ( $\theta$ ), the current of the pump ( $I$ ), the torque-constant of the pump motor ( $k$ ), as well as the two-dimensional matrices of the pressure across the pump ( $H$ ) and the hydraulic torque applied on the shaft ( $T$ ) are used to define the fluid and rotor acceleration by computing the following differential equations:

$$\frac{dQ}{dt} = \frac{1}{L} \left( H(Q(t), \omega(t)) - (p_{ds}(t) - p_{us}(t)) \right) \quad S3.1$$

$$\frac{d\omega}{dt} = \frac{1}{\theta} \left( -T(Q(t), \omega(t)) + k \cdot I(t) \right) \quad S3.2$$

with  $Q$  and  $\omega$  being the flowrate and the rotational speed of the pump. The values of the constants used in S3.1 and S3.2 were retrieved from Amacher et al.<sup>160</sup>

### Appendix C2. Numerical model of HeartMate 3

The mathematical representation of the state-of-the-art HeartMate 3 pump (HM3, Abbott, Abbott Park, IL, USA) was developed based on the universal hydraulic model for blood pumps described by Boës et al.<sup>183</sup> This model, exploits turbomachinery principles to enable the estimation of the pump flow rate based on the head pressure across the pump ( $H$ ) and the rotational speed of the pump ( $\omega$ ), while it accounts for frictional and incidence losses, part-load recirculation, and fluid inertia. More precisely, the discretized estimate of the pump flow ( $Q_{est}$ ) is given by:

$$Q_{est}(k+1) = Q_{est}(k) + \frac{T_s}{L} \left( \alpha \omega^2 - R_1 \omega Q_{est}(k) - R_2 Q_{est}^2(k) - H(k) \right) + \begin{cases} 0, & Q_{est}(k) > q_{inf} \\ R_{rec} (Q_{est} - q_{inf})^2, & Q_{est}(k) < q_{inf} \end{cases} \quad S3.3$$

where  $k$  ranges from 1 to the number of samples acquired minus 1 and  $T_s$  is the sampling time.

The values of the constants  $L$ ,  $\alpha$ ,  $R_1$ ,  $R_2$ ,  $R_{rec}$  and  $q_{inf}$  were retrieved from Boës et al.<sup>183</sup>.

### **Appendix C3. Numerical model of the cardiovascular system**

In the present study, a numerical model of the cardiovascular system (CVS) was employed to imitate both physiological and pathological conditions of the human heart. The model, which was obtained from Colacino et al.<sup>67</sup>, and was implemented in MATLAB/Simulink as described by Ochsner et al.<sup>53</sup>, is detailed in these sources. The subsystems of the numerical CVS are represented using lumped parameter models, and their electrical analogs utilized to implement and solve the corresponding differential equations are depicted in Supplementary Figure C7. The model encompasses both systemic and pulmonary circulations, which are modeled using five-element Windkessel models for the arterial systems and classic Windkessel models for the venous systems. The pressure in the arterial systems is regulated through a baroreflex mechanism, while the unstressed volume of the systemic veins is regulated by cardiac output autoregulation, and the resistance of the systemic veins is adapted through Rsv autoregulation. The contracting heart, which is comprised of two active atria and two active ventricles, is modeled based on the principle of time-varying elastance. An extension to the model described by Ochsner et al.<sup>182</sup> allows also the simulation of ventricular suction.



## Supplemental Tables

**Supplemental Table C1.** Parameter sets of the experiments used in the study. SVR, systemic vascular resistance; PVR, pulmonary vascular resistance; UVV, unstressed venous volume; HR, heart rate; LVP, left ventricular pressure; PF, pump flow. The contractility is expressed as a percentage of the healthy heart value.

Experiment	Scenario	Time (s)	SVR (mmHg/s/mL)	PVR (mmHg/s/mL)	UVV (ml)	HR (bpm)	Contractility (%)	Noise LVP (-)	Noise PF (-)
Exp0	Rest	[0 200]	1.11	0.1	2520	60	34	0	0
Exp1	Preload variation	[0, 35, 40, 55, 65, 200]	1.11	0.1	[2520, 2520, 2270, 2270, 2720, 2720]	90	34	0	0
Exp2	Afterload variation	[0, 35, 40, 55, 65, 200]	[1.11, 1.11, 0.51, 0.51, 1.91, 1.19]	0.1	2520	90	34	0	0
Exp3	Sleep to wake	[0, 35, 40, 200]	[1.65, 1.65, 1.11, 1.11]	0.1	[2740, 2740, 2520, 2520]	90	34	0	0

Exp4	Contractility variation	[0, 50, 100, 150, 200]	1.11	0.1	2520	90	[34, 34, 51, 51, 17]	0	0
Exp5	Rest to exercise	[0, 35, 40, 200]	[0.98, 0.98, 0.5, 0.5]	[0.08, 0.08, 0.03, 0.03]	[2520, 2520, 2020, 2020]	[60, 60, 80, 80]	34	0	0

**Supplemental Table C2.** Weighting factors for each dynamic experiment that aim to increase the influence of the experiments that the patient encounters more frequently in the everyday life in the optimization process. The subscript numbers correspond to the number of the dynamic experiments described in Table C1. *so*, single objective; *mo*, multi-objective.

Parameter	1DOF-PID <sub>so</sub>	1DOF-PID <sub>mo</sub>	2DOF-PID <sub>so</sub>	2DOF-PID <sub>mo</sub>	PDD-ILC
$b_0$	-	-	-	-	0.2
$b_1$	-	-	-	-	0.2
$b_2$	0.4	0.4	0.4	0.4	0.15
$b_3$	0.3	0.3	0.3	0.3	0.15
$b_4$	0.15	0.15	0.15	0.15	0.15
$b_5$	0.15	0.15	0.15	0.15	0.15

**Supplemental Table C3.** Constraint values for the control parameters of each controller and optimization problem. *so*, single objective; *mo*, multi-objective.

1DOF-PID <sub>so,mo</sub>	2DOF-PID <sub>so,mo</sub>	PDD-ILC
$0 \leq K_p \leq 600$	$0 \leq K_{p,p} \leq 600$	$0 \leq \mu \leq 2$
$0 \leq K_I \leq 600$	$0 \leq K_{I,p} \leq 600$	$0 \leq \eta \leq 1$
$0 \leq K_D \leq 600$	$0 \leq K_{D,p} \leq 600$	$0 \leq Q \leq 600$
	$-100 \leq K_{p,a} \leq 100$	$0 \leq R \leq 1$
	$-100 \leq K_{D,a} \leq 100$	$0 \leq k_p \leq 7$
		$0 \leq k_D \leq 7$

**Supplemental Table C4.** Patient-specific parameters for the generation of artificial patients suffering from high blood pressure (HBP). *CVS*, cardiovascular system.

Manipulated CVS Parameter	Severity						
	Initial Value	Low (HBP <sub>L</sub> )		Mild (HBP <sub>M</sub> )		High (HBP <sub>H</sub> )	
		Value	% of change	Value	% of change	Value	% of change
Aortic valve resistance (mmHg·s/mL)	0.01935	0.02129	10	0.02903	50	0.03871	100
Aortic valve inertance (mmHg·s <sup>2</sup> /mL)	0.00042	0.00046	10	0.00057	35	0.00072	70
Mitral valve resistance (mmHg·s/mL)	0.00750	0.00825	10	0.01126	50	0.01501	100
Mitral valve inertance (mmHg·s <sup>2</sup> /mL)	0.00056	0.0006	10	0.00067	20	0.00073	30



**Supplemental Table C5.** Patient-specific parameters for the generation of artificial patients suffering from Aortic and mitral valve stenosis (HVS). *CVS, cardiovascular system.*

Manipulated CVS Parameter	Severity						
	Initial Value	Low (HVS <sub>L</sub> )		Mild (HVS <sub>M</sub> )		High (HVS <sub>H</sub> )	
		Value	% of change	Value	% of change	Value	% of change
Systemic arterial resistance (mmHg·s/mL)	0.11650	0.12815	10	0.17475	50	0.23300	100
Systemic arterial inertance (mmHg·s <sup>2</sup> /mL)	0.05015	0.05516	10	0.07522	50	0.10030	100
Arterial compliance (mL/mmHg)	0.95166	0.85650	-10	0.47583	-50	0.19033	-80
Systemic arterial compliance (mL/mmHg)	0.77200	0.69480	-10	0.38600	-50	0.15440	-80

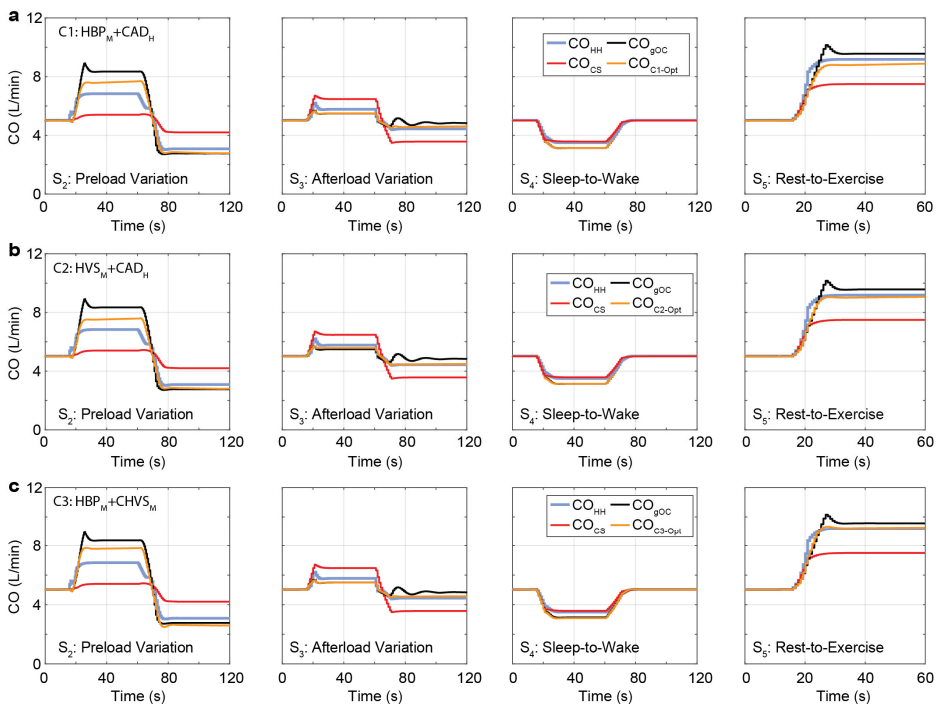
**Supplemental Table C6.** Patient-specific parameters for the generation of artificial patients suffering from Aortic and mitral valve stenosis (HVS). *CVS, cardiovascular system.*

Manipulated CVS Parameter	Severity						
	Initial Value	Low (CAD <sub>L</sub> )		Mild (CAD <sub>M</sub> )		High (CAD <sub>H</sub> )	
		Value	% of change	Value	% of change	Value	% of change
Contractility (-)	1.0	0.45	-55	0.35	-65	0.25	-75

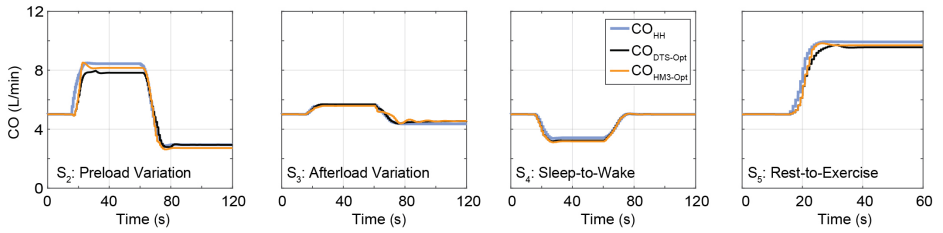
**Supplemental Table C7.** Disease-specific cases generated by combining high blood pressure (HBP), heart valve insufficiency (HVI) and the coronary artery disease (CAD). *CVS, cardiovascular system.*

<b>Cases</b>	<b>Combined diseases</b>
<b>C1</b>	Medium severity HBP and high severity CAD ( $HBP_M + CAD_H$ )
<b>C2</b>	Medium severity HVS and high severity CAD ( $HVS_M + CAD_H$ )
<b>C3</b>	Medium severity HBP and medium severity HVS ( $HBP_M + HVS_M$ )

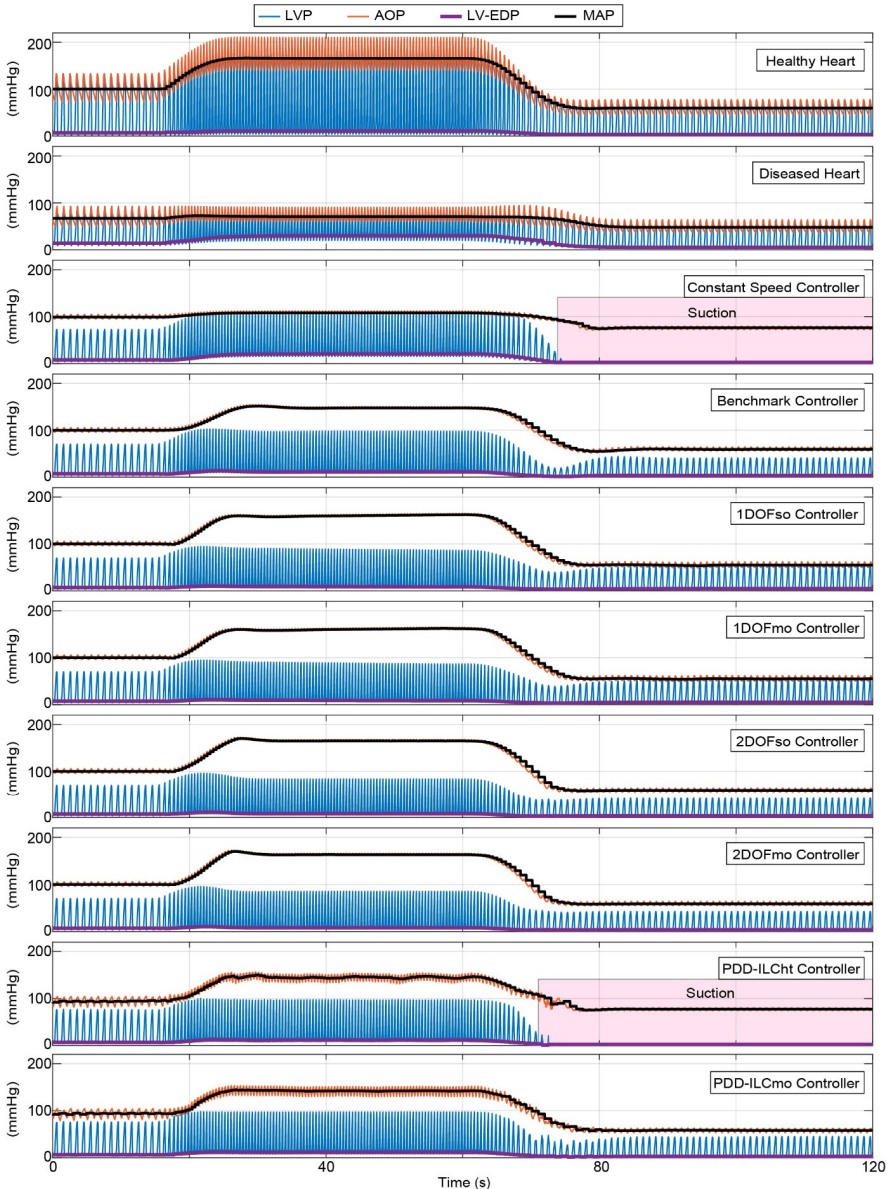
## Supplemental Figures



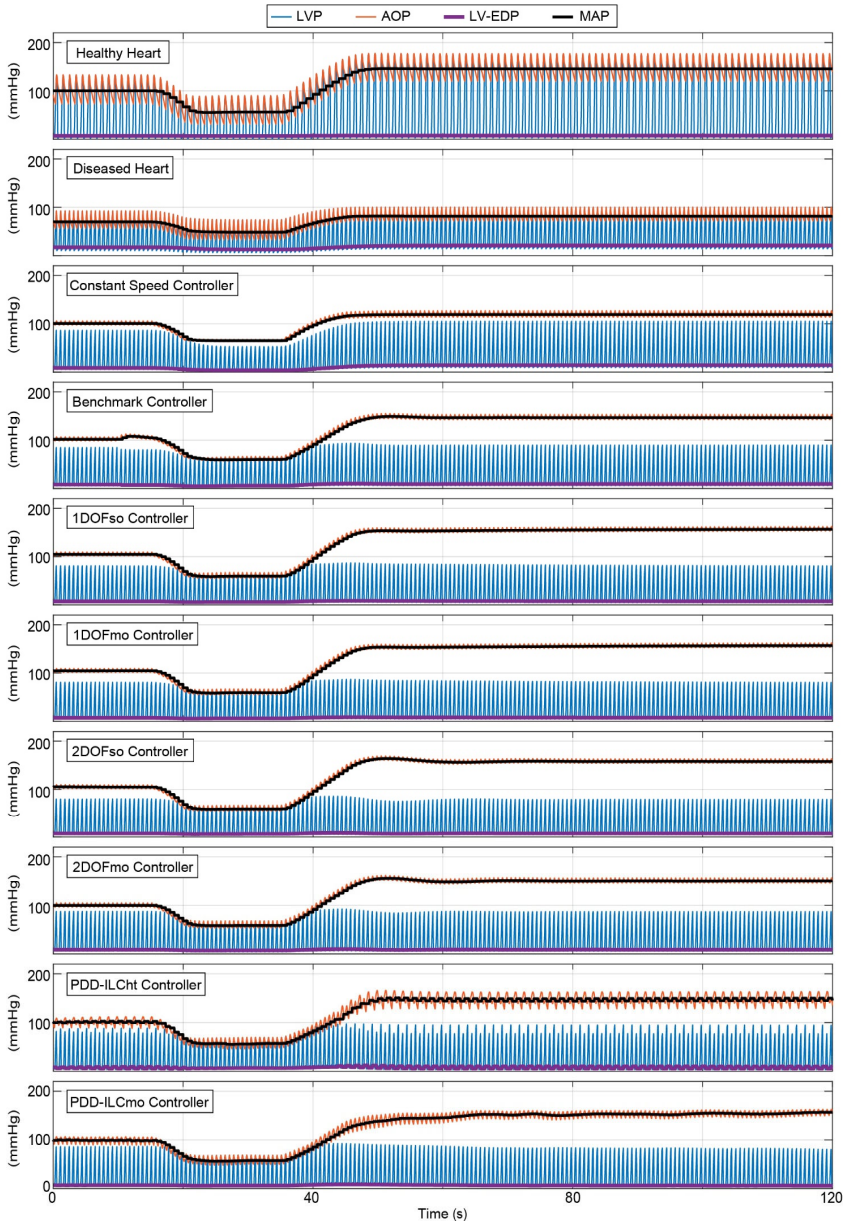
**Supplemental Figure C1.** Comparison of the performance of the 2DOF-PID controller optimized for the specific disease case with the performance of the generic optimized 2DOF-PID controller (gOC), the constant speed controller (CS), and the response of the healthy heart (HH) during the dynamic experiments  $S_2 - S_5$ . A) Disease case C1, where medium severity HBP and high severity CAD is simulated. B) Disease case C2, where medium severity HVS and high severity CAD is simulated. C) Disease case C3, where medium severity HBP and medium severity HVS is simulated. *HH*, healthy heart; *CS*, constant speed control; *C1-Opt*, controller optimized for the disease case C1; *C2-Opt*, controller optimized for the disease case C2; *C3-Opt*, controller optimized for the disease case C3; *gOC*, generic optimized controller; *HBP*, high blood pressure; *HVS*, heart valve insufficiency; *CAD*, coronary artery disease.



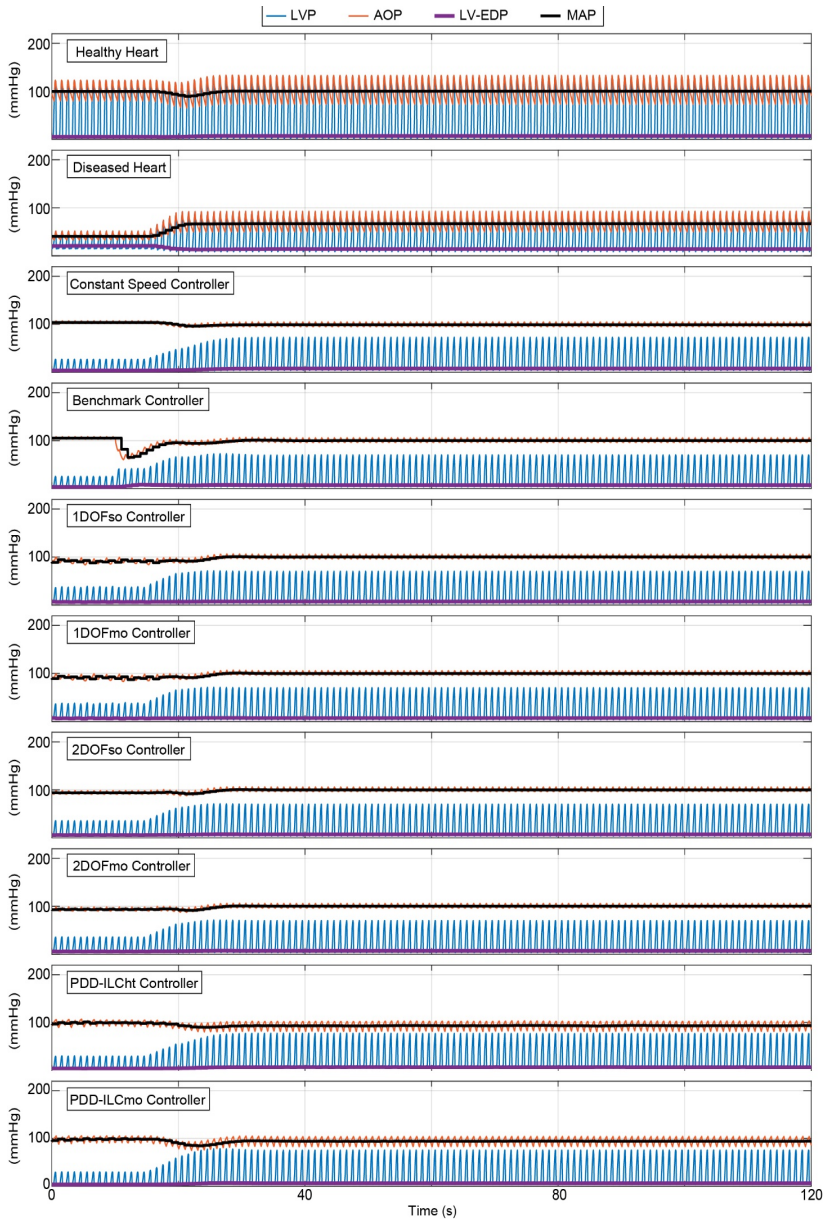
**Supplemental Figure C2.** Evaluation of the performance of the 2DOF-PID controller optimized for the Deltastream and the Heartmate 3 VAD models, when it is implemented to control the Heartmate 3 VAD. The performance is assessed against the physiological response of a healthy heart during the dynamic experiments  $S_2 - S_5$ .



**Supplemental Figure C3.** Assessment of the hemodynamic performance of the healthy heart, the diseased heart, and the controllers developed and optimized during the dynamic experiments of preload variation ( $S_2$ ). The constant speed controller and the hand tuned PDD-ILC present suction event ( $LVP < 0$  mmHg) during low preload conditions. *LVP*, left ventricular pressure; *AOP*, aortic pressure; *LV-EDP*, left ventricular end-diastolic pressure; *MAP*, mean aortic pressure; *so*, single-objective optimization; *mo*, multi-objective optimization; *ht*, hand-tuned.

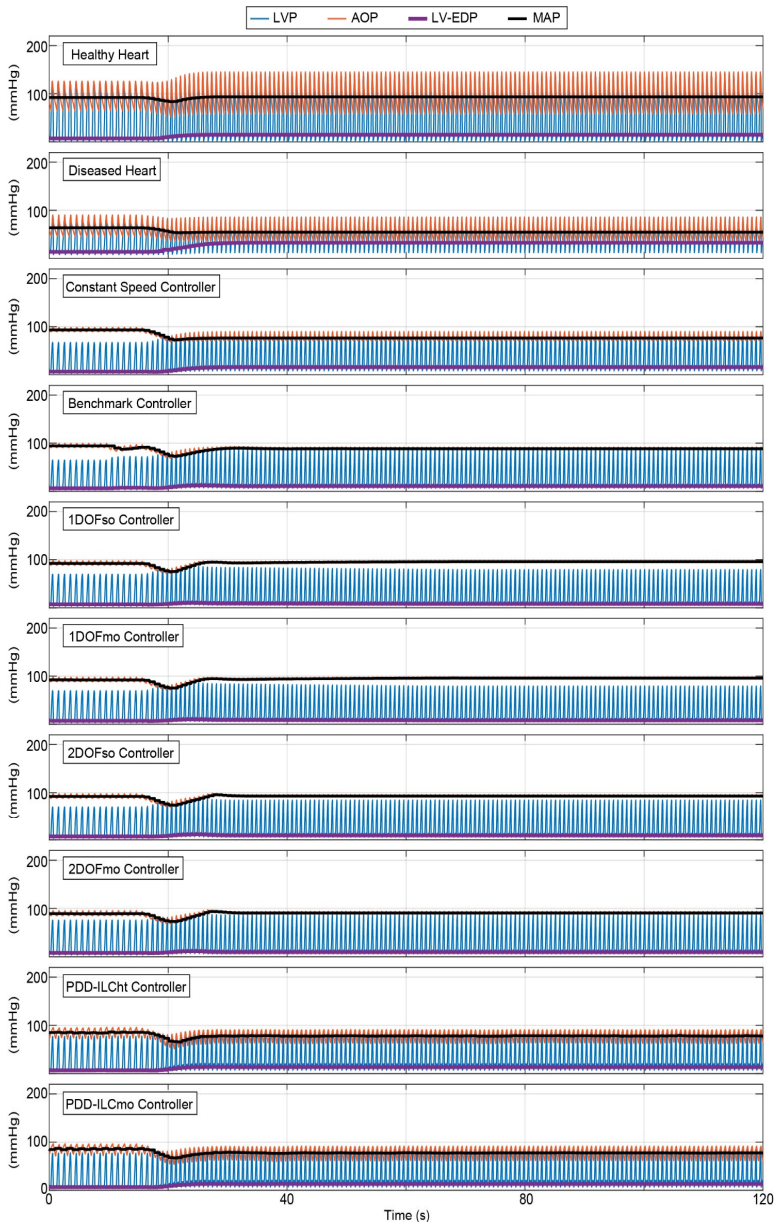


**Supplemental Figure C4.** Assessment of the hemodynamic performance of the healthy heart, the diseased heart, and the controllers developed and optimized during the dynamic experiments of afterload variation ( $\mathcal{S}_3$ ). *LVP*, left ventricular pressure; *AOP*, aortic pressure; *LV-EDP*, left ventricular end-diastolic pressure; *MAP*, mean aortic pressure; *so*, single-objective optimization; *mo*, multi-objective optimization; *ht*, hand-tuned.



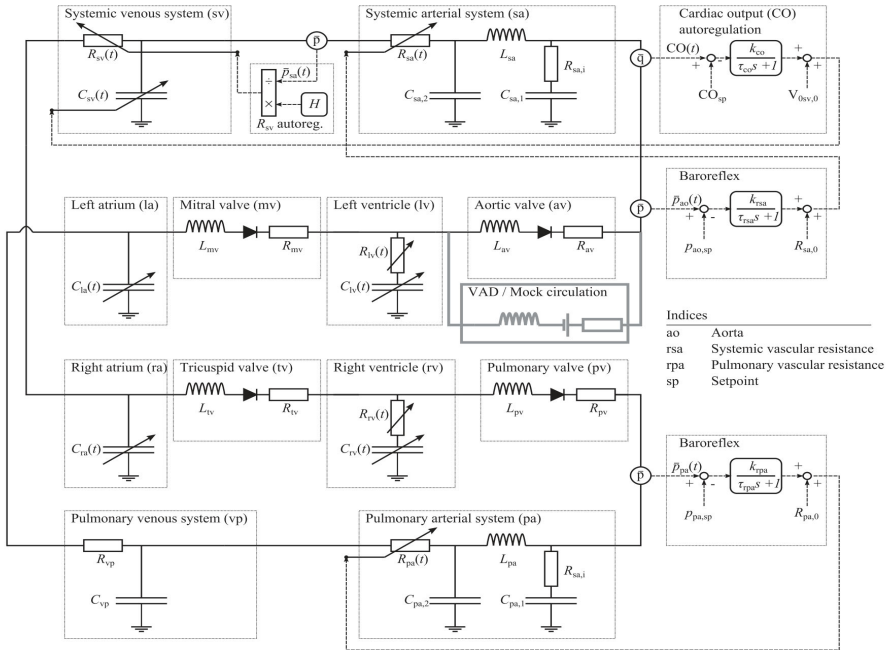
**Supplemental Figure C5.** Assessment of the hemodynamic performance of the healthy heart, the diseased heart, and the controllers developed and optimized during the dynamic experiments of sleep-to-wake scenario ( $S_4$ ). *LVP*, left ventricular pressure; *AOP*, aortic pressure; *LV-EDP*, left ventricular end-diastolic pressure; *MAP*, mean aortic pressure; *so*, single-objective optimization; *mo*, multi-objective optimization; *ht*, hand-tuned.





**Supplemental Figure C6.** Assessment of the hemodynamic performance of the healthy heart, the diseased heart, and the controllers developed and optimized during the dynamic experiments of rest-to exercise scenario ( $S_5$ ). *LVP*, left ventricular pressure; *AOP*, aortic pressure; *LV-EDP*, left ventricular end-diastolic pressure; *MAP*, mean aortic pressure; *so*, single-objective optimization; *mo*, multi-objective optimization; *ht*, hand-tuned





**Supplemental Figure C6.** The electrical analog of the numerical circulation model is depicted in this figure, with the inclusion of the VAD circulation block to demonstrate the interface between the two numerical models. Detailed description and validation of the model can be found in reference.<sup>67</sup>



## ***Bibliography***

1. European Society of Cardiology. *ESC Cardiovascular Realities 2020*. (2020).
2. European Society of Cardiology. *ESC Cardiovascular Realities 2022*. (2022).
3. Roth, G. A. *et al.* Global Burden of Cardiovascular Diseases and Risk Factors, 1990-2019: Update From the GBD 2019 Study. *J. Am. Coll. Cardiol.* **76**, 2982–3021 (2020).
4. Tsao, C. W. *et al.* Heart Disease and Stroke Statistics—2022 Update: A Report From the American Heart Association. *Circulation* **145**, E153–E639 (2022).
5. American Heart Association. *2022 Heart Disease & Stroke Statistical Update Fact Sheet Global Burden of Disease High Blood Cholesterol and Other Lipids*. (2022).
6. Groenewegen, A., Rutten, F. H., Mosterd, A. & Hoes, A. W. Epidemiology of heart failure. *Eur. J. Heart Fail.* **22**, 1342–1356 (2020).
7. Ranek, M. J. *et al.* Pathophysiology of heart failure and an overview of therapies. in *Cardiovascular Pathology* 149–221 (Elsevier, 2022). doi:10.1016/B978-0-12-822224-9.00025-6
8. Friedrich, E. B. & Böhm, M. Treatment of Chronic Heart Failure. *US Cardiol. Rev.* **3**, 90–92 (2006).
9. McDonagh, T. A. *et al.* 2021 ESC Guidelines for the diagnosis and treatment of acute and chronic heart failure. *Eur. Heart J.* **42**, 3599–3726 (2021).
10. Hsu, S., Fang, J. C. & Borlaug, B. A. Hemodynamics for the Heart Failure Clinician: A State-of-the-Art Review. *J. Card. Fail.* **28**, 133–148 (2022).
11. Alexy, T., Lebeis, T. & Cole, R. Heart failure with reduced ejection fraction. *Nat. Rev. Dis. Prim.* **3**, 17059 (2017).
12. Mascolo, A. *et al.* Current and future therapeutic perspective in chronic heart failure. *Pharmacol. Res.* **175**, 106035 (2022).
13. Bloom, M. W. *et al.* Heart failure with reduced ejection fraction. *Nat. Rev. Dis. Prim.* **3**, 17058 (2017).
14. Castiglione, V. *et al.* Biomarkers for the diagnosis and management of heart failure. *Heart Fail. Rev.* **27**, 625–643 (2022).
15. AlOmari, A.-H. H. *et al.* Developments in control systems for rotary left ventricular assist devices for heart failure patients: a review. *Physiol. Meas.*

34, R1–R27 (2013).

16. Khush, K. K. *et al.* The International Thoracic Organ Transplant Registry of the International Society for Heart and Lung Transplantation: Thirty-eighth adult heart transplantation report — 2021; Focus on recipient characteristics. *J. Hear. Lung Transplant.* **40**, 1035–1049 (2021).
17. Mallidi, H. R., Anand, J. & Cohn, W. E. State of the Art of Mechanical Circulatory Support. *Texas Hear. Inst. J.* **41**, 115–120 (2014).
18. Khush, K. K. *et al.* The International Thoracic Organ Transplant Registry of the International Society for Heart and Lung Transplantation: Thirty-sixth adult heart transplantation report — 2019; focus theme: Donor and recipient size match. *J. Hear. Lung Transplant.* **38**, 1056–1066 (2019).
19. McLarty, A. Mechanical Circulatory Support and the Role of LVADs in Heart Failure Therapy. *Clin. Med. Insights Cardiol.* **9s2**, CMC.S19694 (2015).
20. Kirklin, J. K. *et al.* First Annual IMACS Report: A global International Society for Heart and Lung Transplantation Registry for Mechanical Circulatory Support. *J. Hear. Lung Transplant.* **35**, 407–412 (2016).
21. Kirklin, J. K. *et al.* Eighth annual INTERMACS report: Special focus on framing the impact of adverse events. *J. Hear. Lung Transplant.* **36**, 1080–1086 (2017).
22. Theochari, C. A. *et al.* Heart transplantation versus left ventricular assist devices as destination therapy or bridge to transplantation for 1-year mortality: a systematic review and meta-analysis. *Ann. Cardiothorac. Surg.* **7**, 3–11 (2018).
23. McKellar, S. *A History of Mechanical Circulatory Support. Mechanical Support for Heart Failure* (2020). doi:10.1177/175114371301400309
24. Drakos, S. G. The Odyssey of Chronic Cardiac Mechanical Support. *J. Am. Coll. Cardiol.* **63**, 1758–1760 (2014).
25. Schmid Daners, M. *et al.* Left Ventricular Assist Devices: Challenges Toward Sustaining Long-Term Patient Care. *Ann. Biomed. Eng.* **45**, 1836–1851 (2017).
26. Thunberg, C. A., Gaitan, B. D., Arabia, F. A., Cole, D. J. & Grigore, A. M. Ventricular Assist Devices Today and Tomorrow. *J. Cardiothorac. Vasc. Anesth.* **24**, 656–680 (2010).
27. Graefe, R. & Groß-Hardt, S. *Second-generation ventricular assist devices. Mechanical Circulatory and Respiratory Support* (Elsevier Inc., 2020). doi:10.1016/B978-0-12-810491-0.00005-9

28. Wu, W.-T. *et al.* High fidelity computational simulation of thrombus formation in Thoratec HeartMate II continuous flow ventricular assist device. *Sci. Rep.* **6**, 38025 (2016).
29. Han, J. J., Acker, M. A. & Atluri, P. Left ventricular assist devices synergistic model between technology and medicine. *Circulation* **138**, 2841–2851 (2018).
30. Foster, G. *Third-generation ventricular assist devices. Mechanical Circulatory and Respiratory Support* (Elsevier Inc., 2020). doi:10.1016/B978-0-12-810491-0.00005-9
31. Molina, E. J. *et al.* The Society of Thoracic Surgeons Intermacs 2020 Annual Report. *Ann. Thorac. Surg.* **111**, 778–792 (2021).
32. Pagani, F. D. *et al.* Concordance of Treatment Effect: An Analysis of The Society of Thoracic Surgeons Intermacs Database. *Ann. Thorac. Surg.* **113**, 1172–1182 (2022).
33. Wasilewski, G. *et al.* Outcomes in Patients With HeartMate3 Versus HeartWare Ventricular Assist Device Implanted as Destination Therapy. *Transplant. Proc.* **54**, 1049–1053 (2022).
34. Fang, P. *et al.* Insights Into the Low Rate of In-Pump Thrombosis With the HeartMate 3: Does the Artificial Pulse Improve Washout? *Front. Cardiovasc. Med.* **9**, 1–13 (2022).
35. Netuka, I. *et al.* Surrounding Advanced Heart Failure: The Role of the Latest Left Ventricular Assist Devices - European Medical Journal. 12–18 (2020).
36. Jorde, U. P. *et al.* Results of the Destination Therapy Post-Food and Drug Administration Approval Study With a Continuous Flow Left Ventricular Assist Device. *J. Am. Coll. Cardiol.* **63**, 1751–1757 (2014).
37. Sidhu, K., Lam, P. H. & Mehra, M. R. Evolving trends in mechanical circulatory support: Clinical development of a fully magnetically levitated durable ventricular assist device. *Trends Cardiovasc. Med.* **30**, 223–229 (2020).
38. Witman, M. A. H. *et al.* Further Peripheral Vascular Dysfunction in Heart Failure Patients With a Continuous-Flow Left Ventricular Assist Device: The Role of Pulsatility. *JACC Hear. Fail.* **3**, 703–711 (2015).
39. Sathianathan, S., Bhat, G. & Dowling, R. Vasoplegia from Continuous Flow Left Ventricular Assist Devices. *Curr. Cardiol. Rep.* **23**, 101 (2021).
40. Ivak, P., Netuka, I., Kralova-Lesna, I., Wohlfahrt, P. & Pitha, J. Changes in circulating stem cells and endothelial progenitor cells over a 12-month period after implantation of a continuous-flow left ventricular assist device. *Arch. Med. Sci.* **16**, 1440–1443 (2020).

41. Wever-Pinzon, O. *et al.* Pulsatility and the Risk of Nonsurgical Bleeding in Patients Supported With the Continuous-Flow Left Ventricular Assist Device HeartMate II. *Circ. Hear. Fail.* **6**, 517–526 (2013).
42. Kirklin, J. K. *et al.* Seventh INTERMACS annual report: 15,000 patients and counting. *J. Hear. Lung Transplant.* **34**, 1495–1504 (2015).
43. Bozkurt, S. Physiologic outcome of varying speed rotary blood pump support algorithms: a review study. *Australas. Phys. Eng. Sci. Med.* **39**, 13–28 (2016).
44. Hall, J. E. & Guyon, A. C. *Guyton and HALL Textbook of Medical Physiology*. doi:978-0-8089-2400-5
45. Tchoukina, I., Smallfield, M. C. & Shah, K. B. Device Management and Flow Optimization on Left Ventricular Assist Device Support. *Crit. Care Clin.* **34**, 453–463 (2018).
46. Salamonsen, R. F., Mason, D. G. & Ayre, P. J. Response of Rotary Blood Pumps to Changes in Preload and Afterload at a Fixed Speed Setting Are Unphysiological When Compared With the Natural Heart. *Artif. Organs* **35**, E47–E53 (2011).
47. Fukamachi, K. *et al.* Preload Sensitivity in Cardiac Assist Devices. *Ann. Thorac. Surg.* **95**, 373–380 (2013).
48. Stevens, M. C., Stephens, A., AlOmari, A.-H. H. & Moscato, F. Physiological control. in *Mechanical Circulatory and Respiratory Support* 627–657 (Elsevier, 2018). doi:10.1016/B978-0-12-810491-0.00020-5
49. Schmid Daners, M. & Dual, S. A. *Mechanical Support for Heart Failure. Pathophysiological Determinants Relevant in Blood Pump Control* (Springer International Publishing, 2020). doi:10.1007/978-3-030-47809-4
50. Schima, H. *et al.* Noninvasive Monitoring of Rotary Blood Pumps: Necessity, Possibilities, and Limitations. *Artif. Organs* **16**, 195–202 (1992).
51. Chen, Z. *et al.* Flow features and device-induced blood trauma in CF-VADs under a pulsatile blood flow condition: A CFD comparative study. *Int. j. numer. method. biomed. eng.* **34**, e2924 (2018).
52. Colacino, F. M., Moscato, F., Piedimonte, F., Arabia, M. & Danieli, G. A. Left Ventricle Load Impedance Control by Apical VAD Can Help Heart Recovery and Patient Perfusion: A Numerical Study. *ASAIO J.* **53**, 263–277 (2007).
53. Ochsner, G. *et al.* A Novel Interface for Hybrid Mock Circulations to Evaluate Ventricular Assist Devices. *IEEE Trans. Biomed. Eng.* **60**, 507–516 (2013).
54. Petrou, A. *et al.* Viscosity Prediction in a Physiologically Controlled

- Ventricular Assist Device. *IEEE Trans. Biomed. Eng.* **65**, 2355–2364 (2018).
55. Kaufmann, F. & Krabatsch, T. Using medical imaging for the detection of adverse events (“incidents”) during the utilization of left ventricular assist devices in adult patients with advanced heart failure. *Expert Rev. Med. Devices* **13**, 463–474 (2016).
  56. Ochsner, G. *et al.* In Vivo Evaluation of Physiologic Control Algorithms for Left Ventricular Assist Devices Based on Left Ventricular Volume or Pressure. *ASAIO J.* **63**, 568–577 (2017).
  57. Mansouri, M. *et al.* Preload-based Starling-like control of rotary blood pumps: An in-vitro evaluation. *PLoS One* **12**, e0172393 (2017).
  58. Habigt, M. A. *et al.* In vivo evaluation of two adaptive Starling-like control algorithms for left ventricular assist devices. *Biomed. Eng. / Biomed. Tech.* **66**, 257–266 (2021).
  59. Petrou, A. *et al.* A Physiological Controller for Turbodynamic Ventricular Assist Devices Based on Left Ventricular Systolic Pressure. *Artif. Organs* **40**, 842–855 (2016).
  60. Ochsner, G. *et al.* A Physiological Controller for Turbodynamic Ventricular Assist Devices Based on a Measurement of the Left Ventricular Volume. *Artif. Organs* **38**, 527–538 (2014).
  61. Petrou, A. *et al.* Standardized Comparison of Selected Physiological Controllers for Rotary Blood Pumps: In Vitro Study. *Artif. Organs* **42**, E29–E42 (2018).
  62. Ketelhut, M. *et al.* Iterative Learning Control of a Left Ventricular Assist Device. *IFAC-PapersOnLine* **50**, 6684–6690 (2017).
  63. Fetanat, M., Stevens, M., Hayward, C. & Lovell, N. H. A Physiological Control System for an Implantable Heart Pump That Accommodates for Interpatient and Inpatient Variations. *IEEE Trans. Biomed. Eng.* **67**, 1167–1175 (2020).
  64. Petrou, A., Monn, M., Meboldt, M. & Schmid Daners, M. A Novel Multi-objective Physiological Control System for Rotary Left Ventricular Assist Devices. *Ann. Biomed. Eng.* **45**, 2899–2910 (2017).
  65. Waters, T. *et al.* Motor feedback physiological control for a continuous flow ventricular assist device. *Artif. Organs* **23**, 480–486 (1999).
  66. Bullister, E., Reich, S. & Sluetz, J. Physiologic Control Algorithms for Rotary Blood Pumps Using Pressure Sensor Input. *Artif. Organs* **26**, 931–938 (2002).
  67. Moscato, F. *et al.* Left Ventricle Afterload Impedance Control by an Axial

- Flow Ventricular Assist Device: A Potential Tool for Ventricular Recovery. *Artif. Organs* **34**, 736–744 (2010).
68. Wang, Y., Koenig, S. C., Slaughter, M. S. & Giridharan, G. A. Rotary blood pump control strategy for preventing left ventricular suction. *ASAIO J.* **61**, 21–30 (2015).
69. Ferreira, A., Boston, J. R. & Antaki, J. F. A Control System for Rotary Blood Pumps Based on Suction Detection. *IEEE Trans. Biomed. Eng.* **56**, 656–665 (2009).
70. Vollkron, M. *et al.* Development of a Reliable Automatic Speed Control System for Rotary Blood Pumps. *J. Hear. Lung Transplant.* **24**, 1878–1885 (2005).
71. Karantonis, D. M. *et al.* Noninvasive Activity-based Control of an Implantable Rotary Blood Pump: Comparative Software Simulation Study. *Artif. Organs* **34**, E34–E45 (2010).
72. Maw, M. *et al.* A Sensorless Modular Multiobjective Control Algorithm for Left Ventricular Assist Devices: A Clinical Pilot Study. *Front. Cardiovasc. Med.* **9**, 1–11 (2022).
73. Koh, V. C. A. *et al.* A centralized multi-objective model predictive control for a biventricular assist device: An in vitro evaluation. *Biomed. Signal Process. Control* **59**, 101914 (2020).
74. Rüschen, D. *et al.* Minimizing left ventricular stroke work with iterative learning flow profile control of rotary blood pumps. *Biomed. Signal Process. Control* **31**, 444–451 (2017).
75. Ketelhut, M., Stemmler, S., Gesenhues, J., Hein, M. & Abel, D. Iterative learning control of ventricular assist devices with variable cycle durations. *Control Eng. Pract.* **83**, 33–44 (2019).
76. Schima, H. *et al.* First clinical experience with an automatic control system for rotary blood pumps during ergometry and right-heart catheterization. *J. Hear. Lung Transplant.* **25**, 167–173 (2006).
77. Maw, M., Moscato, F. & Gross, C. Novel Solutions for Patient Monitoring and Mechanical Circulatory Support Device Control. in *Mechanical Support for Heart Failure* (eds. Karimov, J. H., Fukamachi, K. & Starling, R. C.) (Springer International Publishing, 2020). doi:10.1007/978-3-030-47809-4
78. Dual, S. A. Measurement principles for a real-time Cardiac Volume Sensor. (2018). doi:doi.org/10.3929/ethz-b-000339587
79. Shin, K.-H., Moon, C.-R., Lee, T.-H., Lim, C.-H. & Kim, Y.-J. Flexible wireless pressure sensor module. *Sensors Actuators A Phys.* **123–124**, 30–35



(2005).

80. Boutry, C. M. *et al.* Biodegradable and flexible arterial-pulse sensor for the wireless monitoring of blood flow. *Nat. Biomed. Eng.* **3**, 47–57 (2019).
81. Ruhhammer, J. *et al.* Magnetic sensor for arterial distension and blood pressure monitoring. *Biomed. Microdevices* **16**, 815–827 (2014).
82. Zhang, T., Ochoa, M., Rahimi, R. & Ziaie, B. A wireless, smartphone-aided magnetic strain sensor for biomedical applications. in *2017 IEEE 30th International Conference on Micro Electro Mechanical Systems (MEMS)* 235–238 (IEEE, 2017). doi:10.1109/MEMSYS.2017.7863384
83. Bingger, P., Zens, M. & Woias, P. Highly flexible capacitive strain gauge for continuous long-term blood pressure monitoring. *Biomed. Microdevices* **14**, 573–581 (2012).
84. Tchanchaleishvili, V. *et al.* Clinical Implications of Physiologic Flow Adjustment in Continuous-Flow Left Ventricular Assist Devices. *ASAIO J.* **63**, 241–250 (2017).
85. Cleven, N. J. *et al.* A Novel Fully Implantable Wireless Sensor System for Monitoring Hypertension Patients. *IEEE Trans. Biomed. Eng.* **59**, 3124–3130 (2012).
86. Dual, S. A. *et al.* Continuous Heart Volume Monitoring by Fully Implantable Soft Strain Sensor. *Adv. Healthc. Mater.* **9**, 2000855 (2020).
87. Vennemann, B., Obrist, D. & Rösigen, T. A smartphone-enabled wireless and batteryless implantable blood flow sensor for remote monitoring of prosthetic heart valve function. *PLoS One* **15**, e0227372 (2020).
88. Von Petersdorff-Campen, K., Dupuch, M. A., Magkoutas, K., Hierold, C. & Schmid Daners, M. Pressure and Bernoulli-based Flow Measurement via a Tapered Inflow VAD Cannula. *IEEE Trans. Biomed. Eng.* **9294**, 1–1 (2021).
89. Hubbert, L., Baranowski, J., Delshad, B. & Ahn, H. First Implantation in Human of a Wireless Miniaturized Intracardiac Pressure Sensor in a Patient with a HeartMate II™. *J. Hear. Lung Transplant.* **33**, S13 (2014).
90. Guglin, M., George, B., Branam, S. & Hart, A. CardioMEMS™ in LVAD Patients: A Case Series. *VAD J.* **2**, 1–6 (2016).
91. Verdejo, H. E. *et al.* Comparison of a Radiofrequency-Based Wireless Pressure Sensor to Swan-Ganz Catheter and Echocardiography for Ambulatory Assessment of Pulmonary Artery Pressure in Heart Failure. *J. Am. Coll. Cardiol.* **50**, 2375–2382 (2007).
92. Granegger, M., Moscato, F., Casas, F., Wieselthaler, G. & Schima, H.

- Development of a Pump Flow Estimator for Rotary Blood Pumps to Enhance Monitoring of Ventricular Function. *Artif. Organs* **36**, 691–699 (2012).
93. Giridharan, G. A. & Skliar, M. Physiological Control of Blood Pumps Using Intrinsic Pump Parameters: A Computer Simulation Study. *Artif. Organs* **30**, 301–307 (2006).
94. Kitamura, T. *et al.* Physical Model-Based Indirect Measurements of Blood Pressure and Flow Using a Centrifugal Pump. *Artif. Organs* **24**, 589–593 (2000).
95. AlOmari, A. H., Savkin, A. V., Karantonis, D. M., Lim, E. & Lovell, N. H. Non-invasive estimation of pulsatile flow and differential pressure in an implantable rotary blood pump for heart failure patients. *Physiol. Meas.* **30**, 371–386 (2009).
96. Malagutti, N. *et al.* Noninvasive Average Flow Estimation for an Implantable Rotary Blood Pump: A New Algorithm Incorporating the Role of Blood Viscosity. *Artif. Organs* **31**, 45–52 (2007).
97. Lai, J. V., Muthiah, K., Macdonald, P. S., Jansz, P. & Hayward, C. S. Estimation of left ventricular assist device pre-load using pump flow waveform analysis. *J. Hear. Lung Transplant.* **36**, 240–242 (2017).
98. Petrou, A. *et al.* Cardiac Output Estimation: Online Implementation for Left Ventricular Assist Device Support. *IEEE Trans. Biomed. Eng.* **68**, 1990–1998 (2021).
99. Magkoutas, K. *et al.* Continuous Monitoring of Blood Pressure and Vascular Hemodynamic Properties with Miniature Extravascular Hall-Based Magnetic Sensor. *JACC Basic to Transl. Sci.* 1–28 (2022).
100. Magkoutas, K., Wang, F., Forster, O., Meboldt, M. & Schmid Daners, M. CARD9: Cardiac Contractility Estimation Based on Left Ventricular Pressure: Comparison of Time Series Classifiers and Graph-based Neural Networks. *ASAIO J.* **68**, 48–48 (2022).
101. Magkoutas, K., Arm, P., Meboldt, M. & Schmid Daners, M. Physiologic Data-Driven Iterative Learning Control for Left Ventricular Assist Devices. *Front. Cardiovasc. Med.* **9**, (2022).
102. Magkoutas, K., Nunes Rossato, L., Heim, M. & Schmid Daners, M. Genetic Algorithm-Based Optimization Framework for Control Parameters of Ventricular Assist Devices Introduction (under preparation). *Biomed. Signal Process. Control* (2022).
103. Magkoutas, K. *et al.* In-vitro Investigation of Endothelial Monolayer Retention on an Inflow VAD Cannula Inside a Beating Heart Phantom.

(2023).

104. Magkoutas, K. *et al.* Control of ventricular unloading using an electrocardiogram-synchronized pulsatile ventricular assist device under high stroke ratios. *Artif. Organs* **44**, E394–E405 (2020).
105. von Petersdorff-Campen, K., Dupuch, M. A., Magkoutas, K., Hierold, C. & Schmid Daners, M. BIO8: Cannula Add-On For Pressure And Flow Measurement In VADs. *ASAIO J.* **68**, 13–13 (2022).
106. Kourouklis, A. P. *et al.* Building an interdisciplinary program of cardiovascular research at the Swiss Federal Institute of Technology– the ETHHeart story. *iScience* **25**, 105157 (2022).
107. *Noncommunicable diseases country profiles 2018*. (World Health Organization, 2018). doi:10.5005/jp/books/11410\_18
108. Avolio, A. P., Butlin, M. & Walsh, A. Arterial blood pressure measurement and pulse wave analysis—their role in enhancing cardiovascular assessment. *Physiol. Meas.* **31**, R1–R47 (2010).
109. North, B. J. & Sinclair, D. A. The Intersection Between Aging and Cardiovascular Disease. *Circ. Res.* **110**, 1097–1108 (2012).
110. Potkay, J. A. Long term, implantable blood pressure monitoring systems. *Biomed. Microdevices* **10**, 379–392 (2008).
111. Lee, J. *et al.* Stretchable and suturable fibre sensors for wireless monitoring of connective tissue strain. *Nat. Electron.* **4**, 291–301 (2021).
112. Lee, J. *et al.* Highly Sensitive Multifilament Fiber Strain Sensors with Ultrabroad Sensing Range for Textile Electronics. *ACS Nano* **12**, 4259–4268 (2018).
113. Amjadi, M., Yoon, Y. J. & Park, I. Ultra-stretchable and skin-mountable strain sensors using carbon nanotubes–Ecoflex nanocomposites. *Nanotechnology* **26**, 375501 (2015).
114. Patel, A. K. *et al.* A Review on Atherosclerotic Biology, Wall Stiffness, Physics of Elasticity, and Its Ultrasound-Based Measurement. *Curr. Atheroscler. Rep.* **18**, 83 (2016).
115. Guinea, G. V. *et al.* Factors influencing the mechanical behaviour of healthy human descending thoracic aorta. *Physiol. Meas.* **31**, 1553–1565 (2010).
116. Chirinos, J. A. Arterial Stiffness: Basic Concepts and Measurement Techniques. *J. Cardiovasc. Transl. Res.* **5**, 243–255 (2012).
117. McGhee, B. H. & Bridges, E. J. Monitoring Arterial Blood Pressure: What

You May Not Know. *Crit. Care Nurse* **22**, 60–79 (2002).

118. Bickley, L. & Szilagyi, P. *Bates' guide to physical examination and history taking*. (Wolters Kluwer Health/Lippincott Williams & Wilkins, 2017). doi:10.1177/000306517202000305
119. Romagnoli, S. *et al.* Accuracy of invasive arterial pressure monitoring in cardiovascular patients: an observational study. *Crit. Care* **18**, 644 (2014).
120. Bowdle, T. A. Complications of invasive monitoring. *Anesthesiol. Clin. North America* **20**, 571–588 (2002).
121. Perloff, D. *et al.* Human blood pressure determination by sphygmomanometry. *Circulation* **88**, 2460–2470 (1993).
122. Wang, C. *et al.* Monitoring of the central blood pressure waveform via a conformal ultrasonic device. *Nat. Biomed. Eng.* **2**, 687–695 (2018).
123. Lipomi, D. J. *et al.* Skin-like pressure and strain sensors based on transparent elastic films of carbon nanotubes. *Nat. Nanotechnol.* **6**, 788–792 (2011).
124. Kang, S. *et al.* Highly Sensitive Pressure Sensor Based on Bioinspired Porous Structure for Real-Time Tactile Sensing. *Adv. Electron. Mater.* **2**, 1600356 (2016).
125. Chen, L. Y. *et al.* Continuous wireless pressure monitoring and mapping with ultra-small passive sensors for health monitoring and critical care. *Nat. Commun.* **5**, 1–10 (2014).
126. Watanabe, N. *et al.* Development and Validation of a Novel Cuff-Less Blood Pressure Monitoring Device. *JACC Basic to Transl. Sci.* **2**, 631–642 (2017).
127. Ogedegbe, G. & Pickering, T. Principles and Techniques of Blood Pressure Measurement. *Cardiol. Clin.* **28**, 571–586 (2010).
128. Morrison, T. M., Choi, G., Zarins, C. K. & Taylor, C. A. Circumferential and longitudinal cyclic strain of the human thoracic aorta: Age-related changes. *J. Vasc. Surg.* **49**, 1029–1036 (2009).
129. Kamoi, S. *et al.* Relationship between Stroke Volume and Pulse Wave Velocity. *IFAC-PapersOnLine* **48**, 285–290 (2015).
130. Furlani, E. P. *Permanent magnet and electromechanical devices: Materials, Analysis, and Applications*. (Academic Press, 2001).
131. Vlachopoulos, C., O'Rourke, M. & Nichols, W. W. *McDonald's Blood Flow in Arteries*. (CRC Press, 2011). doi:10.1201/b13568
132. Peterson, L. H., Jensen, R. E. & Parnell, J. Mechanical Properties of Arteries in Vivo. *Circ. Res.* **8**, 622–639 (1960).

133. Zimmermann, J. M. *et al.* Novel augmented physical simulator for the training of transcatheter cardiovascular interventions. *Catheter. Cardiovasc. Interv.* **95**, 1202–1209 (2020).
134. McGraw, K. O. & Wong, S. P. Forming inferences about some intraclass correlation coefficients. *Psychol. Methods* **1**, 30–46 (1996).
135. Arash Salarian. Intraclass Correlation Coefficient (ICC). (2022).
136. Yang, G.-Z. Introduction. in *Implantable Sensors and Systems* (ed. Yang, G.-Z.) 1–17 (Springer International Publishing, 2018). doi:10.1007/978-3-319-69748-2\_1
137. Yu, L., Kim, B. & Meng, E. Chronically Implanted Pressure Sensors: Challenges and State of the Field. *Sensors* **14**, 20620–20644 (2014).
138. Abe, Y. *et al.* Physiological control of a total artificial heart: conductance- and arterial pressure-based control. *J. Appl. Physiol.* **84**, 868–76 (1998).
139. Eddleman, E. E., Swartzell, R. H., Bancroft, W. H., Baldone, J. C. & Tucker, M. S. The use of the systolic time intervals for predicting left ventricular ejection fraction in ischemic heart disease. *Am. Heart J.* **93**, 450–454 (1977).
140. Baumert, M. *et al.* Mean nocturnal respiratory rate predicts cardiovascular and all-cause mortality in community-dwelling older men and women. *Eur. Respir. J.* **54**, 1802175 (2019).
141. Goetze, S. *et al.* Ambulatory respiratory rate trends identify patients at higher risk of worsening heart failure in implantable cardioverter defibrillator and biventricular device recipients: a novel ambulatory parameter to optimize heart failure management. *J. Interv. Card. Electrophysiol.* **43**, 21–29 (2015).
142. Mikael, L. de R. *et al.* Vascular Aging and Arterial Stiffness. *Arq. Bras. Cardiol.* 253–258 (2017). doi:10.5935/abc.20170091
143. Virani, S. S. *et al.* *Heart disease and stroke statistics—2020 update: A report from the American Heart Association.* *Circulation* (2020). doi:10.1161/CIR.0000000000000757
144. Roger, V. L. Epidemiology of Heart Failure. *Circ. Res.* **128**, 1421–1434 (2021).
145. Cain, M. T., Firstenberg, M. S. & Cleveland, J. C. Heart Transplant and Ventricular Assist: Cardiac Surgery and Heart Failure Perspective. *US Cardiol. Rev.* **15**, (2021).
146. Murali, S. Long-term Circulatory Support – The Left Ventricular Assist System for Advanced Heart Failure. *US Cardiol. Rev.* **1**, 145–147 (2004).

147. Kormos, R. L. *et al.* The Society of Thoracic Surgeons Intermaacs Database Annual Report: Evolving Indications, Outcomes, and Scientific Partnerships. *Ann. Thorac. Surg.* **107**, 341–353 (2019).
148. Loor, G. & Gonzalez-Stawinski, G. Pulsatile vs. continuous flow in ventricular assist device therapy. *Best Pract. Res. Clin. Anaesthesiol.* **26**, 105–115 (2012).
149. Shah, P., Tantry, U. S., Bliden, K. P. & Gurbel, P. A. Bleeding and thrombosis associated with ventricular assist device therapy. *J. Hear. Lung Transplant.* **36**, 1164–1173 (2017).
150. Pak, S. W. *et al.* Prevalence of de novo aortic insufficiency during long-term support with left ventricular assist devices. *J. Hear. Lung Transplant.* **29**, 1172–1176 (2010).
151. van der Merwe, J., Paul, E. & Rosenfeldt, F. L. Early Gastrointestinal Complications From Ventricular Assist Devices is Increased by Non-Pulsatile Flow. *Hear. Lung Circ.* **29**, 295–300 (2020).
152. Li, T. *et al.* Intelligent and strong robust CVS-LVAD control based on soft-actor-critic algorithm. *Artif. Intell. Med.* **128**, 102308 (2022).
153. Soucy, K. G., Koenig, S. C., Giridharan, G. A., Sobieski, M. A. & Slaughter, M. S. Rotary Pumps and Diminished Pulsatility. *ASAIO J.* **59**, 355–366 (2013).
154. Kato, T. S. *et al.* Effects of continuous-flow versus pulsatile-flow left ventricular assist devices on myocardial unloading and remodeling. *Circ. Hear. Fail.* **4**, 546–553 (2011).
155. Letsou, G. V. *et al.* Improved left ventricular unloading and circulatory support with synchronized pulsatile left ventricular assistance compared with continuous-flow left ventricular assistance in an acute porcine left ventricular failure model. *J. Thorac. Cardiovasc. Surg.* **140**, 1181–1188 (2010).
156. Naito, N. *et al.* Rotational speed modulation used with continuous-flow left ventricular assist device provides good pulsatility†. *Interact. Cardiovasc. Thorac. Surg.* **26**, 119–123 (2018).
157. Ando, M. *et al.* Electrocardiogram-Synchronized Rotational Speed Change Mode in Rotary Pumps Could Improve Pulsatility. *Artif. Organs* **35**, 941–947 (2011).
158. Ising, M. S., Sobieski, M. A., Slaughter, M. S., Koenig, S. C. & Giridharan, G. A. Feasibility of Pump Speed Modulation for Restoring Vascular Pulsatility with Rotary Blood Pumps. *ASAIO J.* **61**, 526–532 (2015).
159. Soucy, K. G. *et al.* Rotary pump speed modulation for generating pulsatile

- flow and phasic left ventricular volume unloading in a bovine model of chronic ischemic heart failure. *J. Hear. Lung Transplant.* **34**, 122–131 (2015).
160. Amacher, R. *et al.* Numerical Optimal Control of Turbo Dynamic Ventricular Assist Devices. *Bioengineering* **1**, 22–46 (2013).
161. Zeile, C. *et al.* An Intra-Cycle Optimal Control Framework for Ventricular Assist Devices Based on Atrioventricular Plane Displacement Modeling. *Ann. Biomed. Eng.* **49**, 3508–3523 (2021).
162. Amacher, R., Ochsner, G. & Schmid Daners, M. Synchronized pulsatile speed control of turbodynamic left ventricular assist devices: Review and prospects. *Artif. Organs* **38**, 867–875 (2014).
163. Ising, M. *et al.* Flow Modulation Algorithms for Continuous Flow Left Ventricular Assist Devices to Increase Vascular Pulsatility: A Computer Simulation Study. *Cardiovasc. Eng. Technol.* **2**, 90–100 (2011).
164. Rebholz, M., Amacher, R., Petrou, A., Meboldt, M. & Schmid Daners, M. High-frequency operation of a pulsatile VAD – a simulation study. *Biomed. Eng. / Biomed. Tech.* **62**, 161–170 (2017).
165. Chi, R., Liu, X., Zhang, R., Hou, Z. & Huang, B. Constrained data-driven optimal iterative learning control. *J. Process Control* **55**, 10–29 (2017).
166. Ziegler, J. G. & Nichols, N. B. Optimum Settings for Automatic Controllers. *J. Dyn. Syst. Meas. Control* **115**, 220–222 (1993).
167. Mansouri, M., Salamonsen, R. F., Lim, E., Akmeliawati, R. & Lovell, N. H. Preload-based starling-like control for rotary blood pumps: Numerical comparison with pulsatility control and constant speed operation. *PLoS One* **10**, 1–16 (2015).
168. Prinzing, A. *et al.* Left ventricular assist devices—current state and perspectives. *J. Thorac. Dis.* **8**, E660–E666 (2016).
169. Du, Y. *et al.* Heart Transplantation: A Bibliometric Review From 1990-2021. *Curr. Probl. Cardiol.* 101176 (2022). doi:10.1016/j.cpcardiol.2022.101176
170. Monteagudo-Vela, M., Krasopoulos, G., Athanasiou, T., Tsui, S. & Kourliouros, A. Impact of third-generation left ventricular assist devices on quality of life: Scoping review and meta-analysis. *Artif. Organs* 1–7 (2022). doi:10.1111/aor.14186
171. Frazier, O. H. Unforeseen Consequences of Therapy With Continuous-Flow Pumps. *Circ. Hear. Fail.* **3**, 647–649 (2010).
172. Mehra, M. R. *et al.* A Fully Magnetically Levitated Left Ventricular Assist Device — Final Report. *N. Engl. J. Med.* **380**, 1618–1627 (2019).

173. Medvedev, A. L. *et al.* Unlocking the box: basic requirements for an ideal ventricular assist device controller. *Expert Rev. Med. Devices* **14**, 393–400 (2017).
174. Pauls, J. P. *et al.* Evaluation of Physiological Control Systems for Rotary Left Ventricular Assist Devices: An In-Vitro Study. *Ann. Biomed. Eng.* **44**, 2377–2387 (2016).
175. Bakouri, M. Physiological Control Law for Rotary Blood Pumps with Full-State Feedback Method. *Appl. Sci.* **9**, 4593 (2019).
176. Wang, Y. *et al.* Sensorless Physiologic Control, Suction Prevention, and Flow Balancing Algorithm for Rotary Biventricular Assist Devices; Sensorless Physiologic Control, Suction Prevention, and Flow Balancing Algorithm for Rotary Biventricular Assist Devices. *IEEE Trans. Control Syst. Technol.* **27**, 717 (2019).
177. Abdel-Basset, M., Abdel-Fatah, L. & Sangaiah, A. K. Metaheuristic Algorithms: A Comprehensive Review. in *Computational Intelligence for Multimedia Big Data on the Cloud with Engineering Applications* 185–231 (Elsevier, 2018). doi:10.1016/B978-0-12-813314-9.00010-4
178. Acharya, D. & Das, D. K. Swarm optimization approach to design PID controller for artificially ventilated human respiratory system. *Comput. Methods Programs Biomed.* **198**, 105776 (2021).
179. Aly, A. A. PID Parameters Optimization Using Genetic Algorithm Technique for Electrohydraulic Servo Control System. *Intell. Control Autom.* **02**, 69–76 (2011).
180. Hultmann Ayala, H. V. & dos Santos Coelho, L. Tuning of PID controller based on a multiobjective genetic algorithm applied to a robotic manipulator. *Expert Syst. Appl.* **39**, 8968–8974 (2012).
181. Simaan, M. A., Ferreira, A., Chen, S., Antaki, J. F. & Galati, D. G. A Dynamical State Space Representation and Performance Analysis of a Feedback-Controlled Rotary Left Ventricular Assist Device. *IEEE Trans. Control Syst. Technol.* **17**, 15–28 (2009).
182. Ochsner, G., Amacher, R. & Schmid Daners, M. Emulation of ventricular suction in a hybrid mock circulation. in *2013 European Control Conference (ECC)* 3108–3112 (IEEE, 2013). doi:10.23919/ECC.2013.6669530
183. Boes, S. *et al.* Hydraulic Characterization of Implantable Rotary Blood Pumps. *IEEE Trans. Biomed. Eng.* **66**, 1618–1627 (2019).
184. Sayyaadi, H. Optimization basics. in *Modeling, Assessment, and Optimization of Energy Systems* 327–430 (Elsevier, 2021). doi:10.1016/B978-0-12-816656-



7.00006-3

185. Caciagli, A., Baars, R. J., Philipse, A. P. & Kuipers, B. W. M. Exact expression for the magnetic field of a finite cylinder with arbitrary uniform magnetization. *J. Magn. Magn. Mater.* **456**, 423–432 (2018).
186. Derby, N. & Olbert, S. Cylindrical magnets and ideal solenoids. *Am. J. Phys.* **78**, 229–235 (2010).



# *Curriculum vitae*

## **Personal Data**

Name	Konstantinos Magkoutas
Date of Birth	16.03.1992
Citizen of	Zurich, Switzerland
Nationality	Greek
Email	<a href="mailto:magkoutk@ethz.ch">magkoutk@ethz.ch</a> , <a href="mailto:kmagkout@gmail.com">kmagkout@gmail.com</a>

## **Education**

2018 - 2022	<b>Doctor of Science (Dr. sc. ETH Zurich)</b> in Mechanical Engineering, Product Development Group Zurich, ETH Zurich (ETHZ), Switzerland
2017 - 2018	<b>Master of Science (M.Sc.)</b> in Gas Turbine Technology (Thermal Power), Propulsion Engineering Center, Cranfield, United Kingdom (first class honor degree)
2010 - 2016	<b>Diploma (Dipl. Ing) in Mechanical Engineering</b> , Dept. of Mechanical Engineering, Thessaloniki, Greece

## **Professional Experience**

2018 - 2022	<b>Research associate</b> , Product Development Group Zurich, ETHZ, Switzerland
2016 - 2017	<b>Warehouse management</b> , Hellenic Air-force (Army), Thessaloniki, Greece
2014 – 2014 (3 months)	<b>Project engineer</b> , Internship, LABOR S.A., Athens, Greece

## **Honors**

2017	<b>Awarded 5000£ bursary towards the completion of Thermal Power MSc program</b> , Cranfield University, Propulsion Engineering Center, School of Aerospace, Transport and Manufacturing
2015	<b>3<sup>rd</sup> Place Business Plan award for Self-Printing business proposal</b> , Aristotle University of Thessaloniki, Dept. of Mechanical Engineering, Thessaloniki Greece

## ***List of Publications***

- [1] Magkoutas, K. *et al.* Continuous Monitoring of Blood Pressure and Vascular Hemodynamic Properties with Miniature Extravascular Hall-Based Magnetic Sensor. *JACC Basic to Transl. Sci.* 1–28 (2023) (accepted for publication)
- [2] Magkoutas, K., Wang, F., Forster, O., Meboldt, M. & Schmid Daners, M. CARD9: Cardiac Contractility Estimation Based on Left Ventricular Pressure: Comparison of Time Series Classifiers and Graph-based Neural Networks. *ASAIO J.* 68, 48–48 (2022).
- [3] Magkoutas, K., Arm, P., Meboldt, M. & Schmid Daners, M. Physiologic Data-Driven Iterative Learning Control for Left Ventricular Assist Devices. *Front. Cardiovasc. Med.* **9**, (2022).
- [4] Magkoutas, K., Nunes Rossato, L., Heim, M. & Schmid Daners, M. Genetic Algorithm-Based Optimization Framework for Control Parameters of Ventricular Assist Devices Introduction. *Biomed. Signal Process. Control* (2023).
- [5] Magkoutas, K. *et al.* In-vitro Investigation of Endothelial Monolayer Retention on an Inflow VAD Cannula Inside a Beating Heart Phantom. (2023). (under revision)
- [6] von Petersdorff-Campen, K., Dupuch, M. A., Magkoutas, K., Hierold, C. & Schmid Daners, M. BIO8: Cannula Add-On For Pressure And Flow Measurement In VADs. *ASAIO J.* **68**, 13–13 (2022).
- [7] Dual, S. A. *et al.* Continuous Heart Volume Monitoring by Fully Implantable Soft Strain Sensor. *Adv. Healthc. Mater.* **9**, 1–11 (2020).
- [8] Kourouklis, A. P. *et al.* Building an interdisciplinary program of cardiovascular research at the Swiss Federal Institute of Technology– the EHeart story. *iScience* **25**, 105157 (2022).
- [9] Magkoutas, K., Efstathiadis, T. & Kalfas, A. Experimental investigation of geometry effects and performance of five-hole probe in measuring jets in crossflow. *E3S Web Conf.* 345, 01005 (2022).
- [10] Petrou, A. *et al.* Cardiac Output Estimation: Online Implementation for Left Ventricular Assist Device Support. *IEEE Trans. Biomed. Eng.* **68**, 1990–1998 (2021).
- [11] von Petersdorff-Campen, K., Dupuch, M. A., Magkoutas, K., Hierold, C. & Schmid Daners, M. Pressure and Bernoulli-based Flow Measurement via a Tapered Inflow VAD Cannula. *IEEE Trans. Biomed. Eng.* **9294**, 1–1 (2021).
- [12] Magkoutas, K. *et al.* Control of ventricular unloading using an electrocardiogram-synchronized pulsatile ventricular assist device under high stroke ratios. *Artif. Organs* **44**, E394–E405 (2020).